A role for the Sarcolemmal membrane associated protein isoform 3 in development.

Taha Rehmani

Thesis submitted to the University of Ottawa in partial fulfillment of the requirements for the Ph.D. degree in Cellular and Molecular Medicine

Department of Cellular and Molecular Medicine

Faculty of Medicine

University of Ottawa,

Ottawa, Ontario, Canada

Permissions:

For the following articles published in MDPI:

- Rehmani T., Mlynarova J, Byers J, Salih M, Tuana BS. (2021). Specific Deletion of the FHA Domain Containing SLMAP3 Isoform in Postnatal Myocardium Has No Impact on Structure or Function. *Cardiogenetics.* 2021; 11(4):164-184.

- Rehmani T., Salih M. & Tuana B.S. (2019). Cardiac-Specific Cre Induces Age-Dependent Dilated Cardiomyopathy (DCM) in Mice. *Molecules 26;24(6).*

Abstract

Sarcolemmal membrane associated proteins (SLMAPs) belong to a superfamily of tail anchored membrane proteins. The SLMAP gene alternatively splices to generate numerous isoforms broadly defined as SLMAP1 (~35 kDa), SLMAP2 (~45 kDa) and SLMAP3 (~80-95kDa). Notably, SLMAP3, the largest isoform is ubiquitously expressed and developmentally regulated, and has been linked to muscle formation, heart failure, and sudden cardiac death. SLMAP3 possesses a Forkhead-Associated (FHA) domain and regulates Hippo signaling via the STRIPAK complex, influencing cellular growth, death, and organogenesis. Employing a cre-lox mediated knockout approach, we targeted the SLMAP3 isoform in prenatal and postnatal mouse tissues to unravel its functional significance. Utilizing αMHC-MerCreMer, αMHC-cre, Nkx2.5-cre, and CMV-cre mouse lines, we investigated SLMAP3's role in postnatal, perinatal, prenatal hearts, and in a global context.

Using αMHC-MerCreMer and αMHC-cre mice we knockout (KO) SLMAP3 in postnatal and perinatal mouse hearts. However, *in-vivo* analyses revealed no significant alterations in cardiac structure or function in aged SLMAP3-deficient mice under normal or stressed conditions. Furthermore, the absence of SLMAP3 did not affect Hippo signaling. Interestingly, during longevity studies we discovered that the αMHC-cre mice were developing a lethal dilated cardiomyopathy (DCM) by 7 months of age due to robust cre activity within the myocardium. Cre caused a DNA damage response through the downregulation of activated p38 and increased expression of JNK, p53, and Bax, known inducers of cardiomyocyte death resulting in fibrosis. Thus, our data urges caution when employing this model and to use appropriate cre only controls.

To examine role of SLMAP3 during cardiac development we nullified SLMAP3 using the Nkx2.5-cre, ablating SLMAP3 during early cardiogenesis and up to adulthood. Hearts from SLMAP3- KO mouse embryos were noticeably smaller, with all four chambers displaying thinner myocardium. This phenotype was not linked to Hippo signaling or cell proliferation as SLMAP3-KO Embryonic day (E)12.5 hearts showed no changes in Hippo signaling or changes in proliferative events using pH3 or Ki67 markers.

Microscopy analysis indicated that SLMAP3-KO cardiomyocytes were significantly smaller than Wt. Mediators of the cardiomyocyte hypertrophic response AKT1 and MTOR1 were not significantly altered in KO hearts, thus cardiac size was regulated through alternate mechanisms. Remarkably, the SLMAP3-KO hearts recovered with normal physiology after the postnatal period. We noted a marked increase of SLMAP1 and SLMAP2 expression spanning from early cardiogenesis into adulthood equally in Wt and SLMAP3-KO hearts. The dynamic regulation of these isoforms may underscore their potential compensatory role in cardiac development in the absence of SLMAP3.

The global KO of SLMAP3 using CMV-cre was embryonic lethal, presenting with stunted growth and craniorachischisis. These phenotypes were not associated with dysfunctional Hippo signaling or cell proliferation. E8.5 and E9.5 SLMAP3-KO neural plates displayed reduced length and width signifying defective convergent extension. Planar cell polarity (PCP) components, disheveled-2 and -3, and the activity of PCP targets, phospho-ROCK2, phospho-cofilin and phospho-JNK1/2 were dysregulated in SLMAP3-KO E12.5 brain lysates. Cytoskeletal proteins, actin, Nestin, and apical marker PKC zeta, were not polarized to their specified apical or basal domains nor were adherens and tight junctions in SLMAP3-deficient neural tubes and neuroepithelial cells (NEPCs) implicating perturbed apical-basal polarity (ABP). Proteomic analysis of SLMAP3 revealed associations with centrosomal proteins (Pcm1), Golgi (Golgb1), transport proteins (Kif5c) and the polarity protein, Scribble. Loss of SLMAP3 resulted in abnormal centrosomal localization, fragmented Golgi apparatus and mislocalized Scribble in neural tubes and NEPCs. Our data define a critical role for SLMAP3 in neurulation through mechanism that impacts centrosomal and Golgi dynamics.

Overall, this data defines the role of SLMAP3 as a critical component that regulates embryonic development, particularly during neurulation and cardiogenesis without impacting Hippo signaling. This research advances our understanding of the role of SLMAP3 in normal development and function with potential involvement in various diseases states, including, cardiogenesis, neural tube defects, and stunted growth.

Table of Contents

List of Figures

Chapter One:

Chapter Two:

Chapter Three:

Chapter Four:

Chapter Five

Chapter Six:

List of Tables

Chapter Two:

Chapter Three:

Chapter Four:

Chapter Five:

List of Abbreviations

ABP	Apical-basal polarity
AJ	Adherens junctions
AKT1	RAC (Rho family)-alpha serine/threonine-protein kinase
ANOVA	Analysis of variance
BMP	Bone Morphogenetic Protein
C.E.	Convergent Extension
CHD	Congenital Heart Disease
CMV	Cytomegalovirus
CNS	Central Nervous System
Cre	Causes recombination
CRN	Craniorachischisis
DCM	Dilated cardiomyopathy
DLHP	Dorsolateral Hinge Point
DSB	Double strand breaks
DVL	Dishevelled
E(n)	Embryonic day (n)
EC	Excitation-contraction
ECG	Electrocardiogram
ECHO	Echocardiography
ECM	Extracellular matrix
EEA1	Early endosomal antigen 1
EF	Ejection fraction
ER	Endoplasmic reticulum
ERC	Endosomal recycling complex
FGF	Fibroblast growth factor
FHA	Forkhead associated domain
FHF	First Heart Field
Flox	Flanked with loxP
Fzd	Frizzled
FS	Fractional shortening
Gy	Gray
GLUT4	Glucose transporter 4
H&E	Hematoxylin and Eosin
HCM	Hypertrophic cardiomyopathy
Hs90	Heat shock 90 protein
I.P.	Intraperitoneal
IP	Immunoprecipitation
ISO	Isoproterenol
IVS; d/s	Intraventricular septum; diastole/systole
JNK	c-Jun N-terminal kinase
KD	Knockdown
Ki67	Antigen Kiel 67
KO	Knockout
LV	Left Ventricle
LVID; d/s	Left ventricular intradiameter; diastole/systole

LVPW; d/s Left ventricular posterior wall; diastole/systole
MER Modified estrogen receptor
MHP Median Hinge Point
MHC Myosin Heavy Chain
MS Mass-spectroscopy
MTOC Microtubule organizing center
MTOR1 Mammalian target of rapamycin complex 1
NEPC Neuroepithelial cells
NT Neural tube
NTC Neural tube closure
NTD Neural tube defect
OFT Outflow tract
PCP Planar cell polarity
PCR Polymerase chain reaction
P(n) Postnatal day (n)
pH3 Phosphorylated Histone 3
PKCζ Protein kinase C, zeta
PP2A Protein Phosphatase 2A
ROCK Rho-associated protein kinase
SCRIB Scribble
SDS-PAGE Sodium dodecyl sulfate polyacrylamide gel electrophoresis
sgRNA Single guide RNA
SHF Secondary Heart Field
shRNA Small hairpin RNA
siRNA Small interfering RNA
SLMAP Sarcolemmal membrane associated protein
SR Sarcoplasmic reticulum
STRIPAK Striatin Interacting Phosphatases and Kinases
TAM Tamoxifen
TBST Tris-buffered saline tween
TG Transgenic
TGF Transforming growth factor
TGN Transgolgi network
TJ Tight Junctions
TM1/TM2 Transmembrane domain 1/2
VAMP Vesicle associated membrane protein
VANGL Van-Goh associated protein
Wt Wildtype
YAP Yes-associated protein
α-MyHC alpha myosin heavy chain

Acknowledgements

First and foremost, I'd like to thank Dr. Balwant Tuana. I cannot express the gratitude and appreciation for the mentorship and guidance these past few years. I can say I would not be where I am without you and for all my future endeavors, I will utilize the tools you nurtured within me and to always FOCUS. I would also like to thank my TAC members, Dr. Mario Tiberi, Dr. Erik Suuronen, and Dr. Jeff Dilworth, for all the helpful feedback over the years.

I'd like to thank the members of the Tuana Lab, past and present. My first thanks go out to Maysoon Salih, your expertise, advise and encouragement lifted me, and I will always be grateful. To Ana, I feel incredibly lucky to have been your Ph.D. colleague, our cooperative nature and scientific dialogue elevated us as scientists and made our research results as profound as it is. To the Central Perk club, Ana, Mayra, Chloe, and my Arsenal brother Aiman, I couldn't have done it without you and the constant supply of caffeine.

I would like to thank my family. My parents, Nadeem and Uzma, your constant support is the main reason I am here today, I hope I make you proud. Ibrahim and Umar, my brothers and best friends, their wives Isbah, Manal, and my two nieces Inaya and Alya, for the constant support, food, and amazing company. To my second-generation siblings, Ayesha and Humza, for providing laughter, keeping me updated on the youth slang, high-school drama, and game nights. To my soon-to-be wife, Farah, for coming into my life at the perfect time.

Finally, I'd like to thank Arsenal FC. North London Forever.

Chapter One: General Introduction

1.1 Sarcolemmal Membrane Associated Protein

Sarcolemmal membrane associated proteins, or SLMAPs, are a family of tail anchored membrane proteins. SLMAP is encoded in chromosome 3p.13-21 in humans spanning approximately 122kbp, consisting of 24 exons and is highly conserved across different species (Guzzo et al. 2004). We discovered that the SLMAP gene codes for three transcripts: 3.5 kbp, 4.5 kbp, and 5.9 kbp (Wigle et al. 1997) which were revealed to be alternatively spliced and generated from a single locus. The three transcripts of SLMAP are translated into three isoforms: SLMAP1 (~35 kDa), SLMAP2 (~45kDa), and SLMAP3 (~80-91kDa) each with their own unique methionine codon (Wielowieyski et al. 2000). The SLMAP isoforms have their own unique variants due to alternative splicing of various exons within them which predict approximately dozens of variants of SLMAP. The 12 most common and characterized variants have been described in Figure 1 (Aken et al. 2016). The isoforms exhibit tissue-specificity as SLMAP3 is ubiquitously expressed whereas SLMAP1 and SLMAP2 were robustly expressed within the myocardium and skeletal muscle (Wigle et al. 1997). SLMAP is developmentally regulated due to the robust expression noted in mouse embryonic hearts at embryonic day(E) 9, E13 and E18 (Guzzo et al. 2005).

Structurally SLMAP isoforms are highly conserved (>90%) to one other towards the c-terminus however display diversity at n-terminal regions especially when the largest SLMAP3 isoform is compared to the shorter SLMAP1 and SLMAP2. This is because SLMAP3 houses an additional coiled-coil region and the forkhead associated domain (FHA) at it's amino-terminus, which have implicated SLMAP3 in cell cycle regulation and to localize within microtubule

organizing center (MTOC) (Guzzo et al. 2004). The conserved c-terminal region for SLMAP isoforms includes a coiled-coil domain and a transmembrane domain. The leucine rich coiled coil domain promotes protein-protein interaction through homo and heterodimerization (Guzzo et al. 2004). There are two transmembrane domains of SLMAP, TM1 or TM2, generated through mutually exclusive splicing of exon 23 or 24, respectively (Guzzo et al. 2005). The transmembrane domains localize SLMAP to subcellular compartments within the cell as immunofluorescent analysis indicated TM1 and TM2 localize to the cell membrane, sarcolemma, sarcoplasmic/endoplasmic reticulum (SR/ER), and nucleus however TM2 additionally localizes to mitochondria (Byers et al. 2009). SLMAPs share a structural homology with other tail anchored proteins such as Syntaxin and VAMP which are involved in membrane trafficking and fusion (Nader et al. 2012). We found that SLMAP colocalizes with SR proteins, Caveolin-3 and ryanodine receptor in adult rat cardiomyocytes suggesting that SLMAP is present at T-tubule membrane and SR suggesting a potential role in excitation-contraction (EC) coupling (Guzzo et al. 2005). The c-terminal transmembrane domain allows SLMAP to target different areas of the cardiomyocyte suggesting that SLMAP plays a role in membrane organization (Guzzo et al. 2004).

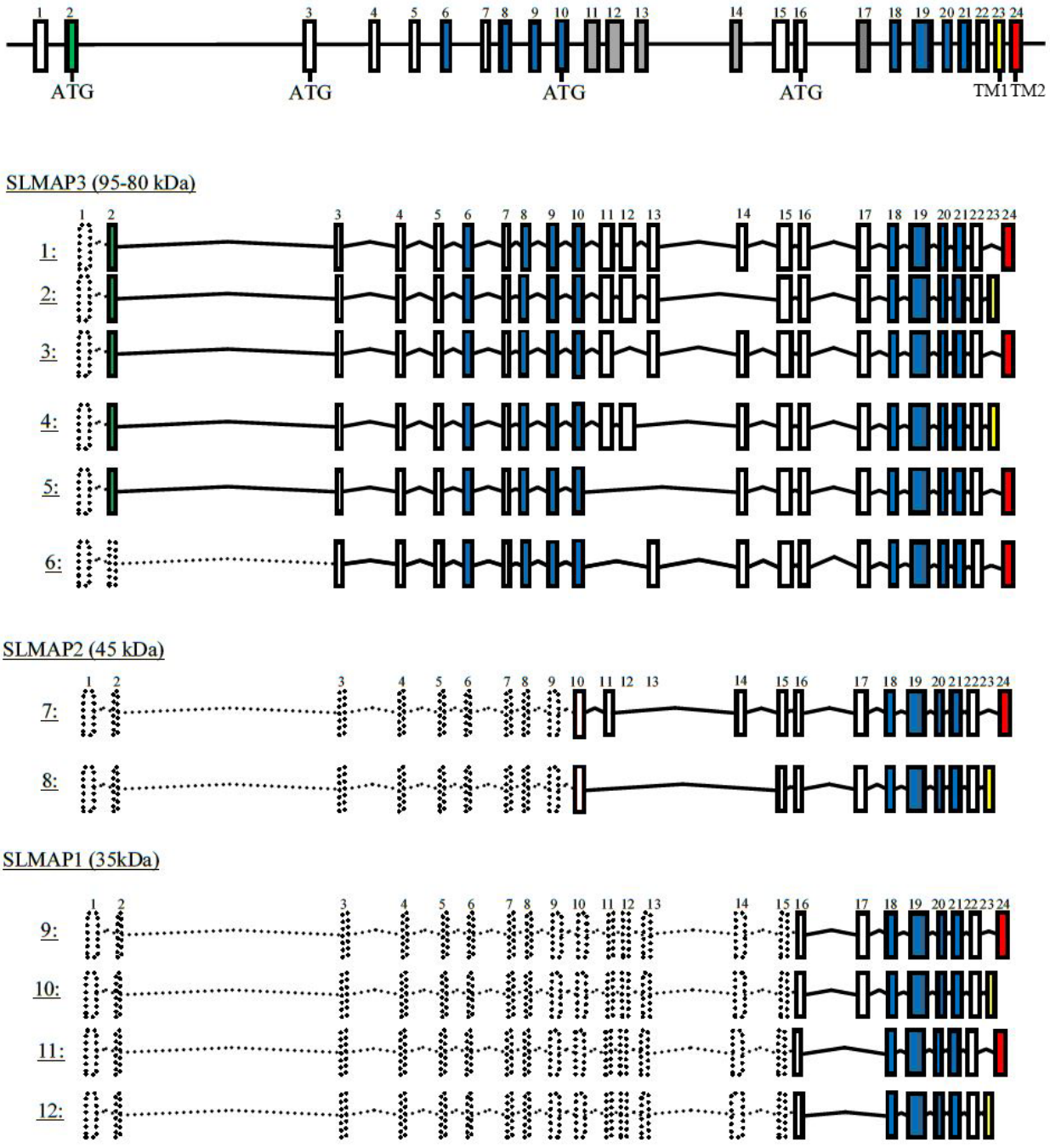

Figure 1. *Intron-exon junction of mouse SLMAP gene and its splice variants.* SLMAP consists of 24 exons (black) and alternatively splices to generate numerous isoforms grouped as three isoforms, SLMAP1 (35 kDa), SLMAP2 (45 kDa) and SLMAP3 (80-95 kDa). Start codon for SLMAP3, SLMAP2 and SLMAP1 are found at exon 2/3, 10 or 16 respectively. Alternative splicing of exons 11, 12, 13, 14, and 17 results in each isoform presenting unique variants. Exon 2 (green) codes for the FHA domain. Exons 6, 8, 9, 10, 18, 19, 20 and 21 (blue) code for coiled-coil LZ domains. Mutually exclusive exons 23 (yellow) and 24 (red) code for TM1 or TM2. Reprinted with permission from *(Rehmani et al. 2021)*

1.1.1 Implied roles of SLMAP in cell biology

Our lab has shown that SLMAP3 can integrate as a component of the microtubule organizing center (MTOC) and may serve a role in centrosomal functions based on staining with centrosome marker, γ-tubulin in NIH/3T3 cells (Guzzo et al. 2004). This interaction was mediated by FHA domain as truncation of this domain in mutated SLMAP3 decreased its localization to the centrosome (Guzzo et al. 2004). The FHA domain has binding partners involved in spindle bipolarity and centrosome separation, therefore implicating SLMAP3 as an important regulator of cell cycle (Sueishi, Takagi, and Yoneda 2000). In support of this, flow-cytometry analysis of overexpressing SLMAP3 NIH/3T3 cells showed an increase in proliferation compared to wildtype (Guzzo et al. 2004).

Further, SLMAP has been implicated in diabetes and diabetic retinopathy (Mohamed Farhan et al. 2022). A study showed that SLMAP can regulate trafficking of GLUT4 in the *Tally Ho* mouse model: a mouse that is susceptible to type 2 diabetes when given a high-fat diet. In these diabetic mice, a significant increase in cytosolic but not cell surface GLUT4 was observed which is similar to human patients exhibiting type 2 diabetes. These diabetic mice also had elevated levels of SLMAP1 and SLMAP2 in both the cytosol and plasma membrane suggesting an association between SLMAP and GLUT4 (Chen and Ding 2011). Intriguingly, when *Tally Ho* adipocytes were treated with SLMAP siRNA, this resulted in decreased glucose uptake implicating an impaired trafficking role of GLUT4 to the plasma membrane (Chen and Ding 2011). This study concluded that the tail anchored membrane homology shared between SLMAP and SNARE protein suggest SLMAP1 and SLMAP2 maybe be involved in fusion and trafficking of proteins such as GLUT4.

Protein-protein interaction studies have shown that SLMAP binds to the large multicomponent protein complex known as the STRIPAK (striatin interacting phosphatase and kinase) complex (Goudreault et al. 2009). STRIPAK complexes are diverse, containing up to 10 different protein families with many variants present within a cell simultaneously participating in diverse physiological functions such as tissue development, cell growth and homeostasis (Shi, Jiao, and Zhou 2016). The STRIPAK variant that binds SLMAP is commonly composed of; striatin-1/3, PP2A (protein phosphatase 2A-A structural subunit), PP2A-C (protein phosphatase 2A-Catalytic subunit), SIKE1 (suppressor of IKBKE1), STRIP1 (striatin interacting protein 1), CCM3 (cerebral cavernous malformation 3), MOB3, misshapen kinase 1 (MINK1) and germinal cell kinases III i.e. STK4, STK24 or STK25 (Hwang and Pallas 2013) (**Figure 2**). Single subunits of STRIPAK have also been found at other cellular locations, for example, striatin and STRIP have been detected at the nuclear envelope and the Golgi, while SLMAP reside at mitochondria and the endoplasmic reticulum (Kück, Radchenko, and Teichert 2019). STRIPAK complexes are conserved in fungus, Drosophila, mice and humans and shown to regulate various functions ranging from cell fusion, polarity vegetative growth and sexual development, thus suggesting a conserved role for SLMAP-STRIPAK across many organisms (Tang et al. 2019; Elramli et al. 2019; Nordzieke et al. 2015).

STRIPAK complexes are implicated in numerous signaling pathways, with recent studies indicating that the SLMAP-STRIPAK complex is a negative regulator of the Hippo signaling pathway. The Hippo pathway is a signaling cascade that plays a role in organogenesis, cell proliferation, and apoptosis (Zheng and Pan, 2019). The Hippo signaling cascade begins with activation of Hippo activating kinase, MST1/2, through external signals, causing it to physically interact with and phosphorylate SAV1. Phosphorylation of SAV1 results in the MST1/2-SAV1

complex to phosphorylate downstream component LATS1/2 which will phosphorylate the Hippo gene regulatory targets; YAP/TAZ, anchoring these co-transcriptional activators to the cytoplasm. Inhibiting or negatively regulating Hippo signaling causes a dephosphorylation cascade, where YAP/TAZ translocate into nucleus where they bind to transcriptional co-factors (TEADs) to promote proliferation and repress apoptosis (Yu, Zhao, and Guan 2015). SLMAP is shown to interact with phosphorylated MST1 and MST2, via the FHA domain of SLMAP3 to auto-phosphorylated linker regions of MST1/2. SLMAP3 will then recruit the STRIPAK-PP2A complex to MST1/2 complex causing the MST1/2 active sites (T180/T183) to dephosphorylate via PP2A, thereby negatively regulating the Hippo signaling pathway; enhancing proliferation and repressing apoptosis in 293FT cells (Bae et al. 2017). This finding was touted as a potential cancer therapeutic, as tumors have low Hippo signaling, thus dysregulating SLMAP-STRIPAK complex may inhibit the activity of YAP/TAZ (Couzens et al. 2013; Hauri et al. 2013). A recent study has shown that SLMAP containing biomolecular condensates can regulate the Hippo signaling pathway in HEK293 cells (Wang et al. 2022). The positive regulators of Hippo signaling pathway, AMOT and KIBRA, are activated during osmotic stress or cell contact inhibition, undergoing liquid-liquid phase separation to form biomolecular condensates, a subcellular "membraneless" organelle (Wang et al. 2022). This study showed that SLMAP-STRIPAK forms its own condensate which can coalesce with AMOT/KIBRA to inhibit Hippo signaling (Wang et al. 2022). Early in *Drosophila* development, apposing cells of the eye disc are established as either retinal progenitors or support cells of the peripodial epithelium, SLMAP-STRIPAK suppresses Hippo kinase activity with development and promote peripodial fate (Neal, Zhou, and Pignoni 2020).

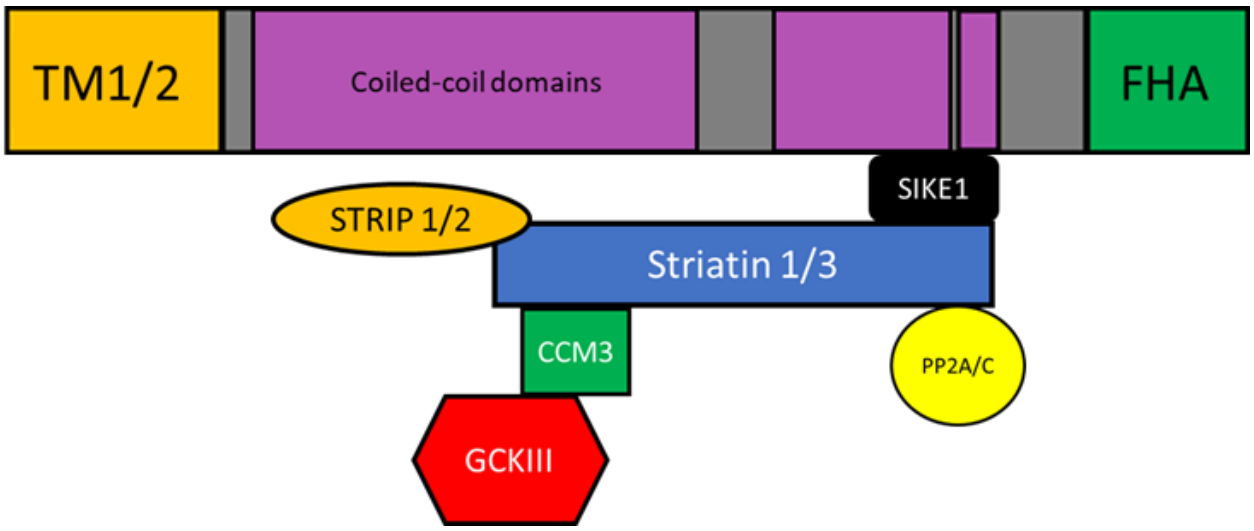

Figure 2. *A simplified model for SLMAP-STRIPAK complex in cell signaling.* SLMAP3 houses three unique domains, forkhead associated domain (FHA; green), Coiled-coil domains (C.C; purple) and alternatively spliced TM1 or TM2 domain (TM1/2; orange). SLMAP3 integrates with STRIPAK complex via SIKE1 at C.C domains. The FHA (forkhead associated) domain of SLMAP3 will interact with phosphorylated MST1/2 that can impact downstream cell signaling. Modified with permission from Rehmani, Tuana Lab.

The STRIPAK-SLMAP complex has been implicated in regulating early myogenesis. A study found that depletion of SLMAP resulted in a significant upregulation of the Hippo signaling pathway resulting in the reduction in size of the posterior compartment of adult *Drosophila* wings (Zheng et al. 2017). Further, using MEF2-GAL4 to cause a muscle specific depletion of SLMAP during pupal stages in *Drosophila* resulted in viable but flightless flies thus impacting flight muscle morphogenesis. This finding suggested that SLMAP had an essential role during developmental stages of myofibril assembly and muscle fiber growth (Kaya-Çopur et al. 2021)., This finding was similarly observed in our SLMAP3-depleted C2C12 myoblast cell, as these myoblasts were unable to fuse to form myotubes thus SLMAP3 (~80 kDa) appears to be indispensable during early skeletal myogenesis, (Guzzo et al. 2004). In skeletal muscle satellite cells of goats, research showed that silencing SLMAP resulted in up-regulation of MyoD, and down-regulation of MyoG and Myosin7, key genes that regulate myoblast and myotube

formation (Qi et al. 2023). Thus, SLMAP appears to regulate skeletal muscle formation during early and postnatal growth in different model organisms, suggesting a conserved role for SLMAP during myogenesis.

STRIPAK-SLMAP-MST1/2 was shown to respond to extracellular and genotoxic stress coordinating to aide in the repair of DNA double strand breaks (DSBs). Upon genotoxic stress, the cGAS/STING/TBK1 pathway can activate STRIPAK-SLMAP to strengthen the binding to MST1/2 to inhibit ZMYND8 recruitment to prevent DSB, facilitating efficient DNA repair in cancer cell lines. Thus, demonstrating protective role of STRIPAK-SLMAP3 through a Hippo independent role (An et al. 2022).

These results suggest that SLMAP-STRIPAK play a significant role regulating Hippo signaling in human and mouse cell lines, fungi, and *Drosophila* however the magnitude of its role is yet to be characterized in an *in-vivo* mammalian model (Jeong et al. 2021).

1.1.2 Roles of SLMAP in cardiac biology

SLMAP was originally discovered in the sarcolemma of mammals by our research group (Wigle et al. 1997) and given its structural features, binding partners, location, and function SLMAP has been implicated in cardiomyopathies. All three SLMAP isoforms are implicated in dilated cardiomyopathy (DCM), as their protein expression was downregulated in patients exhibiting DCM (Nader et al. 2019). Further, the knockdown of SLMAP isoforms in H9C2 cardiomyoblast cell were unable to handle isoproterenol (ISO), thus phenotypically mimicking heart failure. SLMAP3 has been proposed as a biomarker for the transition to cardiac failure, as SLMAP3 protein expression is altered in a mouse model for congestive heart failure (Prévilon et al. 2013). Thus, SLMAP may qualify as a biomarker for heart disease.

Radiation-induced cardiovascular disease is an unfortunate side-effect of thoracic radiotherapy for cancer patients. Researchers discovered that radiating adult rats with 27.6 Gray caused SLMAP to overexpress at 1.5 months due to hypomethylation and may serve as a protective mechanism against radiation induced cardiac effects (Sallam et al. 2022). Interestingly, decreased SLMAP protein levels were observed in cardiac tissues of Mayak workers diagnosed with ischemic heart diseases after occupational exposure to external gamma rays (Azimzadeh et al. 2020). This supports the involvement of SLMAP in multiple models of cardiovascular disease.

Myocardin is a master regulator of smooth muscle differentiation to develop blood vessels. A study was conducted where myocardin was overexpressed in smooth muscle cells to uncover novel targets that can facilitate smooth muscle differentiation (Swärd et al. 2019). This study revealed that SLMAP was shown to be significantly upregulated, thus SLMAP is implicated in forming myocardial blood vessels in mice (Swärd et al. 2019).

SLMAP has been implicated in Brugada's syndrome, a cardiac arrythmia disease presenting with extended conduction intervals and ST-segment elevation resulting in sudden cardiac death (Brugada et al. 2014). Brugada's syndrome has been linked to the sodium channel, Nav1.5, aberrant expression or trafficking of Nav1.5 can result in Brugada's syndrome in human patients (Hu et al. 2009). In a clinical study performed in Japan, some Brugada patients carried a mutated variant of the SLMAP gene (Ishikawa et al. 2012). Exogenous expression of mutant SLMAP isoforms inhibited trafficking of Nav1.5 to the cell surface in transfected HEK293 cells. Patch clamp analysis revealed that cells expressing mutant SLMAP isoforms had a lower current density compared to Wt SLMAP in transfected tsA-201 (Ishikawa et al. 2012). Silencing the mutated SLMAP isoform with siRNA rescued the trafficking defect of Nav1.5, thus implicating SLMAP in trafficking of Nav1.5 for normal function. (Ishikawa et al. 2012).

To further explore the role of SLMAP in cardiac biology, our lab created a cardiac-specific gain of function mouse model that amplified expression of SLMAP1-TM2 (SLMAP1-Tg). Immunohistochemical analysis of 6-week-old transgenic mouse hearts showed a significant increase in vesicle formation within the myocardium which directly correlated to the expression levels of SLMAP1. SLMAP1-Tg affected cardiac membrane structures, ER and SR dilating and forming uneven membranes (Nader et al. 2012). SR-localized calcium signalling (RyR2, Serca2a and CSQ) proteins expression was dramatically decreased in the SLMAP1-Tg mouse hearts, thus implicating SLMAP1 as a modulator of EC coupling by affecting intracellular calcium homeostasis (Nader et al. 2012).

Our analysis identified these enlarged vesicles as enlarged early endosomes based on the positive staining with early endosome markers, EEA1 and Rab5 in the SLMAP1-Tg hearts (Dewan 2016). As trafficking appeared to be impacted, we sought to investigate the expression

of GLUT4 as previously published results suggested an association between GLUT4 and SLMAP. Our protein expression analysis indicated a non-transcriptional upregulation of GLUT4 in SLMAP1-Tg hearts suggesting it was upregulated via alternate mechanisms such as intracellular recycling (Dewan 2016). In support of this we observed a co-localization of the recycling endosome marker (Rab11) in compartments present on the enlarged vesicles (Rehmani et al. 2016). GLUT4 was significantly more localized to the cell surface in SLMAP1-Tg neonatal cardiomyocytes. Finally, Seahorse metabolic analysis indicated that SLMAP1-Tg cardiomyocyte's glucose uptake and metabolism was significantly higher (Dewan 2016). Thus, these results suggest that SLMAP1 can regulate intracellular trafficking to regulate membrane proteins such as GLUT4.

Our next aim was to examine the role of SLMAP3 and examine if it has redundant functions to SLMAP1-Tg. To achieve this, we generated a transgenic mouse that overexpressed cardiac-specific SLMAP3-TM2 (SLMAP3-Tg). We did not observe any noticeable cardiac remodeling or enlarged vesicle formation and GLUT4 protein expression was not affected (Tuana, not published). SLMAP3-Tg presented with minor defects in cardiac function and electrophysiology due to a reduction in protein and transcript levels of calcium handling proteins (SERQA2, CSQ) and Nav1.5 (Mlynarova et al. 2019), however the phenotype was non-lethal. Thus, overexpression of SLMAP3 and SLMAP1 resulted in similar changes in calcium handling proteins and Nav1.5, however SLMAP3-Tg mice did not present with enlarged vesicles or GLUT4 changes suggesting that SLMAP3 and SLMAP1 have similar yet distinct roles in the mouse myocardium.

Exploring the *in-vivo* overexpression model for SLMAP has aided in understanding its role in the mouse myocardium, however it's precise role in mammalian biology still needed to be

addressed. To achieve this, I proposed to utilize a cre-lox mouse model to knockout SLMAP in mice and determine SLMAP role in prenatal and postnatal cellular biology.

1.1.3 Generating a SLMAP knockout mouse model

The cre-lox system is a site-specific recombination system used to modify DNA through system derived from P1 bacteriophage (Hochman et al. 1983). The Cre (causes recombination) is a recombinase that binds to a specific 34 bp sequence known as LoxP site, Cre will recombine the sequence by extracting it from the genome where LoxP sites are located (Missirlis, Smailus, and Holt 2006). The simplicity of cre with no additional requirements for the recombination such as cofactors or accessory proteins to regulate its expression, and loxP site being non-endogenously found in mammals, allows the Cre-Lox system to be an ideal candidate for genetic engineering in cells and animal models (Kuhn and Torres 2002). Eukaryotic model must undergo genetic modification to contain loxP sites that will flank the sequence of interest to cause recombination (Branda and Dymecki 2004). Flanking a region of interest with loxP or "floxed" will determines the type of genetic modification that takes place in the model ranging from inversing sequence, translocation of sequences or causing genomic deletions (Orban, D, and Marth 1992). Therefore, we aimed to generate a flox-SLMAP gene, aiming to excise the floxed region to generate our SLMAP knockout mouse model.

To generate the flox-SLMAP mouse, we chose to flank exon 3 of the mouse SLMAP gene with loxP sites. We theorized that as the first start site of the SLMAP gene was located at exon 3 excising this start site would prevent the translation of SLMAPs and introduce a frameshift mutation that results in premature stop codon which could result in the knockout of all three isoforms. To achieve this, we utilized a targeting construct vector for SLMAP using neomycin insertion cassette with exon 3 of the mouse SLMAP gene flanked with two loxP sites (Rehmani

et al. 2021). The vector was microinjected into embryonic stem cells and implanted into C57BL/6 blastocysts. The founder flox-SLMAP animals were confirmed through PCR genotyping and were maintained through breeding with C57BL/6 mice. The flox-SLMAP mice were viable, fertile, and displayed no significant morphological or physiological abnormalities (Rehmani et al. 2021).

A unique feature of the cre-lox mouse model is the ability to control the temporal and spatial expression of cre by using the appropriate cre driving mouse line. The activity of cre in mice can be spatially regulated by the promoter sites it has been inserted with, for example the cre gene can be inserted downstream of α-myosin heavy chain (αMHC) promoter to sequester cre expression specifically within perinatal hearts, as the expression of αMHC is temporally regulated at these phase respectively (Agah et al. 1997). Cre can be temporally regulated with the fusion of a modified estrogen receptor (MER), which will confine cre to cytoplasm until addition of an estrogen analog, tamoxifen (TAM) (Sohal et al. 2001). When experimental mice reach desired timepoints, they can be injected with TAM, releasing the Cre-MER fusion protein from the cytoplasm and shuttle to the nucleus allowing recombination to occur (Sohal et al. 2001). Finally, if global expression of cre is required, the CMV-cre mouse line express cre as early as zygote implantation, causing cre to be active in all tissues during embryonic and postnatal development (Schwenk, Baron, and Rajewsky 1995).

The cre-lox system has demonstrated to have its pitfalls (Schmidt et al. 2000). Constitutively active Cre recombinase can be toxic as studies have shown that it can inhibit DNA replication and increase DNA damage, however regulating the concentration or activity of cre can minimize toxicity (Janbandhu, Moik, and Fässler 2013) This has been demonstrated to stem from the presence of endogenous lox-like sequences within the mammalian genome that can be

targeted by Cre (Thyagarajan et al. 2000; Ito et al. 2011). There is a significant amount of evidence that suggests that Cre is cardiotoxic. Numerous publications using the inducible αMHC-MerCreMer shows that large doses of tamoxifen excessively stimulate cre activity resulting in decreased cardiac function through upregulation of apoptotic markers, decreased metabolism, increased stress markers, and increased cardiomyocyte death (Koitabashi et al. 2009; Bersell et al. 2013). However, this myopathy is transient; cessation of tamoxifen treatment prompts heart function to return to normal (Hall et al. 2011). Consistent with this, a study displayed that the non-inducible αMHC-cre model, resulted in a non-fatal hypertrophic cardiomyopathy (HCM) by six month of age (Pugach et al. 2015). Another study showed that the high-level expression of αMHC-cre resulted in different strain of adult mice to perish before reaching 3 months in age (Buerger et al. 2006).

We aim to examine loss of SLMAP in the heart and globally to properly assess the role of SLMAP during prenatal and postnatal development. To examine loss of SLMAP in postnatal myocardium we will cross our flox-SLMAP mice with the αMHC-MerCreMer mouse. The αMHC-cre mouse is utilized to ablate SLMAP in perinatal hearts. In prenatal mouse hearts, we utilize the Nkx2.5-cre mice. Finally, to assess global impact of SLMAP we cross with the CMV-cre to examine role of SLMAP during early stages of gastrulation, where we discovered the nullification of SLMAP lead to neural tube defects.

1.2 Cardiac morphogenesis, maturation and maintenance

1.2.1 Cardiac Morphogenesis

The adult mammalian heart is the main component of the cardiovascular system, with four chambers of cardiac muscle (myocardium) that are the right atrium, right ventricle, left atrium and left ventricle, working in tandem to collect and distribute blood supplying the body with oxygen and nutrients (Hall 2011). The myocardium is comprised of cardiomyocytes and non-muscular cells such endocardial cells, cardiac fibroblasts, conduction system cells and endothelial cells (Pinto et al. 2016). The non-muscular cell types, namely endothelial cells account for the majority of cells within the myocardium however cardiomyocytes make up for ~75% volume of the myocardium (Pinto et al. 2016). The development of the heart is divided into two phases, cardiogenesis and maturation (Guo and Pu 2020) (**Figure 3A**). During embryogenesis, the first functional organ is the heart, arising from progenitor cells situated across the anterior lateral plate mesoderm that will undergo significant morphogenetic processes beginning as a cardiac crescent will then transition into a linear heart tube, a looping heart, and then finally the 4-chambered heart (**Figure 3A**) (Bruneau 2002). These precardiac-mesodermal cells exit the primitive streak during gastrulation and localize to splanchnic mesoderm (Meilhac et al. 2014). Here, these progenitor cells will express transcription factors Nkx2.5, Mef2, GATA4, Tbx5, Isl-1 and Hand, working in tandem to control expression of cardiac genes to mediate cardiogenesis (Schleich et al. 2013). Major players in cardiac progenitor specification, differentiation and migration include Hippo signaling pathway, canonical/non-canonical Wnt signaling, fibroblast growth factors (FGFs), transforming growth factor (TGF)β superfamily, bone morphogenetic proteins (BMPs) and Nodal/Activin (Heallen et al. 2011; Brade et al. 2013). In mice, the stage-by-stage development of the heart begins at E7.5 as the expression of these transcription factors transform precardial cells into the cardiac crescent, a crescent shaped

epithelium, localized sub-cranially at the ventral part of the embryo (**Figure 3B**) (Srivastava 2006). At this stage, these cells will aggregate to form the first heart field (FHF) and secondary heart field (SHF) cells, differentiating at different timepoints to modulate myocardium formation and chamber septation (Kelly, Buckingham, and Moorman 2014). During linear heart tube formation, FHF will undergo a convergence from mediolateral regions to fuse at the midline to form the beating heart tube, pooling blood into embryonic ventricle through the inflow tube before being pushed out through the outflow tube (E8.25) (van den Berg et al. 2009) (**Figure 3B**). The FHF and SHF will migrate towards the arterial and venous poles, contributing to the growth of the linear tube until looping of the heart will take place (Christoffels and Jensen, 2020). Looping will bend along the midline to create an "S" shaped heart and begin forming chambers such as the left and right ventricle and a more developed outflow tract, as the heart will increase 5-fold in length (E9.5) (Buijtendijk, Barnett, and van den Hoff 2020) (**Figure 3B**). The FHF will differentiate and proliferate to form both atria and ventricles, and the SHF cells will migrate anteriorly and posteriorly; the anterior SHF will contribute in the formation of the right ventricle while the posterior SHF will contribute towards the left and right atria, thus generating the immature four-chambered heart (E10.5), which will undergo further remodeling to become fully septated by E14.5 (Colombo et al. 2018; van den Hoff et al. 2001) (**Figure 3B**). The outflow tract (OFT) will septate to form the aorta or pulmonary artery via the SHF primarily (Savolainen, Foley, and Elmore 2009). The non-muscular cells also arise from FHF and SHF lineages through opposing interaction between FGF and BMP signaling which can induce to form the epicardium, the outer most heart layer, by E9.5-E11.5 in mice, which contribute to formation of fibroblasts and endothelial cells (Brade et al. 2013).

Aberrations in cardiogenic processes such as mutations or dysregulation in cardiac transcription factors i.e. NKX2-5, GATA4, TBX5 can culminate in congenital heart defects (CHDs), a group of birth defects that affects one or more structures within the heart impacting function. CHD's manifest approximately 1% of live births, and these cardiac malformations are implicated in nearly 30% of prenatal mortalities (Vincent and Buckingham 2010). CHD can include minor abnormalities such as atrial or ventricle septal defect that may resolve within the first year of life, whereas critical CHDs such as OFT defects including tetralogy of Fallot can cause life-threatening symptoms and may require surgical intervention (Wang et al. 2019). Despite the prevalence of CHDs, the precise etiological causes remain undiscovered. Identifying the genetic contributors and precise molecular mechanisms to CHDs will enhance diagnostic, prognostic, and therapeutic strategies for affected individuals.

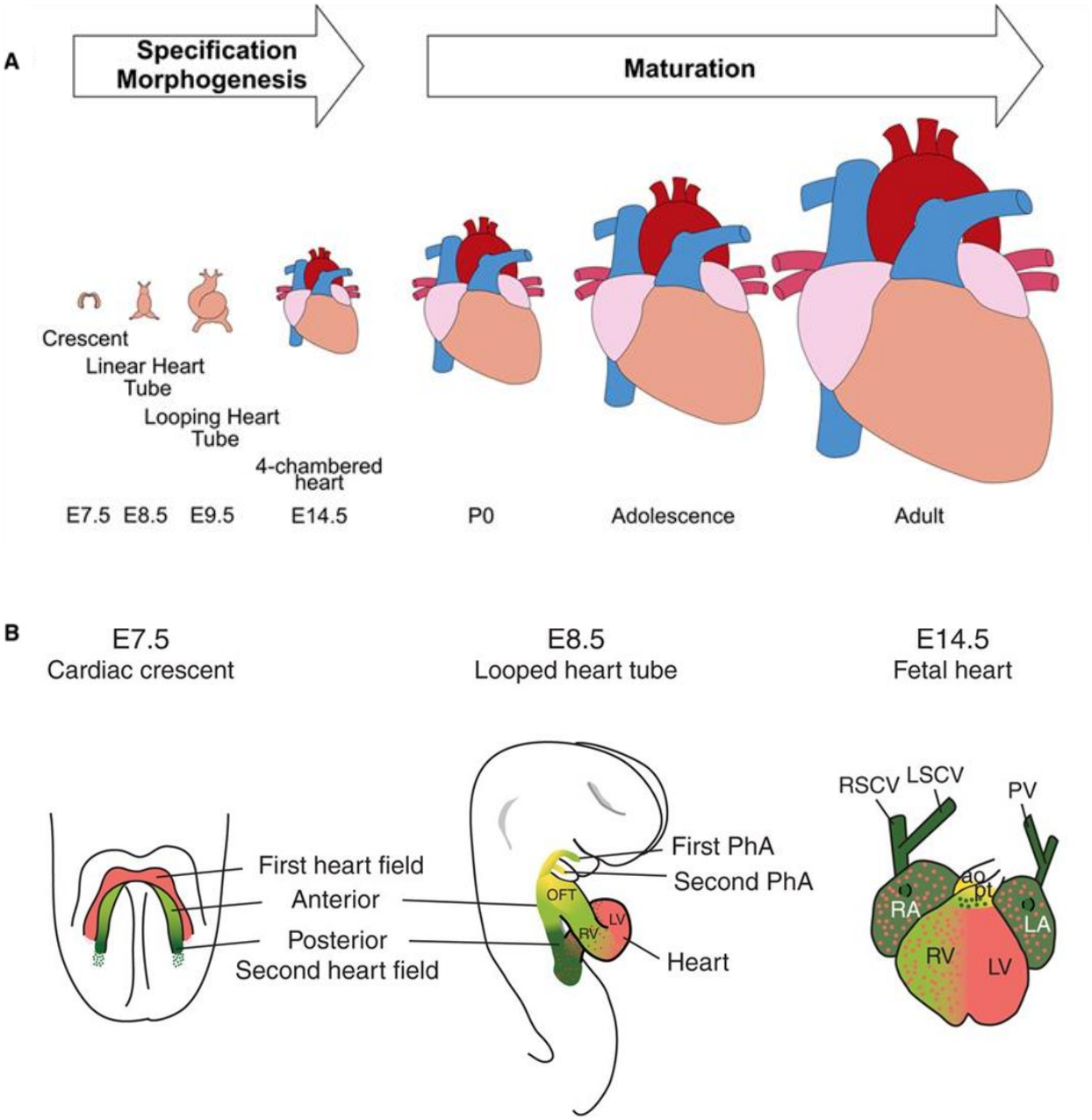

Figure 3. *Cardiac development and regionalization.* A. Conceptual scheme of the maturation phase of heart development. Mouse stages are labeled at bottom. Images modified with permission from Guo et al, Circ Res, 2020. B. First (red) and second (green) heart fields and anterior (pale green/yellow) or posterior (dark green) subdomains of the second heart field are shown at different stages of heart and head development. Regions of the heart with a dual origin are shown with colored dots. Modified with permission from Sigolène M, Cold Spring Harb Perspect Med, 2014.

1.2.2 Cardiac maturation and maintenance

After the morphogenesis of 4-chambered heart, the next stage of cardiac development is known as cardiac maturation, enlargement of the myocardium due to cardiomyocyte hypertrophy (**Figure 3A**) (Christoffels and Jensen, 2020). Cardiomyocyte hypertrophy is characterized by volumetric expansion of cardiomyocytes upon their exit from the cell cycle a few days after birth, as postnatal cardiomyocytes are non-proliferative (Mahmoud et al. 2014). This hypertrophy will entail an enhancement to sarcomere organization, increased electrophysiology, calcium handling, multinucleation and mitochondrial enlargement (Karbassi et al. 2020). Through these processes, the cardiomyocyte will form the fully mature heart that will be highly organized, dynamic to regulate myocardium contraction (systole) and relaxation (diastole) by mediating action potentials and metabolizing energy through the increased mitochondrial density, and the binucleation of cardiomyocytes will allow cardiomyocyte to increase in size and mass (Severs 2000; Hall 2011) (**Figure 4)**. Cardiomyocytes undergo a significant amount of physical stress due to beating continuously, therefore their maturation and hypertrophy is essential to maintain the body when considering the low turnover rate, thus aberrations during maturation can result in heart diseases (Tadevosyan et al. 2021).

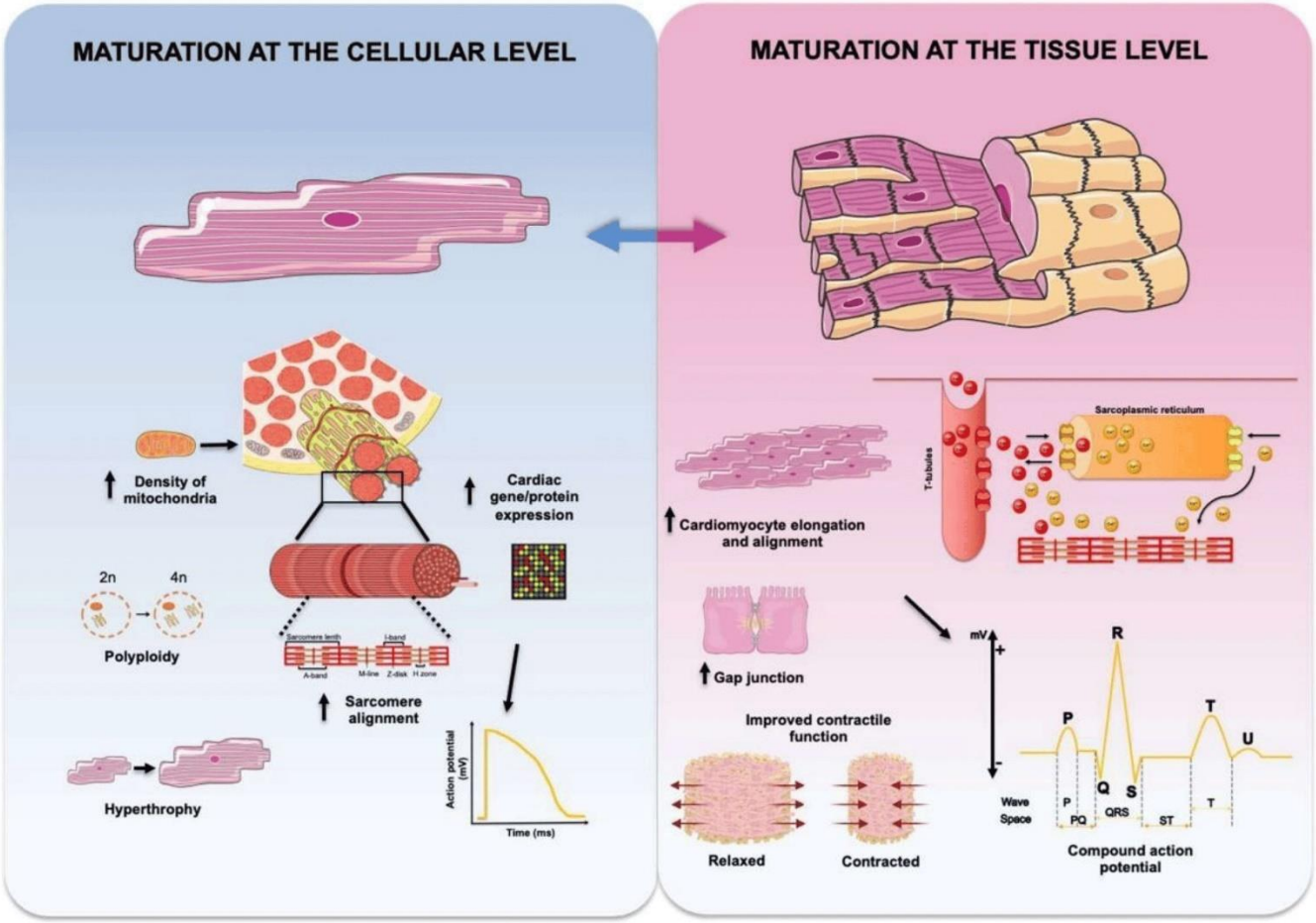

Figure 4. *Cardiac maturation at cellular and tissue level.* Cardiac maturation at the level of cardiomyocytes (blue-shaded background) can be experimentally ascertained by a more adult-like cardiac gene expression profile, changes in sarcomeric ultrastructure resulting in sarcomere elongation and alignment, increased mitochondrial density to accommodate for higher energy demand, and massive growth in cardiomyocyte size (hypertrophy) with increased percentage of polyploid cells. Electrophysiologically, cardiomyocyte maturation results in a more negative resting membrane potential and increased duration and amplitude of action potential. Cardiac maturation at the tissue level (pink-shaded background) is characterized by elongated cardiomyocytes preferentially aligned along a specific axis, increased expression of Cx43 and distinct localization of gap junction proteins, and improvements in impulse propagation and synchronization of cardiac contraction, leading to cardiomyocytes performing as a functional syncytium. Maturation at the tissue level results in increased contractility and force generation and, electrophysiologically can be registered as compound action potentials reminiscent of surface ECG recordings. Image reprinted from Tadevosyan et al, IJMS, 2021

The mature cardiomyocytes contain the functional unit of contraction, the sarcomere. The sarcomere consists of Z lines, thin, thick and elastic filaments (Xiao and Shaw 2015) (**Figure 4**). The sarcomere of cardiomyocytes is highly integrated into the EC coupling which include three crucial structural entities: the t-tubule domain, intercalated disc at the cell-cell junction, and the lateral membrane domain (Balse et al. 2012). The t-tubule domains are invaginations of the sarcolemma that interact with the SR and through this interaction mediate calcium ion homeostasis in the cardiomyocyte (Ibrahim et al. 2011). The systole of the myocardium is mediated through cardiomyocyte action potentials which are carried forward by plasma membrane ion channels that accurately control calcium (Ca^{2+}), sodium (Na^{+}), and potassium (K^{+}) ions (Nerbonne and Kass 2005). The initial inward flux of Na^{+} ions through sodium channels causes depolarization on the membrane, activates the voltage gated Ca^{2+} exchanger present on the t-tubule to interact with the SR calcium exchanger to push Ca^{2+} from the SR to the cytosol (Amin, Hanno, and Wilde 2010; Santana, Cheng, and Lederer 2010) (**Figure 4**). This free Ca^{2+} will generate a contraction through interaction with troponin C and the thick and thin filaments (Yin, Ren, and Guo 2015). Finally, the outward flux of K^{+} ions repolarizes resetting the heart back to rest or diastole to refill the myocardium with blood (Woodcock and Matkovich 2005). Defects in ion channel function can cause cardiac arrhythmias (irregular heartbeat) (Amin, Hanno, and Wilde 2010).

Heart disease is the second leading cause of death in Canada (Statistics Canada 2014). A specific type of heart disease, cardiomyopathy, is a disease which leads to structural changes within the myocardium (Yacoub 2014). The two common phenotypic classifications of cardiomyopathies are HCM and DCM (Wexler et al. 2009). These cardiomyopathies are defined to take place ‘in the absence of coronary heart disease, hypertension, valvular or congenital heart

disease' (Yacoub 2014). These structural changes are a result of pathological cardiac remodeling, which occurs when the heart attempts to compensate for a pressure or volume overload by enlarging the LV (Burchfield, Xie, and Hill 2013).

HCM is characterized by asymmetric hypertrophy, resulting in a significant thickness of the LV myocardium (Hensley et al. 2015). This pathological hypertrophy results in decreased cardiac function and is identified as an early symptom of heart failure (Marian and Roberts 2001). Research spanning the last decade has identified over 100 mutations spanning ten genes which result in HCM, majority of cases have mutations contractile proteins such as β-MHC, troponin and myosin-binding protein C (Marian and Roberts 2001; Seidman and Seidman 1998; Wexler et al. 2009). DCM is the most common characterized cardiomyopathy that also enlarges the LV but through a different mechanism. Patients exhibiting DCM have thin and stretched LV walls, that result in reduced systolic function (Luk et al. 2009; Yotti, Seidman, and Seidman 2019). Thinning of the myocardium also causes cardiomyocyte necrosis, triggering disorganization of the contractile function within cardiomyocytes (Westendorp et al. 2012). DCM is also linked to genetic mutations in cardiac contractile protein units such as myosin heavy chain and troponin (McNally, Golbus, and Puckelwartz 2013). Interestingly, both cardiomyopathies are linked to mutated proteins localized to the sarcomere driving the implication that alterations to cardiac sarcomere can result in changes to cardiac function.

As, SLMAP is localized to the sarcolemma of cardiomyocytes, can regulate calcium and sodium ion channel expression and implicated in Hippo signaling, it may play a key role in regulating cardiomyocyte development or maturation. Therefore, we sought to investigate the role of SLMAP in cardiac development, maturation, and maintenance.

1.3 Neural tube formation

When we caused a global knockout of SLMAP we observed the presence of the fatal neural tube defect, craniorachischisis. Neural tube defects (NTDs) are caused by defective closure of the neural plate to form a hollow neural tube in a morphogenetic process known as neurulation, an essential first-step in generating descendant tissues: central nervous system (CNS) and the brain, in diverse organisms (Nikolopoulou et al. 2017). In mammals, neurulation begins during early gastrulation, where ectoderm and underlying notochord induces neural fate to form a layer of differentiated ectodermal cells known as neuroepithelial cells (Wang et al. 2019). These neuroepithelial cells form a pseudostratified epithelial sheet known as neural plate, which will undergo subsequent elongation and thickening (Wang et al. 2019). The shaping of the neural plate involves a conserved morphogenetic process known as convergent extension, a cell intercalation process that drives convergence of cells/tissue towards the midline of the embryo at the medial-lateral axis whilst simultaneously elongating across the anterior-posterior axis, resulting in narrower and elongated tissue and embryo (**Figure 5**) (Shi 2022). Convergent extension will lengthen and converge the neural plate coupled with extrinsic forces of the surrounding mesenchyme known as paraxial mesoderm and the surface non-neuronal ectoderm to elevate the neural plate towards the midline and form a hinge point (**Figure 5**) (de Goederen et al. 2022). Folding of neural plate will generate a single hinge point known as medial hinge point (MHP) and/or dorsolateral hinge point (DLHP) depending on the location of neurulation event (closure sites) along the anterior-posterior axis (McShane et al. 2015). Bending of the neural plate has been antagonistically regulated by sonic hedgehog (Shh) signaling from the notochord and bone morphogenetic (BMP) signaling to regulate MHP and DLPH formation (Copp and Greene 2010).

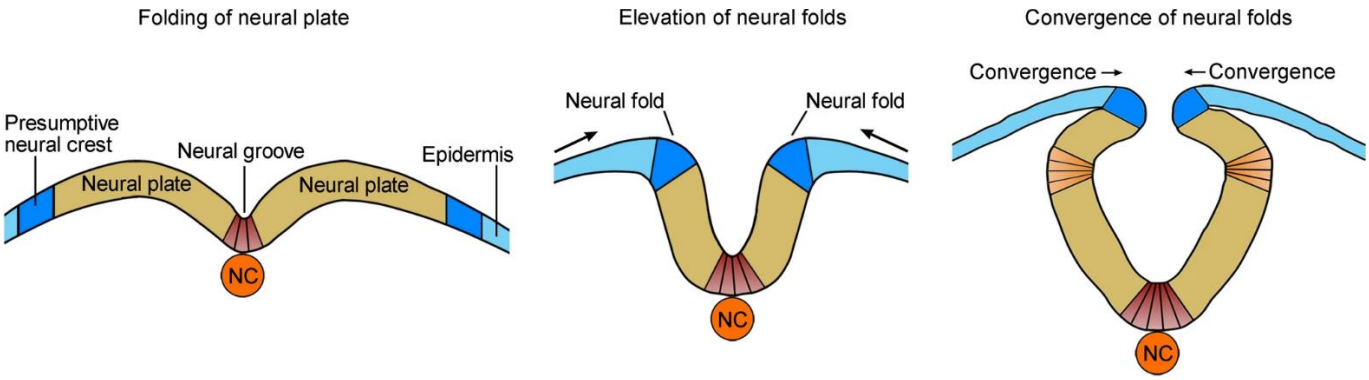

Figure 5. *Neural plate formation and neural tube closure.* Transverse sections in successive stages of neurulation show bending of the neural plate and convergence of the neural folds with presumptive neural crest approaching at the dorsal midline. Apical constriction generates wedge-shaped cells at the notochord (NC)-anchored medial hinge point (red) corresponding to the floor plate and at the dorsolateral hinge points (orange). These hinge points promote bending of the neural plate and convergence of the neural folds. Image from Shi, De-Li, Cell. Mol. Life Sci, 2022 reprinted with permission.

In mice, there are 3 closure sites that initiate neural tube closure (NTC) which instigates bidirectional "zippering" anteriorly and posteriorly to close the neural tube (Zohn and Sarkar, 2008). Closure site 1 is located under the hindbrain-cervical region, closure begins at E8.5, and zippers in both directions. Closure 2 is at the midbrain-forebrain boundary and closure 3 is further anterior to forebrain (Zohn, 2020). The zippering of neural tube at lower sacral-coccygeal region to tail bud will not take place here as it is regulated by a similar, yet alternate morphogenetic process known as secondary neurulation (Zohn, 2020). Secondary neurulation is not achieved through formation of neural plate, however neuromesodermal cells from paraxial mesoderm will "canalize" to form neuroepithelial cells through mesenchymal-to-epithelial cell transition that will surround each other and organize to form a lumen, generating a hollow neural tube (Lee and Gleeson 2020).

The narrowing and elongation of the neural plate through convergent extension is regulated by the non-canonical Wnt signaling pathway known as planar cell polarity (PCP) (Ybot-Gonzalez et al. 2007; Wang et al. 2006). PCP or non-canonical Wnt signaling is a global directional cue given to multicellular tissues, which affect cell polarity, orientation, and migration (Wallingford, 2012). PCP signaling regulates numerous vertebrate processes such as gastrulation, ear patterning, neural tube closure, cardiogenesis, hair follicle alignment, and ciliary elongation (Park, Haigo, and Wallingford 2006; Kelly and Chen 2009; Wu et al. 2011; Guo, Hawkins, and Nathans 2004). PCP signal originates at the cell surface through specific Wnt ligands that bind to a family of specialized membrane protein receptors, frizzled (Fz) (Zallen 2007), activating the downstream cytoplasmic protein disheveled (DVL), a signal transducer that will activate two independent and parallel pathways impacting cytoskeletal reorganization and transcriptional regulation (Wallingford and Habas, 2005) (**Figure 6A**). Both pathways are impacted through disheveled activation of small GTPases RhoA and Rac1 (Wallingford and Habas, 2005). RhoA can activate RhoA-associated kinase, ROCK, which impacts cytoskeletal organization by regulating the downstream activity of actin-severing protein, cofilin1 (Mahaffey et al. 2013). Cofilin1 disassembles actin filaments, when overactive or suppressed cannot induce closure, thus regulating cofilin is essential in maintaining actin assembly during NTC (Gurniak, Perlas, and Witke 2005; Escuin et al. 2015). Rac1 activates c-Jun N-terminal kinases (JNK) signaling by stimulating JNK activity via phosphorylation (Boutros et al. 1998). JNK signaling is highly implicated in regulating cytoskeletal dynamics by targeting actin through MARCKS resulting in NTDs in mice (Sabapathy et al. 1999; Björkblom et al. 2012). The "core" PCP proteins, Van-Gogh Like-protein 1/2 (VANGL1/2) and Prickle are asymmetrically localized at the anterior side of the cell, whilst Frizzled-3/6 protein(Fzd3/6) and DVLs are at anterior (Devenport 2014). They coordinate a multidirectional signal to cells simultaneously via

antagonizing effects of DVL, Scribble (Scrib) and Prickle proteins, resulting in cytoskeleton rearrangement by modulating cofilin-1 and JNK1/2 activity (Devenport 2014) (**Figure 6B**). Therefore, PCP can propagate signal to adjacent cells via FZD3/6 to VANGL1/2 establishing planar polarity throughout the entire tissue (Zallen 2007).

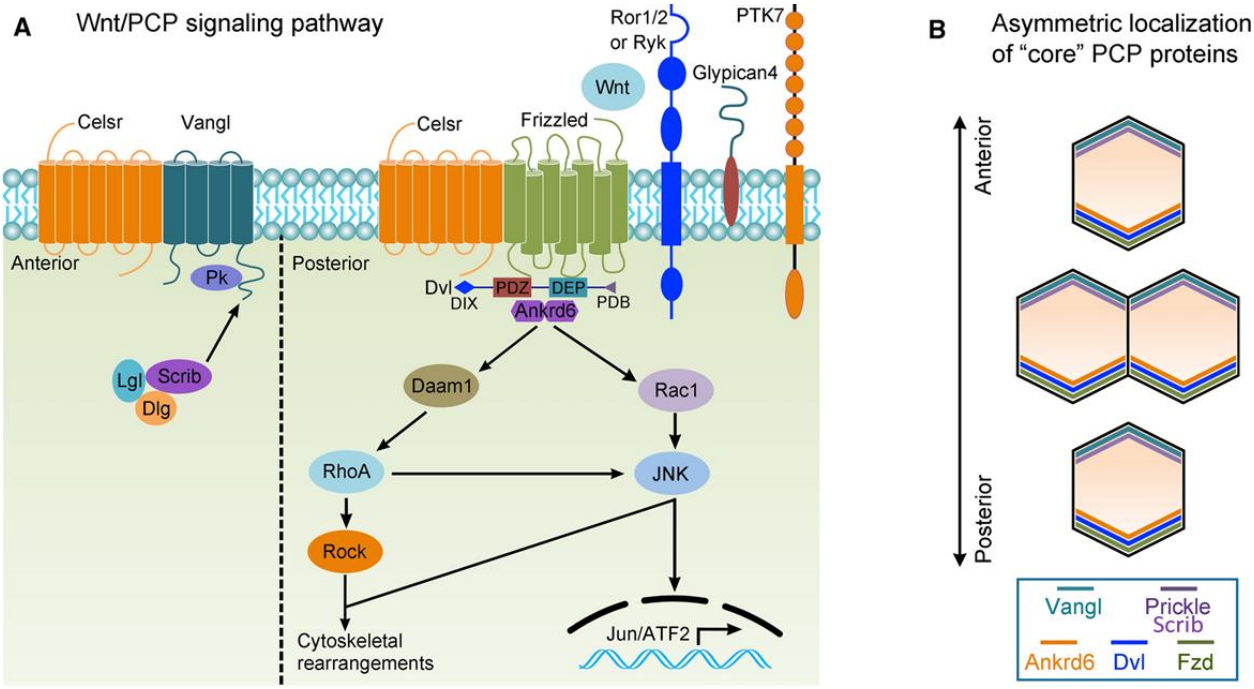

Figure 6. *Wnt/PCP signaling pathway and asymmetric distribution of "core" PCP protein complexes.* A Wnt/PCP signaling is induced by non-canonical Wnt ligands binding to Fzd receptors and co-receptors such as Ror2, Ryk, glypican4/Knypek, and PTK7. Dvl-activated downstream effector proteins relay the signal to induce cytoskeletal rearrangements and/or transcription responses. The "core" PCP proteins form two separate complexes localized to opposite cell borders. The C-terminal cytoplasmic region of Vangl interacts with Prickle (Pk) and Scrib, which may contribute to the anterior localization of the Vangl-Prickle complex within a cell. Celsr protocadherins form homodimers between adjacent cells to propagate polarity information. Dvl family proteins function as important scaffolds in different Wnt signaling pathways. The N-terminal DIX (blue diamond) is involved in Wnt/ß-catenin signaling, while the central PDZ, the C-terminal DEP domains, and the extreme C-terminus PDZ domain-binding motif (PDB, purple triangle) regulate Wnt/PCP signaling. B Diagram shows the asymmetric subcellular localization of "core" PCP proteins within the epithelial plane. Image modified from Shi, De-Li, Cell. Mol. Life Sci, 2022 reprinted with permission *(Shi 2022)*.

The pseudostratified neuroepithelium possesses characteristics of epithelial tissues in which cells are divided into an apical, lateral or basal domain (Buckley and St Johnston 2022). The apical domain faces the external environment, lateral domain contains adherent proteins that stabilize cell-cell contact and basal domain interacts with basement membrane, an extracellular matrix that layers between epithelia and other tissues (Buckley and St Johnston 2022). The partition of these domains defines an apical-basal polarity (ABP) axis within these cells, in which cellular processes and organelles are localized to these domains for proper epithelial tissue maintenance and morphogenesis, such as the neuroepithelium (Eom, Amarnath, and Agarwala 2012). PCP and ABP lie orthogonal to maintain cell polarity and shape across two axes for greater control on cell and tissue homeostasis. The loss of apical-basal polarity can impact the way the epithelial cells behave disrupting their cell-cell adhesion and prevent proper morphogenesis (Ivanov 2008). Organelle localization can help define proper ABP, for example the localization of centrosome and Golgi to apical regions for the growth of microtubule network and transportation of protein-trafficking vesicles to appropriate regions (Ravichandran, Goud, and Manneville 2020; Carvajal-Gonzalez, Mulero-Navarro, and Mlodzik 2016). Further, the nucleus of neuroepithelial cells is extremely dynamic as it will migrate and widen the cells at the apical or basal domain depending on which stage of cell cycle, in a process known as interkinetic nuclear migration (Niessen, Leckband, and Yap 2011). The narrowing of cells at apical region through interkinetic nuclear migration is an essential morphogenetic process to mediate apical constriction. Apical constriction plays a pivotal role in bending the neural plate to form the hinge points (Martin and Goldstein 2014). This process involves the actomyosin contraction of the apical side of neuroepithelial cells in the neural plate, leading to a wedge-like shape that facilitates the bending and eventual formation of neural tube (Eom, Amarnath, and Agarwala 2012). Actomyosin contractile networks, primarily composed of actin filaments and myosin

motors, are key drivers of apical constriction (Buckley and St Johnston 2022). These networks are regulated by convergent extension and PCP signaling to activate the small GTPase RhoA and its effector Rho-associated kinase (ROCK), which modulate cytoskeletal dynamics and cell contractility in mice (Escuin et al. 2015; Butler et al. 2019).

In parallel, the formation and maintenance of adherens junctions and tight junctions are crucial for the integrity and function of the developing neural tube (Punovuori, Malaguti, and Lowell 2021). Adherens junctions, primarily mediated by the transmembrane proteins, cadherins, are essential for establishing cell-cell adhesion among neuroepithelial cells (Rogers, Sorrells, and. 2018). These junctions link the actin cytoskeleton of adjacent cells, thereby contributing to the mechanical stability of the tissue and facilitating the transmission of contractile forces necessary for tube formation (Grego-Bessa, Hildebrand, and Anderson 2015). Tight junctions, on the other hand, form a seal between adjacent cell membranes, regulating paracellular permeability and maintaining the cellular barrier function (Hartsock and Nelson 2008). Proteins like claudins and occludins are integral components of tight junctions and ensure the selective passage of substances between cells (Hartsock and Nelson 2008). The interplay between apical constriction, adherens junctions, and tight junctions ensures that as neuroepithelial cells change shape and the neural tube forms, and disruptions in these processes can lead to neural tube defects, as dysregulation of junctions could could cause the loss of cell polarity (Williams et al. 2014).

NTDs are one of the most common birth defects, affecting 1/1000 live births worldwide (Mitchell 2005). NTDs can range from mild to lethal diseases which are linked to the closure sites (Butler and Wallingford 2017). At closure site 1, impacting neurulation will result in an open spinal cord and brain, known as craniorachischisis, a lethal phenotype (Butler and

Wallingford 2017). However, affecting caudal zippering of closure site 1 will cause milder phenotypes such as spina bifida, which can be treatable depending on size and location of lesion (Greene and Copp 2014). Affecting closure sites 2 and 3 can cause exencephaly, open forebrain, or anencephaly, no brain, which are lethal (Greene and Copp 2014).

There are numerous mechanisms that have been linked to NTDs however, with over 200 genes have been identified, with majority being linked to folate metabolism and PCP signaling (Kindt et al. 2018; Robinson A et al. 2012). As loss of SLMAP was found to cause NTDs we aimed to determine what mechanisms can result in this phenotype to regard SLMAP gene as an important biomarker for NTDs.

1.4 Statement of Problem

SLMAP is developmentally regulated and localized to numerous subcellular organelles within cells. SLMAP is highly expressed in the myocardium, however some SLMAP isoforms exhibit tissue specific expression while SLMAP3 is ubiquitously expressed. Gain of function studies have implied roles for SLMAP within muscle including cardiac tissues however the precise function remains unexplored. In this thesis, I sought to investigate the role of SLMAP by nullifying expression in a global and tissue specific manner. Therefore, I hypothesized that *the loss of SLMAP will impact cardiac health and embryonic development*. I tested my hypothesis with the following aims:

Aim 1: Can SLMAP regulate myocardial maintenance?

To address this aim we generated postnatal cardiac-specific knockout of SLMAP by crossing with αMHC-MerCreMer mice. We characterized our knockout model and evaluated lack of SLMAP in normal and stressed hearts. Our results were described in our manuscript entitled "Specific deletion of the FHA domain containing SLMAP3 isoform in postnatal myocardium has no impact on structure or function", published in *Cardiogenetics* in October 2021 (Chapter 2)

Aim 2: Can SLMAP regulate myocardial maturation or development?

We aimed to investigate the perinatal and prenatal cardiac-specific knockout of SLMAP using αMHC-Cre and Nkx2.5-cre mouse lines. We discovered that αMHC-cre caused DCM in aged cre mice. We characterized this previously unreported phenotype and found it to be associated with overexposure to cre causing DNA damage which resulted in DCM. These results were described in "Cardiac-Specific Cre Induces Age-Dependent Dilated Cardiomyopathy (DCM) in Mice" published in *Molecules* in March 2019 (Chapter 3). Our cardiac-specific

prenatal SLMAP3 knockout results were described in our manuscript "Deletion of sarcolemmal membrane associated protein isoform 3 (SLMAP3) from cardiac progenitors delays embryonic growth of myocardium", which will be submitted for publication in *IJMS* (Chapter 4).

Aim 3: Can SLMAP regulate neurulation?

The prenatal knockout of SLMAP embryos presented with neural tube defects. We aimed to evaluate mechanisms that prevent proper neurulation from taking place. Our results were described in our manuscript entitled "SLMAP3 is essential to complete neurulation by directing cellular polarity through a structural mechanism that impacts centrosomal and Golgi dynamics" which has been submitted for publication to *Life Science Alliance,* 2023 (Chapter 5).

Chapter Two: Specific deletion of the FHA domain containing SLMAP3 isoform in postnatal myocardium has no impact on structure or function.

cardiogenetics

MDPI

Specific deletion of the FHA domain containing SLMAP3 isoform in postnatal myocardium has no impact on structure or function.

Taha Rehmani[1], Jana Mlynarova[1,2], Joseph Byers[3], Maysoon Salih[1,4] and Balwant S. Tuana[1]*

Cardiogenetics **2021**, *11*(4), 164-184; https://doi.org/10.3390/cardiogenetics11040018

Received: 31 August 2021 / Revised: 23 September 2021 / Accepted: 29 September 2021 / Published: 4 October 2021

Author Contributions: conceptualization, T.R., M.S., J.B. and B.S.T.; methodology, T.R., M.S. J. B, and B.S.T; data analysis, T.R., J.M. and B.S.T.; investigation, T.R., J.M. M.S. and J.B; visualization: T.R and B.S.T.; writing—original draft preparation, T.R.; Project administration: M.S. and B.S.T.; writing—review and editing, B.S.T.; supervision M.S. and B.S.T.; funding acquisition, B.S.T.

Funding: This research was funded by the Canadian Institute of Health Research project grant, grant number 220996-151999, to B.S.T.

Acknowledgments: We would like to thank Mona Nemer and her lab staff for providing the αMHC-MerCreMer animals, sharing breeding strategies and Rick Seymour for assisting our ECHO analysis.

Conflicts of Interest: *The authors declare that the research was conducted in the absence of any commercial or financial relationships that could be construed as a potential conflict of interest.*

Abstract

Sarcolemmal membrane associated proteins (SLMAPs) belong to the superfamily of tail-anchored membrane protein know to regulate diverse biological processes including protein trafficking and signal transduction. Mutations in SLMAP have been linked to Brugada and defective sodium channel Nav1.5 shuttling. The SLMAP gene is alternatively spliced to generate numerous isoforms broadly defined as SLMAP1 (~35 kDa), SLMAP2 (~45 kDa) and SLMAP3 (~80-95kDa), which are highly expressed in myocardium. The SLMAP3 isoform exhibits ubiquitous expression carrying a FHA domain and is believed to negatively regulate Hippo signaling to dictate cell growth/death and differentiation. Using αMHC-MerCreMer-flox system to target SLMAP gene we specifically deleted the SLMAP3 isoform in postnatal mouse hearts without any changes in the expression of SLMAP1/SLMAP2 isoforms. The in-vivo analysis of mice with SLMAP3 cardiac deficiency revealed no significant changes to heart structure or function in young or aged mice without or with isoproterenol induced stress. SLMAP3-deficient hearts revealed no obvious differences in cardiac size, function, or hypertrophic response. Further, molecular analysis indicated that SLMAP3 loss had minor impact on sodium channel (Nav1.5) expression without effecting cardiac electrophysiology in postnatal myocardium. Surprisingly, loss of SLMAP3 did not impact Hippo signaling in postnatal myocardium. We conclude that FHA domain containing SLMAP3 isoform has no impact on Hippo signaling or sodium channels in postnatal myocardium which is able to function and respond normally to stress in its absence. Whether SLMAP1/SMAP2 isoforms can compensate for the loss of SLMAP3 in the affairs of postnatal heart remains to be determined.

2.1 Introduction

Sarcolemmal Membrane Associated Proteins (SLMAPs) belong to a superfamily of tail anchored membrane proteins such as junctophilin, SNAP-25, calnexin involved in diverse functions including E-C coupling, neurotransmitter release and ER stress [1]. The SLMAP gene contains alternative start sites and can alternatively splice to generate many SLMAP isoforms that are expressed in a tissue specific manner, developmentally regulated and highly conserved across species [2]. We defined SLMAP isoforms into three main sub-groups based on molecular size of polypeptides generated: SLMAP1 (~35 kDa), SLMAP2 (~45kDa), and SLMAP3 (~80-95kDa) [3]. SLMAP3 is ubiquitously expressed while SLMAP1 and SLMAP2 are expressed in a tissue-specific manners [2,3]. All SLMAP isoforms share a common c-terminus with a single transmembrane anchor, which can be alternatively spliced to target diverse subcellular membranes [4]. The N-terminal sequences are divergent with additional coiled-coil domains with an N-terminal forkhead-associated domain (FHA) found in SLMAP3 [5,6]. The FHA domain is found in numerous kinases and phosphatases and acts as regulator for phosphoprotein interactions, specifically with phospho-threonine residues [7]. Recently SLMAP3's FHA has been shown to regulate the Hippo signaling pathway via the STRIPAK (striatin interacting phosphatase and kinase) complex [8,9]. Hippo signaling is believed to regulate organogenesis, tissue homeostasis, proliferation and apoptosis, including cardiac development and maintenance [10,11,12]. Unregulated activity of Hippo signaling in mouse myocardium can result in lethal phenotypes but can also aide in cardiac tissue repair and healing in post myocardial infarction or in pressure overload [13,14,15,16,17]. SLMAP is believed to interact with phosphorylated MST1/2 kinases via it`s FHA domain and recruit STRIPAK-PP2A to dephosphorylate transcriptional coactivators YAP/TAZ and negatively regulate Hippo to increase proliferation and repress apoptosis [18,19,20,21]

We have previously shown that endogenous cardiac SLMAPs co-localize with E-C coupling machinery including the ryanodine receptor 2 (RyR2) and caveloin-3 and the targeted expression of SLMAP1 in postnatal mouse myocardium lead to mild aberrations in electrophysiology and function due to reduced expression of E-C coupling proteins potentially causing alterations in calcium dynamics [22,23]. Ishikawa and colleagues discovered a mutation in the SLMAP gene within a Japanese population that were diagnosed with Brugada's syndrome, a channelopathy causing sudden cardiac death due to irregular electrical impulses associated with abnormal expression of the sodium ion channel, NaV1.5 [24,25]. They found that mutated SLMAP prevented the trafficking of Nav1.5 to the cell surface in transfected HEK293 cells implicating SLMAP as a regulator Nav1.5 protein trafficking [24]. In transgenic mice with cardiac-specific SLMAP3 expression, there was no noticeable cardiac remodeling however we observed a defect in cardiac function and electrophysiology due to a reduction in protein and transcript levels of Nav1.5, further implying a relationship between SLMAP and Nav1.5 in myocardium [26]. Although, studies have uncovered some unique properties of cardiac SLMAP, its precise molecular function needs to be fully interrogated.

Here, we highlight the procedure to generate a knockout mouse model using the αMHC-MerCreMer-lox method aimed to target the SLMAP gene and examine its impact in postnatal myocardium. Our strategy resulted in the cardiac specific deletion of the SLMAP3 isoform in the postnatal mouse heart while the expression of SLMAP1 and SLMAP2 remained unaffected. We further report the phenotypic assessment and any molecular impact of the cardiac specific loss of the SLMAP3 isoform in the postnatal heart under normal and β-adrenergic agonist, isoproterenol (ISO), induced stress.

2.2 Materials and Methods

2.2.1 Generating transgenic flox-SLMAP mouse lines

A targeting construct vector for SLMAP was developed using neomycin insertion cassette. Exon 3 of the mouse SLMAP gene was flanked with loxP sites and the vector was microinjected into embryonic stem cells which were implanted into C57BL/6 blastocysts. The founder (F0) flox-SLMAP mice were confirmed through genotyping and maintained through breeding with C57BL/6 mice (Cyagen Biosciences Inc).

The αMHC-MerCreMer mice were obtained from Dr. Mona Nemer and maintained by breeding with C57BL/6.

2.2.2 Generating and genotyping the SLMAP knockout mice

Breeding scheme to generate a cre-lox mice lines for SLMAP knockout is shown (**Figure 1**). Mice were genotyped by extracting genomic DNA from ear clips by boiling for 10 minute at 95ºC in 180µL of 50mM NaOH per ear. DNA solution was then neutralized using 20µL of 1M Tris-Cl pH 8.0. SLMAP KO/KD mice were identified by polymerase chain reaction (PCR) using DreamTaq Green PCR Master Mix 2x (Thermoscientific) for the PCR mix. Forward F2 primer (5`-CCT GGA GAG CCT CCG TGT GAG T- 3') and reverse R2 primer (5`-GTC AAC TGC CCA ATG TAC AGA AAT AGT AAG -3`) targeted loxP site 1 on flox-SLMAP gene. Forward Cre-F (5'-ACG ACC AAG TGA CAG CAA TG-3`) and reverse Cre-R primer (5'-AAC CAG CGT TTT CGT TC-3') detected Cre gene. PCR product in Cre+ animals resulted in bands that were ~425bp. PCRs were visualized by Red Safe (Sigma) staining on a 1% agarose gel.

Mice were handled in accordance with the guidelines set by Canadian Council on Animal Care, Guide to the Care and Use of Experimental Animals, 2 vols. (Ottawa, Ont.: CCAC, 1980-1993)

and Animals for Research Act, R.S.O. 1990, c.A. 22. All animal protocols and procedures were approved by the Animal Care Committee of the University of Ottawa.

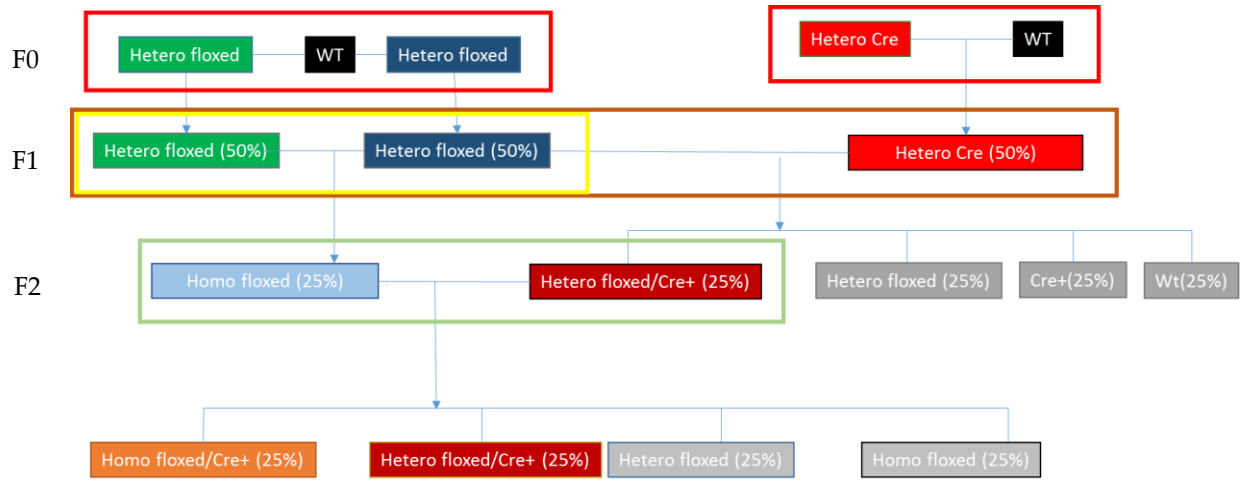

Figure 1. *Breeding diagram for αMHC-MerCreMer/Flox-SLMAP animals*. Breeding diagram to produce mice that contain floxed SLMAP alleles and cre. F0 generation indicates the hetero-flox-SLMAP (green/dark blue) and hetero-cre (red) mice. The hetero-floxed and hetero-cre mouse lines were maintained separately with Wt. The separated hetero-flox mice offspring were bred together to generate the homo-floxed mice (blue), labelled in the F1 generation. Additionally, the F1 generation indicates the production of knock down (KD) mice (Dark red; heterofloxed and hetero-cre) after breeding a hetero-cre mouse with a hetero-floxed mouse. F2 generation highlights the SLMAPKO (Orange; homofloxed and cre) mice generated by breeding homo-floxed animal with a KD animal.

2.2.3 Activation of Cre and assessing recombination of floxed SLMAP

Tamoxifen (Sigma-Aldrich) was administered into animals to activate MerCreMer. 500 µg of Tamoxifen was dissolved into 10 ml of peanut oil (Sigma-Aldrich), aliquoted into 10 different tubes and frozen at -20ºC for long term storage. Tamoxifen was injected intraperitoneally in 5-week-old animals at a dose of 30 µg tamoxifen/g of animal for 3 days. Tamoxifen treated hearts were analyzed by PCR genotyping as described above. The forward primer F2 (5`-CCT GGA GAG CCT CCG TGT GAG T- 3') and reverse primer R1 (5'-GGA GAG ACT ATC ACA GCC

ACA GGA-3'), coding for sequences between loxP sites; exon 3 and intron sequences were used for amplification.

2.2.4 Protein isolation from mouse heart

Hearts of adult mice (8-12 weeks of age) were collected after CO_2 euthanasia and immediately frozen at −80 °C. Each heart was later washed with ice-cold 1× phosphate buffered saline (PBS) and homogenized using a Fisher handheld Maximizer homogenizer (Thermo Fisher Scientific) in ice-cold lysis buffer (1 mM ethylene glycol tetraacetic acid (EGTA), 1 mM ethylenediaminetetraacetic (EDTA), 20 mM Tris base, 1% Triton, 150 mM sodium chloride, 1× complete mini EDTA-free protease inhibitor cocktail (Roche), and 1× PhosSTOP (Roche). The suspension was centrifuged for 15 min at 12,000× g to separate the proteins from the cell debris. The supernatant containing heart protein lysate was collected in Eppendorf tubes and stored in a freezer at −80 °C.

2.2.5 SDS-PAGE and Western Blotting

10-20 µg of protein lysate was loaded in each well of a 5–15% SDS-PAGE gel. The gels were transferred overnight on a polyvinylidene fluoride (PVDF) membrane (Bio-Rad) in a buffer containing 25 mM Tris, 190 mM Glycine, and 20% methanol. All membranes were blocked at room temperature for 1 h in Tris-buffered saline (TBST) containing 1 M Tris, 290 mM NaCl, 0.1% Tween 20, pH 7.4, and 5% nonfat dry milk. Primary antibodies (listed in Table 1) were incubated overnight at 4 °C with 5% bovine serum albumin (BSA). Membranes were washed 5 times for 5 min each in TBST prior to adding the appropriate horseradish peroxidase-labeled secondary antibody (Jackson ImmunoResearch) in a 1:10,000 dilution in TBST with 5% nonfat dry milk. Membranes were shaken slowly at room temperature for 1 h while incubating with secondary antibody, followed by 5 washes for 5 min each with TBST. Membranes were treated

with a BioRad western blotting kit (Bio-Rad, Hercules, CA, USA) and developed using ChemiDoc machines (Bio-Rad, Hercules, CA, USA). Bands were quantified by densitometry using Image Lab software v.6.0.0 (Bio-Rad) Membranes were stripped (25 mM glycine, 10% SDS, and pH 2.2 in dH2O) and reprobed with different antibodies. When using stain-free technology, stain-free gels (Bio-Rad) and low-fluorescence PVDF membranes (Bio-Rad) were used.

Table 1. List of antibodies used in this study. All antibodies used in this study are listed with the corresponding distributor, catalog number, and dilution used for western blot.

Antibody	Manufacturer	Dilution
SLMAP	Novus Biologicals (NBP1-81397)	1:1000
Nav1.5	Alomone Labs (ASC-005)	1:600
Striatin	BD Transduction Laboratories (610838)	1:1000
PP2A-C α/β subunit	Santa Cruz Biotechnology (sc-80665)	1:200
PP2A-A α subunit	Millipore Sigma (07-250)	1:600
Phospho-YAP (S127)	Cell Signaling Technology (13008S)	1:1000
YAP	Cell Signaling Technology (14074S)	1:1000
Phospho-MST1/2 (T183/180)	Cell Signaling Technology (49332S)	1:1000
KRS2(MST1)	Santa Cruz (sc-515051)	1:200

2.2.6 Quantitative PCR

Total mRNA from mouse hearts was extracted using the RNeasy Fibrous Tissue Kit (Qiagen). The concentration and purity of the obtained mRNA was determined by measurement of 260/230 nm absorbance ratio and 280/260 absorbance ratio [27] using NanoDrop 2000 UV-Vis Spectrophotometer (Thermo Fisher Scientific). RNA was used as a template to generate cDNA using SuperScript II reverse transcription protocol following the manufacturer's guidelines (Invitrogen). RT-qPCR was carried out BioRad CFX96 system and Luna Universal qPCR mater mix according to manufacturers instructions. Equal amounts of cDNA were utilized in real-time PCR using primers for SLMAP3 cDNA (SLPN-F: 5'-GGA ATT CGA TGC CGT CAG CCT TGG C -3', 558-R: 5'-TTG CTC GTC TTG TGA TCA AAC CAG -3'), total SLMAP cDNA (GTY-F: 5'-GAA AAG CCT ATC GAA ATC AAG TTG-3', GTY-R: 5'-ACC TTC TTA AGC TCT TCT TGC AAA G-3') and 18S Ribosome control (forward: 5'-AAT ACA TGC CGA CGG GCG CT -3', Reverse: 5'AGT GGG TAA TTT GCG CGC CT-3'). Fold change was calculated using the ΔΔCt method.

2.2.7 Echocardiography

All echocardiographic analysis was performed using the VEVO 2100 system (FUJIFILM VisualSonics). Adult mice were anesthetized using 2% isoflurane and strapped onto a heated pad facing upwards, exposing the thoracic cavity. A 40 MHz probe was used to capture short-axis B-mode and M-mode images of the left ventricle. VEVO v1.6 software (FUJIFILM VisualSonics) was utilized for measuring LV wall thickness and inner diameters in diastole and systole. The formulas used by the VEVO v1.6 software to calculate EF, FS, LV mass, and LV Vol;d/s are listed below:

$$\text{EF: } 100 \times \left(\frac{\text{LV Vol; d} - \text{LV Vol; s}}{\text{LV}}\text{Vol; d}\right) \quad (1)$$

$$\text{FS: } 100 \times \left(\frac{\text{LVID; d} - \text{LVID; s}}{\text{LVID}}\text{; d}\right) \quad (2)$$

$$\text{LV mass: } 0.8 \times 1.053 \times ((\text{LVID; d} + \text{LVPW; d} + \text{IVS; d})^3 - \text{LVID; d}^3) \quad (3)$$

$$\text{LV vol; d/s: } ((7.0/(2.4 + \text{LVID; d; s})) \times \text{LVID; (d; s)}\text{^3} \quad (4)$$

2.2.8 Isoproterenol Delivery

Isoproterenol (Sigma-Aldrich, St. Louis, MO, USA) delivery was mediated through the subcutaneous implantation of miniosmotic pumps (2001D Alzet) in 8-week-old mice. 0.9% saline or Isoproterenol (dissolved in 0.9% saline) was delivered at a rate of 30 µg/g/d per animal. Cardiac function was analyzed through echocardiography before pumps were implanted and after seven days. After a week of isoproterenol administration, animals were euthanized and hearts were collected for histological analysis.

2.2.9 Histological analysis

Hearts that were iso-treated were extracted from animals and fixed using 10% Neutral Buffered Formalin (Thermo Fisher Scientific). After fixing for 48 hours, hearts were sectioned 4 μm longitudinally per section. Sectioned hearts were stained with Masson's trichrome to visualize the myocardium, nuclei and collagen.

2.2.10 Electrocardiography

Mice were anesthetized with 2.5% isoflurane. 6-lead surface ECG was recorded after a 5-minute stabilization period of mice in the anesthetized state. ECG intervals and heart rate were analyzed manually from 6–18 most stable waves selected from a 2-minute recorded stream. Analysis was blind to the genotype. Intervals were defined as follows: PP duration from the beginning of the P wave to the end, where the P wave returns to the isoelectric line, PR segment from the end of the P wave to the beginning of R wave, PR interval from the beginning of P wave to the beginning of the R wave, QRS duration from the beginning of the R wave to the point where the negative S wave returns to the isoelectric line and QT interval from the beginning of the R wave to the point where the negative or positive T wave returns to the isoelectric line. Q wave was not visible. QT interval correction was based on Mitchell [28] using the following formula: QTc = QTo/(RRo/100)1/2. P, R, and S wave amplitudes were quantified as the distance between the peak of the wave and isoelectric line connecting the end of P wave and beginning of R wave. Electrocardiograms were recorded using IOX2.4.2.6 (EMKA Technologies, USA). RR interval, heart rate and wave amplitudes (P, R, and S) were analysed by ecgAUTO v2.5.1.18 software (EMKA Technologies, USA).

2.2.11 Statistical Analyses

The statistical analysis was performed using GraphPad Prism software version 8 for Windows (GraphPad Software). All comparisons between wildtype and knockdown or knockout groups were analyzed using two-tailed Student's T-test. To analyze all three groups we utilized ANOVA one-way analysis to evaluate significance. All values and points on graphs represent mean values obtained from multiple experiments. All error bars presented in graphs are represented using the standard error of the mean. All sample size values (n) represent biological replicates.

2.3 Results

2.3.1 Producing the αMHC-MerCreMer-flox-SLMAP mice

The mouse SLMAP gene is approximately 122 kilo-base pair (bp) in length and contains 24 exons. Exons 2, 3, 10, and 16 are believed to contain putative start sites and seven exons (11, 12, 13, 14, 17, 23, and 24) can alternatively splice to generate additional SLMAP isoforms (**Figure 2**) based on our lab findings and proteomic/genomic profiling databases [29,30,31]. We predicted that promoter sequences for SLMAP would reside upstream of exon 2 therefore we targeted the excision of exon 3 to prevent the translation of functional SLMAP as it would cause a frameshift mutation. To generate the cardiac-specific postnatal knockout of SLMAP the cre-lox system was chosen as we could manipulate the temporal and spatial targeting by using the αMHC-MerCreMer mice, ensuring that cre recombinase is expressed specifically in the myocardium, and will remain dormant unless activated by an estrogen analog, tamoxifen [32,33]. To target exon 3, in the mouse SLMAP gene loxP sites, were introduced to flank exon 3. The floxed-SLMAP DNA was microinjected into embryonic stem cells that were transplanted into fertilized mouse ovum (detailed in materials and methods) [34]. Floxed-SLMAP mice were crossbred with αMHC-MerCreMer mice to generate offspring which would contain both a floxed-SLMAP and cre transgene, to undergo a knockout (KO) or knockdown (KD) of SLMAP in postnatal mouse hearts (detailed in materials and methods) [35].

PCR genotyping of ear clippings from individual mice determined the presence of floxed-SLMAP and/or αMHC-MerCreMer. Primers F2/R2 were used to identify floxed-SLMAP by detecting loxP site 1 and primers CreF/CreR, detected αMHC-MerCreMer as modeled in Figure 3A. The flox-SLMAP F2/R2 PCR product was 424 bp in length, whereas wildtype SLMAP was 282 bp in length (**Figure 3B**). Genotyping with CreF/CreR, generated a 425bp amplicon denoting a αMHC-MerCreMer+ mouse (**Figure 3B**). PCR products ran on separate lanes on 1%

agarose gel to separate and size DNA amplicons to determine presence of transgenes in each animal (**Figure 3B**). The lane labelled KO presented two alleles of flox-SLMAP (one DNA band at 424bp) and the αMHC-MerCreMer transgene, signifying a KO mouse (**Figure 3B**). The KD lane presented one flox-SLMAP allele (424 bp), one wt-SLMAP allele (284 bp) and the αMHC-MerCreMer transgene signifying a KD mouse (**Figure 3B**). Finally, the lane that had only one transgene or none signifies a wildtype (Wt) animal as both a flox and a cre are essential for DNA modification to take place (**Figure 3B**) [36].

SLMAP3 (95-80 kDa)

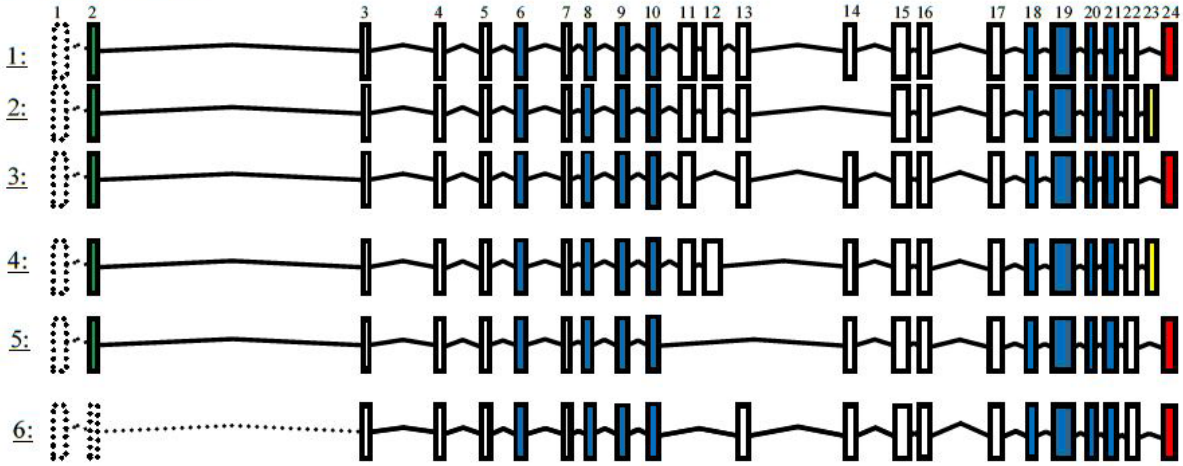

SLMAP2 (45 kDa)

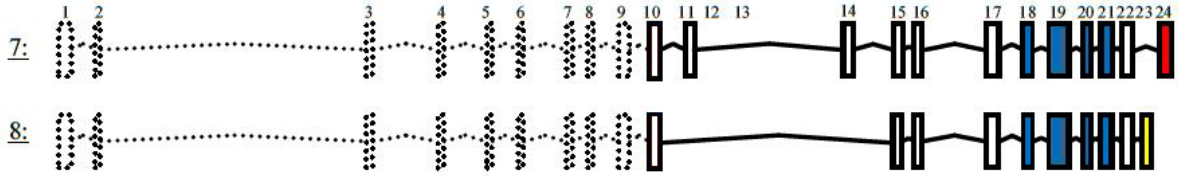

SLMAP1 (35kDa)

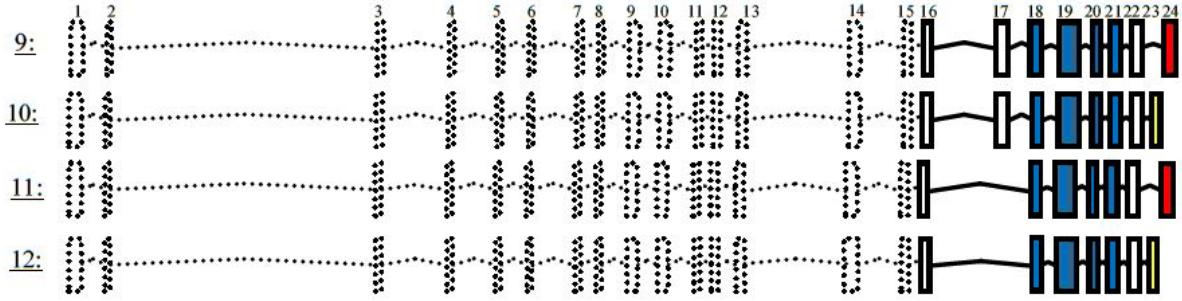

Figure 2. *Intron-exon junction of mouse SLMAP gene and its splice variants*. SLMAP consists of 24 exons (black) and alternatively splices to generate numerous isoforms grouped as three isoforms, SLMAP1 (35 kDa), SLMAP2 (45 kDa) and SLMAP3 (80-95 kDa). Start codon for SLMAP3, SLMAP2 and SLMAP1 are found at exon 2/3, 10 or 16 respectively. Alternative splicing of exons 11, 12, 13, 14, and 17 results in each isoform presenting unique variants. Exon 2 (green) codes for the FHA domain. Exons 6, 8, 9, 10, 18, 19, 20 and 21 (blue) code for coiled-coil LZ domains. Mutually exclusive exons 23 (yellow) and 24 (red) code for TM1 or TM2.

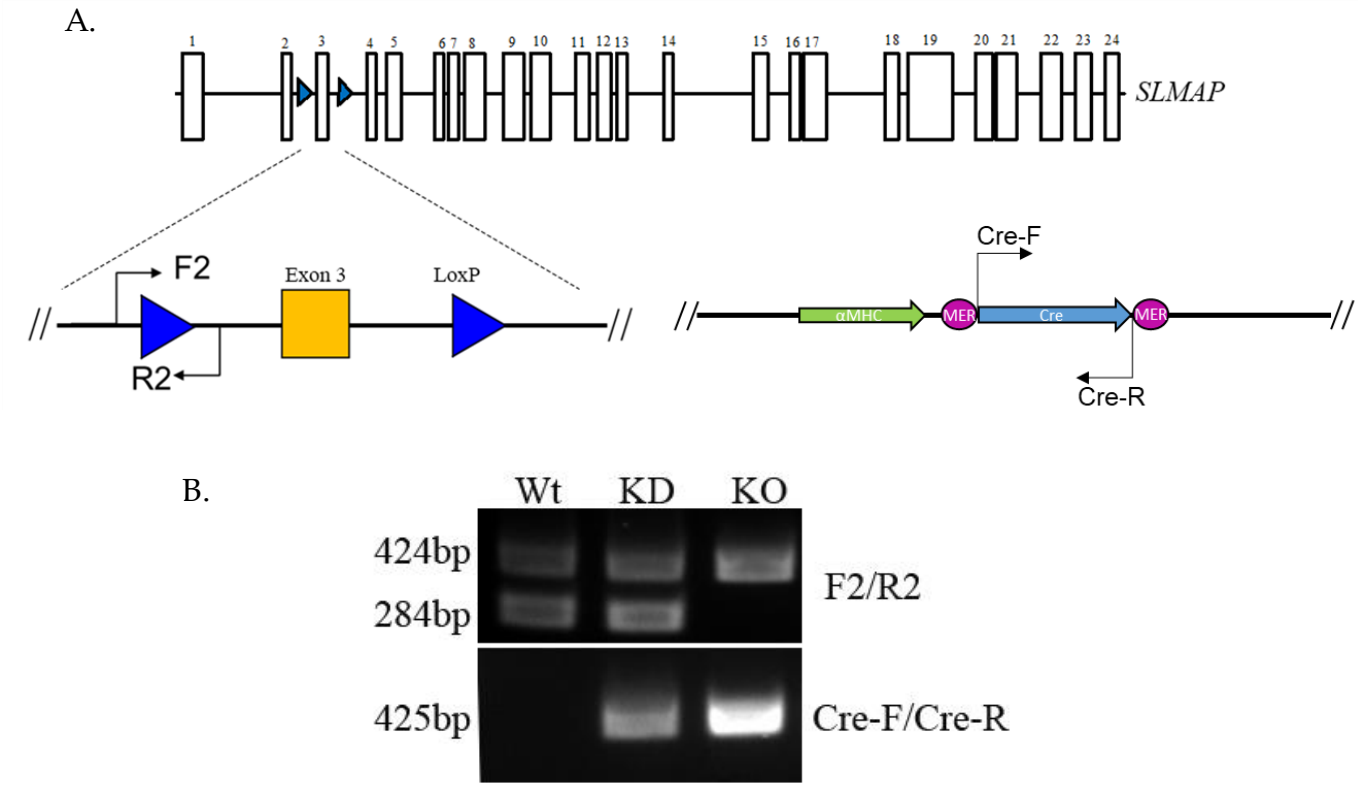

Figure 3. *PCR genotyping detects floxed-SLMAP and αMHC-MerCreMer gene in mice.* A. Schematic representation of primers F2/R2 identifying loxP site 1 on flox-SLMAP gene and primers Cre-F/Cre-R identifying αMHC-MerCreMer gene. B. PCR amplicons run on separate lanes on an 1% agarose gel labelled Wt, KD, or KO identifying a wildtype, knocked-down or knockout mouse respectively.

2.3.2 Cleavage of floxed-SLMAP by activating αMHC-MerCreMer

After generating flox-SLMAP/αMHC-MerCreMer+ mice we wanted to ensure loxP sites flanking SLMAPs exon 3 and surrounding introns were correctly targeted. This was assessed through PCR amplification of tamoxifen-treated hearts of Wt and KD mice. Studies have shown that administration of 30 μg of tamoxifen/g of body weight for 3 days via intraperitoneal injections is the most effective method for inducing MerCreMer activity because it results in the highest recombination efficiency [33,37]. After tamoxifen treatment, we extracted DNA from KD and Wt hearts and performed PCR using primers F2/R1, targeting the sequence between the two loxP sites, modeled in Figure 3A. Excision of the floxed region would reduce the F2/R1 product to 400bp while the unaffected SLMAP gene's F2/R1 product would remain 1400bp in size (**Figure 4A**). PCR products ran individually on 1% agarose gels to separate and size the DNA amplicons from Wt and KD hearts (**Figure 4B**). Amplicons from KD hearts produced bands at 1400 and 400 bp, demonstrating that only floxed SLMAP allele is targeted by active cre enzyme (**Figure 4B**). Floxed-SLMAP/ αMHC-MerCreMer- (Wt) hearts produced an amplicon at 1400 bp, signifying that cre is necessary to cleave floxed genes (**Figure 4B**). Therefore, the activation of αMHC-MerCreMer via tamoxifen successfully excised loxP flanked exon 3 from the floxed-SLMAP gene.

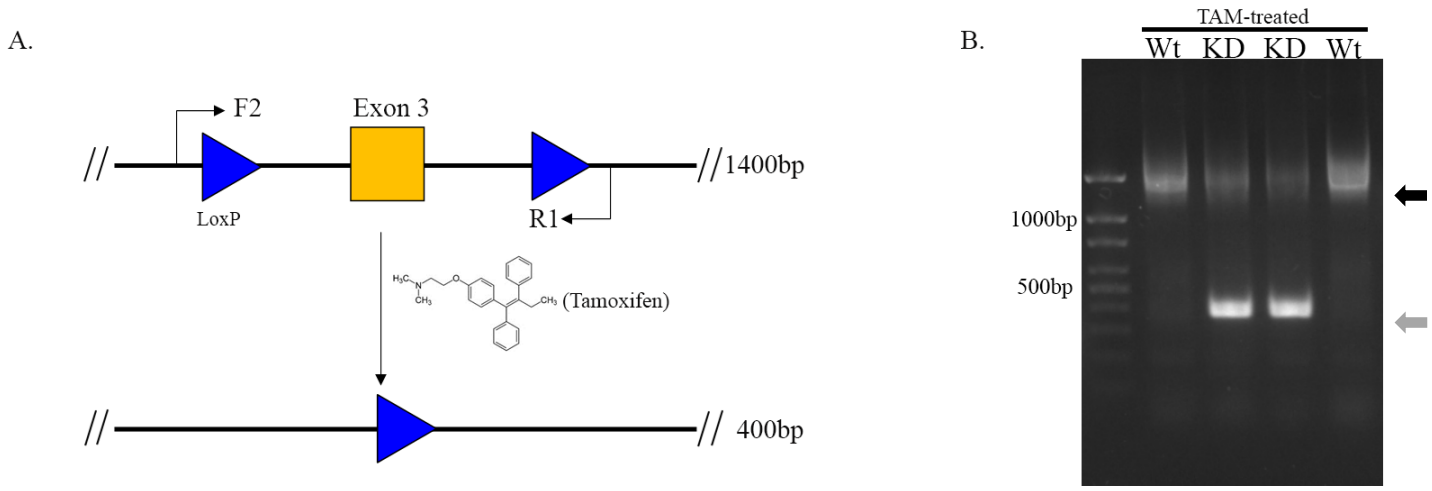

Figure 4. *Administration of tamoxifen cleaves exon 3 of floxed SLMAP gene by activating αMHC-MerCreMer in mouse hearts.* A) Schematic representing cleavage of exon 3 in a KD mouse after treatment with tamoxifen B) PCR genotyping of hearts treated with tamoxifen (TAM) using primers F2/R1. Wt lanes indicate unaltered SLMAP which results in 1400 bp band. KD lanes result in two bands being present, cleaved SLMAP band (400bp; grey arrow) and an unaltered SLMAP gene (1400bp; black arrow).

2.3.3 Protein and transcript expression of SLMAPs in Wt, KD and KO mice

Next, we wanted to assess the impact on SLMAP protein levels in KD and KO mice. Adult mice were tamoxifen treated and left for a minimum of three weeks before cardiac lysates were evaluated for protein expression and western blot analysis on mice designated KD had a significant reduction in the expression of SLMAP3 (-45.81% ± 9.58%, $\rho<0.05$, n=6) relative to the Wt (**Figure 5A**), however no changes were noted in the expression of SLMAP1 or SLMAP2 isoforms. In KO mice, western blot analysis indicated the total loss of SLMAP3 (-89.31% ± -14.50%, $\rho<0.001$, n =10) but there were no changes noted in the expression of SLMAP1 (1.91% ± 31.94%, $\rho=0.955$, n=10) or SLMAP2 (12.86% ± 35.02%, $\rho=0.74$, n=10) in KO hearts when compared to Wt littermates (**Figure 5A**).

The transcript levels of the SLMAP isoforms in tamoxifen-treated postnatal mouse hearts with specific primers; SLPN-F/558-R and GTY-F/GTY-R target exons at the 5' end, which are

translated in SLMAP3 but absent in SLMAP1 and SLMAP2 (**Figure 2**) [2]. We targeted the 5' region with primers SLPN-F/588-R which would amplify SLMAP3 transcript only. We observed a significant decrease in SLMAP3 transcripts in the KD (-55.22% ± 27.%, n=19, $\rho<0.001$) and KO (-93.47% ± 31.20%, n=13, $\rho<0.001$) hearts (**Figure 5B**). SLMAP1 and SLMAP2 sequences are highly conserved in SLMAP3 therefore we are unable to amplify these distinct isoforms individually. Instead, we used GTY-F/ GTY-R, a primer that targets all three isoforms to determine if there are any differences in total SLMAP mRNA expression. Total SLMAP expression in KD (-1.29% ± 38.35%, n=10, $\rho=0.759$) and KO (-34.12% ± 40.71%, n=9, $\rho=0.759$) hearts revealed no significant differences compared to Wt (**Figure 5B**). Therefore, targeting exon 3 of the SLMAP gene impacts SLMAP3 (expressed at very low levels) but not the abundantly expressed SLMAP1 or SLMAP 2 transcripts [2].

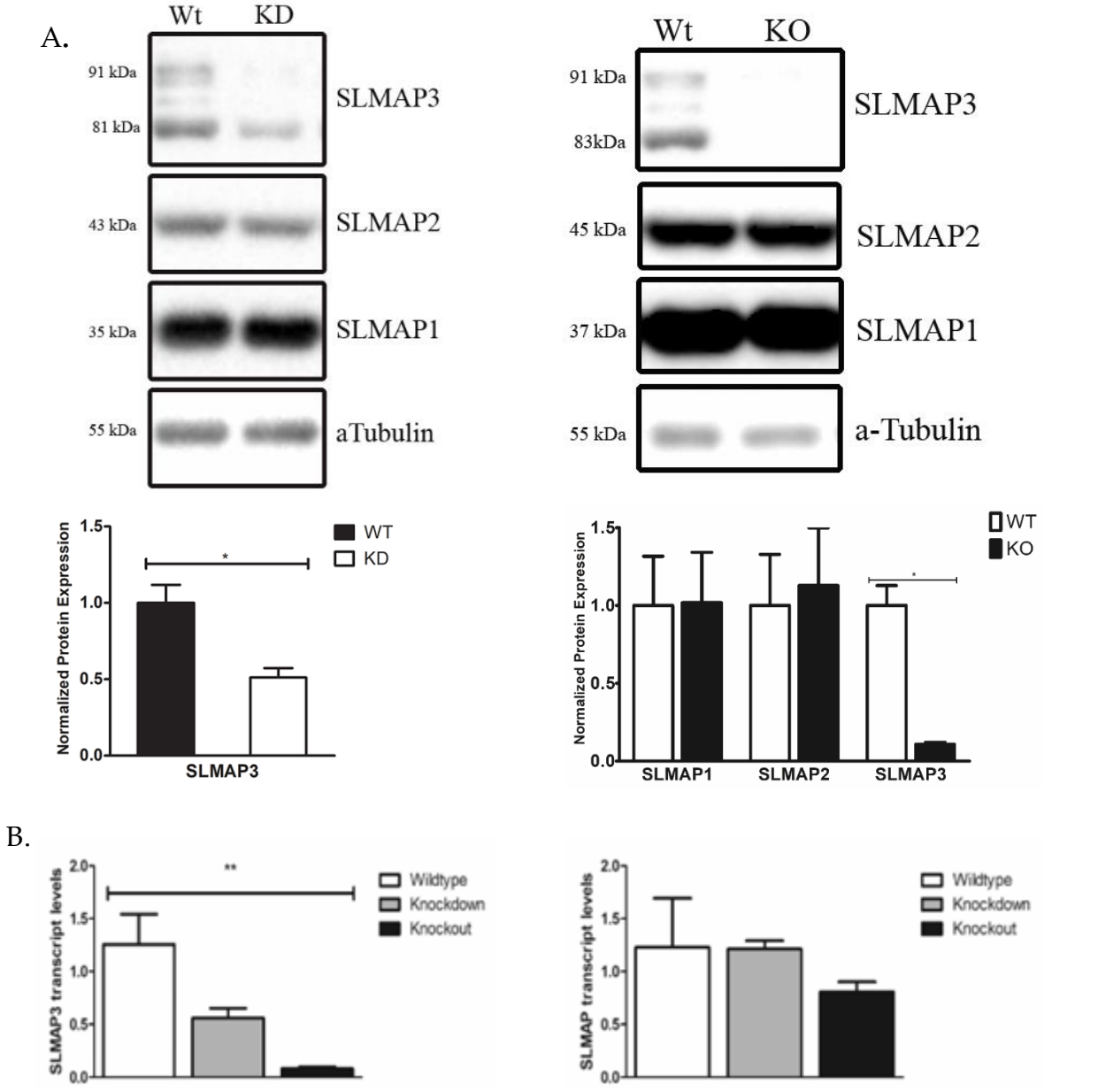

Figure 5. *Protein and transcript expression of SLMAP isoforms in targeted mice*. A. Western blot examining SLMAP protein expression in Wt, KD and KO hearts. Bar graphs represent normalized protein expression evaluated via densitometry analysis by using α-Tubulin as a loading control. n=10. *$\rho<0.05$, ρ value was calculated using non-paired two-way t-test. B. SLMAP3 and total SLMAP transcripts levels in KD and KO hearts compared to Wt. Fold change was calculated using 18S-Ribosome as the normalizing control. n=9. **$\rho<0.001$, ρ value was calculated using ANOVA statistical analysis.

2.3.4 Cardiac structure and function of SLMAP3-deficient hearts

Although only SLMAP3 was affected in our cre-lox model, we asked about its impact in adult mouse hearts, as SLMAP3 has been implicated in many cardiac-specific roles [22,23,24,26]. Transthoracic echocardiography (ECHO) was performed on 5-week post-tamoxifen (post-TAM) mice biweekly for 19 weeks to observe any changes to cardiac structure and function by measuring left ventricle (LV) wall thickness (intraventricular septum (IVS) and left ventricular posterior wall (LVPW)) and the left ventricular intradiameter (LVID) during systole and diastole. These measurements are used to calculate cardiac function including the ejection fraction (EF) and fractional shortening (FS), which measure percentage of cardiac output and LV muscle contraction respectively [38]. ECHO did not reveal any structural abnormalities in the young (5-week post-TAM) or old (24-week post-TAM) SLMAP3-deficient hearts when compared to Wt (**Figure 6A**). Further, analysis of LV walls revealed no significant changes to IVS or LVPW wall thickness during systole or diastole in young or old SLMAP3deficient hearts when compared to wildtype (**Supplement Table 1**). Further cardiac functional analysis indicated no significant differences in EF or FS in SLMAP3-deficient hearts (**Figure 6B**). The only difference noted between the age groups was an increase in LV mass however, that was most likely due to age-related cardiac growth which was similar among Wt and targeted mice (**Supplemental Table 1**). Therefore, a deficiency of SLMAP3 did not impact cardiac structure or function in the postnatal young or adult mouse hearts.

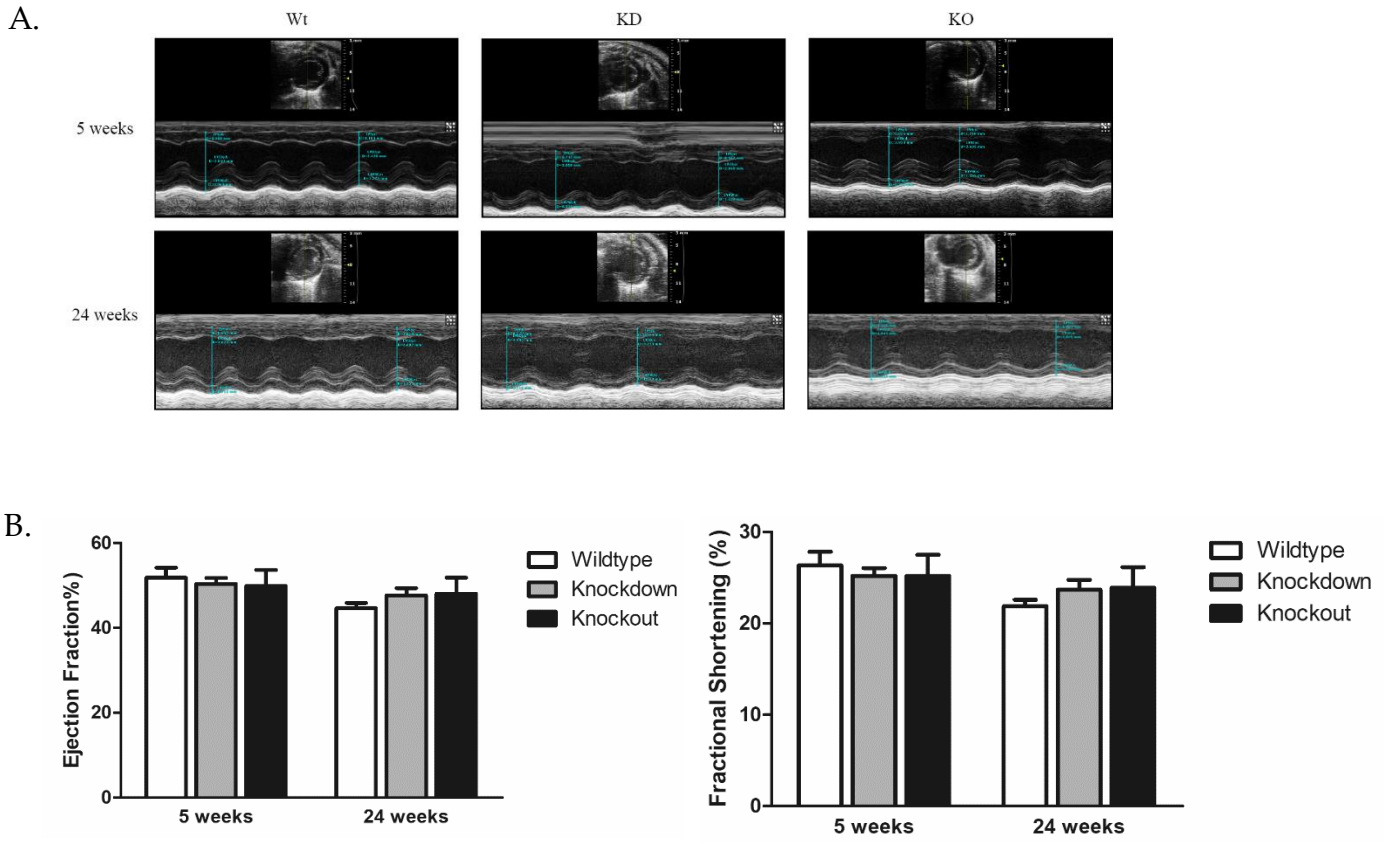

Figure 6. *Echocardiography and left ventricular function of SLMAP3-deficient hearts.* A) Representative short axis m-mode images of Wt, KD and KO hearts at 5 weeks and 24 weeks post tamoxifen. B) Bar graphs represent cardiac functional analysis via ejection fraction(%) and fractional shortening(%) of young and aged SLMAP3-deficient hearts. *n*=10.

2.3.5 Impact of isoproterenol induced stress on SLMAP3-KO hearts

Our next aim was to administer cardiac stressor isoproterenol (ISO) to cardiac depleted SLMAP3 mice to evaluate the impact of stress on the myocardium [39]. ISO is a non-selective β-adrenergic agonist, overstimulating the adrenergic receptors found on cardiomyocytes forcing rapid contractions resulting in pathological cardiac hypertrophy [40]. Seven-day delivery of ISO (30ug/g) or saline-control was mediated through mini-osmotic pumps that were subcutaneously implanted in tamoxifen-treated eight-week-old adult mice that were genotyped KO or Wt. ECHOs were performed before pumps were implanted (preISO) and seven days after implantation (postISO). PostISO ECHOs revealed a significant change in LV wall thickness in KO and Wt hearts (**Figure 7A**). LV walls, IVS (~25% increase, n=7, $p<0.05$) and LVPW (~20% increase, n= 7, $\rho<0.05$) were significantly thicker in postISO mice in both Wt and KO hearts when compared to their preISO measurements (**Figure 7B**). Unsurprisingly the weight of the hearts increased (~25% increase, n=7, $\rho<0.05$) as a consequence of cardiac hypertrophy. The similarity in heart weight and dimensions between the two iso-treated groups indicates the hypertrophic stress response is identical between the SLMAP3-KO and wildtype heart (**Supplemental Table 2**).

Hearts dosed with saline or ISO underwent histological analysis to observe changes to all chambers of the myocardium. Wt and KO hearts were fixed, sectioned longitudinally and stained with Masson's trichrome. Masson's trichrome stains the cardiomyocytes, nucleus and collagen thus we are able to visualize the myocardium and detect fibrotic cells. After seven-day ISO treatment SLMAP3-KO hearts displayed no obvious structural differences nor did we detect any evidence of fibrosis when compared to Wt (**Figure 8**).

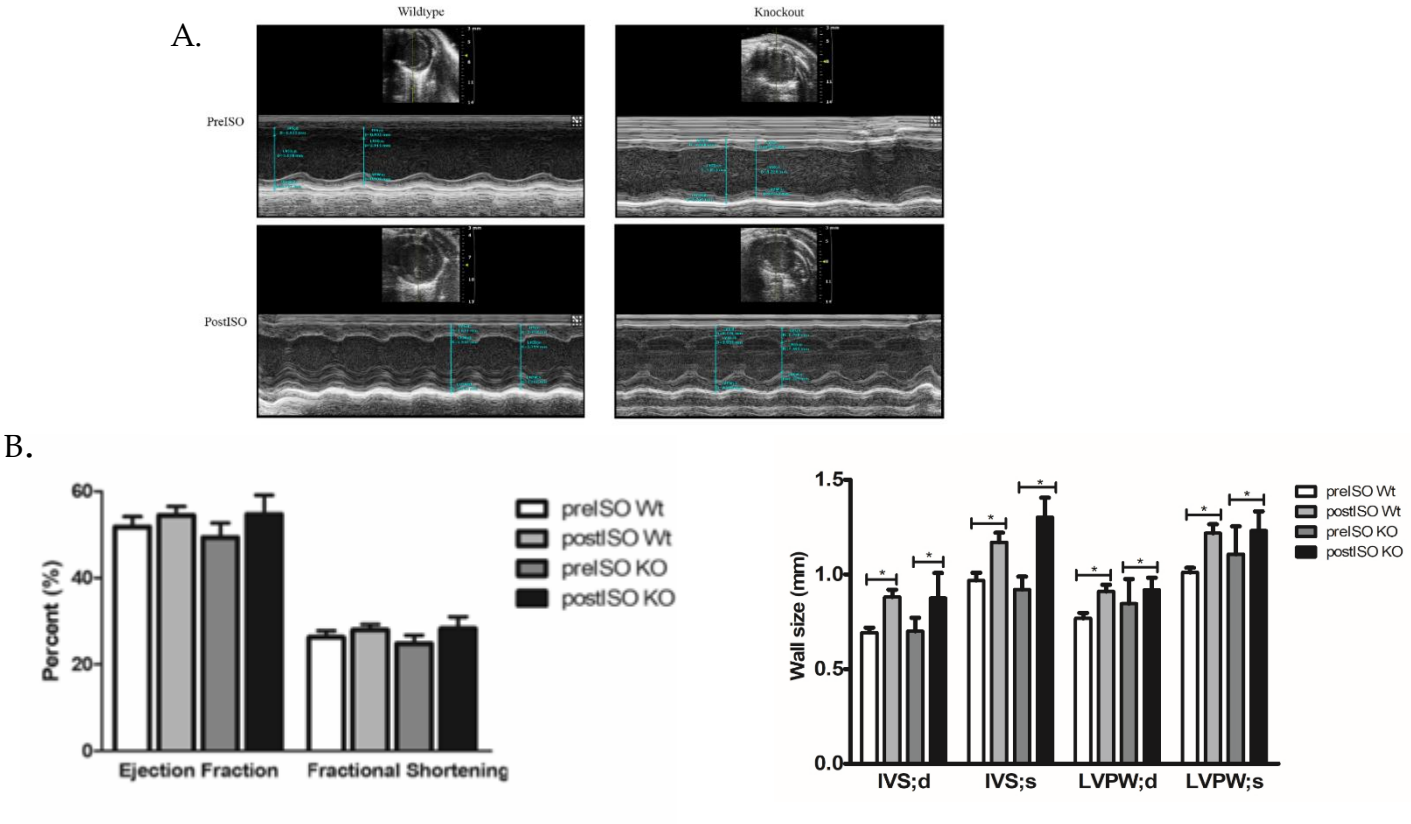

Figure 7. *Echocardiography and left ventricular function in ISO challenged Wt and SLMAP3-KO hearts*. A) Representative short axis m-mode images of Wt and KO mice preISO and postISO. B) Left ventricular functional analysis and changes in wall sizes between pre-/postISO treated Wt and KO hearts. *n*=7. *ρ<0.05, ρ value was calculated using paired two-way t-test.

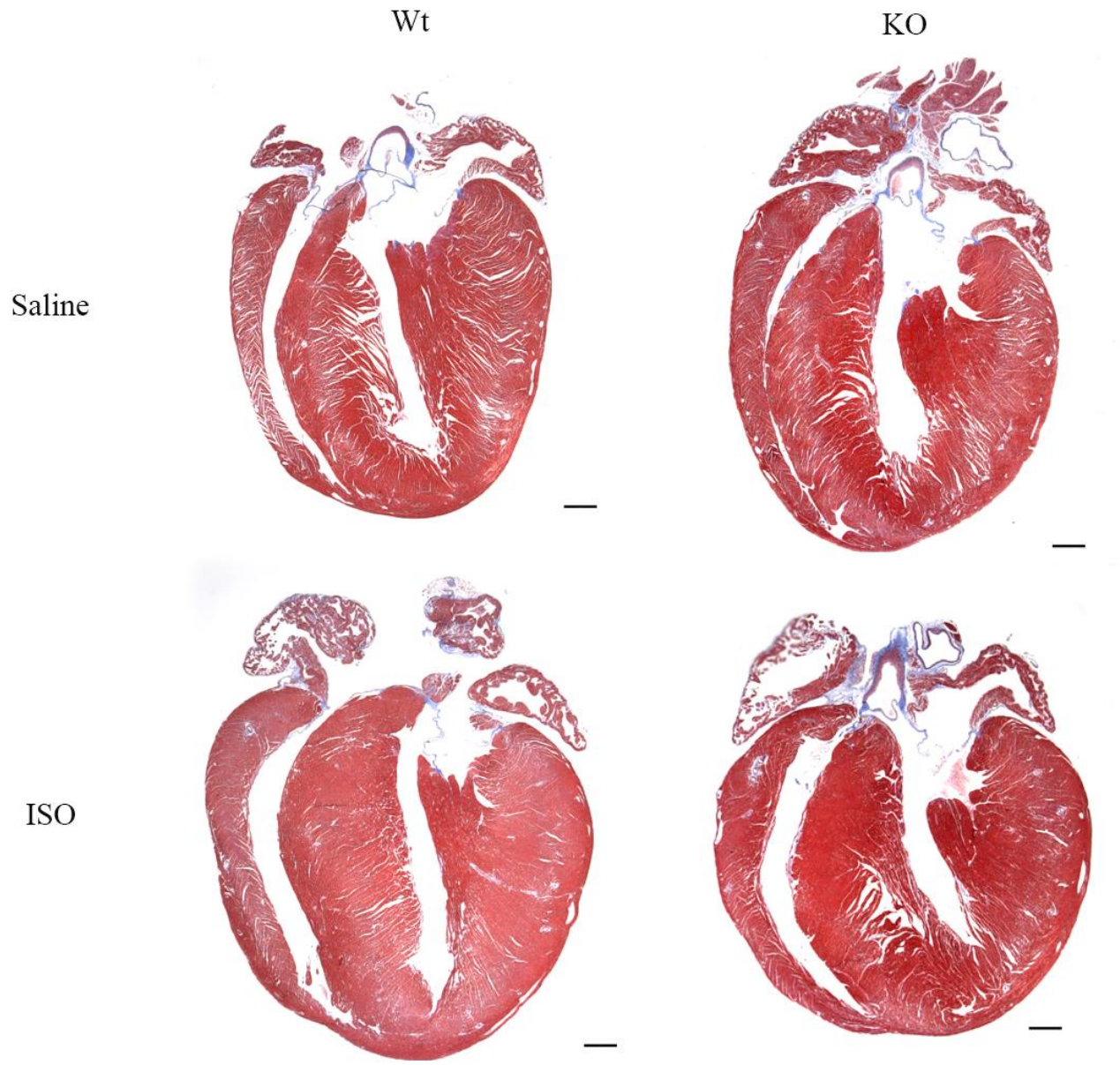

Figure 8. *Histological analysis of ISO challenged Wt and SLMAP3-KO mouse hearts*. Representative sectioning of Wt or KO hearts after one week of saline or ISO with Masson's trichome stain to visualize the myocardium, nucleus and fibrosis. Scale bar = 500 µm x 12.5 magnification.

2.3.6 STRIPAK complex and Hippo signaling in SLMAP3-KO myocardium.

Several studies have indicated that SLMAP3 via it`s FHA domain can regulate Hippo signaling by recruiting MST1/MST2 which comprises STRIPAK. The core STRIPAK components (striatin, PP2A-A, PP2A-C) were assessed by western blotting of cardiac lysates together with MST1/2 and YAP. Striatin (n=6, ρ=0.58), PP2A-A (n=6, ρ=0.69), PP2A-C (n=6, ρ=0.28) protein levels were not significantly altered in adult SLMAP3-KO hearts compared to Wt (**Figure 9**). The phosphorylation of MST1/2 (T183) and YAP (S127) was evaluated and quantified and the phospho-YAP to total YAP ratio (n=6, ρ=0.34) and phospho-MST1 to total MST1 (n=6, ρ=0.36) was not significantly altered in postnatal SLMAP3-KO hearts compared to Wt (**Figure 9**).

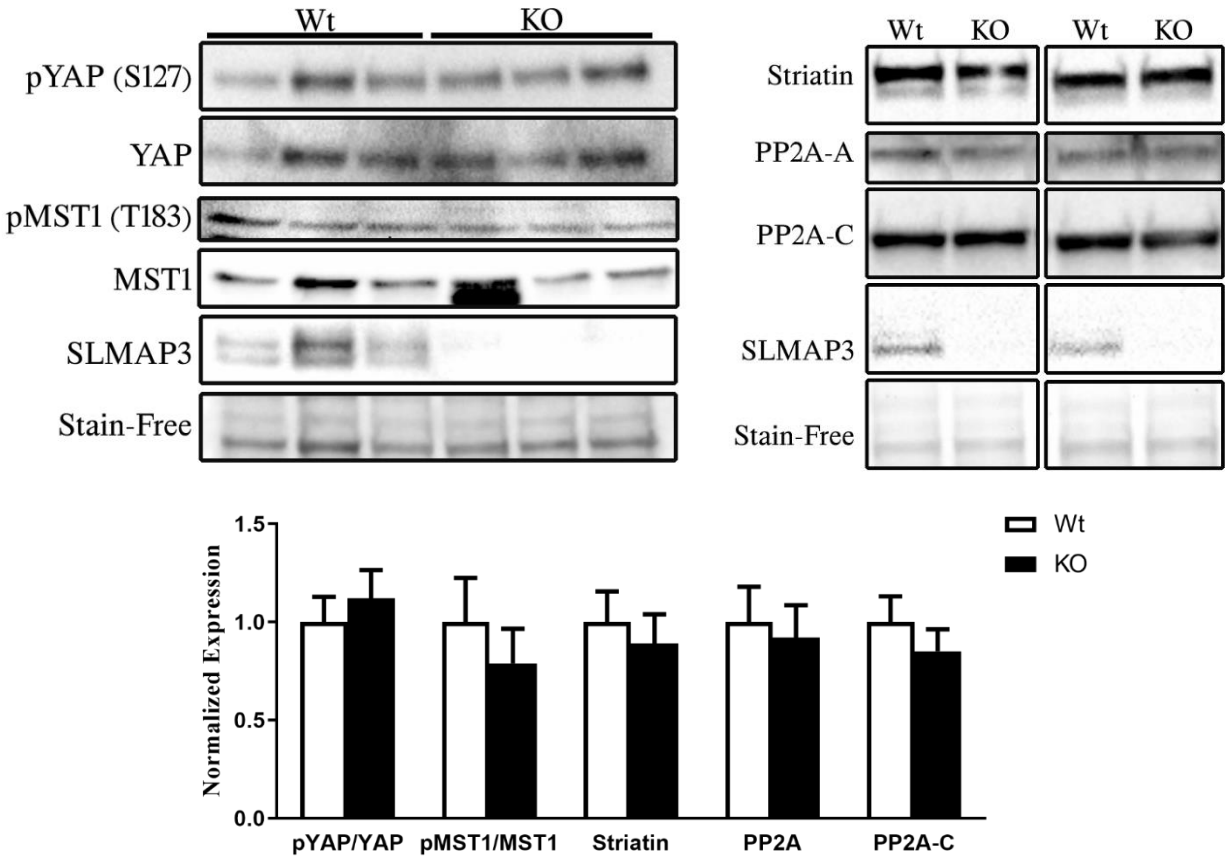

Figure 9. *Stripak complex and Hippo signaling in SLMAP3-KO hearts***.** Western blot of Wt and KO adult mouse heart lysates evaluating protein expression STRIPAK components (striatin, PP2A-A, PP2A-C) and phosphorylation of MST1 (T183) and YAP (S127). Bar graphs represent expression of indicated proteins by normalizing with total protein visualized by Stain-Free™ as a loading control or to total MST1 or total YAP. *n*=6.

2.3.7 Nav1.5 expression and electrophysiology in SLMAP3-deficient myocardium.

Mutations in the human SLMAP gene have been linked to Brugada with inappropriate Nav1.5 shuttling [24,26]. Western blot analysis indicated that there was a modest albeit significant decrease of Nav1.5 protein levels in KD (-9.81% ± -6.00%, $\rho<0.05$, n=3) and KO heart lysates (-16.66% ± -6.69%, $\rho<0.05$, n=3) when compared to Wt (**Figure 10A**). Since Nav1.5 plays a major role in initiating the E-C coupling cascade, we determined if modest decrease of Nav1.5 can impact electrophysiology of SLMAP3-deficient hearts [41]. 6-lead surface electrocardiography (ECG) in a mice aged up to 28 weeks showed no significant changes between Wt and SLMAP3-deficient hearts (**Figure 10B**). Electrical properties were quantified and P, R, Q, S, T waves in each ECG reading, defined in Figure 10B. Our analysis showed that the PP duration, PR segment, PR interval, QRS duration and QTc interval were not significantly altered between Wt and SLMAP3-deficient hearts (**Table 2**). Further, P, R and S amplitudes did not significantly vary in SLMAP3-deficient hearts when compared to Wt (**Table 2**). Therefore the decrease in Nav1.5 protein expression did not significantly alter cardiac electrophysiology in SLMAP3-deficient hearts.

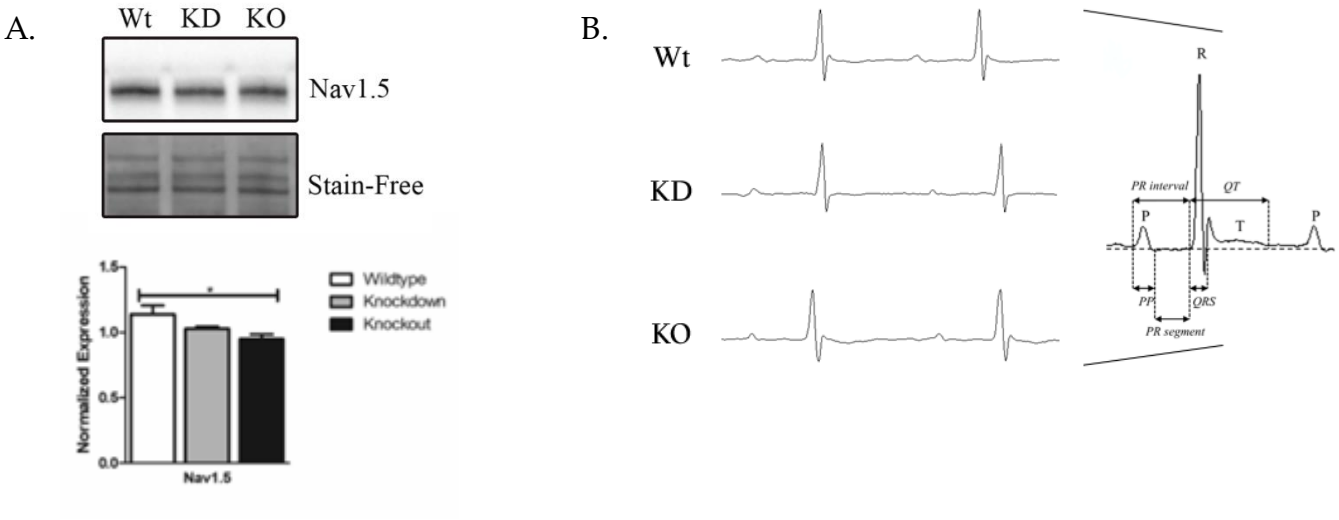

Figure 10. *Nav1.5 expression and electrocardiography in SLMAP3-deficient hearts.* A. Western blot with anti-Nav1.5 in Wt, KD and KO adult mouse hearts lysates. Bar graphs represents quantification of Nav1.5 expression normalized to total protein loading visualized by Stain-Free™. B. Representative electrograms of lead ii acquired by surface 6-lead ECG in Wt, KD and KO adult mice. *n*=3. *ρ<0.05, ρ value was calculated using ANOVA statistical analysis.

Table 2. *Electrocardiography of SLMAP3-deficienct hearts.* Paramters of electrocardiography in Wt, KD, and KO adult mice (detailed in materials and methods). *n*=3. ρ value was calculated using ANOVA statistical analysis.

Electrocardiography parameter	Wt	KD	KO	*p*-value
RR (ms)	123.370 ± 3.163	127.5 ± 2.644	123.407 ± 3.271	0.5738
HR (bpm)	487.4 ± 12.771	471.224 ± 9.847	487.248 ± 13.116	0.5787
PP duration (ms)	8.941 ± 0.177	8.168 ± 0.737	8.023 ± 0.651	0.5197
PR segment (ms)	29.738 ± 0.684	29.429 ± 4.568	28.781 ± 1.557	0.9148
PR interval (ms)	45.185 ± 0.737	44.685 ± 2.428	41.558 ± 0.883	0.2764
QRS duration (ms)	11.954 ± 1.289	10.298 ± 0.549	11.613 ± 0.773	0.4568
QTc interval (ms)	46.010 ± 2.508	40.969 ± 6.033	45.713 ± 2.166	0.6262
P amplitude (mV)	0.0531 ± 0.009	0.069 ± 0.01	0.067 ± 0.003	0.3765
R amplitude (mV)	25.670 ± 0.730	21.351 ± 0.789	0.620 ± 0.027	0.5823
S amplitude (mV)	-0.248 ± 0.023	-0.204 ± 0.031	-0.219 ± 0.046	0.6749

2.4 Discussion

Mutations in SLMAP have been linked to Brugada while it has also been shown to be a component of the STRIPAK complex involved in regulating Hippo signaling. To define the precise role of SLMAP within postnatal myocardium we generated a cardiac-specific knockout of SLMAP using the cre-lox system by targeting exon 3 of the SLMAP gene with a view to nullify it`s expression. We employed the αMHC-MerCreMer method to define the impact of SLMAP loss on myocardium in a temporal manner i.e. in the postnatal myocardium by using tamoxifen to activate cre and excise floxed SLMAP [33].

To our surprise, cleaving exon 3 of mouse SLMAP gene only impacted the transcript and protein levels of SLMAP3. The expression and levels of SLMAP1 and SLMAP2 isoforms remained unchanged while SLMAP3 levels were significantly decreased in KD and lost in KO animals. We hypothesized that loss of SLMAP3 would impact the growth/function of postnatal myocardium since SLMAP3 houses the FHA domain, which was shown to integrate MST1/2 to regulate Hippo signaling [18,19,20,21]. In addition, the loss of SLMAP3 may influence Nav 1.5 shuttling and the electrical properties of myocardium [24]. ECHO analysis indicated that SLMAP3-deficient hearts showed no significant changes in cardiac structure or function in the acute or chronic loss of SLMAP3. Administration of ISO to experimental animals did not expose any underlying phenotypes to this stressor of the myocardium. ECHO and histological analysis indicated an identical hypertrophic phenotype in iso-treated KO and Wt hearts implying an unaffected stress response in SLMAP3 KO hearts. These results suggest that SLMAP3 does not play a role in this aspect of cardiac structure or function and we believe this may be due to compensation by the abundant levels of SLMAP1 and SLMAP2 that remain unchanged in the SLMAP3-KO mouse myocardium. SLMAP1 and SLMAP2 could compensate due to the

significant homology between these isoforms and their robust expression in the myocardium relative to SLMAP3 (~9x greater) [5]. We theorize that SLMAP1 and SLMAP2 are not affected by cleavage of exon 3 because they might be regulated by alternate promoters [42]. SLMAP1 and SLMAP2 are arguably truncated variants of SLMAP3 and contain unique in-frame start codons at exon 10 and 16 which could be regulated by promoters upstream of these start codons [1].

Several studies have indicated that the expression and localization of Nav1.5 can be impacted by SLMAP3 [24,26]. In SLMAP3-KO hearts, there was a minor but significant decrease in Nav1.5 protein expression. However, ECG analysis of adult mice with cardiac SLMAP3-deficiency displayed no significant differences in any parameters when compared to Wt. Researchers have shown that mice with at least 50% decrease of Nav1.5 display defects in atrioventricular conduction parameters, without presenting any obvious cardiac phenotypes [43]. This was also noted in our SLMAP3 overexpressing transgenic mice as Nav1.5 transcript levels were reduced by 55%, similarly displaying atrioventricular conduction defects with no overt defects in myocardium [26]. Additionally, we found the SLMAP3-Tg myocardium had decreased transcript levels of Nav1.5 and Serca2a, but this was not seen in SLMAP1-Tg hearts, implying that SLMAP3 may uniquely modulate gene expression in-vivo and further implying a relationship between SLMAP3 and Nav1.5 [26]. Ishikawa et al, linked mutations in human SLMAP gene at exons 8 (SLMAP3-specific) and exon 21 (all SLMAP isoforms) in Brugada patients. When mutated SLMAP3 or SLMAP1 protein were expressed in HEK293 they inhibited trafficking of expressed hNav1.5 to cell surface [26]. SLMAP isoforms can homo- and heterodimerize via coiled-coil domains [5], and the overexpression of SLMAP3 could potentially sequester

endogenous SLMAPs and interacting proteins to subcellular domains impacting the mechanism that regulates expression/trafficking of Nav1.5, although this is yet to be fully interrogated.

The forkhead associated (FHA) domain in SLMAP3 has been shown to recruit MST1/2 kinase to negatively regulate the Hippo pathway via the STRIPAK complex [44,45]. Evidence indicates that loss of SLMAP3 in human cells and Drosophila positively regulates Hippo signaling i.e. increased phosphorylation of MST1/2 (T183) and YAP (S127) [18,19,20,21,46] however no significant differences were noted in phosphorylation of MST1/2 or YAP in SLMAP3-KO hearts compared to wildtype myocardium. When Hippo signaling is upregulated in adult mouse hearts via overexpression of cardiac-specific MST1/2 and/or deletion of YAP it led to cardiomyopathies and heart failure [47,48]. Therefore if loss of SLMAP3 would have affected Hippo signaling similarly, it would result in similar phenotypes in postnatal mouse hearts. It is notable that Hippo deficiency in adult myocardium leads to dysfunction in pressure overload [49] while it reversed the systolic heart failure after infarction [50]. Although, we used ISO to stress the heart we did not observe any cardiac dysfunction or changes in Hippo signaling. Whether injury such as myocardial infarction or pressure overload would impact Hippo in SLMAP3 deficient hearts and function remains to be investigated [51]. If and how the abundant expression of SLMAP1 and SLMAP2 isoforms in postnatal myocardium may compensate for SLMAP3 loss in terms of Hippo signaling and function remains to be examined. The lack of change in Hippo signalling due to SLMAP3 loss could also be due to the extremely low proliferative rates of cardiomyocytes in postnatal heart development since Hippo signaling reaches its peak as early as 10 days of age in mice [52,53]. Thus, the lack of phenotype in SLMAP3-deficient postnatal myocardium could be due to lack of proliferative programing in mature cardiomyocytes [54,55]. Studies to evaluate the impact of SLMAP3 by targeting its prenatal/perinatal expression, where

cardiomyocyte proliferation/growth is critical are now in progress together with nullifying SLMAP1 and SLMAP2 isoforms [56,57].

2.5. Conclusions

In conclusion, cardiac-specific loss of SLMAP3 in postnatal myocardium did not significantly alter structure/function or activity of Hippo signalling in mouse hearts. Although a minor decrease in Nav1.5 expression was noted, it did not affect cardiac electrophysiology in adult SLMAP3-deficient hearts. We theorize that isoforms SLMAP1 and SLMAP2 may compensate for SLMAP3 due to their robust expression in the adult myocardium. To further investigate in-vivo roles of SLMAPs studies are in progress to nullify expression of all SLMAP isoforms during prenatal/perinatal cardiac development.

2.6 References

1. Wielowieyski, P.; Sevinc, S.; Guzzo, R.; Salih, M.; Wigle, J.; Tuana, B. Alternative splicing, expression, and genomic structure of the 3' region of the gene encoding the sarcolemmal-associated proteins (SLAPs) defines a novel class of coiled-coil tail-anchored membrane proteins. J Biol Chem 2000, 275 (49), 38474-38481.

2. Wigle, J.; Demchyshyn, L.; Pratt, M.; Staines, W.; Salih, M.; Tuana, B. Molecular cloning, expression, and chromosomal assignment of sarcolemmal-associated proteins. A family of acidic amphipathic alpha-helical proteins associated with the membrane. J Biol Chem 1997, 272 (51), 32384-32394.

3. Guzzo, R.; Wigle, J.; Salih, M.; Moore, E.; Tuana, B. Regulated expression and temporal induction of the tail-anchored sarcolemmal-membrane-associated protein is critical for myoblast fusion. Biochem J 2004, 381 (3), 599-608.

4. Byers, J.; Guzzo, R.; Salih, M.; Tuana, B. Hydrophobic profiles of the tail anchors in SLMAP dictate subcellular targeting. BMC Cell Biol 2009, 10 (48).

5. Guzzo, R.; Sevinc, S.; Salih, M.; Tuana, B. A novel isoform of sarcolemmal membrane-associated protein (SLMAP) is a component of the microtubule organizing centre. J Cell Sci. 2004 May 1;117(Pt 11):2271-81. 2004, 117 (11), 2271-2281.

6. Letunic, I.; Bork, P. 20 years of the SMART protein domain annotation resource. Nucleic Acids Res 2018, 46 (D1), D493-D496.

7. Mahajan, A.; Yuan, C.; Lee, H.; Chen, E.; Wu, P.; Tsai, M. Structure and function of the phosphothreonine-specific FHA domain. Sci Signal 2008, 1 (51).

8. Couzens, A.; Knight, J.; Kean, M.; Teo, G.; Weiss, A.; Dunham, W.; Lin, Z.; Bagshaw, R.; Sicheri, F.; Pawson, T.; Wrana, J.; Choi, H.; Gingras, A. Protein interaction network of the mammalian Hippo pathway reveals mechanisms of kinase-phosphatase interactions. Sci Signal 2013, 6 (302).

9. Goudreault, M.; D'Ambrosio, L.; Kean, M.; Mullin, M.; Larsen, B.; Sanchez, A.; Chaudhry, S.; Chen, G.; Sicheri, F.; Nesvizhskii, A.; Aebersold, R.; Raught, B.; Gingras, A. A PP2A Phosphatase High Density Interaction Network Identifies a Novel Striatin-interacting Phosphatase and Kinase Complex Linked to the Cerebral Cavernous Malformation 3 (CCM3) Protein. Mol Cell Proteomics 2009, 8 (1), 157-171.

10. Zheng, Y.; Pan, D. The Hippo Signaling Pathway in Development and Disease. Dev Cell 2019, 50 (3), 264-282.

11. Wang, J.; Liu, S.; Heallen, T.; Martin, J. The Hippo pathway in the heart: pivotal roles in development, disease, and regeneration.. Nat Rev Cardiol 2018, 15 (11), 672-684.

12. Misra, J.; Irvine, K. The Hippo Signaling Network and Its Biological Functions. Annu Rev Genet 2018, 52, 65-87.

13. Zhou, Q.; Li, L.; Zhao, B.; Guan, K. L. The Hippo pathway in heart development, regeneration, and diseases. Circulation research 2015, 116 (8), 1431-1447.

14. von, G. A.; Lin, Z.; Schlegelmilch, K.; Honor, L.; Pan, G.; Buck, J.; Ma, Q.; Ishiwata, T.; Zhou, B.; Camargo, F.; Pu, W. YAP1, the nuclear target of Hippo signaling, stimulates heart growth through cardiomyocyte proliferation but not hypertrophy. Proc Natl Acad Sci U S A 2012, 109 (7), 2394-2399.

15. Xin, M.; Kim, Y.; Sutherland, L.; Murakami, M.; Qi, X.; McAnally, J.; Porrello, E.; Mahmoud, A.; Tan, W.; Shelton, J.; Richardson, J.; Sadek, H.; Bassel-Duby, R.; Olson, E. Hippo pathway effector Yap promotes cardiac regeneration. Proc Natl Acad Sci U S A. 2013 Aug 20;110(34 2013, 110 (34), 13839-13844.

16. Heallen, T.; Zhang, M.; Wang, J.; Bonilla-Claudio, M.; Klysik, E.; Johnson, R.; Martin, J. Hippo pathway inhibits Wnt signaling to restrain cardiomyocyte proliferation and heart size. Science 2011, 332 (6028), 458-461.

17. Byun, J.; Del Re, D.; Zhai, P.; Ikeda, S.; Shirakabe, A.; Mizushima, W.; Miyamoto, S.; Brown, J.; Sadoshima, J. Yes-associated protein (YAP) mediates adaptive cardiac hypertrophy in response to pressure overload. J Biol Chem 2019, 294 (10), 3603-3617.

18. Jeong, B.; Bae, S.; Ni, L.; Zhang, X.; Bai, X.; Luo, X. Cryo-EM structure of the Hippo signaling integrator human STRIPAK. Nat Struct Mol Biol 2021, 28 (3), 290-299.

19. Hauri, S.; Wepf, A.; van Drogen, A.; Varjosalo, M.; Tapon, N.; Aebersold, R.; Gstaiger, M. Interaction proteome of human Hippo signaling: modular control of the co-activator YAP1. Mol Syst Biol 2013, 9 (713).

20. Bae, S.; Ni, L.; Osinski, A.; Tomchick, D.; Brautigam, C.; Luo, X. SAV1 promotes Hippo kinase activation through antagonizing the PP2A phosphatase STRIPAK. eLife 2017, 6 (30278).

21. Zheng, Y.; Liu, B.; Wang, L.; Lei, H.; Pulgar Prieto, K.; Pan, D. Homeostatic Control of Hpo/MST Kinase Activity through Autophosphorylation-Dependent Recruitment of the STRIPAK PP2A Phosphatase Complex. Cell Reports 2017, 21 (12), 3612-3623.

22. Guzzo, R. M.; Salih, M.; Moore, E. D.; Tuana, B. Molecular properties of cardiac tail-anchored membrane protein SLMAP are consistent with structural role in arrangement of excitation-contraction coupling apparatus. Am J Physiol Heart Circ Physiol 2005, 288 (4), H1810-H1819.

23. Nader, M.; Westendorp, B.; Hawari, O.; Salih, M.; Stewart, A. F.; Leenen, F. H.; Tuana, B. S. Tail-anchored membrane protein SLMAP is a novel regulator of cardiac function at the sarcoplasmic reticulum. Am J Physiol Heart Circ Physiol 2012, 302 (5), 1138-1145.

24. Ishikawa, T.; Sato, A.; Marcou, C.; Tester, D.; Ackerman, M.; Crotti, L.; Schwartz, P.; On, Y.; Park, J.; Nakamura, K.; Hiraoka, M.; Nakazawa, K.; Sakurada, H.; Arimura, T.; Makita, N.; Kimura, A. A novel disease gene for Brugada syndrome: sarcolemmal membrane-associated protein gene mutations impair intracellular trafficking of hNav1.5. Circ Arrhythm Electrophysiol 2012, 5 (6), 1098-1107.

25. Brugada, R.; Campuzano, O.; Sarquella-Brugada, G.; Brugada, J.; Brugada, P. Brugada syndrome. Methodist Debakey Cardiovasc J 2014, 10 (1), 25-28.

26. Mlynarova, J.; Trentin-Sonoda, M.; Gaisler da Silva, F.; Major, J.; Salih, M.; Carneiro-Ramos, M.; Tuana, B. SLMAP3 isoform modulates cardiac gene expression and function. PLoS One 2019, 14 (4), e0214669.

27. Bustin, S. A. Quantification of mRNA using real-time reverse transcription PCR (RT-PCR): trends and problems. J Mol Endocrinol 2002, 29 (1), 23-29.

28. Mitchell, G.; Jeron, A.; Koren, G. Measurement of heart rate and Q-T interval in the conscious mouse. Am J Physiol 1998, 274 (3), H747-H751.

29. Aken, B.; Ayling, S.; Barrell, D.; Clarke, L.; Curwen, V.; Fairley, S.; Fernandez, B. J.; Billis, K.; García, G. C.; Hourlier, T.; Howe, K.; Kähäri, A.; Kokocinski, F.; Martin, F.; Murphy, D.; Nag, R.; Ruffier, M.; Schuster, M.; Tang, Y.; Vogel, J.; White, S. The Ensembl gene annotation system. Database 2016, 2016 (baw093), Release 90.

30. Consortium, U. UniProt: a worldwide hub of protein knowledge. Nucleic Acids Res 2019, 47 (D1), D506-D515.

31. Schmidt, T.; Samaras, P.; Frejno, M. G. S.; Barnert, M.; Kienegger, H.; Krcmar, H.; Schlegl, J.; Ehrlich, H. C.; Aiche, S.; Kuster, B.; Wilhelm, M. ProteomicsDB. Nucleic acids research 2018, 4 (46), D1271-D1281.

32. Davis, J.; Maillet, M.; Miano, J.; Molkentin, J. Lost in transgenesis: A user's guide for genetically manipulating the mouse in cardiac research. Circ. Res 2012, 111, 761-777.

33. Sohal, D. S.; Nghiem, M.; Crackower, M. A.; Witt, S. A.; Kimball, T. R.; Tymitz, K. M.; Penninger, J. M.; Molkentin, J. D. Temporally regulated and tissue-specific gene manipulations in the adult and embryonic heart using a tamoxifen-inducible Cre protein. Circ Res. 2001, 89 (1), 20-25.

34. Demayo, J.; Wang, J.; Liang, D.; Zhang, R.; Demayo, F. Genetically Engineered Mice by Pronuclear DNA microinjection. Curr Protoc Mouse Biol 2012, 2, 245-262.

35. Ayadi, A.; Ferrand, G.; Cruz, I.; Warot, X. Mouse Breeding and Colony Management. Current Protocols in Mouse Biology 2011, 1, 239-264.

36. Kuhn, R.; Torres, R. M. Cre/LoxP Recombination System and Gene Targeting. Transgenesis Techniques 2002, 180 (V), 175-204.

37. Bersell, K.; Choudhury, S.; Mollova, M.; Polizzotti, B. D.; Ganapathy, B.; Walsh, S.; Wadugu, B.; Arab, S.; Kühn, B. Moderate and high amounts of tamoxifen in αMHC-MerCreMer mice induce a DNA damage response, leading to heart failure and death. Disease Models & Mechanisms 2013, 6 (6), 1459-1469.

38. Yang, X.; Liu, Y.; Rhaleb, N.; Kurihara, N.; Kim, H.; Carretero, O. Echocardiographic assessment of cardiac function in conscious and anesthetized mice. Am J Physiol 1999, 277 (5), 1967-1974.

39. Zhang, G.; Kimura, S.; Nishiyama, A.; Shokoji, T.; Rahman, M.; Yao, L.; Nagai, Y.; Fujisawa, Y.; Miyatake, A.; Abe, Y. Cardiac oxidative stress in acute and chronic isoproterenol-infused rats. Cardiovasc Res 2005, 65 (1), 230-238.

40. Major, J.; Salih, M.; Tuana, B. Interplay between the E2F pathway and β-adrenergic signaling in the pathological hypertrophic response of myocardium. J Mol Cell Cardiol 2015, No. 84, 179-190.

41. Dong, . C.; Wang, Y.; Ma, A.; Wang, T. Life Cycle of the Cardiac Voltage-Gated Sodium Channel NaV1.5. Frontiers in physiology 2020, 11 (609733).

42. Ayoubi, T.; Van De Ven, W. Regulation of gene expression by alternative promoters. FASEB J 1996, 4 (10), 453-460.

43. Papadatos, G.; Wallerstein, P.; Head, C.; Ratcliff, R.; Brady, P.; Benndorf, K.; Saumarez, R.; Trezise, A.; Huang, C.; Vandenberg, J.; Colledge, W.; Grace, A. Slowed conduction and ventricular tachycardia after targeted disruption of the cardiac sodium channel gene Scn5a. Proc Natl Acad Sci 2002, 99, 6210-6215.

44. Bae, S.; Ni, L.; Luo, X. STK25 suppresses Hippo signaling by regulating SAV1-STRIPAK antagonism. eLife 2020, 9, e54863.

45. Chen, R.; Xie, R.; Meng, Z.; Ma, S.; Guan, K. STRIPAK integrates upstream signals to initiate the Hippo kinase cascade. Nat Cell Biol 2019, 21 (12), 1565-1577.

46. Kaya-Çopur, A.; Marchiano, F.; Hein, M.; Alpern, D.; Russeil, J.; Luis, N.; Mann, M.; Deplancke, B.; Habermann, B.; Schnorrer, F. The Hippo pathway controls myofibril assembly and muscle fiber growth by regulating sarcomeric gene expression. Elife 2021, 10, e63726.

47. Del Re, D.; Yang, Y.; Nakano, N.; Cho, J.; Zhai, P.; Yamamoto, T.; Zhang, N.; Yabuta, N.; Nojima, H.; Pan, D.; Sadoshima, J. Yes-associated protein isoform 1 (Yap1) promotes cardiomyocyte survival and growth to protect against myocardial ischemic injury. J Biol Chem 2013, 288 (6), 3977-3988.

48. Yamamoto, S.; Yang, G.; Zablocki, D.; Liu, J.; Hong, C.; Kim, S.; Soler, S.; Odashima, M.; Thaisz, J.; Yehia, G.; Molina, C.; Yatani, A.; Vatner, D.; Vatner, S.; Sadoshima, J. Activation of Mst1 causes dilated cardiomyopathy by stimulating apoptosis without compensatory ventricular myocyte hypertrophy. J Clin Invest 2003, 111 (10), 1463-1474.

49. Ikeda, S.; Mizushima, W.; Sciarretta, S.; Abdellatif, M.; Zhai, P.; Mukai, R.; Fefelova, N.; Oka, S.; Nakamura, M.; Del Re, D.; Farrance, I.; Park, J.; Tian, B.; Xie, L.; Kumar, M.; Hsu, C.; Sadayappan, S.; Shimokawa, H.; Lim, D.; Sadoshima, J. Hippo Deficiency Leads to Cardiac Dysfunction Accompanied by Cardiomyocyte Dedifferentiation During Pressure Overload. Circ Res 2019, 124 (2), 292-305.

50. Leach, J.; Heallen, T.; Zhang, M.; Rahmani, M.; Morikawa, Y.; Hill, M.; Segura, A.; Willerson, J.; Martin, J. Hippo pathway deficiency reverses systolic heart failure after infarction. Nature 2017, 550 (7675), 260-264.

51. Wang, P.; Mao, B.; Luo, W.; Wei, B.; Jiang, W.; Liu, D.; Song, L.; Ji, G.; Yang, Z.; Lai, Y.; Yuan, Z. The alteration of Hippo/YAP signaling in the development of hypertrophic cardiomyopathy. Basic Res Cardiol 2014, 109 (5), 435-438.

52. Heallen, T.; Morikawa, Y.; Leach, J.; Tao, G.; Willerson, J. T.; Johnson, R. L.; Martin, J. F. Hippo signaling impedes adult heart regeneration. Development 2013, 140 (23), 4683-4690.

53. Bergmann, O.; Bhardwaj, R.; Bernard, S.; Zdunek, S.; Barnabé-Heider, F.; Walsh, S.; Zupicich, J.; Alkass, K.; Buchholz, B.; Druid, H.; Jovinge, S.; Frisén, J. Evidence for cardiomyocyte renewal in humans. Science 2009, 324 (5923), 98-102.

54. Alkass, K.; Panula, J.; Westman, M.; Wu, T.; Guerquin-Kern, J.; Bergmann, O. No Evidence for Cardiomyocyte Number Expansion in Preadolescent Mice. Cell 2015, 163 (4), 1026-1036.

55. Heallen, T.; Kadow, Z.; Wang, J.; Martin, J. Determinants of Cardiac Growth and Size. Cold Spring Harb Perspect Biol 2020, 2 (3), a037150.

56. Yutzey, K. Cardiomyocyte Proliferation: Teaching an Old Dogma New Tricks. Circ Res 2017, 120 (4), 627-629.

57. Porrello, E.; Mahmoud, A.; Simpson, E.; Hill, J.; Richardson, J.; Olson, E.; Sadek, H. Transient regenerative potential of the neonatal mouse heart. Science 2011, 331 (6020), 1078-1080.

Supplementary Materials: The following are available online at www.mdpi.com/xxx/s1

Supplementary Table 1. *ECHO analysis on young and old SLMAP3-deficient hearts.* Left ventricular functional analysis, measurements of wall sizes and intradiameter during diastole and systole in 5-week and 24-week old mice with cardiac SLMAP3 deficiency. ρ-value was calculated using ANOVA statistics analysis. *n=6*. IVS; intraventricular septum, LVID; Left ventricular intradiameter, LVPW; Left ventricular posterior wall, EF; ejection fraction, FS; fractional shortening, LV mass; left ventricular mass, LV volume; left ventricular volume, d/s; diastole/systole, LV/BW; left ventricular mass/body weight.

5 week post TAM	WT	KD	KO	P<0.05
IVSd; mm	0.676 ± 0.034	0.734 ± 0.047	0.721 ± 0.039	N
IVSs; mm	0.953 ± 0.06	1.003 ± 0.070	0.933 ± 0.066	N
LVIDd; mm	3.997 ± 0.103	3.843 ± 0.090	3.985 ± 0.082	N
LVIDs; mm	2.946 ± 0.101	2.876 ± 0.079	2.983 ± 0.123	N
LVPWd; mm	0.762 ±0.046	0.806 ± 0.056	0.811 ± 0.068	N
LVPWs; mm	1.014 ± 0.062	1.012 ± 0.069	1.025 ± 0.077	N
EF; %	51.836 ± 2.325	50.400 ± 1.389	49.897 ± 3.708	N
FS; %	26.330 ± 1.500	25.217 ± 0.843	25.207 ± 2.294	N
LV Mass; µg	82.088 ± 5.574	84.629 ± 7.178	88.795 ± 7.312	N
LV Vold; µL	70.554 ± 4.213	64.103 ± 3.414	69.625 ± 3.380	N
LV Vols; µL	34.133 ± 2.715	31.921 ± 2.148	35.085 ± 3.566	N
Body Weight; g	27 ± 2.070	28.714 ± 1.899	26 ± 2.470	N
LV/BW; mg/g	2.734 ± 0.132	2.684 ± 0.124	3.078 ± 0.135	N

24 week post TAM	WT	KD	KO	P<0.05
IVSd; mm	0.744 ± 0.0182	0.729 ± 0.024	0.79 ± 0.013	N
IVSs; mm	1.000 ± 0.029	1.000 ± 0.052	0.996 ± 0.081	N
LVIDd; mm	4.194 ± 0.121	4.146 ± 0.063	3.981 ± 0.042	N
LVIDs; mm	3.281 ± 0.116	3.166 ± 0.076	3.028 ± 0.051	N
LVPWd; mm	0.870 ± 0.039	0.7630 ± 0.025	0.86 ± 0.049	N
LVPWs; mm	1.074 ± 0.047	0.9600 ± 0.041	1.096 ± 0.077	N
EF; %	44.6045 ± 1.2557	47.611 ± 1.764	48.028 ± 3.780	N
FS; %	21.8941 ± 0.6923	23.699 ± 1.062	23.897 ± 2.270	N
LV Mass; µg	103.9300 ± 6.4618	91.016 ± 2.667	97.316 ± 4.744	N
LV Vold; µL	79.1529 ± 5.2612	76.422 ± 2.683	69.260 ± 1.978	N
LV Vols; µL	44.2800 ± 3.6378	40.199 ± 2.192	35.846 ± 1.747	N
Body Weight; g	34.4286 ± 2.8523	35.75 ± 3.75	34.75 ± 0.629	N
LV/BW; mg/g	3.2291 ± 0.1749	2.680 ± 0.226	2.809 ± 0.169	N

Supplementary Table 2. *ECHO analysis on ISO-treated SLMAP3-KO hearts.* Measurement of left ventricular mass and wall sizes during diastole and systole in preISO and postISO Wt and KO mouse hearts. ρ-value was calculated using two-tailed student. *n=7*. IVS; intraventricular septum, LVID; Left ventricular intradiameter, LVPW; Left ventricular posterior wall, EF; ejection fraction, FS; fractional shortening, LV mass; left ventricular mass, LV volume; left ventricular volume, d/s; diastole/systole.

Parameters	preISO WT	postISO WT	ρ-value
IVSd; mm	0.687 ± 0.019	0.860 ± 0.030	0.000243881
IVSs; mm	0.964 ± 0.030	1.212 ± 0.048	0.001577668
LVPWd; mm	0.794 ± 0.031	0.917 ± 0.026	0.008476034
LVPWs; mm	1.044 ± 0.031	1.227 ± 0.035	0.002630256
LV Mass; mg	82.61 ± 3.756	111.2 ± 7.461	0.002448262

Parameters	preISO KO	postISO KO	ρ-value
IVSd; mm	0.710 ± 0.0369	0.873 ± 0.0676	0.004832328
IVSs; mm	0.973 ± 0.0358	1.199 ± 0.084	0.029518316
LVPWd; mm	0.721 ± 0.0368	0.905 ± 0.038	0.010458202
LVPWs; mm	0.976 ± 0.0675	1.169 ± 0.038	0.014591292
LV Mass; mg	80.29 ± 4.746	101.74 ± 11.82	0.041526465

Chapter Three: Cardiac-Specific Cre Induces Age-Dependent Dilated Cardiomyopathy (DCM) in Mice

molecules

MDPI

Article

Cardiac-Specific Cre Induces Age-Dependent Dilated Cardiomyopathy (DCM) in Mice

Taha Rehmani, Maysoon Salih and Balwant S. Tuana *

Department of Cellular and Molecular Medicine, Faculty of Medicine, University of Ottawa, Ottawa, ON, K1H 8M5, Canada; trehmani@uottawa.ca (T.R.); msalih@uottawa.ca (M.S.)
* Correspondence: btuana@uottawa.ca (B.S.T); Tel.: +613-562-5800 (ext. 8578)

Academic Editor: Morris Karmazyn

Molecules **2019**, *24*(6), 1189; https://doi.org/10.3390/molecules24061189

Received: 28 February 2019 / Revised: 18 March 2019 / Accepted: 19 March 2019 / Published: 26 March 2019

(This article belongs to the Special Issue Cardiovascular Diseases Prevention and Therapy)

Author Contributions: conceptualization, T.R., M.S. and B.S.T.; methodology, T.R and M.S.; data analysis, T.R and B.S.T; investigation, T.R.; visualization: T.R.; writing—original draft preparation, T.R.; Project administration: M.S. and B.S.T.; writing—review and editing, B.S.T.; supervision M.S. and B.S.T.; funding acquisition, B.S.T.**Funding:** This research was funded by the Canadian Institute of Health Research project grant, grant number 220996-151999, to B.S.T.

Acknowledgments: We would like to thank Dr. Burgon for donating the αMHC-cre animals for our studies.

Conflicts of Interest: The authors declare no conflicts of interest.

Abstract: The genetic modification of the mouse genome using the cre-lox system has been an invaluable tool in deciphering gene and protein function in a temporal and/or spatial manner. However, it has its pitfalls, as researchers have shown that the unregulated expression of cre recombinase can cause DNA damage, the consequences of which can be very detrimental to mouse health. Previously published literature on the most utilized cardiac-specific cre, αMHC-cre, mouse model exhibited a nonlethal hypertrophic cardiomyopathy (HCM) with aging. However, using the same αMHC-cre mice, we observed a cardiac pathology, resulting in complete lethality by 11 months of age. Echocardiography and histology revealed that the αMHC-cre mice were displaying symptoms of dilated cardiomyopathy (DCM) by seven months of age, which ultimately led to their demise in the absence of any HCM at any age. Molecular analysis showed that this phenotype was associated with the DNA damage response through the downregulation of activated p38 and increased expression of JNK, p53, and Bax, known inducers of myocyte death resulting in fibrosis. Our data urges strong caution when interpreting the phenotypic impact of gene responses using αMHC-cre mice, since a lethal DCM was induced by the cre driver in an age-dependent manner in this commonly utilized model system.

Keywords: cardiac-specific-cre; dilated cardiomyopathy; cre-lox system; mouse model; cardiotoxic; DNA damage

3.1 Introduction

Genetic manipulations in model organisms are the crux of biological and medical research in terms of ascribing physiological or pathological roles for the gene of interest [1]. Through modifications of a model organism's genome, it has been possible to discover, verify, and establish complex roles of genes and the proteins they encode [2]. The genetically modified mouse model is very attractive, as mice share a very similar genetic profile, anatomy, and disease progression to humans [3]. Genetic modifications of the mouse take place through the manipulation of mouse embryonic stem cells by taking advantage of the stem cells' natural inclination toward homologous recombination to selectively replace the endogenous target gene sequence with modified exogenous DNA [4]. Significant strides in genetic engineering have allowed us to utilize many models and systems for modifying the genome, such as the cre-lox system [5].

The cre-lox system is a site-specific recombination system used to modify DNA through manipulation derived from the P1 bacteriophage [6]. It is a two-part system where the recombinase, cre, binds to a specific 34-base pair sequence known as a loxP site [7]. To employ cre-lox, the gene of interest is modified to be flanked by two loxP sites (floxed), and thus when the cre enzyme is introduced it cleaves the flanked sequence and merges the two excision points together, resulting in a smaller sequence and thus permanently modifying the floxed gene [8,9]. The use of cre-lox is enticing because the modification by the cre recombinase of the gene target can be controlled in a temporal and spatial manner [10]. Specific promoter sequences driving the expression of cre recombinase result in tissue-specific expression, excising floxed genes only within the specific cell of interest [11]. The fusing of *cre* to modified estrogen receptors (Mer) retains cre in the cytosol until it is activated by an estrogen analog, tamoxifen [12]. The simplicity

of cre, with no additional requirements for recombination (such as cofactors or accessory proteins) and loxP sites which are not endogenous in mammals, makes the cre-lox system an ideal candidate for genetic engineering in cells and animal models [13].

To target the floxed genes of mouse myocardium, researchers have implemented the use of the cardiac specific promoter α-myosin heavy chain (*αMHC*) to ensure that cre is expressed only within cardiomyocytes [14]. This specific cre has been widely utilized for targeting floxed genes within the mouse heart to elucidate gene function and impacts on the myocardium [15,16]. This system, however, has demonstrated pitfalls [15-17].

Overactive cre recombinase can be toxic, as studies have shown that it can inhibit DNA replication and increase DNA damage: However, regulating the concentration or activity of cre can minimize toxicity [18]. This may be due to the presence of endogenous lox-like sequences within the mammalian genome that can be targeted by cre [19,20]. Evidence suggests that cre is cardiotoxic, as numerous publications using the inducible *αMHC-MerCreMer* have shown that large doses of tamoxifen overstimulate cre, resulting in decreased cardiac function through enhanced myocyte death/fibrosis and DNA damage [21,22]. The focus has been mostly on the MerCreMer model: however, in a non-inducible αMHC-cre model, there has only been one study highlighting the development of a nonfatal hypertrophic cardiomyopathy (HCM) that presents in six-month-old mice [16]. We report here that in the same αMHC-cre mice, an age-dependent fatal dilated cardiomyopathy (DCM) was prevalent. We believe this to be an important finding, as this cardiac-specific cre model has been used in over 150 studies, with 14 publications highlighting an age-dependent fatal DCM attributed to their respective gene modifications without utilizing the appropriate cre-only controls in a timed manner. The DCM appeared to be

a byproduct of cre cardiotoxicity, resulting from an accumulation of DNA damage. We hope our results will further highlight the pitfall of using long-term cardiac-specific cre as well as encourage the use of proper cre-only controls during gene manipulation studies in the postnatal heart.

3. 2. Results

3.2.1. The Change in Lifespan of αMHC-cre Mice

We employed mice that express αMHC-cre that have been used in a large variety of cardiac gene manipulation studies [14]. The genotype of these animals was determined through PCR to differentiate wild-type (Wt) littermates and establish the αMHC-cre only (Cre+) experimental animals. Primers *Cre-F* and *Cre-R* were used to detect *cre* by synthesizing a DNA amplicon 425 base pair (bp) in length: Wt animals lack such an insert (seen in respective agarose gel lanes (**Figure 1A**). We examined 11 Cre+ and 11 wild-type littermates to determine any impact of timed cre exposure in the myocardium and on mouse survival (**Figure 1B**). We observed a 50% loss of Cre+ mice by approximately 8 months of age, with the remainder dying before 11 months of age (**Figure 1B)**. All Cre+ animals were seen to be in pain and distress (body condition scoring = 2-) [23]. Thus, mice carrying *αMHC-cre* underwent age-dependent death, with complete loss within one year of age. This data is consistent with the notion that cre is cardiotoxic and that this particular cre mouse model exhibits timed lethality [15].

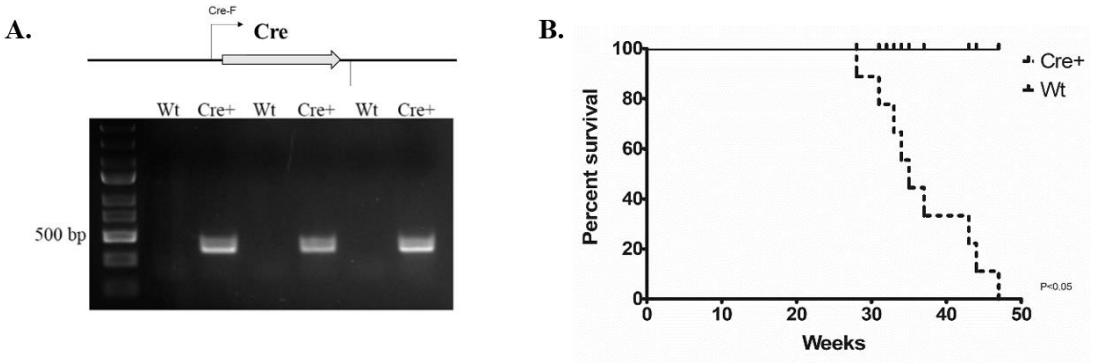

Figure 1. Long-term exposure to αMHC-cre resulted in complete lethality in mice by 11 months of age. (**A**) PCR genotyping using primers Cre-F/Cre-R to identify Wt or Cre+ littermates. Wt lanes indicate a wild-type genotype, whereas Cre+ lanes indicate the presence of *αMHC-cre* (425 bp). (**B**) Kaplan–Meier survival curve analysis of Cre+ mice compared to Wt littermates. Cre+ animals began dying at 7 months, dropping off intermittently until 11 months of age ($p < 0.05$, $n = 11$).

3.2.2. αMHC-cre Mice Presented with an Age-Dependent Dilated Cardiomyopathy

Given the age-dependent lethality noted in the αMHC-cre mice, we examined any changes in cardiac structure and function to discover the cause. Transthoracic echocardiography (ECHO) was performed in an age-dependent manner in mice, beginning at three months of age and repeated monthly until they perished. The left ventricle wall thickness (interventricular septum (IVS), left ventricle posterior wall (LVPW)) and the left ventricle internal diameter (LVID) in systole and diastole were determined. These measurements were used to evaluate cardiac function by calculating the ejection fraction (EF), fractional shortening (FS), which measure percentage of blood output and muscle contraction respectively [24]. Table 1 shows a comprehensive evaluation of the data acquired at different time points for ECHOs in Wt and Cre+ mice. Before six months of age, αMHC-cre and Wt mice had identical left ventricle structure and function (**Figure 2**). However, at six months of age, the left ventricle wall of αMHC-cre was thinner with the presence of dilation compared to Wt hearts (**Figure 2**). At seven months, a significantly thinner IVS;d(18.62% decrease, $n = 8$, $p < 0.05$) and LVPW;d (16.3% decrease, $n = 8$, $p < 0.05$) and a significantly larger ventricle interdiameter at systole (29.5% increase, $n = 8$, $p < 0.05$) in Cre+ hearts compared to Wt was notable (**Table 1**). An analysis of these changes indicated a significant reduction in the EF (37.25% decrease, $n = 8$, $p < 0.05$) and FS (40.76% decrease, $n = 8$, $p < 0.05$) in Cre+ hearts when compared to Wt (**Figure 3**). Thinning of the left ventricle wall and a dilation of the chamber were clear indications of a lethal phenotype: Dilated cardiomyopathy (DCM). This phenotype was further exacerbated as αMHC-cre animals aged, resulting in an even greater change in cardiac structure and significantly diminished function at eight months of age (**Figures 2 and 3**). Therefore, αMHC-cre induced an age-

dependent DCM, which significantly reduced cardiac function and resulted in observable respiratory distress and death.

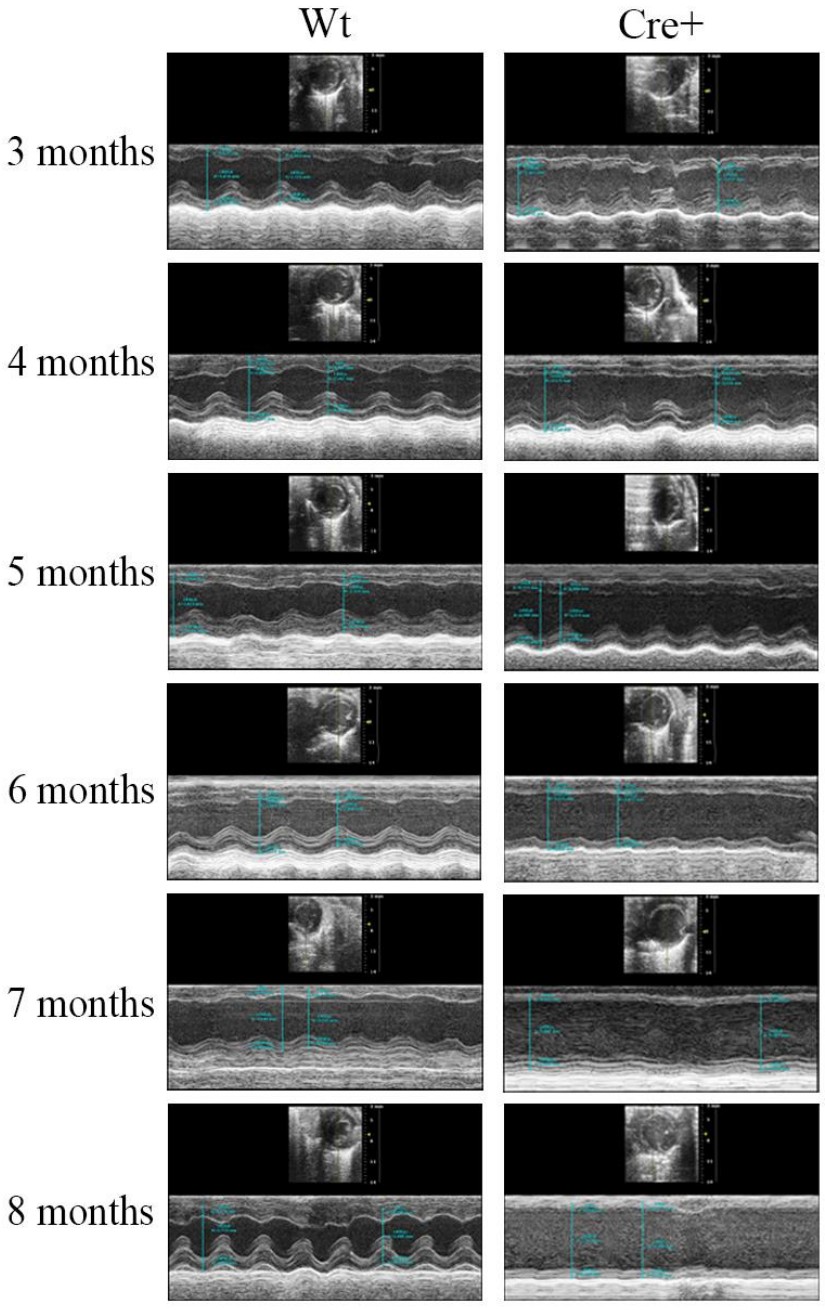

Figure 2. Echocardiography imaging revealed significant comparisons between aging Wt and Cre+ hearts. Representative short-axis m-mode transthoracic echocardiography (ECHO) images of wild-type and Cre+ animals at 3–8 months of age (n = 8).

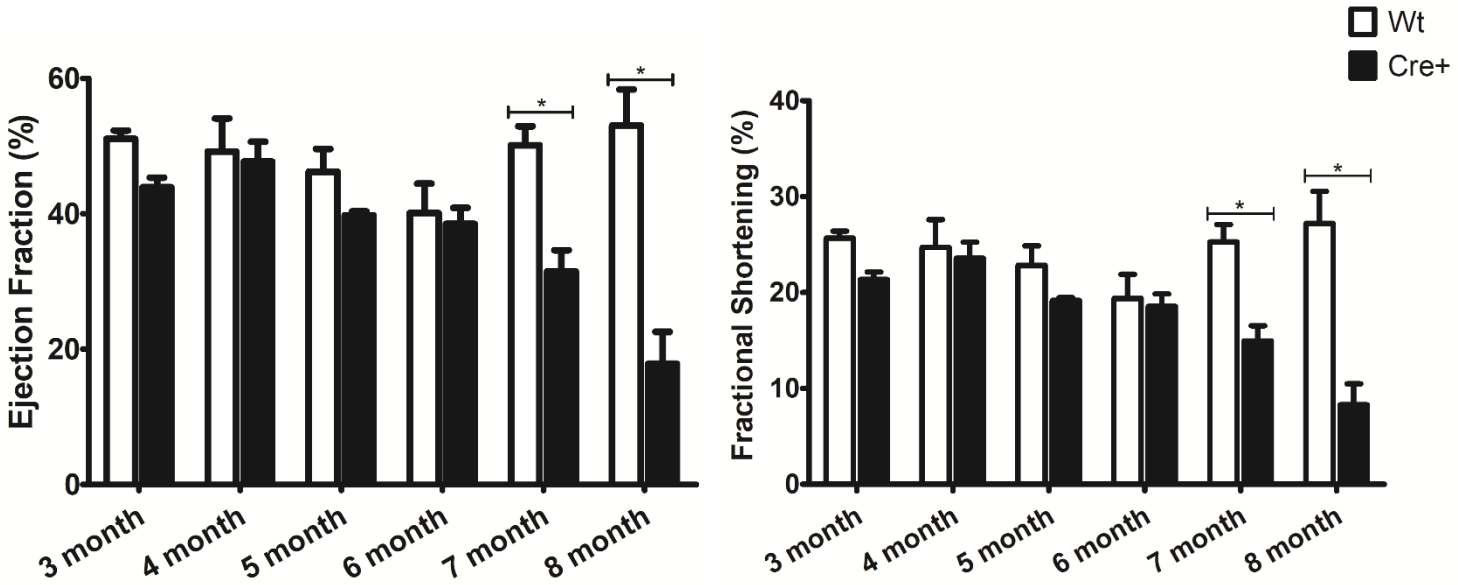

Figure 3. Age-dependent changes in cardiac function to Wt and Cre+ hearts. Cardiac function was analyzed with ECHO and the calculated ejection fraction and fractional shortening in Wt and Cre+ animals 3–8 months of age is presented. (* indicates a p value less than 0.05, $n = 8$).

Table 1. Left ventricular wall thickness and functional analysis of Wt and Cre+ animals. Left ventricle analysis on Wt and Cre+ mice from ECHO studies from 3 to 8 months of age. Functional analysis was done via measurements of left ventricle wall sizes and interdiameters during diastole and systole. IVS: Interventricular septum; LVID: Left ventricular interdiameter; LVPW: Left ventricular posterior wall; EF: Ejection fraction; FS: Fractional shortening; LV mass: Left ventricular mass; LV volume: Left ventricular volume; d/s: Diastole/systole. Here, *n* = *8*.

3 months	**Wt**	**Cre+**	***p*-value**	**4 months**	**Wt**	**Cre+**	***p*-value**
IVS;d (mm)	0.630 ± 0.025	0.620 ± 0.027	0.291692478	IVS;d (mm)	0.645 ± 0.028	0.675 ± 0.033	0.788462538
IVS;s (mm)	0.841 ± 0.024	0.752 ± 0.042	0.088168344	IVS;s (mm)	0.840 ± 0.031	0.799 ± 0.006	0.063367682
LVID;d (mm)	3.988 ± 0.120	3.891 ± 0.062	0.844773361	LVID;d (mm)	3.945 ± 0.130	3.816 ± 0.170	0.854738647
LVID;s (mm)	2.965 ± 0.104	3.062 ± 0.078	0.533414051	LVID;s (mm)	2.983 ± 0.210	2.923 ± 0.180	0.816015832
LVPW;d (mm)	0.752 ± 0.039	0.703 ± 0.009	0.421564695	LVPW;d (mm)	0.741 ± 0.033	0.692 ± 0.031	0.163169522
LVPW;s (mm)	0.950 ± 0.058	0.865 ± 0.023	0.186036258	LVPW;s (mm)	0.917 ± 0.021	0.903 ± 0.052	0.612779363
EF (%)	51.078 ± 1.225	43.930 ± 1.415	0.050885727	EF (%)	49.190 ± 4.900	47.703 ± 2.932	0.626142978
FS (%)	25.670 ± 0.730	21.351 ± 0.789	0.040507965	FS (%)	24.692 ± 2.920	23.568 ± 1.676	0.592817029
LV Mass (mg)	77.478 ± 6.617	69.760 ± 0.624	0.462915868	LV Mass (mg)	76.123 ± 4.930	70.596 ± 4.086	0.474495439
LV Vol;d (μL)	69.792 ± 4.975	65.625 ± 2.444	0.828743538	LV Vol;d (μL)	68.114 ± 5.262	63.086 ± 6.373	0.875915463
LV Vol;s (μL)	34.230 ± 2.917	36.890 ± 2.231	0.540609259	LV Vol;s (μL)	35.345 ± 5.924	33.372 ± 4.70	0.832144194
Heart Rate (bpm)	475.063 ± 31.085	426.813 ± 25.030	0.24795013	Heart Rate (bpm)	442.375 ± 15.083	488.813 ± 18.431	0.131686783
5 months	**Wt**	**Cre+**	***p*-value**	**6 months**	**Wt**	**Cre+**	***p*-value**
IVS;d (mm)	0.703 ± 0.055	0.621 ± 0.033	0.221718131	IVS;d (mm)	0.645 ± 0.0270	0.623 ± 0.025	0.582227989
IVS;s (mm)	0.867 ± 0.037	0.760 ± 0.032	0.066845485	IVS;s (mm)	0.770 ± 0.046	0.773 ± 0.036	0.944541382
LVID;d (mm)	4.015 ± 0.070	4.24 ± 0.022	0.011199612	LVID;d (mm)	3.860 ± 0.086	4.267 ± 0.050	0.000984789
LVID;s (mm)	3.010 ± 0.094	3.428 ± 0.029	0.007459428	LVID;s (mm)	3.111 ± 0.115	3.480 ± 0.073	0.015556863
LVPW;d (mm)	0.771 ± 0.045	0.720 ± 0.019	0.292980414	LVPW;d (mm)	0.741 ± 0.013	0.670 ± 0.022	0.037445862
LVPW;s (mm)	0.941 ± 0.033	0.853 ± 0.036	0.123190118	LVPW;s (mm)	0.881 ± 0.058	0.840 ± 0.038	0.533692627
EF (%)	46.214 ± 3.352	39.801 ± 0.561	0.070796387	EF (%)	40.113 ± 4.339	38.503 ± 2.380	0.728792586
FS (%)	22.836 ± 2.019	19.160 ± 0.307	0.081406368	FS (%)	19.377 ± 2.510	18.545 ± 1.313	0.75158218
LV Mass (mg)	85.180 ± 7.413	82.324 ± 3.134	0.711666602	LV Mass (mg)	73.251 ± 2.367	79.583 ± 3.594	0.228762289
LV Vol;d (μL)	70.721 ± 2.901	80.372 ± 0.981	0.010393045	LV Vol;d (μL)	64.510 ± 3.442	81.820 ± 2.206	0.000959293
LV Vol;s (μL)	38.018 ± 2.791	48.402 ± 0.994	0.006305021	LV Vol;s (μL)	38.590 ± 3.453	50.370 ± 2.421	0.015009289
Heart Rate (bpm)	468.229 ± 19.224	437.563 ± 22.691	0.470433394	Heart Rate (bpm)	456.333 ± 23.479	457.083 ± 21.667	0.985755943

7 months	Wt	Cre+	*p*-value	8 months	Wt	Cre+	*p*-value
IVS;d (mm)	0.652 ± 0.046	0.530 ± 0.017	0.004871736	IVS;d (mm)	0.672 ± 0.038	0.525 ± 0.020	0.002876701
IVS;s (mm)	0.852 ± 0.075	0.655 ± 0.028	0.004820388	IVS;s (mm)	0.897 ± 0.038	0.583 ± 0.023	2.01935E-05
LVID;d (mm)	4.153 ± 0.107	4.710 ± 0.085	0.00075479	LVID;d (mm)	3.992 ± 0.087	5.0120 ± 0.733	0.002527764
LVID;s (mm)	3.100 ± 0.078	4.015 ± 0.146	0.000380906	LVID;s (mm)	2.911 ± 0.181	4.613 ± 0.218	0.000506287
LVPW;d (mm)	0.731 ± 0.035	0.612 ± 0.0260	0.010122283	LVPW;d (mm)	0.729 ± 0.043	0.607 ± 0.029	0.037276373
LVPW;s (mm)	0.960 ± 0.063	0.735 ± 0.033	0.001783791	LVPW;s (mm)	0.899 ± 0.048	0.658 ± 0.047	0.009337212
EF (%)	50.140 ± 2.792	31.463 ± 3.171	0.000971708	EF (%)	53.049 ± 5.311	17.836 ± 4.746	0.001064173
FS (%)	25.264 ± 1.830	14.966 ± 1.571	0.000618349	FS (%)	27.203 ± 3.350	8.287 ± 2.190	0.000655345
LV Mass (mg)	83.423 ± 9.092	80.60 ± 2.389	0.667096037	LV Mass (mg)	78.378 ± 3.758	90.433 ± 6.474	0.242979928
LV Vol;d (μL)	76.765 ± 4.640	103.311 ± 4.489	0.001168324	LV Vol;d (μL)	69.821 ± 3.655	120.755 ± 9.005	0.00328618
LV Vol;s (μL)	38.055 ± 2.364	71.912 ± 6.740	0.002004722	LV Vol;s (μL)	33.135 ± 5.253	100.210 ± 10.261	0.001357712
Heart Rate (bpm)	458.750 ± 33.700	488.292 ± 20.507	0.509364526	Heart Rate (bpm)	426.833 ± 45.470	503.890 ± 12.685	0.308473653

3.2.3. Lack of Hypertrophy and Robust DCM in αMHC-cre Mice

Here, αMHC-cre mice exhibited a notable age-dependent DCM that led to their demise. A previous study indicated the presence of hypertrophic cardiomyopathy at 6 months of age in these αMHC-cre mice [16]. To determine if the αMHC-cre mice developed any HCM, we evaluated the wall thickness of mice beginning at 3 months of age, and no observable or significant thickening of ventricle walls was seen in ECHOs from the Wt or Cre+ animals (Table 1). Sex-separated analysis on 4–6-month-old female Cre+ mice versus Wt littermates indicated no difference in hypertrophy (**Figure 4**). In fact, female Cre+ hearts at 6 months of age trended toward ventricular wall thinning, not thickening (**Figure 4**). Thus, the collective (male/female) or female-only ECHO data suggested that αMHC-cre exhibited a robust DCM in an age-dependent manner in the absence of any notable HCM.

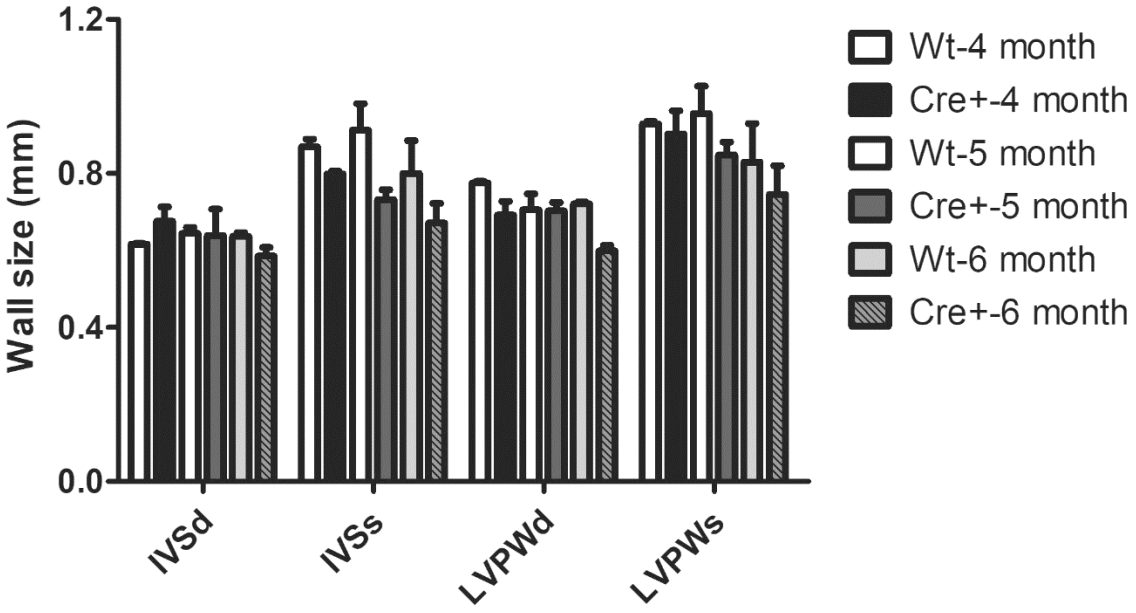

Figure 4. Left ventricular wall parameters in female Wt and Cre+ hearts. Left ventricle wall thickness of 4 to 6-month-old female mice. Here, $n = 3$. IVS: Interventricular septum; LVID: Left ventricular internal diameter; LVPW: Left ventricular posterior wall; d/s: Diastole/systole.

3.2.4. αMHC-cre Mice Exhibited Dilated Hearts and Fibrosis

The presence of a lethal DMC in the aged αMHC-cre mice was surprising and was further examined by histological analysis. Hearts from 8-month-old wild-type and αMHC-cre mice were fixed, sectioned, and stained with Masson's trichrome to visualize the myocardium (red stain) and acquire evidence of any overt fibrosis (blue stain). Hearts from the Cre+ mice had significantly thinner walls and a dilated chamber compared to Wt (**Figure 5**). Magnification of the image at 5× revealed significant blue staining indicative of fibrosis in the Cre+ hearts (arrows). The thin walls, dilated ventricle, and evident fibrosis confirmed that aged αMHC-cre mice were exhibiting DCM, and this was noticeably absent in the hearts of Wt mice [25].

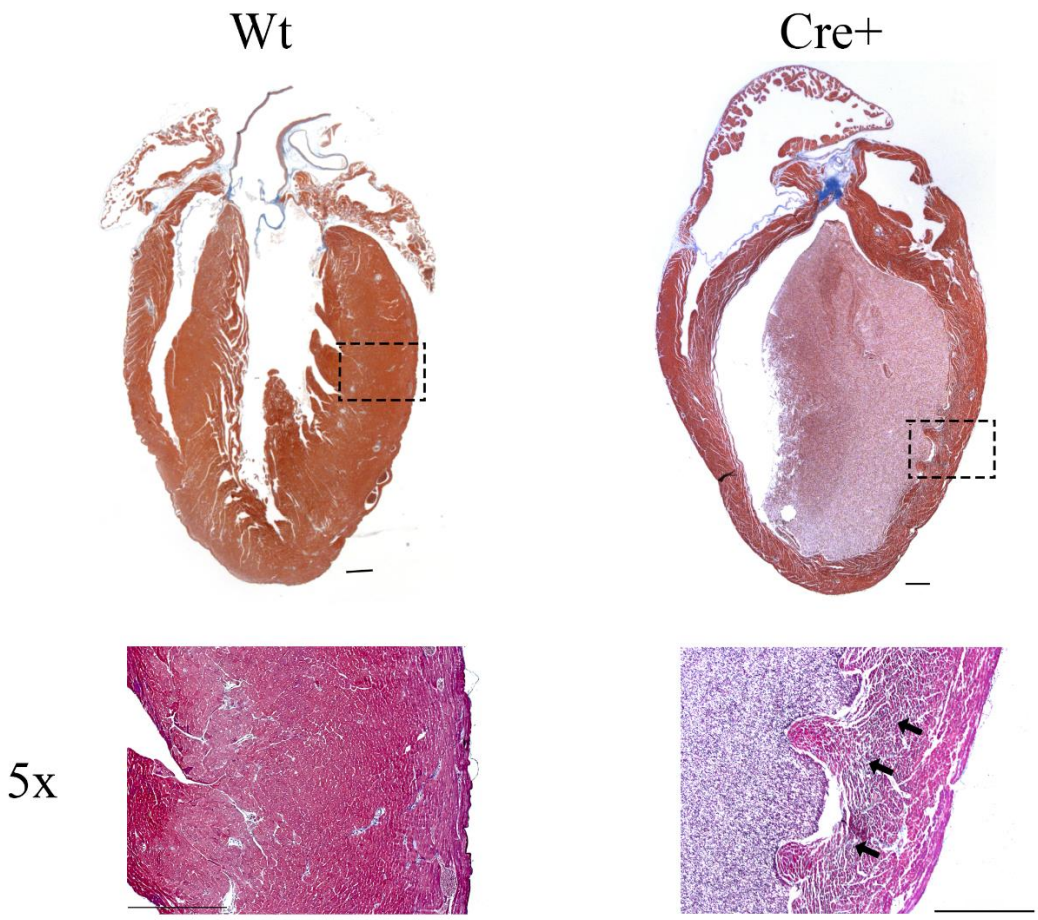

Figure 5. Histological analysis of 8-month-old Wt and Cre+ hearts. Representative images of 8-month-old wild-type and Cre+ mouse hearts that underwent histological sectioning and staining, imaged under a brightfield microscope. Masson's trichrome stain was used to visualize the myocardium walls (red) and fibrosis (blue). In addition, 5× magnification using a brightfield microscope was used to identify the presence of fibrosis in Wt or Cre+ hearts, marked with black arrows in fibrotic regions. Scale bar = 500 μm.

3.2.5. A DNA Damage Response Presented in αMHC-cre Myocardium

Cre recombinase has been shown to cause DNA damage when overly stimulated or highly expressed [26]. Though steps are taken to reduce the amount of cre in cells, hemizygous (one allele) MerCreMer animals have been shown to cause phenotypes when overly stimulated by tamoxifen [21,22]. The αMHC-cre mice were examined for any changes in DNA damage by evaluating phospho-p38 and p53, both shown to be upregulated when DNA stress is applied [27,28]. The relative amount of DNA stress response proteins assessed with western blots of lysates isolated from 8-month-old Wt and αMHC-cre myocardium (**Figure 6**) showed a sizable increase in the expression of p53 in two Cre+ hearts, while no change was noted in one of the Cre+ hearts compared to Wt hearts (38.9% ± 41.5%, $n = 3$, $p = 0.47$). A substantial decrease of phosphorylated p38 in two Cre+ hearts was observed, while the other remained unaffected when compared to Wt (−40.8% ± −16.8%, $n = 3$, $p = 0.10$). JNK (c-Jun NH_2 Kinases) is negatively regulated by p38, while JNK itself has been demonstrated to positively regulate p53 [29,30]. Western blot data indicated that all three Cre+ hearts had a modest increase in JNK (84.9% ± 59.3%, $n = 3$, $p = 0.29$) compared to Wt (**Figure 6**). The death protein Bax, which is a direct downstream target of p53 signaling, was significantly increased in Cre+ myocardium (213.8% ± 71.4%, $n = 3$, $p = 0.04$) compared to Wt myocardium (**Figure 6**) [31]. Taken together, the expression data showed that αMHC-cre resulted in increased amounts of DNA damage, which activated the stress kinase pathway, potentially causing myocyte loss and fibrosis, leading to DCM (**Figure 7**).

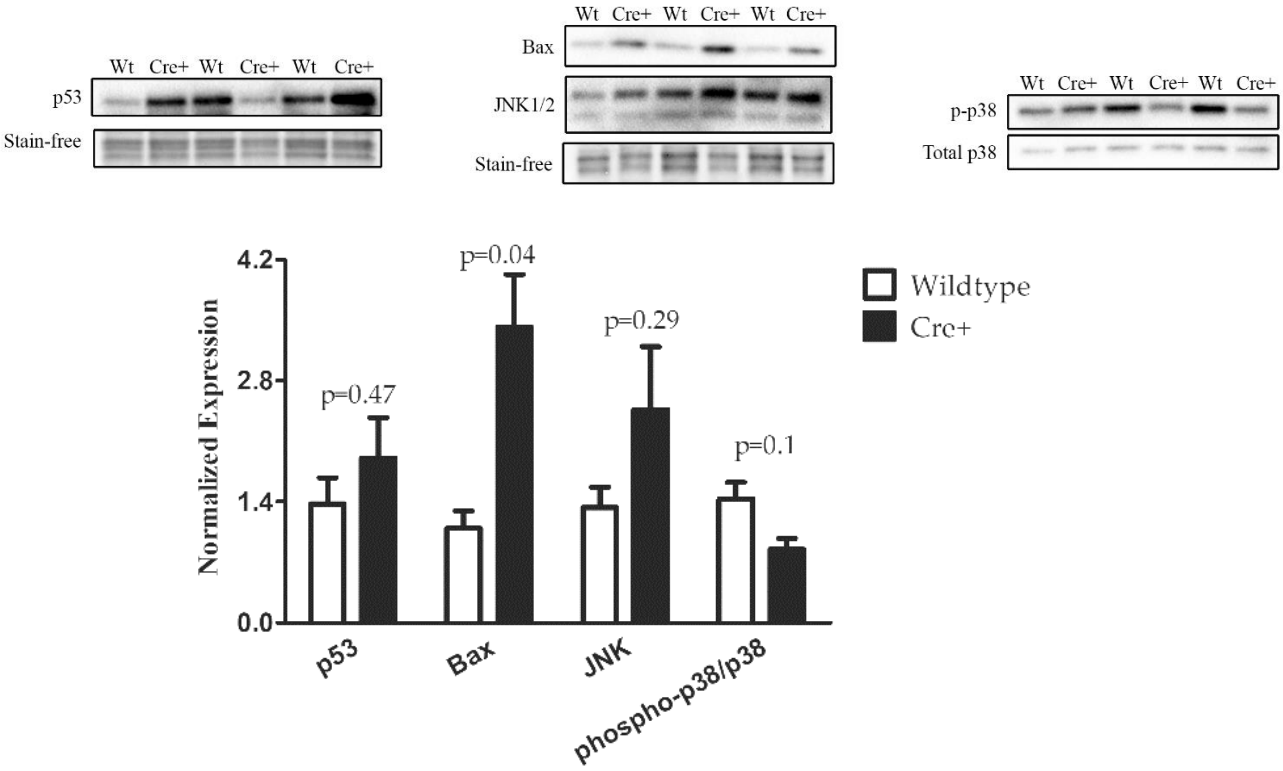

Figure 6. *Expression of DNA damage markers in Wt and Cre+ hearts*. (**A**) Western blot was utilized to determine the expression of DNA damage related (p53, p38, JNK) to the pro-death protein Bax in 8-month-old Wt or Cre+ hearts. (**B**) Bar graphs representing relative expressions of p53, Bax, and JNK normalized to total proteins visualized by stain-free technology (Bio-Rad, Hercules, U.S.A). Phospho-p38 was normalized to total p38.

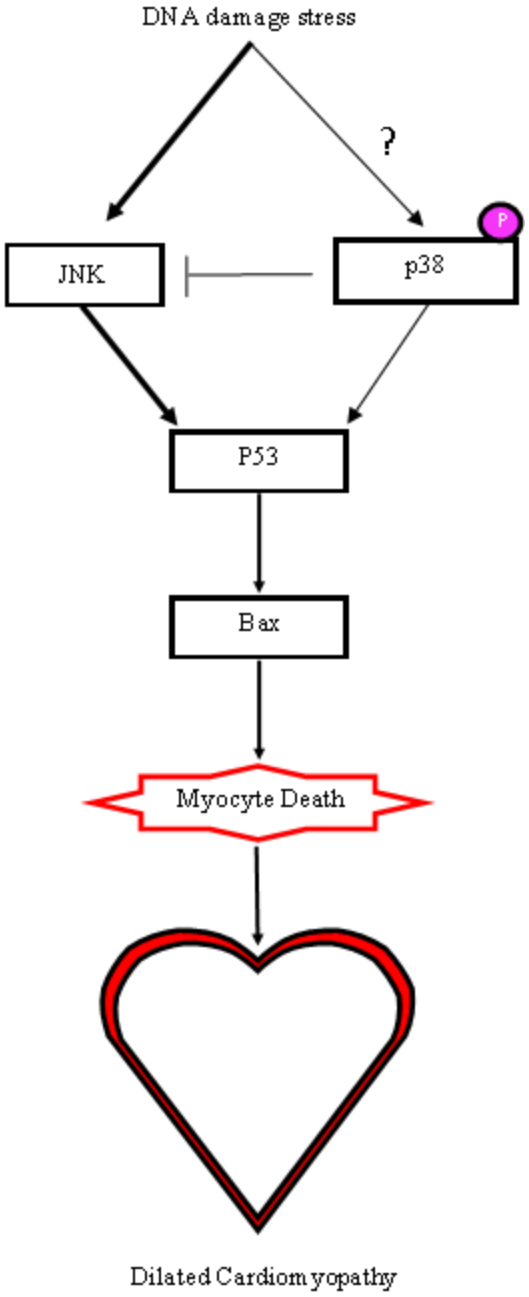

Figure 7. Proposed molecular mechanism for the induction of DCM in αMHC-cre mice. The decrease in p38 activity enhanced JNK, resulting in an upregulation of the p53/Bax causing myocyte death. The change in p38 activity due to cre-induced DNA damage and external signaling initiated a cascade that eventually resulted in DCM.

3.3. **Discussion**

The cre-lox system is an important tool that is used to determine gene function in many different models. The toxicity of cre is well documented, and without the use of proper controls, it can go unobserved. In this study, we showed that the most utilized αMHC-cre mice could develop an age-dependent DCM in the absence of hypertrophy. This cardiac phenotype is unique and distinct from recently published data using the same αMHC-cre mice, where the mice developed an age-dependent nonlethal HCM [16]. Histological analysis via Masson's trichrome staining of 8-month-old hearts clearly identified thin walls, a dilated chamber, and fibrosis in the Cre+ hearts, which are typical symptoms of DCM. ECHO analysis showed that by seven months of age, the left ventricle walls of Cre+ hearts were significantly thinner and dilated compared to wild-type hearts. Interestingly, no observable hypertrophy was present in αMHC-cre hearts at any age examined or when sex-separated analysis was performed. The accumulation of DNA damage, as seen with the increase in p53 and the pro-death protein Bax (which are associated with apoptosis and cell death), was notable in αMHC-cre hearts [32,33]. p53 has been demonstrated to be impacted by DNA damage and directly targets the expression of genes involved in cell cycle arrest and apoptosis. [27]. Phosphorylation of p38 has been shown to increase in the presence of environmental stress and signal the launch of an apoptotic response [29,34]. Our data indicated a markedly decreased activation of p38 and an increase in JNK in Cre+ hearts, providing an alternative mechanism of myocyte death, as p38 has been shown to negatively regulate JNK [35,36]. The upregulation of JNK positively regulated the activity of p53, potentially leading to Bax-mediated myocyte death and the increased fibrosis notable in the dilated αMHC-cre myocardium, as modeled in Figure 7 [37–39]. There was considerable variation in the level of DNA damage within the αMHC-cre hearts, although they

all exhibited a robust DCM. While individual (two) αMHC-cre hearts exhibited some very dramatic changes, no overall significant changes to p53, JNK, and p38 were evident due to variation (one heart) among the cohort. This indicated that there were multiple factors that impacted the exhibition of the DNA damage response in αMHC-cre myocardium, which in turn may determine the extent of the cardiac phenotype.

Cardiomyopathy is associated with structural changes within the myocardium due to pathological remodeling, when the heart enlarges the left ventricle to compensate for a pressure or volume overload [40, 41]. The mechanism through which αMHC-cre causes cardiomyopathy remains unclear, as two phenotypes (HCM or DCM) were found to be expressed within the same cardiac-specific cre model and mouse strain. The molecular changes to p53 and Bax were similar, with the cell death pathways activated leading to the two different phenotypes i.e., DCM or HCM. However, it is difficult to reconcile how myocyte cell loss would lead to an HCM given that robust fibrosis was apparent [16]. The one difference noted between the two studies, however, was the upregulated expression of phospho-p38 seen in HCM [16]. Studies have demonstrated that activated p38 signals a hypertrophic response in cardiomyocytes through the upregulated gene expression of atrial natriuretic peptide, brain natriuretic peptide, and alpha-skeletal actin [42]. Further, the consistent activation of p38 displayed dilated cardiomyopathy in adult mouse hearts probably due to depressed function as a consequence of the fetal gene program [43]. However, a decreased activation of p38 was found in patients exhibiting symptoms of DCM and end-stage heart failure [44], a molecular signature and phenotype similar to the aged cre mice in our studies. Our data showed that the decreased activity of p38 could impact JNK and transgenic mice with increased JNK activity exhibited

DCM, while overactive JNK was reported in patients exhibiting idiopathic DCM [38, 45–47]). p38 and JNK are stress kinases regulated by extracellular signals, which can be influenced through differences in animal husbandry, diets, genetics, and environmental stresses [34]. DCM or HCM has also been attributed to such diverse factors [48,49]. Although the specific effect of the molecular changes in p38 and JNK in the mouse heart remains controversial, there is a definite impact on cardiac health [47,50]. Therefore, molecular changes due to DNA damage (and its extent) induced by cre exposure are likely impacted by diverse factors, including environmental stress, which in turn may determine distinct pathology.

DCM has been previously implicated in two different cardiac-specific cre models, indicating the extremely cardiotoxic nature of the cre recombinase. The use of tamoxifen stimulates the activation of αMHC-MerCreMer, resulting in a transient DCM that may result in lethality with a tamoxifen overdose [21] while the high-level expression of αMHC-cre resulted in mice perishing before reaching 3 months of age [51]. This αMHC-cre mouse model was a different strain, FVB, compared to the C57B6 strain utilized here. The FVB model was generated under different conditions, which yielded offspring with different expressers of cre recombinase, with high expressers leading to DCM in young mice and lower expressers not showing any phenotypes although the impact of age was not examined [51]. Thus, regulating the amount of cre is critical in hearts, and the use of low-expressing cre can minimize off-target effects. However, consistent with other reports (15, 16, 51) we further stress that caution, even with the low-level expression of αMHC-cre, as two cardiac phenotypes, due to chronic cre exposure, can be exhibited in an age-dependent fashion. Fourteen studies that have utilized αMHC-cre mice have reported age-dependent DCM, which was attributed to a respective

genetic modification. However, cre-only controls at the appropriate age were lacking or not shown [52–65]. Further, in many of the studies lacking cre controls, the respective gene targets (EP4, ESRRβ, ATE1, Mdm4, NEMO/IKKgamma, the glucocorticoid receptor) had not been previously or subsequently shown to cause DCM [52–57]. Our data strongly urges the use of an appropriate cre control in a timed manner which will reveal a more accurate result of any impact of the genetic modification of interest.

In conclusion, our findings show that caution must be exercised when performing long-term studies using αMHC-cre mice, as different cardiac phenotypes can arise from low-level chronic cre exposure. The use of cre-only controls is critical and interrogating the impact of environment on the expression of DCM versus HCM in these αMHC-cre mice may help reveal the mechanisms differentiating the two phenotypes.

3.4. Materials and Methods

3.4.1. Maintenance of αMHC-cre Mouse Colonies

The αMHC-cre mice were generously donated by Dr. Patrick Burgon (University of Ottawa, Faculty of Medicine, Ottawa) for our experiments. The mouse colony was maintained through backcrossing transgenic males with wild-type C57B6 females (Charles Rivers Laboratories, Wilmington, U.S.A). Mice were genotyped by extracting genomic DNA from ear clips by boiling for 10 min at 95 °C in 180 µL of 50 mM NaOH per ear. DNA solution was then neutralized using 20 µL of 1 M Tris-Cl, pH 8.0. The αMHC-cre (Cre+) or wild-type (Wt) mice were identified by polymerase chain reaction (PCR) using a DreamTaq Green PCR Master Mix 2× (Thermo Fisher Scientific, Waltham, U.S.A) for the PCR mix. To determine Cre+ animals, we utilized forward primer Cre-F (5′-ACG ACC AAG TGA CAG CAA TG-3′) and reverse primer Cre-R (5′-AAC CAG CGT TTT CGT TC-3′). PCRs were visualized by Red Safe (Sigma-Aldrich, St. Louis, U.S.A) staining on a 1% agarose gel.

Mice were handled in accordance with the guidelines set by Canadian Council on Animal Care, *Guide to the Care and Use of Experimental Animals, 2 vols.* (Ottawa, Ont.: CCAC, 1980-1993) and *Animals for Research Act*, R.S.O. 1990, c.A. 22. All animal protocols and procedures were approved by the Animal Care Committee of the University of Ottawa.

3.4.2. Protein Isolation from Mouse Hearts

Hearts of adult mice were collected after CO_2 euthanasia and immediately frozen at −80 °C. Each heart was later washed with ice-cold 1X phosphate buffered saline (PBS) and homogenized using a Fisher handheld Maximizer homogenizer (Thermo Fisher Scientific, Waltham, U.S.A) in ice-cold lysis buffer (1 mM ethylene glycol tetraacetic acid (EGTA), 1 mM ethylenediaminetetraacetic (EDTA), 20 mM Tris base, 1% Triton, 150 mM sodium chloride, 1×

complete mini EDTA-free protease inhibitor cocktail (Roche, Basel, Switzerland), and 1× PhosSTOP (Roche, Basel, Switzerland)). The suspension was centrifuged for 15 min at 12,000 *g* to separate the proteins from the cell debris. The supernatant containing protein was collected in Eppendorf tubes and stored in a freezer at −80 °C.

3.4.3. SDS-PAGE and Western Blots

For western blotting experiments, 10 µg of protein was loaded in each well of a 5%–15% SDS-PAGE gel. The gels were transferred overnight on a polyvinylidene fluoride (PVDF) membrane (Bio-Rad, Hercules, U.S.A) in a buffer containing 25 mM Tris, 190 mM Glycine, and 20% methanol. All membranes were blocked at room temperature for 1 h in Tris-buffered saline (TBST) containing 1 M Tris, 290 mM NaCl, 0.1% Tween 20, pH 7.4, and 5% nonfat dry milk. Primary antibodies were incubated overnight at 4 °C with 5% bovine serum albumin (BSA). A comprehensive list of primary antibodies, manufacturers, and working dilutions are shown in Table 2. Membranes were washed 5 times for 5 min each in TBST prior to adding the appropriate horseradish peroxidase-labeled secondary antibody (Jackson ImmunoResearch, West Grove, U.S.A) in a 1:10,000 dilution in TBST with 5% nonfat dry milk. Membranes were shaken slowly at room temperature for 1 h while incubating with secondary antibody, followed by 5 washes for 5 min each with TBST. Membranes were treated with a BioRad western blotting kit (Bio-Rad, Hercules, U.S.A)) and developed using ChemiDoc machines (Bio-Rad, Hercules, U.S.A). Bands were quantified by densitometry using Image Lab software v.6.0.0 (Bio-Rad, Hercules, U.S.A)). Membranes were stripped (25 mM glycine, 10% SDS, and pH 2.2 in dH_2O) and reprobed with different antibodies. When using stain-free technology, stain-free gels (Bio-Rad, Hercules, U.S.A)) and low-fluorescence PVDF membranes (Bio-Rad, Hercules, U.S.A)) were used.

Table 2. List of antibodies used in this study. All antibodies used in this study are listed with the corresponding distributor, catalog number, and dilution used for western blot.

Antibody	Manufacturer	Dilution
Phospho-p38	Cell Signaling Technology (9215)	1:1000
p38	Santa Cruz (sc-81621)	1:250
p53	Santa Cruz (sc-126)	1:250
JNK	Cell Signaling Technology (9252)	1:1000
BAX	Cell Signaling Technology (2772)	1:1000

3.4.4. Echocardiography

All echocardiographic analysis was done using the VEVO 2100 system (FUJIFILM VisualSonics, Toronto, Canada). Adult mice were anesthetized using 2% isoflurane and strapped onto a heated pad facing upwards, exposing the thoracic cavity. A 40 MHz probe was used to capture short-axis B-mode and M-mode images of the left ventricle. VEVO v1.6 software (FUJIFILM VisualSonics, Toronto, Canada) was utilized for measuring LV wall thickness and inner diameters in diastole and systole. The formulas used by the VEVO v1.6 software to calculate EF, FS, LV mass, and LV Vol;d/s are listed below:

$$\text{EF: } 100 \times ((\text{LV Vol;d} - \text{LV Vol;s})/\text{LV Vol;d}) \quad (5)$$

$$\text{FS: } 100 \times ((\text{LVID;d} - \text{LVID;s})/\text{LVID;d}) \quad (6)$$

$$\text{LV mass: } 0.8 \times 1.053 \times ((\text{LVID;d} + \text{LVPW;d} + \text{IVS;d})^3 - \text{LVID;d}^3) \quad (7)$$

$$\text{LV vol; d/s: } ((7.0/(2.4 + \text{LVID;d/s})) \times \text{LVID;d/s}^3 \quad (8)$$

3.4.5. Histological Analysis

Hearts were extracted from animals and fixed using 10% Neutral Buffered Formalin (Thermo Fisher Scientific, Waltham, U.S.A). After fixing for 48 h, hearts were sectioned 4 μm longitudinally per section. Sectioned hearts were stained with Masson's trichrome to visualize the myocardium and fibrosis.

3.4.6. Statistical Analysis

The statistical analysis was performed using GraphPad Prism software version 5 for Windows (La Jolla, USA). All comparisons between wild-type and Cre+ groups were analyzed using two-tailed Student's *T*-test. All error bars presented in graphs are represented using the standard error of the mean. All sample size values (*n*) represent biological replicates (Kaplan-Meier, westerns, and ECHO)

3.5 References

1. Houdebine, L. Transgenic animal models in biomedical research. *Methods Mol. Biol.* **2007**, *360*, 163–202.
2. Hardouin, S.; Nagy, A. Mouse models for human disease. *Clin. Genet.* **2000**, *57*, 237–244.
3. Rosenthal, N.; Brown, S. The mouse ascending: Perspectives for human-disease models. *Nat. Cell. Biol.* **2007**, *9*, 993–999.
4. Soriano, P. Gene targeting in ES cells. *Annu. Rev. Neurosci.* **1995**, *18*, 1–18.
5. Yu, Y.; Bradley, A. Engineering chromosomal rearrangements in mice. *Nat. Rev. Genet.* **2001**, *2*, 780–790.
6. Hochman, L.; Segev, N.; Sternberg, N.; Cohen, G. Site-specific recombinational circularization of bacteriophage P1 DNA. *Virology* **1983**, *131*, 11–17.
7. Sauer, B.; Henderson, N. Site-specific DNA recombination in mammalian cells by the Cre recombinase of bacteriophage P1. *Proc. Natl. Acad. Sci. USA* **1988**, *85*, 5166–5170.
8. Branda, C.; Dymecki, S. Talking about a revolution: The impact of site-specific recombinases on genetic analyses in mice. *Dev. Cell.* **2004**, *6*, 7–28.
9. Hoess, R.; Wierzbicki, A.; Abremski, K. The role of the loxP spacer region in P1 site-specific recombination. *Nucleic Acids Res.* **1986**, *14*, 2287–2300.
10. Tora, L.; White, J.; Brou, C.; Tasset, D.; Webster, N.; Scheer, E.; Chambon, P. The human estrogen receptor has two independent nonacidic transcriptional activation functions. *Cell* **1989**, *59*, 477–487.
11. Gagniuc, P.; Ionescu-Tirgoviste, C. Eukaryotic genomes may exhibit up to 10 generic classes of gene promoters. *BMC Genom.* **2012**, *13*, 512.
12. Littlewood, T.; Hancock, D.; Danielian, P.; Parker, M.; Evan, G. A modified oestrogen receptor ligand-binding domain as an improved switch for the regulation of heterologous proteins. *Nucleic Acids Res.* **1995**, *23*, 1686–1690.
13. Orban, P.; Chui, D.; Marth, J. Tissue- and site-specific DNA recombination in transgenic mice. *Proc. Natl. Acad. Sci. USA* **1992**, *89*, 6861–6865.
14. Agah, R.; Frenkel, P.; French, B.; Michael, L.; Overbeek, P.; Schneider, M. Gene recombination in postmitotic cells. Targeted expression of Cre recombinase provokes cardiac-restricted, site-specific rearrangement in adult ventricular muscle in vivo. *J. Clin. Investig.* **1997**, *100*, 169–179.
15. Davis, J.; Maillet, M.; Miano, J.; Molkentin, J. Lost in transgenesis: A user's guide for genetically manipulating the mouse in cardiac research. *Circ. Res.* **2012**, *111*, 761–777.
16. Pugach, E.; Richmond, P.; Azofeifa, J.; Dowell, R.; Leinwand, L. Prolonged Cre expression driven by the α-myosin heavy chain promoter can be cardiotoxic. *J. Mol. Cell. Cardiol.* **2015**, *86*, 54–61.
17. Schmidt, E.; Taylor, D.; Prigge, J.; Barnett, S.; Capecchi, M. Illegitimate Cre-dependent chromosome rearrangements in transgenic mouse spermatids. *Proc. Natl. Acad. Sci. USA* **2000**, *97*, 13702–13707.
18. Janbandhu, V.; Moik, D.; Fässler, R. Cre recombinase induces DNA damage and tetraploidy in the absence of loxP sites. *Cell Cycle* **2013**, *13*, 462–470.
19. Thyagarajan, B.; Guimarães, M.; Groth, A.; Calos, M. Mammalian genomes contain active recombinase recognition sites. *Gene* **2000**, *244*, 47–54.
20. Ito, M.; Yamanouchi, K.; Naito, K.; Calos, M.; Tojo, H. Site-specific integration of transgene targeting an endogenous lox-like site in early mouse embryos. *J. Appl. Genet.* **2011**, *52*, 89–94.
21. Koitabashi, N.; Bedja, D.; Zaiman, A.; Pinto, Y.; Zhang, M.; Gabrielson, K.; Takimoto, E.; Kass, D. Avoidance of transient cardiomyopathy in cardiomyocyte-targeted tamoxifen-induced MerCreMer gene deletion models. *Circ. Res.* **2009**, *105*, 12–15.
22. Bersell, K.; Choudhury, S.; Mollova, M.; Polizzotti, B.D.; Ganapathy, B.; Walsh, S.; Wadugu, B.; Arab, S.; Kühn, B. Moderate and high amounts of tamoxifen in αMHC-MerCreMer mice induce a DNA damage response, leading to heart failure and death. *Dis. Models Mech.* **2013**, *6*, 1459–1469.
23. Burkholder, T.; Foltz, C.; Karlsson, E.; Linton, C.; Smith, J. Health evaluation of experimental laboratory mice. *Curr. Protoc. Mouse Biol.* **2012**, *12*, 145–165.
24. Yang, X.; Liu, Y.; Rhaleb, N.; Kurihara, N.; Kim, H.; Carretero, O. Echocardiographic assessment of cardiac function in conscious and anesthetized mice. *Am. J. Physiol.* **1999**, *277*, 1967–1974.
25. Luk, A.; Ahn, E.; Soor, G.; Butany, J. Dilated cardiomyopathy: A review. *J. Clin. Pathol.* **2009**, *62*, 219–225.

26. Loonstra, A.; Vooijs, M.; Beverloo, H.; Allak, B.; van Drunen, E.; Kanaar, R.; Berns, A.; Jonkers, J. Growth inhibition and DNA damage induced by Cre recombinase in mammalian cells. *Proc. Natl. Acad. Sci. USA* **2001**, *98*, 9209–9214.
27. Prives, C.; Hall, P. The p53 pathway. *J. Pathol.* **1999**, *187*, 112–126.
28. Cuadrado, A.; Nebreda, A.R. Mechanisms and functions of p38 MAPK signalling. *Biochem. J.* **2010**, *429*, 403–417.
29. Raingeaud, J.; Gupta, S.; Rogers, J.; Dickens, M.; Han, J.; Ulevitch, R.; Davis, R. Pro-inflammatory cytokines and environmental stress cause p38 mitogen-activated protein kinase activation by dual phosphorylation on tyrosine and threonine. *J. Biol. Chem.* **1995**, *270*, 7420–7426.
30. Ichijo, H.; Nishida, E.; Irie, K.; ten Dijke, P.; Saitoh, M.; Moriguchi, T.; Takagi, M.; Matsumoto, K.; Miyazono, K.; Gotoh, Y. Induction of apoptosis by ASK1, a mammalian MAPKKK that activates SAPK/JNK and p38 signaling pathways. *Science* **1997**, *275*, 90–94.
31. Lalier, L.; Cartron, P.; Juin, P.; Nedelkina, S.; Manon, S.; Bechinger, B.; Vallette, F. Bax activation and mitochondrial insertion during apoptosis. *Apoptosis* **2007**, *12*, 887–896.
32. Ozaki, T.; Nakagawara, A. Role of p53 in cell death and human cancers. *Cancers* **2011**, *3*, 994–1013.
33. MacLellan, W.; Schneider, M. Death by design. Programmed cell death in cardiovascular biology and disease. *Circ. Res.* **1997**, *81*, 137–144.
34. Cuenda, A.; Rousseau, S. p38 MAP-Kinases pathway regulation, function and role in human diseases. *Biochim. Biophys. Acta* **2007**, *1773*, 1358–1375.
35. Sui, X.; Kong, N.; Ye, L.; Han, W.; Zhou, J.; Zhang, Q.; He, C.; Pan, H. p38 and JNK MAPK pathways control the balance of apoptosis and autophagy in response to chemotherapeutic agents. *Cancer Lett.* **2014**, *28*, 174–179.
36. Miura, H.; Kondo, Y.; Matsuda, M.; Aoki, K. Cell-to-Cell heterogeneity in p38-mediated cross-inhibition of JNK causes stochastic cell death. *Cell Rep.* **2018**, *24*, 2658–2668.
37. Williams, A.; Schumacher, B. p53 in the DNA-damage-repair process. *Cold Spring Harb. Perspect Med.* **2016**, *6*, 5.
38. Picco, V.; Pagès, G. Linking JNK activity to the DNA damage response. *Genes Cancer* **2013**, *4*, 360–368.
39. Donauer, J.; Schreck, I.; Liebel, U.; Weiss, C. Role and interaction of p53, BAX and the stress-activated protein kinases p38 and JNK in benzo(a)pyrene-diolepoxide induced apoptosis in human colon carcinoma cells. *Arch. Toxicol.* **2012**, *86*, 329.
40. Burchfield, J.; Xie, M.; Hill, J. Pathological ventricular mechanisms. *Circulation* **2013**, *128*, 388–400.
41. Yacoub, M. Decade in review—Cardiomyopathies: Cardiomyopathy on the move. *Nat. Rev. Cardiol.* **2014**, *11*, 628–629.
42. Zechner, D.; Thuerauf, D.; Hanford, D.; McDonough, P.; Glembotski, C. A role for the p38 mitogen-activated protein kinase pathway in myocardial cell growth, sarcomeric organization, and cardiac-specific gene expression. *J. Cell. Biol.* **1997**, *6*, 115–127.
43. Liao, P.; Georgakopoulos, D.; Kovacs, A.; Zheng, M.; Lerner, D.; Pu, H.; Saffitz, J.; Chien, K.; Xiao, R.; Kass, D.; et al. The in vivo role of p38 MAP kinases in cardiac remodeling and restrictive cardiomyopathy. *Proc. Natl. Acad. Sci. USA* **2001**, *98*, 12283–12288.
44. Lemke, L.; Bloem, L.; Fouts, R.; Esterman, M.; Sandusky, G.; Vlahos, C. Decreased p38 MAPK activity in end-stage failing human myocardium: p38 MAPK alpha is the predominant isoform expressed in human heart. *J. Mol. Cell. Cardiol.* **2001**, *33*, 1527–1540.
45. Haq, S.; Choukroun, G.; Lim, H.; Tymitz, K.; del Monte, F.; Gwathmey, J.; Grazette, L.; Michael, A.; Hajjar, R.; Force, T.; et al. Differential activation of signal transduction pathways in human hearts with hypertrophy versus advanced heart failure. *Circulation* **2001**, *103*, 670–677.
46. Wang, Y.; Su, B.; Sah, V.; Brown, J.; Han, J.; Chien, K. Cardiac hypertrophy induced by mitogen-activated protein kinase kinase 7, a specific activator for c-Jun NH2-terminal kinase in ventricular muscle cells. *J. Biol. Chem.* **1998**, *273*, 5423–5426.
47. Liang, Q.; Molkentin, J. Redefining the roles of p38 and JNK signaling in cardiac hypertrophy: Dichotomy between cultured myocytes and animal models. *J. Mol. Cell. Cardiol.* **2003**, *35*, 1385–1394.
48. Elliott, P.; Andersson, B.; Arbustini, E.; Bilinska, Z.; Cecchi, F.; Charron, P.; Dubourg, O.; Kühl, U.; Maisch, B.; McKenna, W.; et al. Classification of the cardiomyopathies: A position statement from the European Society of Cardiology working group on myocardial and pericardial diseases. *Eur. Heart J.* **2008**, *29*, 270–276.

49. Maron, B.; Towbin, J.; Thiene, G.; Antzelevitch, C.; Corrado, D.; Arnett, D.; Moss, A.; Seidman, C.; Young, J. Contemporary definitions and classification of the cardiomyopathies. *Circulation* **2006**, *113*, 1807–1816.
50. Arabacilar, P.; Marber, M. The case for inhibiting p38 mitogen-activated protein kinase in heart failure. *Front Pharm.* **2015**, *6*, 102.
51. Buerger, A.; Rozhitskaya, O.; Sherwood, M.; Dorfman, A.; Bisping, E.; Abel; E.D.; Pu, W.; Izumo, S.; Jay, P. Dilated cardiomyopathy resulting from high-level myocardial expression of Cre-recombinase. *J. Card. Fail.* **2006**, *12*, 392–398.
52. Harding, P.; Yang, X.; Yang, J.; Shesely, E.; He, Q.; LaPointe, M. Gene expression profiling of dilated cardiomyopathy in older male EP4 knockout mice. *Am. J. Physiol. Heart Circ. Physiol.* **2010**, *298*, 623–632.
53. Kurosaka, S.; Leu, N.; Pavlov, I.; Han, X.; Ribeiro PA, X.T.B.R.; Saha, S.; Wang, J.; Cornachione, A.; Mai, W.; Yates, J.; et al. Arginylation regulates myofibrils to maintain heart function and prevent dilated cardiomyopathy. *J. Mol. Cell Cardiol.* **2012**, *53*, 333–341.
54. Kratsios, P.; Huth, M.; Temmerman, L.; Salimova, E.; Al Banchaabouchi, M.; Sgoifo, A.; Manghi, M.; Suzuki, K.; Rosenthal, N.; Mourkioti, F. Antioxidant amelioration of dilated cardiomyopathy caused by conditional deletion of NEMO/IKKgamma in cardiomyocytes. *Circ. Res.* **2010**, *106*, 133–144.
55. Xiong, S.; Van Pelt, C.; Elizondo-Fraire, A.; Fernandez-Garcia, B.; Lozano, G. Loss of Mdm4 Results in p53-Dependent Dilated Cardiomyopathy. *Circulation* **2007**, *115*, 2925–2930.
56. Oakley, R.; Ren, R.; Cruz-Topete, D.; Bird, G.; Myers, P.; Boyle, M.; Schneider, M.; Willis, M.; Cidlowski, J. Essential role of stress hormone signaling in cardiomyocytes for the prevention of heart disease. *Proc. Natl. Acad. Sci. USA* **2013**, *110*, 17035–17040.
57. Rowe, G.; Asimaki, A.; Graham, E.; Martin, K.; Margulies, K.; Das, S.; Saffitz, J.; Arany, Z. Development of dilated cardiomyopathy and impaired calcium homeostasis with cardiac-specific deletion of ESRRβ. *Am. J. Physiol. Heart Circ. Physiol* **2017**, *312*, 662–671.
58. Huang, J.; Min Lu, M.; Cheng, L.; Yuan, L.; Zhu, X.; Stout, A.; Chen, M.; Li, J.; Parmacek, M. Myocardin is required for cardiomyocyte survival and maintenance of heart function. *Proc. Natl. Acad. Sci. USA* **2009**, *106*, 18734–18739.
59. Lim, B.; Xiong, D.; Dorner, A.; Youn, T.; Yung, A.; Liu, T.; Gu, Y.; Dalton, N.; Wright, A.; Evans, S.; et al. Coxsackievirus and adenovirus receptor (CAR) mediates atrioventricular-node function and connexin 45 localization in the murine heart. *J. Clin. Investig.* **2008**, *118*, 2758–2770.
60. Jacoby, J.; Kalinowski, A.; Liu, M.; Zhang, S.; Gao, Q.; Chai, G.; Ji, L.; Iwamoto, Y.; Li, E.; Schneider, M.; et al. Cardiomyocyte-restricted knockout of STAT3 results in higher sensitivity to inflammation, cardiac fibrosis, and heart failure with advanced age. *Proc. Natl. Acad. Sci. USA* **2003**, *100*, 12929–12934.
61. Wai, T.; García-Prieto, J.; Baker, M.; Merkwirth, C.; Benit, P.; Rustin, P.; Rupérez, F.; Barbas, C.; Ibañez, B.; Langer, T. Imbalanced OPA1 processing and mitochondrial fragmentation cause heart failure in mice. *Science* **2015**, *350*, 6365.
62. Collins, H.; He, L.; Zou, L.; Litovsky, S.; Yang, Q.; Young, M.; Marchase, R.; Chatham, J. Stromal interaction molecule 1 is essential for normal cardiac homeostasis through modulation of ER and mitochondrial function. *Am. J. Physiol. Heart Circ. Physiol* **2014**, *306*, 1231–1239.
63. Liu, L.; Trent, C.; Fang, X.; Son, N.; Jiang, H.; Blaner, W.; Hu, Y.; Yin, Y.; Farese, R.J.; Homma, S.; et al. Cardiomyocyte-specific loss of diacylglycerol acyltransferase 1 (DGAT1) reproduces the abnormalities in lipids found in severe heart failure. *J. Biol. Chem.* **2014**, *289*, 29881–29891.
64. Levkau, B.; Schäfers, M.; Wohlschlaeger, J.; von Wnuck Lipinski, K.; Keul, P.; Hermann, S.; Kawaguchi, N.; Kirchhof, P.; Fabritz, L.; Stypmann, J.; et al. Survivin determines cardiac function by controlling total cardiomyocyte number. *Circulation* **2008**, *117*, 1583–1593.
65. Hilfiker-Kleiner, D.; Hilfiker, A.; Fuchs, M.; Kaminski, K.; Schaefer, A.; Schieffer, B.; Hillmer, A.; Schmiedl, A.; Ding, Z.; Podewski, E.; et al. Signal transducer and activator of transcription 3 is required for myocardial capillary growth, control of interstitial matrix deposition, and heart protection from ischemic injury. *Circ. Res.* **2004**, *95*, 187–195.

Sample Availability: Samples of any compounds are available from the authors.

Chapter Four: Deletion of sarcolemmal membrane associated protein isoform 3 (SLMAP3) from cardiac progenitors delays embryonic growth of myocardium

International Journal of
Molecular Sciences

MDPI

Deletion of Sarcolemmal Membrane-Associated Protein Isoform 3 (SLMAP3) in Cardiac Progenitors Delays Embryonic Growth of Myocardium without Affecting Hippo Pathway

Taha Rehmani[1], Ana Paula Dias[1], Marsel Kamal, Maysoon Salih[1,] and Balwant S. Tuana[1]*

[1] Department of Cellular and Molecular Medicine, Faculty of Medicine, University of Ottawa, 451 Smyth Road, K1H 8M5, Ottawa, ON, Canada; trehmani@uottawa.ca (T.R.), adias085@uottawa.ca (A.D), mkama089@uottawa.ca (M.K.) msalih@uottawa.ca (M.S)

* Correspondence: btuana@uottawa.ca (B.S.T); Tel.: +613-562-5800 (ext. 8578)

Received: 22 December 2023; Revised: 18 February 2024; Accepted: 21 February 2024

Author Contributions: T.R.: project conceptualization, methodology, validation, formal analysis, investigation, resources, data visualization and manuscript writing;

A.P.D: project conceptualization, investigation, data visualization and manuscript writing;

M.K., investigation, data visualization

M.S.: investigation, resources and methodology;

B.S.T.: project conceptualization, supervision, manuscript review and funding acquisition.

Abstract: The slmap gene is alternatively spliced to generate many isoforms that are abundant in developing myocardium. The largest protein isoform SLMAP3 is ubiquitously expressed and has been linked to cardiomyopathy, Brugada syndrome and Hippo signaling. To examine any role in cardiogenesis, mice homozygous for floxed slmap allele were crossed with Nkx2.5-cre mice to nullify its expression in cardiac progenitors. Targeted deletion of the slmap gene resulted in the specific knockout (KO) of the SLMAP3 (~91 KDa) isoform without any changes in the expression of the SLMAP2 (~43 kDa) or the SLMAP1 (~35 kDa) isoforms which continued to accumulate to similar levels as seen in Wt embryonic hearts. The loss of SLMAP3 from cardiac progenitors resulted in decreased size of the developing embryonic hearts evident at E9.5 to E16.5 with four small chambers and significantly thinner left ventricles. The proliferative capacity assessed with the phosphorylation of histone 3 or with Ki67 in E12.5 hearts was not significantly altered due to SLMAP3 deficiency. The size of embryonic cardiomyocytes, marked with anti-Troponin C, revealed significantly smaller cells, but their hypertrophic response (AKT1 and MTOR1) was not significantly affected by the specific loss of SLMAP3 protein. Further, no changes in phosphorylation of MST1/2 or YAP were detected in SLMAP3-KO embryonic myocardium, ruling out any impact on Hippo signaling. Rat embryonic cardiomyocytes express the three SLMAP isoforms and their knockdown (KD) with sh-RNA, resulted in decreased proliferation and enhanced senescence but without any impact on Hippo signaling. Collectively, these data show that SLMAP is critical for normal cardiac development with potential for the various isoforms to serve compensatory roles. Our data imply novel mechanisms for SLMAP action in cardiac growth independent of Hippo signaling.

Keywords: SLMAP3, STRIPAK complex, Hippo signaling, cardiomyocyte maturation, cardiac morphogenesis

4.1 Introduction

During embryogenesis, the first functional organ is the heart, derived from mesoderm and endoderm due to the expression of cardiogenic transcription factors Nkx2.5, Mef2, GATA, Tbx and Hand that work in tandem to differentiate precardiac cells and to control the expression of cardiac genes to mediate cardiac morphogenesis [1]. Cardiac morphogenesis or cardiogenesis is the stage-by-stage development of the heart during embryogenesis beginning at embryonic day 7.5 (E7.5) in mice, where cardiogenic mesoderm cells coalesce at splanchnic mesoderm to form the cardiac crescent. Cells within the cardiac crescent are divided into a collection of cells known as the first heart field (FHF), which migrate to venous poles to form the linear heart tube (E8.5) [2,3] . A subgroup of cells derived from FHF known as secondary heart field (SHF) migrate caudally to further develop the linear heart tube into the looping heart (E9.5). The FHF cells differentiate and proliferate to form the left atria and ventricle, and the SHF cells migrate anteriorly and posteriorly; the anterior SHF cells give rise to the right ventricle and aorta, while the posterior SHF cells generate the atria and the pulmonary artery in maturing embryos, thus generating the immature four-chambered heart (E10.5), which septate to form mature four-chamber heart by E14.5 [4,5]. During the late stages of cardiac development, immature cardiomyocytes grow and increase cardiac function due to a series of structural, metabolic, and transcriptional modifications in a process referred to as cardiomyocyte maturation [6]. Cardiomyocytes will exit the cell cycle shortly after birth; therefore, cardiac growth is sustained

through cardiomyocyte maturation to maintain the growing supply of nutrients and oxygen demands of the growing body [7]. Impacting cardiac development at the morphogenesis or maturation stage can increase the risk of developing congenital heart disease and predisposing individuals to later-stage cardiomyopathies. Therefore, understanding the mechanisms that govern cardiac maturation and/or morpho-genesis is of much interest.

We have defined the sarcolemmal membrane-associated proteins SLMAP1 (~35 kDa), SLMAP2 (~45 kDa), and SLMAP3 (~80–95 kDa) (Figure 1) that are expressed in myocardium as early as E9 and continue to be accumulated in cardiomyocytes during their maturation and postnatal development [8,9]. The SLMAPs target subcellular organelles including nuclear envelope, endoplasmic/sarcoplasmic reticulum, mitochondria, and the microtubule organizing center (MTOC) [10,11]. The SLMAPs have been shown to associate with cardiac myosin, colocalize with a-actinin and calcium release channels, as well as being found in close apposition to the sarcolemma [9]. Aberrant SLMAP expression has been shown to cause heart failure due to gene mutations present in Brugada patients [12]. Studies indicate that SLMAPs may play roles in regulating the diverse organelles, influence electrophysiology, metabolism, and cardiac function [13–15]. However, the role of SLMAPs in the growth and maturation of myocardium remains un-known. The slmap gene is alternatively spliced to generate numerous isoforms that are expressed in a tissue-specific manner, with SLMAP1 and SLMAP2 being abundant in cardiomyocytes [16]. The C-terminus of all SLMAP isoforms comprises an alternatively spliced transmembrane do-main, TM1 or TM2, which can target different subcellular membranes, while the extended coiled coil leucine zipper domain and the n-terminal sequences diversify the polypeptide structure for cytoplasmic interactions [10,17]. For

example, the SLMAP3 isoform which is ubiquitously ex-pressed carries an n-terminal forkhead-associated (FHA) domain (Figure 1) that can mediate phosphoprotein–protein interactions [11,18] and has been shown to negatively regulate Hippo signaling via the STRIPAK (Striatin-interacting phosphatases and kinases) complex. The Hippo pathway is important for organogenesis through effects on cell proliferation and apoptosis [19]. SLMAP-STRIPAK interactions can inhibit phosphorylation and enhance nuclear translocation of transcriptional co-activators YAP/TAZ and influence TEAD-mediated gene expression [20–22]. Hippo signaling has been linked to cardiac development and maturation and can directly impact the size and function of the myocardium [23–27]. SLMAP3 has been reported to regulate the proliferation of cancer cells through Hippo signaling [28]; whether it can impact this pathway to influence growth and development in vivo remains to be examined. Here, we have engineered the specific removal of SLMAP3 from cardiac progenitors to examine its role in cardiogenesis in mice and its impact on the Hippo pathway.

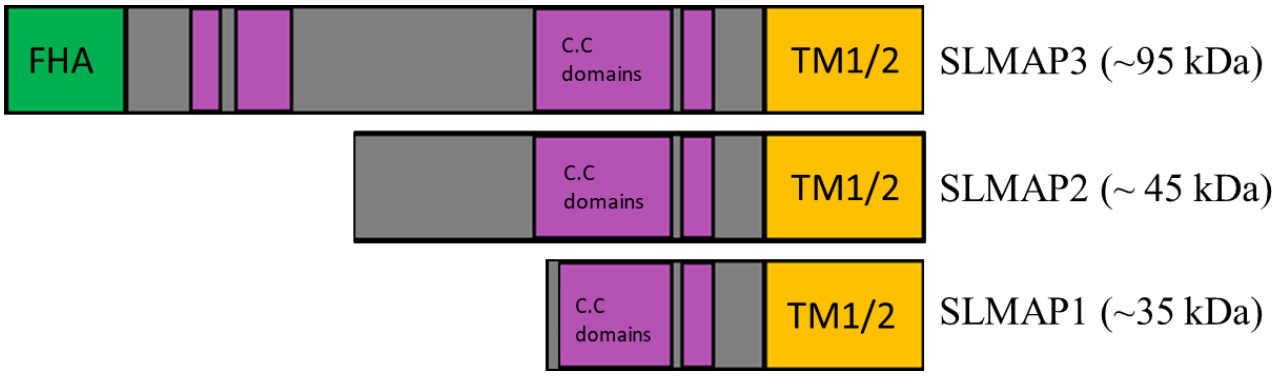

Figure 1. *Sarcolemmal membrane associated protein isoforms and protein domains*. SLMAP gene alternatively splices to generate three main protein isoforms, SLMAP1 (~35 kDa), SLMAP2 (~45 kDa) and SLMAP3 (~95 kDa). FHA (green) symbolizes forkhead associated domain. C.C. domains (purple) symbolize coiled-coil leucine zipper domains. TM1/TM2 (orange) symbolizes alternatively spliced transmembrane domain 1 or 2.

4.2 Results

4.2.1 The specific loss of SLMAP3 isoform in cardiac progenitors delays cardiogenesis

We examined the prenatal knockout of SLMAP gene by crossing floxed SLMAP mice with Nkx2.5-Cre (as early as E7.5) [30] to assess the role of SLMAP during early cardiogenesis. Western blot analysis of E18.5 heart lysates with anti-SLMAP displayed significant loss in SLMAP3 protein levels in heterogyous (KD) mice (-66.05% ± -15.10%, ϱ<0.05, n=3) and knockout (KO) mice (-97.36% ± -11.39%, ϱ<0.05, n=3) while no changes were noted in SLMAP1 or SLMAP2, indicating the generation of mice with the specific loss of SLMAP3 in developing embryonic myocardium (**Figure 2A**). We excised embryos at different developmental stages of cardiac development (E9.5, E12.5, and E16.5) and performed cross-section histology with H&E to visualize Wt and SLMAP3-KO myocardium (**Figure 2B**). Microscopic analysis indicated that prenatal SLMAP3-KO hearts were significantly smaller at every developmental stage, E9.5 (-25.16% ± -11.10%, ϱ<0.05, n=3), E12.5 (-29.36% ± -7.86%, ϱ<0.05, n=3) and E16.5 (-40.27%, ± -6.51%, ϱ<0.05, n=3) compared to Wt littermates (**Figure 2C**). Further, the left ventricular walls were significantly thinner in E9.5 (-48.65% ± -6.61%, ϱ<0.05, n=3), E12.5 (-33.49% ± -5.44 %, ϱ<0.05, n=3) and E16.5 (-41.12%, ± -1.39%, ϱ<0.05, n=3) SLMAP3-KO hearts (**Figure 2C**). However, it is notable that we did not observe any differences in cardiac chamber formation or septation (**Figure 2B**). Thus, this suggests that SLMAP3 protein can regulate normal cardiac growth during cardiogenesis.

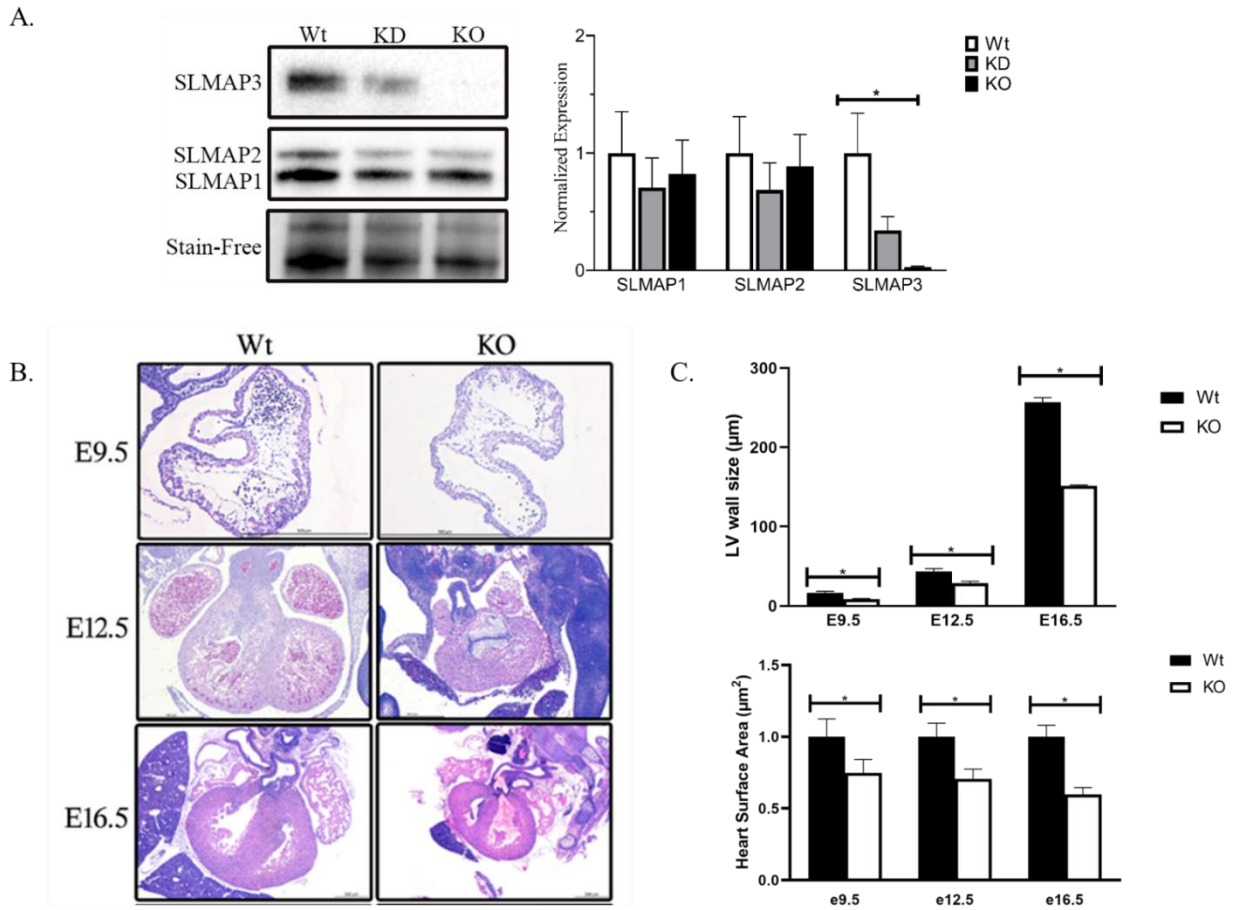

Figure 2. *Embryonic heart development in SLMAP3-KO mice*. A. Representative Western blot displaying SLMAP isoform expression in Wt, KD, and KO in E18.5 mouse heart lysates. Bar graphs represent normalized expression of SLMAP isoforms via densitometry analysis by using Stain-Free™ total protein as a loading control n=6. *;ϱ<0.05. B. Representative sections of Wt and KO hearts at E9.5, E12.5 and E16.5 with H&E stain to visualize nucleus (blue) and the myocardium (pink). Lens Magnification=5x. Scale bar=0.5mm. C. Bar graph represents quantification of measurement of left ventricle wall thickness (upper graph) and heart surface area (lower graph) at indicated embryonic ages in Wt and KO hearts. *;ϱ<0.05.

4.2.2 STRIPAK and Hippo signaling were unaltered in prenatal SLMAP3-KO mice

Given the dramatic effects of SLMAP3 on retardation of cardiac growth and it`s proposed role in Hippo signaling via STRIPAK [22,30] we examined STRIPAK components (striatin, PP2A-A, PP2A-C, Striatin-3) and activity of Hippo in E16.5 Wt and SLMAP3-KO cardiac lysates with Western blot and quantified changes showing that expression of striatin-1 (-2.56% ±-22.05%, ϱ=0.93, n=4), striatin-3 (-0.21% ± -19.46%, ϱ=0.89, n=4), PP2A-A (-16.34% ± -16.23%, ϱ=0.54, n=4), and PP2A-C (23.58% ± 11.65%, ϱ=0.20, n=4) were not significantly affected in KO hearts when compared to Wt (**Figure 3A**). To assess Hippo signaling, we analyzed phosphorylation of MST1 and YAP, however our western blot analysis indicated that phospho-to-total ratio of MST1(-6.61% ± -23.56%, ϱ=0.63, n=4) and phospho-to-total ratio of YAP (-8.43% ± -12.25%, ϱ=0.64, n=4) were unaltered in SLMAP3-KO hearts (**Figure 3B**). Thus, cardiac-specific knockout of SLMAP3 isoform in cardiac progenitors does not regulate Hippo signaling to impact cardiogenesis.

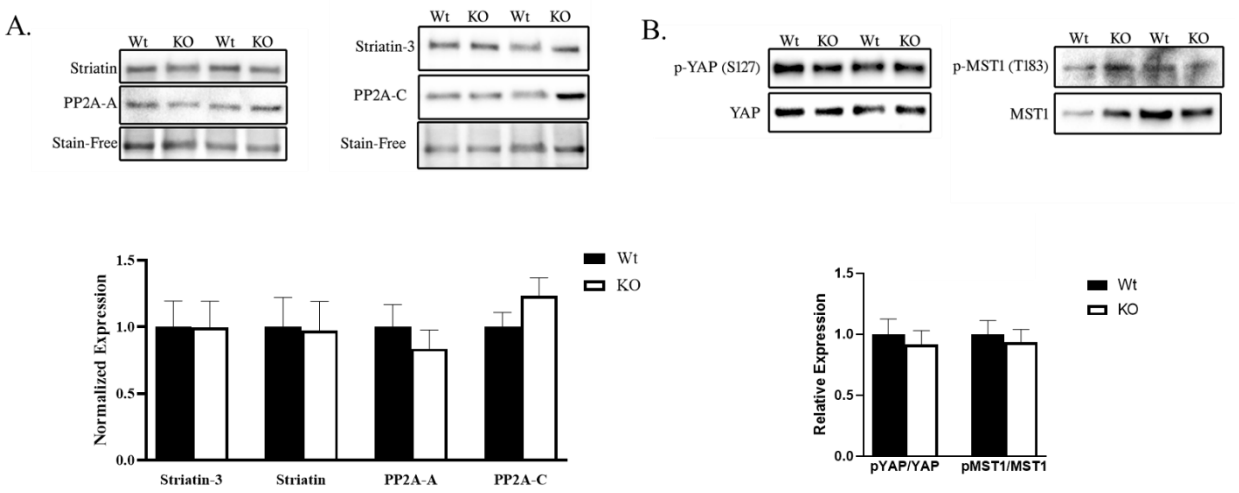

Figure 3. *STRIPAK and Hippo signaling in prenatal loss of SLMAP3.* A. Representative Western blot examining the expression of STRIPAK components (striatin-1, striatin-3, PP2A-A and PP2A-C) in Wt and KO E16.5 hearts. Bar graphs represent normalized expressions of indicated protein to total proteins visualized by Stain-Free™ technology. *N*=3. B. Representative Western blot evaluating phospho to total MST1 and YAP in E16.5 hearts. Bar graphs represent relative expression of phospho-YAP(S127) to total YAP and phospho-MST1 (T183) to total MST1 via densitometry analysis. *N*=3.

4.2.3 Proliferation is not affected in SLMAP3-KO hearts

Cardiac growth is regulated by cardiomyocyte proliferation and hypertrophy mechanisms involving Hippo and other pathways including FGF, Notch, and Wnt signaling [32]. Thus, we evaluated proliferation with immunofluorescence microscopy using two markers for proliferation pH3 and Ki67, costained with cardiomyocyte marker, Troponin C (TnC) in e12.5 hearts from Wt and SLMAP3-KO mouse embryos (**Figure 4**). The pH3 detects cell division at the G2/M phase (**Figure 4A**) while Ki67 tags cells at G1 phase of cell cycle (**Figure 4B**) thus providing a profile of proliferating, however no significant differences in $pH3^+$ or $Ki67^+$ positive cardiomyocytes in SLMAP3-KO vs Wt embryos was detectable (**Figure 4C**). The prenatal loss of SLMAP3 in cardiac progenitors did not impact cardiomyocyte proliferation to delay the notable embryonic development.

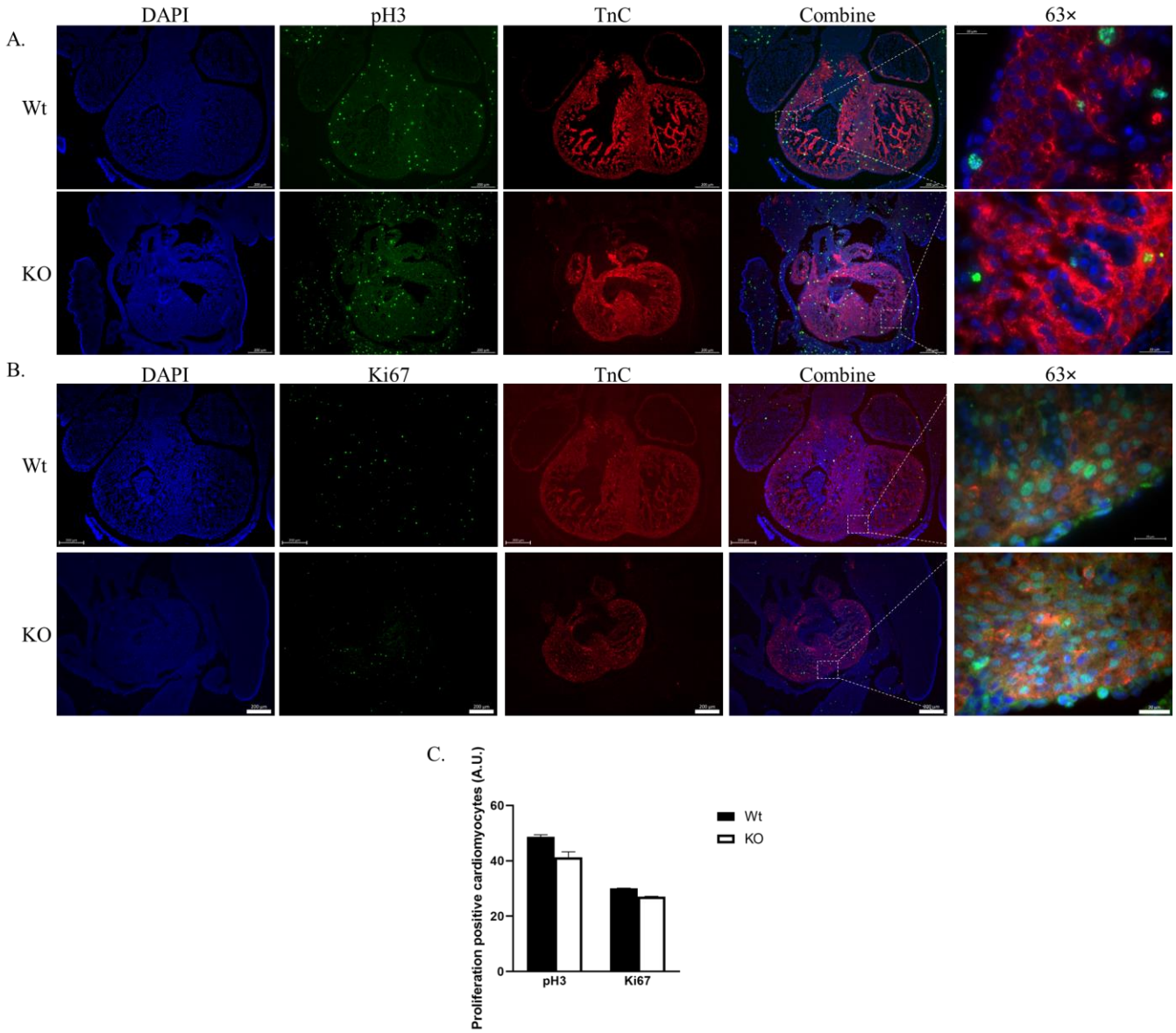

Figure 4. *Proliferation of cardiomyocytes in Wt and SLMAP3-KO embryonic hearts.* Representative immunofluorescent images of sectioned Wt and KO hearts at e12.5. with A. Nucleus (DAPI;blue), phosphorylated Histone 3 (pH3;green) and anti-troponin C (TnC;red) or B. Nucleus (DAPI;blue), Antigen Kiel 67 (Ki6;green), and anti-troponin C (TnC;red). Lens Magnification=5x or 63x. Scale bar= 0.2mm or 0.02mm. C. Bar graph representing pH3 or Ki67 proliferation events within TnC^{+} positive cells. *N*=3.

4.2.4 Cardiomyocyte size is reduced in SLMAP3-KO embryonic hearts

We investigated if cardiomyocyte cell size was affected by loss of SLMAP3. Immunofluorescent images of TnC were used to measure the diameter of cardiomyocytes (white bracket) in E12.5 hearts which indicated that cardiomyocytes surface area was significantly smaller in KO (-19.43% ± -7.55%, $\rho<0.05$, n=3) when compared to Wt (**Figure 5A**). The cardiomyocytes also appeared to be disorganized in SLMAP-KO embryos. Cardiomyocyte hypertrophy is most classically linked to the regulators, Insulin Growth Factor 1 (IGF-1) and downstream targets AKT1 and MTOR1 [33] known to affect cell survival and growth. The activity of AKT1 and MTOR1 assessed in Western blot indicated that phospho-to-total ratios of AKT1 (1.45% ± 26.50%, $\rho=0.97$, n=3) and mTOR (-12.87% ± -51.12%, $\rho=0.64$, n=3) were not significantly altered in E16.5 SLMAP3-KO hearts compared to Wt (**Figure 5B**). Thus, the changes in cardiomyocyte size in SLMAP3-KO hearts do not appear to be regulated by classical hypertrophic signaling.

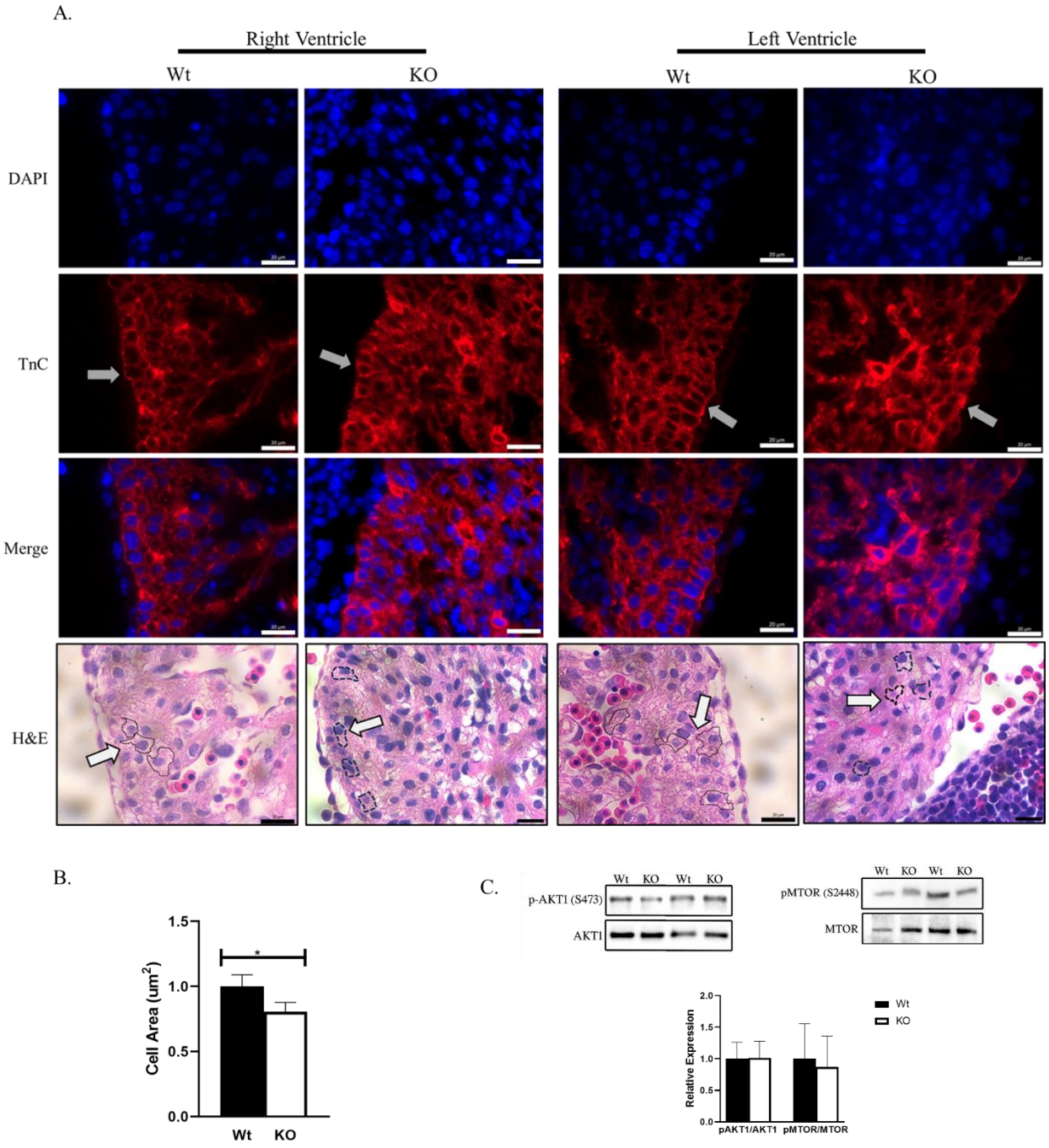

Figure 5. *Cell size and hypertrophy in Nkx2.5/SLMAP3-KO mice.* A. Representative immunofluorescent images of sectioned Wt and KO hearts at e12.5. with nucleus (DAPI;blue) and anti-troponin C (TnC;red). Bar graph represents cardiomyocyte cell area (white brackets) in Wt and KO. *; $\rho<0.05$, n=3. B. Representative western blot looking at expression of phospho-to-total ratios of AKT1 and mTOR and in E16.5 Wt and KO hearts. Bar graphs represent quantification of relative expression of phospho-mTOR (S2448) to total mTOR and phospho-AKT1 (S473) to total AKT1 with densitometry of the Western blots. *N*=3.

4.2.5 SLMAP3-KO hearts exhibit normal size and function during postnatal development

The SLMAP3-KO neonatal pups were born (normal breathing, active movement) and did not present any obvious cardiac phenotypes and survived into adulthood. We sectioned P0 and P7 SLMAP3-KO and Wt hearts and stained with H&E. Surprisingly, at postnatal day 0 (P0) the left ventricle size of KO hearts (-14.19% ± -7.55%, ϱ=0.10, n=3) was almost similar to Wt hearts (**Figure 6A**). At P7, H&E stain revealed no differences in left ventricle wall size in KO hearts (-0.08% ± -0.78%, ϱ=0.97, n=3) (**Figure 6A**). Further, examination of adult SLMAP3-KO with ECHO at 10-week of age indicated no significant differences in cardiac structure or function (**Figure 6B**) with equivalent survival with age as Wt.

We quantified the expression of the other SLMAP isoforms in SLMAP3-KO hearts and Western blot analysis indicated no differences in SLMAP1 and SLMAP2 protein expression in KO vs Wt at E9.5 however the relative expression of SLMAP1/SLMAP3 and SLMAP2/SLMAP3 was 6.5x and 2.2x greater in P0 hearts when compared to E9.5 (**Figure 6C**). The data indicates that as the myocardium develops there is a substantial increase in the expression of the smaller SLMAP isoforms compared to SLMAP3 and loss of SLMAP3 did not influence their expression in embryonic or postnatal myocardium.

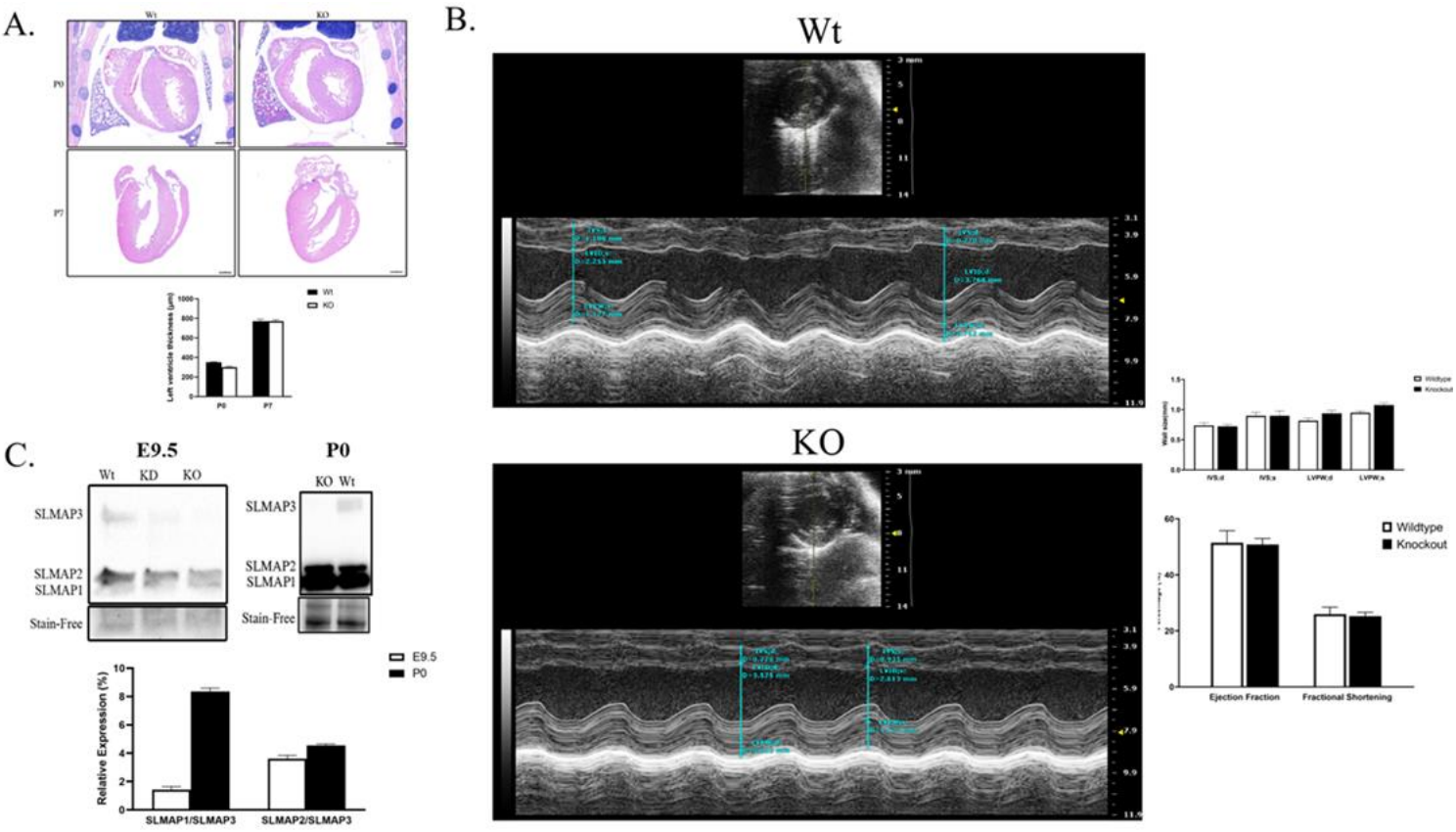

Figure 6. *Analysis of postnatal mouse hearts from Nkx2.5-Cre/SLMAP3-null mice.* A. Representative histological staining of Wt and KO Nkx2.5-Cre/SLMAP3-null P0 and P7 hearts using H&E. Scale bar= 0.5mm. B. Representative short axis echocardiography m-mode images of 10-week-old Wt and KO. Bar graphs represent ejection fraction, fractional shortening and left ventricle wall thickness. LV; Left ventricle. IVS, LVPW; intraventricular septum, LV posterior wall. d,s;diastole, systole. *n*=6. C) Representative Western blot displaying expression of SLMAP isoforms (SLMAP1, SLMAP2 and SLMAP3) in Wt and KO hearts at E9.5 and P0. Bar graph represents the quantification of relative expression of SLMAP1 or SLMAP2 compared to SLMAP3 in E9.5 and P0 Wt hearts. *n*=3

4.2.6 Depletion of SLMAP isoforms in rat embryonic cardiomyocytes (H9C2 cells) impacts their growth

To examine whether all three isoforms expressed in heart are important for the growth of the embryonic myocardium we investigated the expression of SLMAPs in the rat embryonic cardiomyocyte cell line H9C2. Western blots indicate that H9C2 cells express the three SLMAP isoforms-SLMAP-1, 2 and 3 (**Figure 7A**) identical in molecular size to that seen in mouse embryonic hearts (**Figure 6C)**. H9C2 cells transduced with shRNA-S4 (S4) or shRNA-S5 (S5) displayed decrease in SLMAP expression (**Figure 7A**) when compared to the shRNA-Sc (Sc), only S5 drastically reduced expression of all three SLMAP isoforms and was employed in all subsequent studies (**Figure 7A**). Notably, depletion of all SLMAP isoformsin H9C2 cells resulted in a decrease in growth rate (**Figure 7B**). Further, the depletion of SLMAP isoforms lead to increase in X-gal positive cells in the Senescence Associated-β-Galactosidase (SA-β-Gal) Assay (**Figure 7C**) and a decrease in proliferation, as indicated by the reduced number of Ki67 positive cells (**Figure 7D**). Western blots of transduced H9C2 lysates indicated that depletion of SLMAPs had no impact on the phosphorylation of YAP in H9C2 cells (**Figure 7E**). Thus SLMAP isoforms appear to play a important role in growth of cardiomyocytes, independently of Hippo signaling.

.

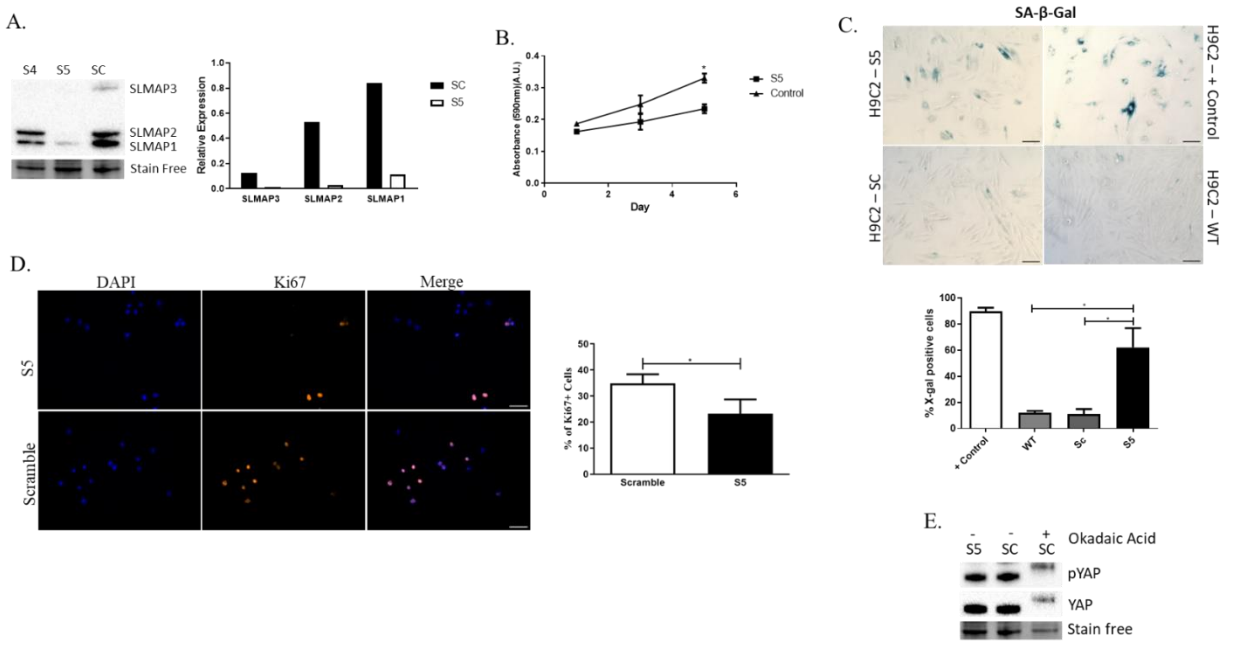

Figure 7. *Reduced SLMAP expression in H9C2 cells impacts cardiomyocyte growth and causes senescense* A. Representative Western blot dispalying expression of SLMAP1, SLMAP2 and SLMAP3 in transduced H9C2 cells. Bar graph represents normalized expression of SLMAPs in Sc, S4 and S5 cells to total proteins visualized by Stain-Free™ technology. B. Line graph displaying crystal violet absorbance measurements on days 1, 3 and 5 after seeding transduced H9C2 and comparing growth rates. C. Immunofluorescence staining of DAPI (Blue; nucleus) and Ki67 (orange) in transduced H9C2 cells. Bar graph represents mean percentage of $Ki67^{+}$ cells per field of view. N=3 D. Senescence analysis on Wt positive (+) control, Wt, and transduced (Sc, S5) H9C2 cells with SA-β-Gal assay. Bar graph represents percentage (%) of X-gal positive cells. E. Representative Western blot evaluating phospho to total YAP in transduced H9C2 and Sc-H9C2 cells treated with okadaic acid as a positive control. Same blot as in A. *; $\rho<0.05$. Scale bar=100 μm.

4.3 Discussion

Here, we report that the specific loss of SLMAP3 isoform in cardiac progenitors by gene targeting with Nkx2.5-cre mice leads to a growth delay in the formation of the heart during early cardiogenesis. The developmental delay in cardiac formation was not due to changes in the proliferation or hypertrophic response in embryonic cardiomyocytes, alt-hough a difference in cell size was evident at E12.5 due to SLMAP3 deletion. Intriguingly, the early delay in cardiogenesis was completely reversed at birth and the postnatal devel-opment and function of the heart was unaffected in these mice in the absence of any SLMAP3. While the expression of SLMAP3 protein was completely nullified in cardiac progenitors, due to Nkx2.5-cre, the expression of the more abundant SLMAP1 and SLMAP2 remained unchanged and continued to accumulate normally during embryonic and postnatal development to levels that were similar to those in wildtype mouse hearts. SLMAP2 and SLMAP1 expression levels remained unaffected, most likely due to the utili-zation of alternative promoters in cardiomyocytes (Salih and Tuana, unpublished data). Whether SLMAP1 and SLMAP2 can compensate for a loss of SLMAP3 function needs to be considered because of the very close structural similarities between these isoforms, which are derived by alternative splicing mechanisms from a single gene (Figure 1). In this regard, SLMAP3 is clearly distinguishable from the other SLMAPs due to its extended N-terminal sequences which encompass an FHA domain that was shown to bind MST1/2 kinases and regulate Hippo to impact proliferation of 293 T cells [30]. The in vivo data here did not support a role for SLMAP3 in the proliferation of embryonic cardiomyocytes or the regulation of MST or YAP phosphorylation, since SLMAP3 deletion had no impact on these parameters during cardiogenesis. The loss of SLMAP3 did not affect Hippo sig-naling in the

postnatal heart either, and the myocardium appeared normal in terms of its structure and function in adulthood. These data are consistent with our studies on the tar-geted deletion of the SLMAP3 isoform in postnatal myocardium [33]. Our previous data have shown that SLMAP is expressed early during cardiogenesis, and thus could influ-ence the growth and maturation of cardiomyocytes. Perhaps the deletion of the other SLMAP isoforms is necessary to observe the critical nature of SLMAP in developing myo-cardium. Cardiac development begins at E7.5 in mice with the formation of the cardiac crescent, when the cardiac homeobox transcription factor Nkx2.5 is highly expressed within cardiac progenitor cells [34]. Nkx2.5-Cre mice are often employed to study genes during early cardiogenesis [29,35], and the deletion of SLMAP3 expression at this stage within FHF and SHF did not apparently impact cardiomyocyte differentiation/migration; however, there was a growth delay in septation with underdeveloped cardiac chambers in these mice hearts at E12.5 but without any obvious structural abnormalities. In order to in-terrogate the potential role of the other SLMAP isoforms, we employed rat embryonic car-diomyocytes (H9C2 cells) that were found to express SLMAP1, SLMAP2, and SLMAP3 with similar molecular characteristics to those in mouse embryonic heart tissue. Our con-structed sh-RNAs-targeting SLMAPs resulted in a significant decrease in the expression of the three SLMAP isoforms accompanied by a profound deficit in growth and proliferation as well as enhanced cellular senescence in these embryonic cardiomyocytes. It is notable that depletion of the three SLMAPs in H9C2 cells had no impact on the main components of Hippo signaling. Thus, the mechanisms of SLMAP action that impact the embryonic growth of cardiomyocytes are independent of any regulation through Hippo signaling. The data support the contention that SLMAP isoforms are collectively critical for

embryon-ic cardiomyocyte growth and that they can potentially compensate for each other since the specific embryonic KO of the SLMAP3 isoform in early heart development was non-lethal. It is conceivable that the more abundant SLMAP1 and SLMAP2 proteins may substitute for the loss of SLMAP3 during cardiogenesis. Given that the knockdown of all three SLMAP isoforms in H9C2 cardiomyocytes lead to defective growth and cellular senes-cence, it would be meaningful to delete SLMAP1 and SLMAP2 in cardiac progenitors in vivo to gauge the contribution of SLMAP to heart development, although the H9C2 data would suggest that it would be lethal. The size of cardiomyocytes was noticeably smaller in embryonic hearts due to Nkx2.5-Cre-mediated SLMAP3 loss, but there was no change in hypertrophic signaling (AKT/mTOR), and nor was there any change in cardiomyocyte numbers. We aim to employ additional stereological analysis by isolating embryonic car-diomyocytes and further staining to decipher the mechanisms that may impact their size and shape at the cellular level.

It is notable that unique structural elements in SLMAP3 (i.e., FHA domain) target the MTOC [11], which has been shown to be critical for mitosis and differentiation [36]. The microtubules and the cytoskeleton serve important roles in cell shape and function, and their contributions to cardiomyocyte growth and size/shape in vivo remain elusive. The data here further point to a unique structural mechanism for SLMAP actions through their interactions with subcellular organelles, microtubules, and the cytoskeleton to guide car-diac development.

Funding: This research was funded by the Canadian Institute of Health Research project grant, grant number 220996-151999, to B.S.T.

Institutional Review Board Statement: Mice were handled in accordance with the guidelines set by Canadian Council on Animal Care, Guide to the Care and Use of Experimental Animals, 2 vols. (Ottawa, Ont.: CCAC, 1980-1993) and Animals for Research Act, R.S.O. 1990, c.A. 22. All animal protocols and procedures were approved by the Animal Care Committee of the University of Ottawa (Protocol #: CMM-1725 and CMM-1723, Renewed: December 2020).

Acknowledgments: We would like to thank Dr. Kyoung-Han Kim and Dr. Lynn Megeney for providing the Nkx2.5-Cre mice and H9C2 cell line. We are thanking all the facilities involved in this study: Cell Biology and Image Acquisition Core (RRID: SCR_021845) and the Louise Pelletier Histology Core Facility (RRID: SCR_021737).

Conflicts of Interest: *The authors declare that the research was conducted in the absence of any commercial or financial relationships that could be construed as a potential conflict of interest.*

4.4 Materials and Methods

4.4.1 Generating and genotyping the SLMAP knockout model

The Nkx2.5-Cre mice [29] were generously donated by Dr. Kyoung-Han Kim and backcrossed with wildtype B6C3F1 mice to generate the B6C3F1 Nkx2.5-cre mice. The generation of our flox-SLMAP, breeding strategies, and PCR genotyping were performed as described previously [33]. Briefly, B6C3F1 flox-SLMAP mice were crossed with B6C3F1 Nkx2.5-cre mice to generate heterozygous floxed-SLMAP;Nkx2.5-cre or knockdown (KD) mice. Crossing KD mice with each other generates homozygous floxed-SLMAP;Nkx2.5-cre or knockout (KO) mice. Mice harboring heterozygous or homozygous Nkx2.5-cre were followed for one year and did not exhibit any abnormalities. Thus, chronic expression of cre did not result in any phenotypes.

For embryo studies, pregnant mothers that were plug checked (day of plug was E0.5) and carrying our experimental embryos at the desired stage were anesthetized with a standard ketamine–xylazine–acepromazine (KXA) drug cocktail during embryo isolation and euthanized after they were harvested. The embryos were dissected in ice cold 1x PBS and whole embryos or prenatal hearts were fixed in 10% neutral buffered formalin for 48-96h or snap-frozen in liquid nitrogen for proteomic analysis. Caudal tissues or tails were used for genotyping.

Mice were handled in accordance with the guidelines set by Canadian Council on Animal Care, Guide to the Care and Use of Experimental Animals, 2 vols. (Ottawa, Ont.: CCAC, 1980-1993) and Animals for Research Act, R.S.O. 1990, c.A. 22. All animal protocols and procedures were approved by the Animal Care Committee of the University of Ottawa.

4.4.2 Protein isolation and western blotting

Hearts of embryonic (E9.5-E18.5) and newborn (P0) mice and immediately frozen at −80 °C. Each heart was later washed with ice-cold 1× phosphate buffered saline (PBS) and homogenized using a Fisher handheld Maximizer homogenizer (Thermo Fisher Scientific) in ice-cold lysis buffer (1 mM ethylene glycol tetraacetic acid (EGTA), 1 mM ethylenediaminetetraacetic (EDTA), 20 mM Tris base, 1% Triton, 150 mM sodium chloride, 1× complete mini EDTA-free protease inhibitor cocktail (Roche), and 1× PhosSTOP (Roche). The suspension was centrifuged for 15 min at 12,000× g to separate the proteins from the cell debris. The supernatant containing protein was collected in Eppendorf tubes and stored in a freezer at −80 °C. Protein quantities were calculated using the BSA method.

For western blotting experiments, 10 μg of protein was loaded in each well of a 5–15% SDS-PAGE gel. The gels were transferred overnight on a polyvinylidene fluoride (PVDF) membrane (Bio-Rad) in a buffer containing 25 mM Tris, 190 mM Glycine, and 20% methanol. All membranes were blocked at room temperature for 1 h in Tris-buffered saline (TBST) containing 1 M Tris, 290 mM NaCl, 0.1% Tween 20, pH 7.4, and 5% nonfat dry milk. Primary antibodies (listed in **Table 1**) were incubated overnight at 4 °C with 5% bovine serum albumin (BSA). Membranes were washed 5 times for 5 min each in TBST prior to adding the appropriate horseradish peroxidase-labeled secondary antibody (Jackson ImmunoResearch) in a 1:10,000 dilution in TBST with 5% nonfat dry milk. Membranes were shaken slowly at room temperature for 1 h while incubating with secondary antibody, followed by 5 washes for 5 min each with TBST. Membranes were treated with a BioRad western blotting kit (Bio-Rad, Hercules, CA, USA) and developed using ChemiDoc machines (Bio-Rad, Hercules, CA, USA). Bands were quantified by densitometry

using Image Lab software v.6.0.0 (Bio-Rad) Membranes were stripped (25 mM glycine, 10% SDS, and pH 2.2 in dH2O) and reprobed with different antibodies. When using stain-free technology, stain-free gels (Bio-Rad) and low-fluorescence PVDF membranes (Bio-Rad) were used.

Table 1. List of antibodies used in this study. All antibodies used in this study are listed with the corresponding distributor, catalog number, and dilution used for western blot (WB) or immunofluorescence (IF).

Antibody	Manufacturer	Dilution
SLMAP	Novus Biologicals (NBP1-81397)	1:1000(WB)
Striatin-1	BD Transduction Laboratories (610838)	1:1000 (WB)
Striatin-3	Novus Biological (NBP-74572)	1:1000 (WB)
STRIP1	Bethyl Laboratories (A304-644A)	1:1000 (WB)
PP2A-C α/β subunit	Santa Cruz Biotechnology (sc-80665)	1:200 (WB)
PP2A-A α subunit	Millipore Sigma (07-250)	1:600 (WB)
Phospho-YAP (S127)	Cell Signaling Technology (13008S)	1:1000 (WB)
YAP	Cell Signaling Technology (14074S)	1:1000 (WB)
pH3	Abcam (ab5176)	1:200 (IF)
Ki67	Abcam (ab15580)	1:200 (IF)
Troponin C (TnC)	Santa Cruz (sc-52265)	1:200 (IF)
pAKT1	Cell Signaling Technology (9018S)	1:1000 (WB)
AKT1	Cell Signaling Technology (9272)	1:1000 (WB)
pMTOR1	Cell Signaling Technology (5536)	1:1000 (WB)
MTOR1	Cell Signaling Technology (2972)	1:1000 (WB)

4.4.3 Echocardiography

All echocardiographic analysis was performed using the VEVO 2100 system (FUJIFILM VisualSonics) identically to our previous publication [33].

4.4.4 Histological and Immunofluorescent analysis

Embryonic and postnatal mouse hearts were fixed using 10% Neutral Buffered Formalin (Thermo Fisher Scientific). After fixing for 48 hours, hearts were sectioned 4 μm longitudinally per section. Paraffin-embedded slides were rehydrated through well-established protocols for rehydration and then incubated with citrate buffer for antigen retrieval [37]. Sectioned hearts were stained with hematoxylin and eosin (H&E) stain to visualize the myocardium and nuclei. For immunofluorescence, rehydrated slides were subjected to 1 hour of 5% BSA in PBS-T (1x PBS, 0.01% Triton X-100) of blocking. After rinsing with PBS, we diluted antibodies according to Table 1 in blocking solution and incubated them overnight at 4^0C. Samples were then washed 5x for 5 mins with PBS and then secondary Alexa-555 (Thermo Fisher Scientific, USA) or Alexa 647 (Thermo Fisher Scientific, USA) were incubated for 1 hour at room temperature. We used VectaShield Plus DAPI (MJS Biolynx, CA) mounting medium with 1.5mm coverslips (Fisher Scientific, USA) sealed with nail polish and imaged when completely dried. Images were captured on Zeiss AxioImager M2 and analyzed using ImageJ.

4.4.5 Creation of short-hairpin RNA (sh-RNA) Lentivirus for depletion of SLMAP3

To stably deplete SLMAP3 expression in H9C2 cells, we designed two shRNAs target-ing mouse SLMAP sequences from exon 22 (Ensembl reference transcript ENSMUST00000139075.8), which were conserved in rat SLMAP gene. The targeting se-quences are 5′-GCAATCAATCACAGATGAGCTCAAA and 5′-GCTGCTGCGAGAGAAAGGAAATAAT, which were called S4 and S5, respectively. The control scramble target sequence is 5′-AGGATAAGCGTCAACGAATAGGTGA, referred to as SC, and was generated by inputting the S5 plasmid sequence into GenScript Sequence Scramble tool [38]. The shRNAs were designed in a lentivirus vector with the VectorBuild-er design tool [39]. VectorBuilder cloned and delivered the plasmids in Escherichia coli (VB UltraStable). Plasmids were isolated via PureYield Plasmid Midprep System protocol (Promega Cooperation, Technical Manual #TM253) and transfected in Lenti-X 293 T cells with the packing and envelope plasmids psPAX2 [40] and pMD2.G [41] via polyeth-yleneimine (PEI), following an established protocol [42]. The supernatants of Lenti-X 293 T cells containing lentiviruses were harvested 48 and 72 h after transfection and filtered with 0.45 μm sterile syringe filter. The viral particles were concentrated via Lenti-X-Concentrator (Clontech, Mountain View, CA, USA, catalog number PT4421-2), and the titer was quantified with the PCR Lentivirus Titer Kit (abm, New York, NY, USA, catalog num-ber LV900).

4.4.6 Maintenance and transduction of H9C2 rat cardiomyocyte cell line

H9C2 cell line was originally acquired from ATCC and gifted by the Megeney Laboratory at University of Ottawa. H9C2 cells were kept at 37°C with 5% carbon dioxide in high humidity. H9C2 media consisted of high glucose (4.5g/L) Dulbecco modified essential media (DMEM) (Multicell, Catalogue #319-005-CL) containing 1.00% pen-strep, 1.00% non-essential amino acids

(Gibco, Reference #11140-050). The H9C2 cell line has been tested in the lab for mycoplasma contamination and tested negative in all instances. The lentiviral reverse transduction was performed following Addgene protocol [43] H9C2 cells were plated at 25,000 cells per cm^2 of growth area and transduced with S4, S5, and Sc at multiplicity of infection (MOI) of 150. Selection for successfully transduced cells was carried out by incorporating puromycin into cell media (3 μg/mL) for 3 days. For induction of YAP phosphorylation to be used as a positive control, H9C2 cells were treated with 1.5 μM okadaic acid for 1 hour. Protein lysate was isolated soon after that.

4.4.7 Senescence analysis on H9C2

Cellular senescence was analyzed via Senescence Beta-Galactosidase Staining Kit protocol outlined by manufacture (Cell Signaling Technology, Cat. #9860). All the cells were plated in triplicates, and cells were quantified in 3 fields of each. Total and positive X-gal cells were counted blindly to avoid any bias. For positive control, we induced cellular senescence in H9C2 WT cells by 600 μm H_2O_2 treatment for 2 hours in two consecutive days.

4.4.8 H9C2 Growth Curve Analysis

Cells were plated at 9000 cells per cm^2 and left overnight to attach. Cells were fixed with 4% paraformaldehyde in 1X PBS, pH 7.4 (warmed to 37°C) for 20 minutes followed by distilled water wash. Samples were incubated with 0.1% crystal violet for 20 minutes at room temperature followed by 4 distilled water washes. Samples were left to air dry at room temperature for a minimum of 2hrs followed by 10% acetic acid incubation for 20 minutes at room temperature, while shaking, to dissolve the crystal violet. Quantification was performed by measuring absorbance of samples at 590 nm relative to each other using Synergy Hybrid

Multi-Mode Microplate Reader (BioTek Instruments, Highland Park, VT, USA). Procedure was performed 3 times corresponding to number of day (days 1, 3, and 5) for each sample.

4.4.9 Statistical Analyses

The statistical analysis was performed using GraphPad Prism software version 8 for Windows (GraphPad Software). All comparisons between wildtype and knockout groups were analyzed using non-paired two-tailed Student's T-test. If three groups were analyzed, we used one-way ANOVA with post hoc Tukey test to determine significance. All values and points on graphs represent mean values obtained from multiple experiments. All error bars presented in graphs are represented using the standard error of the mean. All sample size values (n) represent replicates.

4.5 References

1. Schleich, J.-M.; Abdulla, T.; Summers, R.; Houyel, L. An overview of cardiac morphogenesis. Arch. Cardiovasc. Dis. 2013, 106, 612–623. https://doi.org/10.1016/j.acvd.2013.07.001.

2. Kelly, R.G.; Buckingham, M.E.; Moorman, A.F. Heart Fields and Cardiac Morphogenesis. Cold Spring Harb. Perspect. Med. 2014, 4, a015750. https://doi.org/10.1101/cshperspect.a015750.

3. van den Berg, G.; Abu-Issa, R.; de Boer, B.A.; Hutson, M.R.; de Boer, P.A.; Soufan, A.T.; Ruijter, J.M.; Kirby, M.L.; van den Hoff, M.J.; Moorman, A.F. A caudal proliferating growth center contributes to both poles of the forming heart tube. Circ. Res. 2009, 104, 179–188.

4. Colombo, S.; de Sena-Tomás, C.; George, V.; Werdich, A.A.; Kapur, S.; MacRae, C.A.; Targoff, K.L. Nkx genes establish sec-ond heart field cardiomyocyte progenitors at the arterial pole and pattern the venous pole through Isl1 repression. Devel-opment 2018, 145, dev161497 .

5. Hoff, M.J.v.D.; Kruithof, B.P.; Moorman, A.F.; Markwald, R.R.; Wessels, A. Formation of Myocardium after the Initial Devel-opment of the Linear Heart Tube. Dev. Biol. 2001, 240, 61–76. https://doi.org/10.1006/dbio.2001.0449.

6. Yotti, R.; Seidman, C.E.; Seidman, J.G. Advances in the Genetic Basis and Pathogenesis of Sarcomere Cardiomyopathies. Annu. Rev. Genom. Hum. Genet. 2019, 20, 129–153. https://doi.org/10.1146/annurev-genom-083118-015306.

7. Guo, Y.; Pu, W. Cardiomyocyte Maturation: New Phase in Development. Circ. Res. 2020, 126, 1086–1106.

8. Wigle, J.; Demchyshyn, L.; Pratt, M.; Staines, W.; Salih, M.; Tuana, B. Molecular cloning, expression, and chromosomal as-signment of sarcolemmal-associated proteins. A family of acidic amphipathic alpha-helical proteins associated with the membrane. J. Biol. Chem. 1997, 272, 32384–32394.

9. Guzzo, R.M.; Salih, M.; Moore, E.D.; Tuana, B.S. Molecular properties of cardiac tail-anchored membrane protein SLMAP are consistent with structural role in arrangement of excitation-contraction coupling apparatus. Am. J. Physiol. Heart Circ. Physiol. 2005, 288, H1810–H1819. https://doi.org/10.1152/ajpheart.01015.2004.

10. Byers, J.T.; Guzzo, R.M.; Salih, M.; Tuana, B.S. Hydrophobic profiles of the tail anchors in SLMAP dictate subcellular target-ing. BMC Cell Biol. 2009, 10, 48. https://doi.org/10.1186/1471-2121-10-48.

11. Guzzo, R.M.; Sevinc, S.; Salih, M.; Tuana, B.S. A novel isoform of sarcolemmal membrane-associated protein (SLMAP) is a component of the microtubule organizing centre. J. Cell Sci. 2004, 117, 2271–2281. https://doi.org/10.1242/jcs.01079.

12. Ishikawa, T.; Sato, A.; Marcou, C.; Tester, D.; Ackerman, M.; Crotti, L.; Schwartz, P.; On, Y.; Park, J.; Nakamura, K.; et al. A novel disease gene for Brugada syndrome: Sarcolemmal membrane-associated protein gene mutations impair intracellular trafficking of hNav1.5. Circ. Arrhythm. Electrophysiol. 2012, 5, 1098–1107.

13. Nader, M.; Westendorp, B.; Hawari, O.; Salih, M.; Stewart, A.F.R.; Leenen, F.H.H.; Tuana, B.S. Tail-anchored membrane pro-tein SLMAP is a novel regulator of cardiac function at the sarcoplasmic reticulum. Am. J. Physiol. Circ. Physiol. 2012, 302, H1138–H1145. https://doi.org/10.1152/ajpheart.00872.2011.

14. Mlynarova, J.; Trentin-Sonoda, M.; da Silva, F.G.; Major, J.L.; Salih, M.; Carneiro-Ramos, M.S.; Tuana, B.S. SLMAP3 isoform modulates cardiac gene expression and function. PLoS ONE 2019, 14, e0214669. https://doi.org/10.1371/journal.pone.0214669.

15. Wielowieyski, P.; Sevinc, S.; Guzzo, R.; Salih, M.; Wigle, J.; Tuana, B. Alternative splicing, expression, and genomic structure of the 3′ region of the gene encoding the sarcolemmal-associated proteins (SLAPs) defines a novel class of coiled-coil tail-anchored membrane proteins. J. Biol. Chem. 2000, 275, 38474–38481.

16. Consortium, U. UniProt: A worldwide hub of protein knowledge. Nucleic Acids Res. 2019, 47, D506–D515.

17. Guzzo, R.M.; Wigle, J.; Salih, M.; Moore, E.D.; Tuana, B.S. Regulated expression and temporal induction of the tail-anchored sarcolemmal-membrane-associated protein is critical for myoblast fusion. Biochem. J. 2004, 381, 599–608. https://doi.org/10.1042/bj20031723.

18. Mahajan, A.; Yuan, C.; Lee, H.; Chen, E.S.-W.; Wu, P.-Y.; Tsai, M.-D. Structure and Function of the Phosphothreonine-Specific FHA Domain. Sci. Signal. 2008, 1, re12. https://doi.org/10.1126/scisignal.151re12.

19. Yu, F.; Zhao, B.; Guan, K. Hippo Pathway in Organ Size Control, Tissue Homeostasis, and Cancer. Cell 2015, 163, 811–828.

20. Goudreault, M.; D'Ambrosio, L.M.; Kean, M.J.; Mullin, M.J.; Larsen, B.G.; Sanchez, A.; Chaudhry, S.; Chen, G.I.; Sicheri, F.; Nesvizhskii, A.I.; et al. A PP2A Phosphatase High Density Interaction Network Identifies a Novel Striatin-interacting Phos-phatase and Kinase Complex Linked to the Cerebral Cavernous Malformation 3 (CCM3) Protein. Mol. Cell. Proteom. 2009, 8, 157–171. https://doi.org/10.1074/mcp.m800266-mcp200.

21. Jeong, B.-C.; Bae, S.J.; Ni, L.; Zhang, X.; Bai, X.-C.; Luo, X. Cryo-EM structure of the Hippo signaling integrator human STRIPAK. Nat. Struct. Mol. Biol. 2021, 28, 290–299. https://doi.org/10.1038/s41594-021-00564-y.

22. Couzens, A.L.; Knight, J.D.R.; Kean, M.J.; Teo, G.; Weiss, A.; Dunham, W.H.; Lin, Z.-Y.; Bagshaw, R.D.; Sicheri, F.; Pawson, T.; et al. Protein Interaction Network of the Mammalian Hippo Pathway Reveals Mechanisms of Kinase-Phosphatase Interac-tions. Sci. Signal. 2013, 6, rs15. https://doi.org/10.1126/scisignal.2004712.

23. von Gise, A.; Lin, Z.; Schlegelmilch, K.; Honor, L.B.; Pan, G.M.; Buck, J.N.; Ma, Q.; Ishiwata, T.; Zhou, B.; Camargo, F.D.; et al. YAP1, the nuclear target of Hippo signaling, stimulates heart growth through cardiomyocyte proliferation but not hyper-trophy. Proc. Natl. Acad. Sci. USA 2012, 109, 2394–2399. https://doi.org/10.1073/pnas.1116136109.

24. Heallen, T.; Zhang, M.; Wang, J.; Bonilla-Claudio, M.; Klysik, E.; Johnson, R.L.; Martin, J.F. Hippo Pathway Inhibits Wnt Sig-naling to Restrain Cardiomyocyte Proliferation and Heart Size. Science 2011, 332, 458–461. https://doi.org/10.1126/science.1199010.

25. Xin, M.; Kim, Y.; Sutherland, L.B.; Murakami, M.; Qi, X.; McAnally, J.; Porrello, E.R.; Mahmoud, A.I.; Tan, W.; Shelton, J.M.; et al. Hippo pathway effector Yap promotes cardiac regeneration. Proc. Natl. Acad. Sci. USA 2013, 110, 13839–13844. https://doi.org/10.1073/pnas.1313192110.

26. Xin, M.; Kim, Y.; Sutherland, L.B.; Qi, X.; McAnally, J.; Schwartz, R.J.; Richardson, J.A.; Bassel-Duby, R.; Olson, E.N. Regula-tion of Insulin-Like Growth Factor Signaling by Yap Governs Cardiomyocyte Proliferation and Embryonic Heart Size. Sci. Signal. 2011, 4, ra70. https://doi.org/10.1126/scisignal.2002278.

27. Heallen, T.; Morikawa, Y.; Leach, J.; Tao, G.; Willerson, J.T.; Johnson, R.L.; Martin, J.F. Hippo signaling impedes adult heart regeneration. Development 2013, 140, 4683–4690. https://doi.org/10.1242/dev.102798.

28. Zheng, Y.; Liu, B.; Wang, L.; Lei, H.; Prieto, K.D.P.; Pan, D. Homeostatic Control of Hpo/MST Kinase Activity through Auto-phosphorylation-Dependent Recruitment of the STRIPAK PP2A Phosphatase Complex. Cell Rep. 2017, 21, 3612–3623. https://doi.org/10.1016/j.celrep.2017.11.076.

29. Stanley, E.G.; Biben, C.; Elefanty, A.; Barnett, L.; Koentgen, F.; Robb, L.; Harvey, R.P. Efficient Cre-mediated deletion in car-diac progenitor cells conferred by a 3'UTR-ires-Cre allele of the homeobox gene Nkx2-5. 2002, 46, 431–439.

30. Bae, S.; Ni, L.; Osinski, A.; Tomchick, D.; Brautigam, C.; Luo, X. SAV1 promotes Hippo kinase activation through antagoniz-ing the PP2A phosphatase STRIPAK. eLife 2017, 6, 30278.

31. Brade, T.; Pane, L.S.; Moretti, A.; Chien, K.R.; Laugwitz, K.-L. Embryonic Heart Progenitors and Cardiogenesis. Cold Spring Harb. Perspect. Med. 2013, 3, a013847. https://doi.org/10.1101/cshperspect.a013847.

32. Aoyagi, T.; Matsui, T. Phosphoinositide-3 Kinase Signaling in Cardiac Hypertrophy and Heart Failure. Curr. Pharm. Des. 2011, 17, 1818–1824. https://doi.org/10.2174/138161211796390976.

33. Rehmani, T.; Mlynarova, J.; Byers, J.; Salih, M.; Tuana, B.S. Specific Deletion of the FHA Domain Containing SLMAP3 Iso-form in Postnatal Myocardium Has No Impact on Structure or Function. Cardiogenetics 2021, 11, 164–184. https://doi.org/10.3390/cardiogenetics11040018.

34. George, V.; Colombo, S.; Targoff, K.L. An early requirement for nkx2.5 ensures the first and second heart field ventricular identity and cardiac function into adulthood. Dev. Biol. 2015, 400, 10–22. https://doi.org/10.1016/j.ydbio.2014.12.019.

35. Cambier, L.; Plate, M.; Sucov, H.M.; Pashmforoush, M. Nkx2-5 regulates cardiac growth through modulation of Wnt signal-ing by R-spondin3. Development 2014, 141, 2959–2971. https://doi.org/10.1242/dev.103416.

36. Becker, R.; Leone, M.; Engel, F.B. Microtubule Organization in Striated Muscle Cells. Cells 2020, 9, 1395. https://doi.org/10.3390/cells9061395.

37. Available online: https://www.novusbio.com/support-by-application/Fluorescent-IHC-Staining-of-FFPE-Tissue (accessed on November 1st ,2019).

38. Available online: https://www.genscript.com/tools/create-scrambled-sequence-reference (accessed on October 31st ,2022).

39. Available online: https://en.vectorbuilder.com/design/pLV_shRNA_U6.html-reference (accessed on November 1st ,2022).

40. Available online: https://www.addgene.org/12260/ (accessed on November 1st ,2022).

41. Available online: https://www.addgene.org/12259/ (accessed on November 1st ,2022).

42. Available online: https://www.addgene.org/protocols/lentivirus-production/ (accessed on November 1st ,2022).

43. Available online: https://www.addgene.org/protocols/generating-stable-cell-lines/-reference (accessed on November 1st ,2022)

Chapter Five: SLMAP3 is essential for neurulation through mechanisms that impact centrosomal and Golgi dynamics

SLMAP3 is essential for neurulation through mechanisms that impact centrosomal and Golgi dynamics

Rehmani T[1], Dias A.P.[1], Salih M[1], Tuana B.S. [1*]

Department of Cellular and Molecular Medicine, Faculty of Medicine, University of Ottawa, 451 Smyth Road, K1H 8M5, Ottawa, ON, Canada; trehmani@uottawa.ca (T.R.), adias085@uottawa.ca (A.D), msalih@uottawa.ca (M.S)

*Correspondence: btuana@uottawa.ca (B.S.T); Tel.: +613-562-5800 (ext. 8578)

Submitted to Life Science Alliance on December 12th, 2023: LSA-2023-02545-T

Authors Contributions

T.R.: project conceptualization, methodology, validation, formal analysis, investigation, resources, data visualization and manuscript writing;

A.P.D: project conceptualization, investigation, resources and manuscript writing;

M.S.: investigation, resources and methodology;

B.T.: project conceptualization, supervision, manuscript review and funding acquisition.

Abstract:

SLMAP3 is a tail-anchored membrane protein that targets subcellular organelles and is believed to regulate Hippo. The knockout (KO) of SLMAP3 in mice was lethal presenting with craniorachischisis. Loss of SLMAP3 did not impact Hippo signaling or cell proliferation. SLMAP3-KO Embryos displayed reduced length and width of neural plates signifying arrested convergent extension. Expression of planar cell polarity (PCP) components, disheveled-2 and -3, and activity of downstream targets, phospho-ROCK2, phospho-cofilin and phospho-JNK1/2 was deregulated in SLMAP3-KO E12.5 brains. The cytoskeletal proteins, actin and nestin, and apical PKCζ, were not polarized to their specified apical or basal domains and adherens and tight junctions were mislocalized in neural tubes and neuroepithelial cells (NEPCs) that were deficient in SLMAP3. Proteomics revealed new associations of SLMAP3 with the apical-basal polarity (ABP) protein, Scribble, and components of the centrosome (AKAP9, Pericentrin, Cep170), Golgi (Golgb1, Golga3) and transport machinery (Kif5c). Depletion of SLMAP3 altered the localization of these components with defective differentiation. These data reveal a new role for SLMAP3 in convergent extension through mechanisms that involve centrosomal and Golgi dynamics.

5.1 Introduction:

Organization and dynamics of subcellular organelles play a crucial role in embryonic development, as alterations in their structure and distribution critically impact the spatiotemporal patterning of tissue growth and morphogenesis [1]. During neurulation the neural plate, a layer of specialized ectoderm cells called neuroepithelial cells (NEPCs), will organize in a pseudostratified manner allowing this plate to bend, form bilateral neural folds that will fuse to generate the hollow neural tube (NT) aided by the positioning/movement of organelles [2, 3]. For example, the movement of nuclei during different stages of the cell cycle known as interkinetic nuclear migration shifts nuclei basally to narrow the NEPCs at the apical side to promote apical constriction. Apical constriction initiates the shaping of neuroepithelial cells to a wedge or bottle shaped to enable contractile forces of actin-myosin on apical surface to constrict to bend and fold the neural plate [4]. Further, defining the apical-basal polarity (ABP) axis in these cells is ensuring appropriate distribution (apical or basal) of organelles such as the centrosome and Golgi to maintain the polarity gradient [5]. However, the molecular mechanisms that regulate organelle positioning and movements are not well understood, and if perturbed can result in neural tube defect (NTD), a common structural birth defect in humans where prognosis depends on location of open neural tube, varying from mild disability to death [6, 7].

We have previously defined the sarcolemmal membrane associated protein (SLMAP) as a core component of centrosomes, endoplasmic reticulum, mitochondria, and perinuclear membrane and could impact function of these organelles [8-12]. SLMAPs are categorized as three main polypeptide isoforms, SLMAP1 (35 kDa), SLMAP2 (45 kDa) and SLMAP3 (83-91 kDa), generated by alternative splicing and diverse start sites from a single gene we localized to 3p.13-21 in humans [10,13]. The c-terminal sequences of SLMAP isoforms are highly conserved and comprise coiled-coil domains and an alternatively spliced mutually exclusive transmembrane domain (TM1/TM2) that localize SLMAP to subcellular membranes [8]. The largest isoform, SLMAP3 uniquely houses an N-terminal forkhead associated domain (FHA) that acts as regulator for phosphoprotein interactions and targets the microtubule organizing center (MTOC) [12, 14, 15]. SLMAP3 is ubiquitously expressed and

developmentally regulated [11, 16]. Recent studies have indicated that SLMAP3 can negatively regulate the Hippo signaling pathway by interacting with Hippo activating kinase, MST1/2, and cause a dephosphorylation cascade via the striatin interacting phosphatase and kinases (STRIPAK) complex to modulate the transcriptional coactivators YAP/TAZ, to boost proliferation and repress apoptosis [17-20].

Our aim was to discern the role of SLMAP3 during embryonic development by investigating a previously generated global knockout (KO) of SLMAP3 by crossing flox-SLMAP mouse with the CMV-cre mouse to nullify SLMAP3 during embryogenesis [21-23]. We report here that the loss of SLMAP3 results in embryonic lethality with some embryos presenting with a neural tube defect, craniorachischisis. We found no evidence that loss of SLMAP3 impacts Hippo signaling but rather plays a pivotal role in regulating planar cell polarity (PCP) and ABP for neurulation. The data points to a unique role for SLMAP3 in neural tube development by regulating convergent extension through novel mechanisms that influence dynamics of organelles such as the centrosome and Golgi.

5.2 Materials and Methods:

5.2.1 Generating and genotyping the SLMAP3 knockout mice

The procedure to create flox-SLMAP mouse and mechanism that generates knockout is well described in our previous publication [21, 23]. In this study, we crossed flox-SLMAP mice with CMV-cre mice to create a heterozygous flox-SLMAP mouse that knockdown (KD) SLMAP3 expression we termed "cre-dependant" breeding. As CMV-cre will cleave SLMAP gene at exon 3 in every cell type, we crossed KD-SLMAP mice with Wt mice, to pass on the cleaved-SLMAP gene but not cre. Therefore, for "cre-independent" breeding, crossing male and female mice harboring one copy of cleaved SLMAP, will generate mice that are homozygous for cleaved-SLMAP resulting in our knockout (KO) animals (**Figure 1A**). These mice were genotyped by extracting genomic DNA from ear clips by boiling for 10 minute at 95ºC in 180µL of 50mM NaOH per ear. DNA solution was then neutralized using 20µL of 1M Tris-Cl pH 8.0. SLMAP KO/KD mice were identified by polymerase chain reaction (PCR) using DreamTaq Green PCR Master Mix 2x (Thermoscientific) for the PCR mix. Forward F2 primer (5`-CCT GGA GAG CCT CCG TGT GAG T- 3'), reverse R2 primer (5`-GTC AAC TGC CCA ATG TAC AGA AAT AGT AAG -3`) targeted loxP site 1 and reverse R1 primer (5'-GGA GAG ACT ATC ACA GCC ACA GGA-3') on flox-SLMAP gene **(Figure 1B)**. Primers F2/R2 will identify loxP1 sites, absence of which will suggest cleaved SLMAP3. This is confirmed by primers F2/R1 as cleaved SLMAP gene will produce an amplicon size at 400bp whereas Wt-SLMAP will produce an amplicon size of 1400bp (**Figure 1C**). PCRs were visualized by Red Safe (Sigma) staining on a 1% agarose gel.

Pregnant mothers were plug checked and the morning of first plug was designated as E0.5. Mothers were anesthetized and embryos were dissected away at desired stage in ice-cold 1x PBS. Embryos were either fixed in 10% neutral buffered formalin or tissues (brain, whole embryo) were snap-frozen for protein or transcript analysis and/or cultured for cell analysis.

Mice were handled in accordance with the guidelines set by Canadian Council on Animal Care, Guide to the Care and Use of Experimental Animals, 2 vols. (Ottawa, Ont.: CCAC, 1980-1993) and

Animals for Research Act, R.S.O. 1990, c.A. 22. All animal protocols and procedures were approved by the Animal Care Committee of the University of Ottawa.

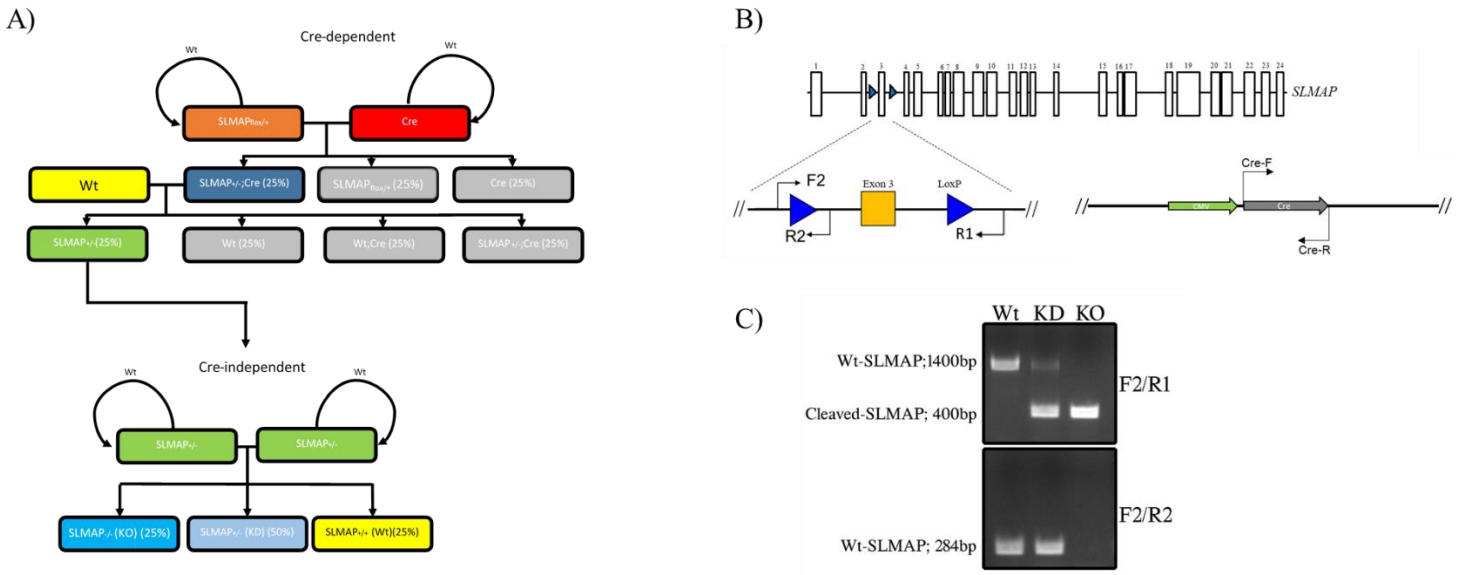

Figure 1. *Breeding diagram to generate global knockout of SLMAP in mice.* A. During the cre-dependent phase, flox-SLMAP mice are crossed with CMV-cre mice to generate offspring which contains one wildtype/one cleaved *SLMAP* allele and *cre* ($SLMAP^{+/-}$:Cre). Backcrossing with a wildtype mouse will produce an animal that contains one cleaved *SLMAP* allele without cre ($SLMAP^{+/-}$), thus beginning the cre-independent breeding phase. Breeding $SLMAP^{+/-}$ together, will generate experimental animals, wildtype Wt ($SLMAP^{+/+}$), knockdown KD ($SLMAP^{+/-}$), and knockout KO ($SLMAP^{-/-}$). B) Schematic representing flox-SLMAP gene, exon 3 flanked with LoxP sites. Primers F2 and R2 target sequences upstream and downstream of LoxP site 1, whereas R1 targets sequence downstream of LoxP site 2. C) PCR amplicons run on separate lanes on a 1% gel to identify amplicon sizes produced from primers F2/R1 pairing and F2/R2 pairing. These will identify Wt, KD, or KO experimental animals.

5.2.2 Histological and Immunofluorescent analysis

We paraffin-embedded the fixed embryos and transversally sectioned them targeting the hindbrain-cervical boundary to examine neural tube closure at this site. Paraffin-embedded slides were processed through well-established protocols for rehydration and citrate buffer antigen retrieval [24]. Sectioned slides were stained with Hematoxylin and eosin stain to identify cells (pink) and nuclei (purple blue) visualizing neural tube and neighboring tissues.

For immunofluorescence of histological sections, rehydrated slides were subjected to 1 hour of 5% BSA in PBS-T (1x PBS, 0.01% Triton X-100) of blocking. After rinsing with PBS, we diluted antibodies according to Table 1 in blocking solution and incubated them overnight at 4ºC. Samples were then washed 5x for 5 mins with PBS and then secondary Alexa-555 (Thermo Fisher Scientific, USA) or Alexa 647 (Thermo Fisher Scientific, USA) were incubated for 1 hour at room temperature. We used VectaShield Plus DAPI (MJS Biolynx, CA) mounting medium with 1.5mm coverslips (Fisher Scientific, USA) sealed with nail polish and imaged when completely dried.

For immunofluorescent imaging of cells, we placed autoclaved circular 1.5 mm coverslips (VWR, USA) in 12-well plates and incubated with poly-l-lysine (MilliporeSigma, USA) according to manufacturer protocol. The poly-l-lysine solution was rinsed with 1x PBS and airdried in hood for 30 minutes before cells were plated onto the wells containing the coverslips. After attachment, cells were rinsed gently with 1x PBS before adding 4% paraformaldehyde for 20 minutes. After washing 3 times for 5 mins with 1x PBS, we blocked and permeabilized cells for 20 minutes with PBS-T (1% BSA, 1x PBS, 0.3% Triton X-100). After 3 more washes for 5 minutes each with 1x PBS, we added primary antibody overnight at 4ºC. Samples were thoroughly washed 5 times for 5 minutes with 1x PBS then we added either secondary Alexa-555 (Thermo Fisher Scientific, Waltham, MA, USA) or Alexa 647 (Thermo Fisher Scientific, Waltham, MA, USA) for 1 hour at room temperature. We used VectaShield Plus DAPI (MJS Biolynx, CA) mounting medium on coverslips, placing them face down on slides, and sealed them with nail polish. Images from the dried slides were captured on Zeiss AxioImager M2 and analyzed using ImageJ and Cell Profiler.

Immunofluorescent imaging of transverse section of E8.5 and E9.5 neural tube experiments were performed by staining sections of 3 Wt and 2 KO embryo for each protein. For apical and basal proteins, measurements were taken the respective domains and comparing to subdomain. Golgi size was measured by measuring the length of Golgi apparatus extension. All measurements assessed mean fluorescent intensity from each embryo and was repeated up to 4 times. The standard deviation represents the variance between embryos and n represents the number of embryos analyzed.

For cell size and Golgi apparatus analysis, we utilized the Cell Profiler software using a published pipeline [25].

5.2.3 Protein isolation and SDS-Page

Whole embryo or e12.5 brains frozen at −80 °C were washed with ice-cold 1× phosphate buffered saline (PBS) and homogenized using a Fisher handheld Maximizer homogenizer (Thermo Fisher Scientific) in ice-cold lysis buffer (1 mM ethylene glycol tetraacetic acid (EGTA), 1 mM ethylenediaminetetraacetic (EDTA), 20 mM Tris base, 1% Triton, 150 mM sodium chloride, 1× complete mini EDTA-free protease inhibitor cocktail (Roche), and 1× PhosSTOP (Roche). The suspension was centrifuged for 15 min at 12,000× g to separate the proteins from the cell debris. The supernatant containing the protein lysate was collected and stored at −80 °C. Approximately 8-10 µg of protein lysate was loaded in each well of a 5–15% SDS-PAGE gel. The gels were transferred overnight on a polyvinylidene fluoride (PVDF) membrane (Bio-Rad) in a buffer containing 25 mM Tris, 190 mM Glycine, and 20% methanol. All membranes were blocked at room temperature for 1 h in Tris-buffered saline (TBST) containing 1 M Tris, 290 mM NaCl, 0.1% Tween 20, pH 7.4, and 5% nonfat dry milk. Primary antibodies (listed in Table 1) were incubated overnight at 4 °C with 5% bovine serum albumin (BSA). Membranes were washed 5 times for 5 min each in TBST prior to adding the appropriate horseradish peroxidase-labeled secondary antibody (Jackson ImmunoResearch) in a 1:10,000 dilution in TBST with 5% nonfat dry milk. Membranes were shaken slowly at room temperature for 1 h while incubating with secondary antibody, followed by 5 washes for 5 min each with TBST. Membranes were treated with a BioRad western blotting kit (Bio-Rad, Hercules, CA, USA) and developed using

ChemiDoc machines (Bio-Rad, Hercules, CA, USA). Bands were quantified by densitometry using Image Lab software v.6.0.0 (Bio-Rad). Membranes were stripped (25 mM glycine, 10% SDS, and pH 2.2 in dH2O) and reprobed with different antibodies. When using stain-free technology, stain-free gels (Bio-Rad) and low-fluorescence PVDF membranes (Bio-Rad) were used.

5.2.4 Primary neuroepithelial cell culture

For primary neuroepithelial cell culture, embryos at E9.5-10.5 were harvested from plug-checked dams and rinsed in ice cold 1x PBS before hindbrain-spinal neural tube was harvested from embryos by shearing the neighboring tissues away by using forceps [26]. The rest of the body was used for PCR genotyping. Isolated neural tube tissues were placed in 300µL 1x Trypsin-LE (ThermoFisher) for 5 minutes at 37°C and pipetted up and down to dissociate neuroepithelial cells. This procedure was repeated up to 3 times for complete breakdown of the neural tube. Cells in Trypsin-LE were inactivated with equal volume of serum-free culture medium and centrifuged at 0.3g for 5 mins to pellet cells. Cells were resuspended with serum-free medium and placed on prepared 1.5mm coverslips for 24-48 hours before proceeding to immunofluorescent imaging (section 2.2). The serum-free culture medium was made following this manuscript [26].

5.2.5 RNA-sequencing

Our RNA-seq methodology was previously described and GEO series accession was previously deposited in NCBI's Gene Expression Omnibus and are accessible through GEO Series accession number: GSE230748 [23, 27]. Briefly, total RNA was isolated from 4 WT and 3 KO E11.5 embryos and submitted to the StemCore Laboratories Genomics Core Facility at University of Ottawa for RNA-sequencing. RNA-seq post-processing and differential expression analysis was prepared by the Ottawa Bioinformatics Core Facility. RNA-sequencing data was uploaded to Galaxy web platform where the data was displayed with heat maps [28].

5.2.6 Immunoprecipitation-Mass Spectroscopy (IP-MS)

Our IP-MS methodology was previously described, and the mass spectrometry proteomics data were previously deposited to the ProteomeXchange Consortium via the PRIDE partner repository with the dataset identifier PXD041687 and 10.6019/PXD041687 [23]. Briefly, IP of SLMAP3 and anti-IgG was performed on E12.5 mouse brain wildtype lysates. The resulting samples were submitted to Montreal Clinical Research Institute for MS.

5.2.7 Creation of short-hairpin RNA Lentivirus for depletion of SLMAP3

To stably deplete SLMAP3 expression in NE-4-C cells, we designed two shRNAs targeting sequences from exon 22 (Ensembl reference transcript ENSMUST00000139075.8). The targeting sequences are 5'-GCAATCAATCACAGATGAGCTCAAA and 5`-GCTGCTGCGAGAGAAAGGAAATAAT, which were called S4 and S5, respectively. The control scramble target sequence is 5'-AGGATAAGCGTCAACGAATAGGTGA, referred to as SC, and was generated by inputting the S5 plasmid sequence into GenScript Sequence Scramble tool [29].The shRNAs were designed in a lentivirus vector with the VectorBuilder design tool [30] VectorBuilder cloned and delivered the plasmids in Escherichia coli (VB UltraStable). Plasmids were isolated via PureYield Plasmid Midprep System protocol (Promega Cooperation, Technical Manual #TM253) and transfected in Lenti-X 293T cells with the packing and envelope plasmids psPAX2 [31] and pMD2.G [32] via polyethyleneimine (PEI), following a established protocol [33]. The supernatants of Lenti-X 293T cells containing lentiviruses were

harvested 48 and 72 hours after transfection and filtered with 0.45 µm sterile syringe filter. The viral particles were concentrated via Lenti-X-Concentrator (Clontech, catalog number PT4421-2) and the titer was quantified with the PCR Lentivirus Titer Kit (abm, catalog number LV900).

5.2.8 Maintenance, transduction, and differentiation of NE-4C cells

NE-4C cells (ATCC #CRL-2925) were grown at 37°C and 5% CO2 in 1x Eagle's minimum essential medium (Wisent) supplemented with 10% FBS (Wisent), 1x Antibiotic-Antimycotic (ThermoFisher) and 2mM L-Glutamine (Invitrogen). The NE-4C cell line has been tested in the lab for mycoplasma contamination and tested negative in all instances. SLMAP depletion was mediated by shRNAs in a lentivirus vector. The reverse transduction was preformed following Addgene protocol [34] but using 25,000 cells per cm^2 of growth area and considering a multiplicity of infection (MOI) of 200. Selection for successfully transduced cells was carried out by treatment of 3 µg/mL puromycin for 4 days. To induce differentiation, transduced NE-4C cells we incubated with 10µm retinoic acid (Millipore Sigma) for >96hrs to generate radial glial and astrocytes, aggregating to form neurospheres [35, 36]. Retinoic acid storage, handling and dilutions were followed through manufacturers protocol.

5.2.9 Real-Time Quantitative PCR

Total mRNA from NE-4C cells was extracted using the RNeasy Fibrous Tissue Kit (Qiagen). The concentration and purity of the obtained mRNA was determined by measurement of 260/230 nm absorbance ratio and 280/260 absorbance ratio using NanoDrop 2000 UV-Vis Spectrophotometer (Thermo Fisher Scientific). RNA was used as a template to generate cDNA using SuperScript II reverse transcription protocol following the manufacturer's guidelines (Invitrogen). RT-qPCR was carried out using the BioRad CFX96 system and Luna Universal qPCR mater mix according to manufacturer instructions. Equal amounts of cDNA were utilized in real-time PCR using primers for SLMAP3 cDNA (SLPN-F: 5'-GGA ATT CGA TGC CGT CAG CCT TGG C -3', 558-R: 5'-TTG CTC GTC TTG TGA TCA AAC CAG -3'), Pax6 (Pax6-F: 5'-CTGAGGAACCAGAGAAGACAGG -3', Pax6-R: 5'-CATGGAACCTGATGTGAAGGAGG -3'), Sox2 (Sox2-F: 5'-AACGGCAGCTACAGCATGATGC -3',

Sox-R: 5'-CGAGCTGGTCATGGAGTTGTAC-3') and Actin loading control (F: 5'-ACCCAGGCATTGCTGACAGGAT-3', R: 5'-CGCAGCTCAGTAACAGTCCGC-3'). Fold change was calculated using the ΔΔCt method. The primers were validated by serial dilution curves and PCR product size.

5.2.10 Image generation

Models utilized in **Figure 6A**, **Figure 8A**, **Figure 9A**, **Figure 10A**, **Figure 11** were created with BioRender.com.

5.2.11 Statistical Analyses

The statistical analysis was performed using GraphPad Prism software version 8 for Windows (GraphPad Software). All comparisons between wildtype or knockout groups were analyzed using two-tailed Student's T-test. To analyze three groups, (Wt vs KD vs KO) we utilized ANOVA one-way to evaluate significance with post-hoc Tukey test. All values and points on graphs represent mean values obtained from multiple experiments. All error bars presented in graphs are represented using the standard error of the mean. All sample size values (n) represent replicates.

Table 1. List of antibodies used in this study. All antibodies used in this study are listed with the corresponding distributor, catalog number, and dilution used for western blot.

Antibody	Manufacturer	Application	Dilution
SLMAP	Novus Biologicals (NBP1-81397)	IF, WB	1:1000
Striatin-1	BD Transduction Laboratories (610838)		1:1000
STRIP1	Bethyl Lab (A304-644a-m)		1:1000
PP2A-A α subunit	Millipore Sigma (07-250)		1:600
PP2A-C α/β subunit	Santa Cruz Biotechnology (sc-80665)		1:1000
Phospho-YAP (S127)	Cell Signaling Technology (13008S)		1:1000
YAP	Cell Signaling Technology (14074S)		1:1000
Phospho-MST1/2 (T183/180)	Cell Signaling Technology (49332S)		1:1000
KRS2(MST1)	Santa Cruz Biotechnology (sc-515051)		1:1000
DVL1	ProteinTech (27384-1-AP)		1:1000
DVL2	Abcam (ab22616)		1:1000
DVL3	Cell Signaling (CS 3218)		1:1000
Phospho-ROCK2 (S1366)	GeneTex (GTX122651)		1:1000
ROCK2	Santa Cruz Biotechnology (sc-398519)		1:1000
Phospho-Cofilin (S3)	Cell Signaling (3313T)		1:1000
Cofilin	Cell Signaling (5175)		1:1000
Phospho-JNK1/2 (T183/Tyr185)	Cell Signaling (9251)		1:1000
JNK1/2	Cell Signaling (9252)		1:1000
PKC zeta	Santa Cruz Biotechnology (sc-17781)		1:1000
Nestin	Millipore (MAB353)		1:1000
N-cadherin	ProteinTech (22018-1-AP)		1:1000
SCRIB (Rbt)	Proteintech (27083-1-AP)		1:1000
SCRIB (M)	Santa Cruz Biotechnology (sc-374139)		1:1000
Pericentrin	Covance/Biolegend (PRB-432C)		1:1000
GM130	BD Biosciences (610822)		1:1000
ZO-1	ProteinTech (21773-1-AP)		1:1000
Sox2	Abcam (ab97959)		1:100
Phalloidin	CF®488A Biotium (89427-132)		1:40
Alexa-555	Rabbit Secondary IgG Fluorescent marker		1/300
Alexa-647	Mouse Secondary IgG Fluorescent marker		1/300

5.3 Results:

5.3.1 Loss of SLMAP3 is embryonic lethal in mice

We developed a strategy for global SLMAP3 knockout (KO) in mice by pairing SLMAP-flox mice and crossing with CMV-cre mice to excise exon 3 which specifically ablated the SLMAP3 isoform expression (91 kDa) but not the expression of SLMAP1 (~35KDa) and SLMAP2 (~45KDa) as indicated in Western blots of E11.5 embryonic lysates (**Figure 2A).** At postnatal day (P)0, SLMAP3-null pups were stillborn, displaying signs of late embryonic lethality and developmental deformities (**Figure 2B**). Microscopic measurements indicated that the SLMAP3-KO embryos were significantly smaller, displayed facial retrusion, and a truncated tail when compared to KD or Wt littermates (**Figure 2B**). We have recently reported similar data regarding the reduction in body weight due to SLMAP3 loss in embryos [23]. Further, 1 out of 3 of SLMAP3-null embryos also exhibited the fatal NTD, craniorachischisis (**Figure 2C**). Craniorachischisis presents with observable open spinal cord and brain extrusion in affected patients [37]

Since SLMAP3 was shown to negatively regulate Hippo signaling pathway via the STRIPAK complex, we investigated if SLMAP3 loss could impact Hippo and account for any observed phenotypes (**Figure 2D**). Western blot analysis on E11.5 whole embryo lysates indicated no significant differences in expression of STRIPAK components (Striatin-1, STRIP1, PP2A/C) or activity in the Hippo activating kinase, MST1/2 or downstream target of Hippo signaling, YAP (**Figure 2E**). RNA-Sequencing of Wt and KO E11.5 embryos and analysis including Euclidean clustering and visualized Heat maps indicated no changes in Hippo related gene expression in the SLMAP3-deficient embryos (**Figure 2F**). It is also notable that major transcriptional programs that regulate embryogenesis such as Sonic Hedgehog, Wnt, or BMP pathways [38] indicated no significant changes to target genes (**Supplemental Table 1**).

During early neurulation at E8.5 SLMAP3-KO embryos were significantly shorter (-25%, $p<0.05$) and the caudal neural plate (posterior neuropore) was significantly wider (31%, $p<0.05$) than Wt embryos, a change that was present in all developmental stages (**Figure 3A**). As craniorachischisis was the most common NTD phenotype noted in the SLMAP3-KO embryos, we transversally sectioned Wt

and SLMAP3-KO embryos at E8.5 and E9.5, to examine hindbrain-cervical boundary (Closure site 1), the boundary closure site where craniorachischisis defects can occur. Immunofluorescent staining of E9.5 neural tube sections with anti-SLMAP indicated a complete loss of SLMAP in KO when compared to Wt, consistent with Western blot data indicating that only SLMAP3 is expressed during neurulation is completely ablated (**Figure 3B**). Neural tubes were displayed in an open conformation and found to be underdeveloped at E8.5 and E9.5 in SLMAP3-KO when neurulation was complete in Wt (**Figure 3C**). Neurulation is regulated by a tissue morphing process known as convergent extension, which narrows tissues at the medial-lateral axis whilst elongating them at the anterior-posterior axis [39]. To determine if SLMAP3-KO embryos display convergent extension defects we analyzed neural plate sections at E8.5 and E9.5 and examined neural plate thickness and neural grove aperture. The loss of SLMAP3 caused significantly thinner neural plates at E8.5 (-27.42%, $p<0.05$) and E9.5 (-13.38%, $p<0.05$) and significantly wider neural grove aperture (772%, $p<0.05$) in e9.5 neural tubes when compared to Wt (**Figure 3D**). The decreased length and broader width of SLMAP-KO embryos coupled with thinner and wider neural plates is consistent with convergent extension deficits [40, 41]. RNA-Seq analysis indicated that target genes commonly associated with neurulation and craniorachischisis were not significantly altered by SLMAP3 loss, implying that NTD phenotype was not occurring via classical mechanisms and suggest a unique role for SLMAP3 during neurulation. (**Figure 3E**).

5.3.2 Loss of SLMAP3 perturbs planar cell polarity signaling

Planar cell polarity (PCP) signaling provides directional cue to multicellular tissues, which affects cell polarity, orientation, and migration essential for convergent extension [42]. The core PCP proteins are asymmetrically distributed throughout the cell, with Van-Gogh Like-protein 1/2 (VANGL1/2) and Frizzled-3/6 protein (Fzd3/6) on opposing ends respectively (Figure 4A). They coordinate a multidirectional signal to cells simultaneously via antagonizing effects of the disheveled isoforms -1, -2, -3 (DVL1, DVL2, DVL3) and Prickle proteins, resulting in cytoskeleton rearrangement by modulating cofilin-1 and JNK1/2 activity (**Figure 4A**) [43]. Therefore, PCP can propagate signal to adjacent cells via VANGL1/2 to FZD3/6 establishing planar polarity throughout the entire tissue [44].

Western blot analysis of E12.5 brain lysates from SLMAP3-KO embryos (**Figure 4B**) indicated there was a significant change in protein expression of DVL3 (-56%, $p<0.05$) and DVL2 (108%, $p<0.05$) compared to wildtype, without any changes in DVL1 (Figure 4C). Further, phospho-to-total ratios of the downstream targets of PCP, ROCK2 (-25, $p<0.05$), cofilin (40%, $p<0.05$) and JNK1/2 (-52%, $p<0.05$) were also significantly altered in SLMAP3-null brain lysates (**Figure 4C**). The expression of other PCP components such as Scribble (Scrib) or VANGL1/2 were not significantly altered (**Supplemental Figure 1A).** To identify if changes in DVL expression could impact canonical Wnt signaling we investigated the activity and expression β-catenin, but no significant changes in their phosphorylation were detected (**Supplemental Figure 1B**). The data suggests that SLMAP3 specifically regulates PCP signaling in brain tissues that descended from the neural tube may affect neurulation. PCP signaling can be affected by aberrant gene expression of PCP components [45], however given that SLMAP3 deficiency had no effect on genes that encode components of PCP (**Figure 4D**), SLMAP3 effect on NT development appear to be mediated via posttranscriptional mechanisms.

5.3.3 Loss of SLMAP3 impacts actin distribution and adherens junctions

Since the activity of cofilin-1 (actin severing protein) was dysregulated in SLMAP3-KO brain, we examined if this could impact actin filament formation at the apical region of the neural tube, as apical constriction of actin in NEP cells is necessary to generate forces that bend the developing NT [4]. Immunofluorescence microscopy on E8.5 & E9.5 Wt and KO embryos with phalloidin, indicated a significant decrease of actin at apical region in E8.5 (-90%, $p<0.05$) and E9.5 (-24%, $p<0.05$) due to SLMAP3 loss (**Figure 5A**).

Because apical actin is important to identify ABP of epithelia we examined if other components involved in this process were mislocalized [46]. Epithelial tissues require ABP to regulate tissue integrity and organization with proper polarity complexes. The atypical protein kinase c zeta (PKCζ) localizes to apical side of epithelial tissues, was found to redistribute to subapical regions in SLMAP3-KO E9.5 neural tubes with a significant (-46%, $p<0.05$) decrease in the apical/subapical distribution ratio (**Figure 5B**). Next, we determined if basal regions are affected by examining Nestin, a neurofilament that localizes to basal region within neuroepithelium and its basal/subbasal distribution ratio was significantly (-22, $p<0.05$) lower in E9.5 KO neural tubes (**Figure 5B**).

The loss of ABP could dysregulate the mediolateral cell-cell contact in epithelial cells by affecting the stability and localization of adherens junctions (AJs), as the proper localization of junctions has conventionally been used to assess the cell polarity [47]. AJs such as cadherins mediate epithelial cell-cell interaction and bind actin filaments at apical ends to aide in apical constriction which is necessary for bending epithelial tissues [48]. During neurulation, the neural plate can express varying cadherins at different developmental stages [49]. At E7.5 it expresses E-cadherin (E-cad), at E8.5 the neural tube will express N-cadherin (N-cad) and by E9.5 N-cad is the predominant cadherin expressed in fused neural tube [50]. The localization of E-cad and N-cad in Wt and KO neural tube sections indicated a significant decrease of N-cad junction intensity at apical regions in E8.5 (-50%, $p<0.05$) and E9.5 (-65%, $p<0.05$) SLMAP3-KO neural tubes and decrease in E-cad mediolateral junction intensity at apical regions in E8.5 (-51.4%, $p<0.05$) and E9.5 (-59.6, $p<0.05$) SLMAP3-KO neural tubes (**Figure 5C**). The transition of

NEPCs expressing E-cad to N-cad and E-cad/N-cad ratio is essential for proper neurulation [51], and Western blot analysis of E12.5 brain lysates revealed that E-cad was significantly upregulated (252%, $p<0.05$) whereas N-cad expression remained stable (-21%, $p=0.57$) in SLMAP3-KO (**Figure 5D**). These data indicate that SLMAP3 regulates ABP within the neuroepithelial tissue for proper distribution of PCP components.

5.3.4 SLMAP3 interacts with centrosomal and Golgi proteins to regulate apical-basal polarity

Given the impact of SLMAP3 loss on neurulation, we sought to evaluate unique SLMAP3 interactors that we performed previously via immunoprecipitation-mass spectroscopy (IP-MS) using anti-SLMAP on E12.5 mouse brains lysates to examine SLMAP3 specific interactions [23]. We observed unique interactions as seen in a protein-protein interaction network in Figure 6A. Interactions with centrosomal proteins (AKAP9, Pericentrin, Cep170), Golgi (Golgb1, Golga3), microtubule transport proteins (Kif5c, Klc1/2/4) and the polarity protein Scrib were notable. Further, GO analysis [52] of highest peptide discovery counts revealed that SLMAP3 binds to numerous facets of cytoskeletal architecture; actin, tubulin and intermediate filaments (**Figure 6B**). The STRIPAK components (striatin-1, PP2A and MAP4K4) were also present in complex with SLMAP3 as described previously [17]. IP of embryonic E12.5 mouse brain lysates with anti-SLMAP and Western blotting indicated the presence of STRN1, Scrib and Nestin in these samples consistent with the MS data (Figure 6C).

The centrosome and Golgi apparatus play a unique role in mediating ABP in epithelial tissues. The centrosome localizes to apical regions, to aid in the transport and migration of cells by nucleating microtubules [53]. The dynamics of Golgi apparatus is important in maintaining polarity, as it dictates the directionality of membrane trafficking and cellular materials [5]. Golgi can reside in apical regions in epithelial cells however during cell migration or delamination, the Golgi apparatus will migrate to basal domains to aid in transport of proteins and organelle movement generating a defined polarity axis [5]. Given the new interactors of SLMAP3 we examined any impact of SLMAP3 deficiency on their localization by immunofluorescent microscopy with centrosomal marker, pericentrin and Golgi marker,

GM130 in E8.5/E9.5 Wt and KO neural tube sections (**Figure 7A**). At E8.5, we observed significantly weaker pericentrin (-72.9%, $p<0.05$) and GM130 (-50.9%, $p<0.05$) staining at the apical region in SLMAP3- KO neural tubes compared to Wt (**Figure 7B**). At E9.5, we similarly observed significantly weaker intensity of pericentrin (-21.7%, $p<0.05$) and GM130 (-70.4%, $p<0.05$) at apical regions in SLMAP3-KO neural tube compared to Wt (**Figure 7B**). The Golgi apparatus appears elongated in Wt NT but was fragmented in SLMAP3-KO with decrease in size in E8.5 (-83.2%, $p<0.05$) and E9.5 (-76.4%, $p<0.05$) (**Figure 7B**).

Scrib regulates ABP and PCP [54] and since SLMAP is associated with Scrib we examined its localization as its expression was not significantly altered due to SLMAP3 deficiency. We observed that in E9.5 neural tubes Scrib was localized at basolateral membrane of NEP cells, whereas in SLMAP3 -KO its localization was reduced (-43.9%, $p<0.05$) and became more dispersed (**Figure 7C**).

To determine if the loss of SLMAP3 would lead to changes in proliferation of NEPCs we performed immunofluorescence with phosphorylated histone-3 (pH3) on E8.5 and E9.5 neural tube sections (**Supplemental Figure 2**) and there were no significant differences in number of pH3-positive NEPCs in the KO neural tube compared to Wt.

5.3.5 NEPCs with SLMAP3-KO display decreased cell size, mislocalization of pericentrin and Golgi fragmentation

We examined the precise distribution of centrosome and Golgi apparatus within NEP cells isolated from Wt and SLMAP3-KO neural tube tissues from E10.5 embryos, cultured in media for 2-3 days and plated onto coverslips (**Figure 8A**). For each immunofluorescence experiment, staining was performed with phalloidin and Nestin to distinguish total cells from NEPCs respectively (**Figure 8B**). Immunofluorescent analysis of phalloidin in nestin-positive cells indicated a significant decrease in cell area (-27%, $p<0.05$), perimeter size (-24%, $p<0.05$), major axis (-23%, $p<0.05$) and minor axis (-39%, $p<0.05$) of the SLMAP3-KO NEPCs compared to Wt (**Figure 8B**). In Wt NEPCs centrosome (pericentrin) appeared adjacent to the nucleus and Golgi (GM130) was tightly bound to centrosomes (**Figure 8C**). However, in SLMAP3-KO NEPCs the centrosome fluorescent signal was significantly weaker (-79%, $p<0.05$) compared to Wt (Figure 8C). Further, the Golgi apparatus had become significantly dispersed, with decreased Golgi compactness (-33%, $p<0.05$) and increased fragmentation (107%, $p<0.05$) in SLMAP3-KO NEPCs.

5.3.6 Knockdown of SLMAP3 in NE-4C cells affects localization of Scrib, AJs and TJs

Due to difficulties with generating SLMAP3-KO embryos and inconsistent isolation of primary NEPCs, we utilized an immortalized mouse neuroepithelial cell line, NE-4C and shRNA to knock down SLMAP3. Two shRNA plasmids (sh-S4, sh-S5), designed to target the SLMAP mRNA at exon 22, **(Figure 9A)** or scramble control (sh-Sc) were packaged into lentivirus and transduced into NE-4C cells (**Figure 9A**). Western blot analysis indicated that were was a significant knockdown of SLMAP3 (91kDa) in S4 (-91.26%, $p<0.05$) and S5 (-92.62%, $p<0.05$) cells relative to the Sc control cells (**Figure 9B**).

Scribble location at junctions was significantly reduced as indicated by immunofluorescence which was now more dispersed throughout the cytosol in S4 and S5 NE-4C cells compared to Sc (**Figure 9B**). Further, immunofluorescence of N-cad in NE-4C cells was significantly downregulated at junctional sites by S4 (-71.9%, $\rho<0.05$) and S5 (-74.6%, $\rho<0.05$) when compared to Sc (**Figure 9C**). Further, we examined the localization of tight junctions (TJs) interconnected to AJs to regulate cell-cell adhesion and barrier function by associating with the actin cytoskeleton to aid in apical constriction of neural tube [55].

The localization of TJ, ZO-1 was significantly decreased at junctional sites by S4 (-61.9%, $\rho<0.05$) and S5 (-19.4%, $\rho<0.05$) when compared with Sc transduced cells (**Figure 9D**) and was significantly more retained in the cytoplasm in S4 (76.9%, $\rho<0.05$) and S5 (25.6%, $\rho<0.05$) when compared with Sc (**Figure 9D**). SLMAP3 deficiency leads to mislocalization of Scrib, AJ and TJ in NE-4C cells implicating a perturbed ABP.

5.3.7 SLMAP3 impacts differentiation of NE-4C cells

NE-4C cells can be differentiated with 10 µm retinoic acid to form progenitor astrocytes or radial glial cells with impact on expression of the molecular markers Sox2 and Pax6 (**Figure 10A**). Sox2 is involved in the regulation of neural stem cell proliferation, self-renewal, and fate determination during neurogenesis [56]. It plays a critical role in maintaining the undifferentiated state of neural stem cells and promoting their differentiation into neurons [56]. Pax6 plays a critical role in neurogenesis by controlling progenitor cell identity, neuronal fate determination, and cortical layer formation [57]. The data indicated that during differentiation in both S4 and S5 transduced cells there was a significantly lower expression of transcript for Sox2 whilst only S5 showed a reduced expression of Pax6 compared to Sc (**Figure 10B**). Immunofluorescence of Sox2 in differentiated, transduced NE-4C cells indicated significantly fewer Sox2+cells in the S4 (-32.6%, $\rho<0.05$) and S5 (-68.7%, $\rho<0.05$) compared to Sc (Figure 10C). Further, the Sox2+ cells would aggregate into neurospheres which were significantly smaller in the S4 (-69%, $\rho<0.05$) and S5(53%, $\rho<0.05$) NE-4C cells compared to Sc (**Figure 10C**).

Since centrosome and Golgi function is important for neuronal differentiation [58], we assessed if deficiency of SLMAP3 could influence the positioning of centrosome or Golgi in differentiating NE-4C cells. Immunofluorescent analysis with pericentrin and GM130 indicates that centrosome localization was not significantly affected however a significant change in Golgi area in S4 (-61%, $\rho<0.05$) and S5(-0.57%, $\rho<0.05$and Golgi compactness in S4 (-12.6, $\rho<0.05$) and S5 (-31.2%, $\rho<0.05$) transduced cells was evident (**Figure 10D**). Golgi fragmentation or impaired Golgi function can impact neuronal

differentiation [59] and the data here points a novel role for SLMAP3 in maintaining normal Golgi structure in neuronal differentiation and NT development as observed in our isolated NEPCs.

5.4 Discussion:

Our data here defines a critical role of SLMAP3 in embryonic development, specifically in developing the neural tube since its loss results in failure to close leading to craniorachischisis. Our data shows that lack of SLMAP3 exhibited changes in centrosomal and Golgi dynamics, perturbing ABP and PCP signaling. NT formation is critically dependent on proper PCP signaling and ABP as perturbations can cause NTDs [60, 61]. The embryonic knockout of SLMAP3 isoform only resulted in embryonic lethality, exemplified by small size, short limbs, faulty tail growth, and craniofacial defects shown here and previously [23]. The embryonic expression of the other SLMAP isoforms remained unchanged and it is notable that tissues such as the NT and brain express only the SLMAP3 isoform and thus were severely compromised during development. We did not observe any defects in embryonic cardiac development like what we previously reported in the conditional KO of the SLMAP3 isoform in the postnatal mouse heart [21]. This is most likely due to the abundant expression of other SLMAP isoforms in cardiac tissue which potentially compensate for the loss of SLMAP3 [21]. While SLMAP3 has recently been linked to Hippo signaling [62, 63], we did not find any impact on this pathway at the phenotypic or molecular level in embryos or tissue null for this SLMAP3 isoform. It appears that SLMAP3 mediates organogenesis through unique mechanisms in cell and tissue specific manner as we recently reported in muscle development [23].

NTDs represent some of the most common birth defects globally, approximately affecting 1:1000 births [3, 64]. Many of these defects are linked to folate metabolism and genetic factors however a significant number of cases remain idiopathic, particularly craniorachischisis [65]. Most observed cases of NTD in SLMAP3-KO mice manifested as craniorachischisis, while the occurrence of spina bifidia and exencephaly was also evident in embryos. SLMAP3 may be a novel biomarker for NTDs particularly

craniorachischisis consistent with phenotypes observed with ablation or suppression of PCP components [66-68].

PCP signaling pathway is essential for convergent extension and SLMAP3-KO embryos display defects with reduced length to width ratios and significantly wider neural plates in E8.5 and E9.5 embryos. SLMAP3-KO in neural tube descendent tissues, brain, revealed substantial changes in the expression of PCP signaling transducers, DVL2 and DVL3 as well as the downstream targets such as ROCK2, Cofilin, and JNK, which are all associated with NTDs [69]. The deficiency in DVL2 and DVL3 has been reported to result in NTDs [70] our data suggests that DVL2 and DVL3 are dysregulated and could contribute to the observed phenotypes. The SLMAP3 mediated regulation in the DVL2/3 protein levels most likely occurs through posttranscriptional mechanisms [71] since there was no change in their gene expression.

The dysregulation of cofilin due to SLMAP3 loss led us to investigate actin within the neural tube, as it is pivotal in facilitating apical constriction, essential for convergent extension and neurulation [72, 73]. Ablating actin cytoskeletal regulators can causes incomplete neurulation at cranial and spinal regions causing NTDs such as exencephaly, anencephaly, spina bifidia [74-76]. Studies have shown that aberrating expression of PCP components such Scrib, Vangl2, DVLs can influence activity of actin cytoskeletal regulators such as cofilin and ROCK to negatively impact convergent extension and apical constriction resulting in craniorachischisis [77]. The findings that SLMAP3 can regulate Cofilin and ROCK further imply a new role for this protein in convergent extension and apical constriction to ensure proper neurulation. The requirement of actin for proper localization of AJs and TJs is well established and the data that SLMAP3 can influence these key regulators further supports a critical role for this protein in PCP/ABP in the context of neurulation [78, 79]. It is notable that SLMAP can accumulate at adjacent cell membranes to potentially influence AJs and TJs.

The absence of SLMAP3 also affected the localization of PKCζ and Nestin to appropriate apical or basal domains suggesting a defective ABP. IP-MS analysis indicated that SLMAP3 predominantly

interacts with centrosomal and Golgi proteins and loss of SLMAP3 in neural tubes and NEPCs led to changes in centrosome organization and Golgi dispersion. Centrosomal and Golgi positioning play an important role in regulating ABP as they are localized apically to mediate microtubule nucleation and transport of vesicles to proper locations in the cell [80]. Centrosomal localization and function has been shown to impact neurulation or neural fold closure in zebrafish and mice [81, 82]. Polarized behavior of Golgi establishes differentiation of neuroepithelial cells to generate radial glia and astrocytes, an essential part of central nervous system formation [83]. Knockout of different Golgi compartments can give rise to a variety of phenotypes such as embryonic lethality and defects in brain development [59, 84]. Our data in NE4C cells and NTs implies that SLMAP3 is essential to maintain Golgi structure which is necessary for differentiation and neurulation. Factors such as Sec24b that can impact the transport of proteins from ER-Golgi and SPCA1 that regulates calcium homeostasis in Golgi are linked to craniorachischisis, suggesting that Golgi dysfunction can contribute to NTDs [85, 86]. We have previously shown that SLMAP can regulate vesicle trafficking and calcium signaling hence Golgi dispersal may impact these processes leading to NTD' due to SLMAP3 depletion [87, 88]. The new interactions of SLMAP3 with components of Golgi and centrosome may promote the close proximity of organelles connected by the microtubule network. While the loss of SLMAP3 did not alter their proximity in undifferentiated NEPCs, there was a marked dispersion of the Golgi apparatus upon differentiation cues. SLMAP3 is also in complex with motor proteins such as kinesins which drive vesicle transport. Thus, the deficiency of SLMAP3 may impact Golgi structure and function leading to defective production and targeting of the observed PCP components. The significant increase in cytosolic E-cad in SLMAP3 deficiency is consistent with a study which shows accumulation of E-cad in Golgi due to defective transport via Scrib [89].

The new finding that SLMAP3 is in a complex with Scrib and that it may guide localization of this protein is of significance as Scrib serves a critical role in ABP, PCP and NT development [54, 90]. The PCP axis lies orthogonal to the ABP polarity axis cooperating to generate polarized cell behavior and arrangements mediating tissue integrity and structure [91]. The link between these two can be in the distribution of their respective protein regulators [92]. Scrib was the first gene to link PCP and ABP, as it

was found to regulate the localization and stability of Vangl2, AJs (ECAD/NCAD), and TJs (ZO-1) thus impacting both polarity pathways to restrict convergent extension, apical constriction, and neurulation [93, 94]. The localization of Scrib is altered due to SLMAP3 deficiency with consequences on targeting junctional domains in NEPCs with profound impact on the localization of AJs and TJs supporting a role for SLMAP3 in Scrib mediated actions. It is notable that mutations in Scrib or its deficiency resemble the phenotypes we report here with the loss of SLMAP3 [93]. The interactions of SLMAP3 with centrosomal and Golgi components as well as the trafficking machinery that critically impacts important players which can guide PCP and ABP define an entirely new mode of action for this tail-anchored membrane protein in developing NT as modeled in Fig 11. In the absence of SLMAP3, the structural aspects of centrosome and Golgi have been impacted which in turn regulate the production, distribution, and localization of DVL2/3, Scrib, TJs, AJs, Nestin, and Actin with smaller cell size so that normal formation and morphogenesis of the NT is interrupted (**Figure 11**).

Conclusion:

Our data show that SLMAP3 is necessary for neural tube closure via interactions with components of PCP and ABP to guide cells behavior for convergent extension and neurulation. New interactions of SLMAP3 point to roles in the function of the centrosome and Golgi which can influence the production and subcellular targeting of components essential for PCP and ABP. SLMAP3 does not influence Hippo signaling and the data define it as a new target in NTDs including craniorachischisis.

Acknowledgements:

We are grateful for the assistance of all the facilities involved in this study: StemCore Laboratories Genomics Core Facility (RRID:SCR_012601); Ottawa Bioinformatics Core Facility (RRID:SCR_022466); Cell Biology and Image Acquisition Core (RRID: SCR_021845); Louise Pelletier Histology Core Facility (RRID: SCR_021737); and the Montreal Clinical Research Institute (IRCM, Quebec, Canada).

Conflicts of Interest: The authors declare no conflicts of interest.

Source of funding: This project was funded with the grants from the Canadian Institute of Health Research (CIHR) to Balwant Tuana.

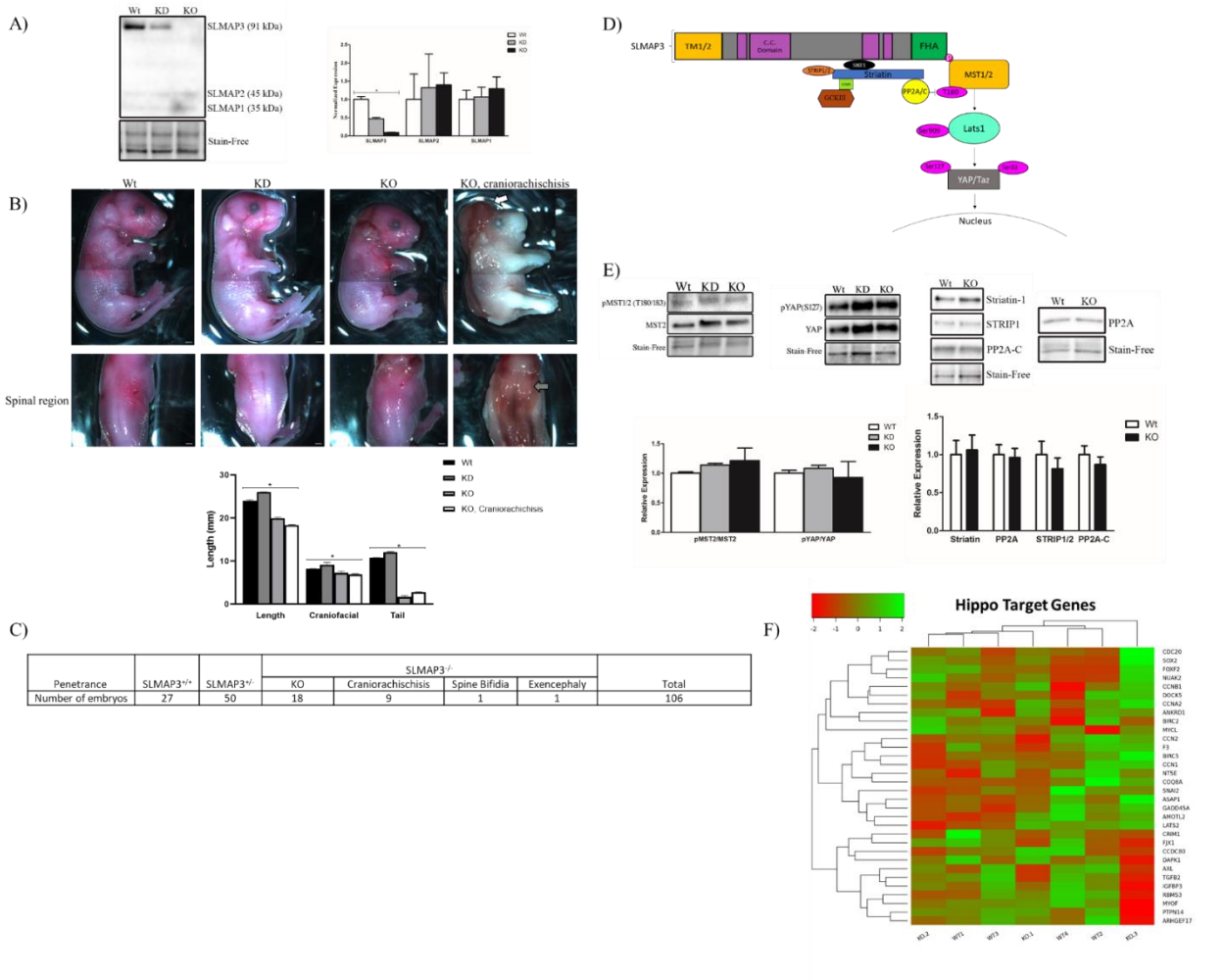

C)

Penetrance	SLMAP3$^{+/+}$	SLMAP3$^{+/-}$	SLMAP3$^{-/-}$				Total
			KO	Craniorachischisis	Spine Bifidia	Exencephaly	
Number of embryos	27	50	18	9	1	1	106

Figure 2. *Loss of SLMAP3 is embryonic lethal without impact on Hippo signaling*. A) Representative western blot image of e11.5 whole embryo lysates genotyped Wt (Wildtype), knockdown (KD) or knockout (KO) incubated with anti-SLMAP to identify SLMAP isoforms expression. Bar graphs represent the expression of indicated proteins by normalizing with total protein visualized by Stain-Free™ technology. N = 6. $P < 0.05$, ρ value was calculated using one-way ANOVA statistical analysis. B) Representative neonatal pups underwent dissection microscopy to magnify the phenotypic differences in animals genotyped Wt, KD, or KO. Images were captured with Stereo V.20 to demonstrate size differences, facial retrusion, tail formation, spine and brain development. Lens magnification=1x, Microscope Magnification=7.5x, Scale bar= 0.1mm. Bar graphs represent length differences, craniofacial retrusion and tail length in experimental animals (KD, KO) compared to wildtype. *$\rho < 0.05$, ρ value was calculated using one way ANOVA statistical analysis. N = 3. C) Table displaying penetrance of embryos displaying NTDs due to a loss of SLMAP3. D) Proposed schematic of SLMAP-STRIPAK components in Hippo signaling. E) Western blots of Wt, KD or KO lysates from E11.5 embryos with anti-STRIPAK components (Striatin-1, STRIP1, PP2A-A/C) and activity of Hippo activating kinase, with anti-phospho/total MST2 and downstream transcriptional co-activator, with anti-phospho/total YAP. Bar graphs represent the relative expression or activity of indicated proteins by normalizing to Stain-Free or the phospho-to-total protein ratio. N = 3. F) Heatmap representing results of RNA-sequencing on E11.5 Wt and KO whole embryos identifying Hippo signaling target genes with Euclidean clustering to group similarities in gene expression and experimental animals. Red color signifies lower log2FC whereas green represents higher log2FC. N = 4.

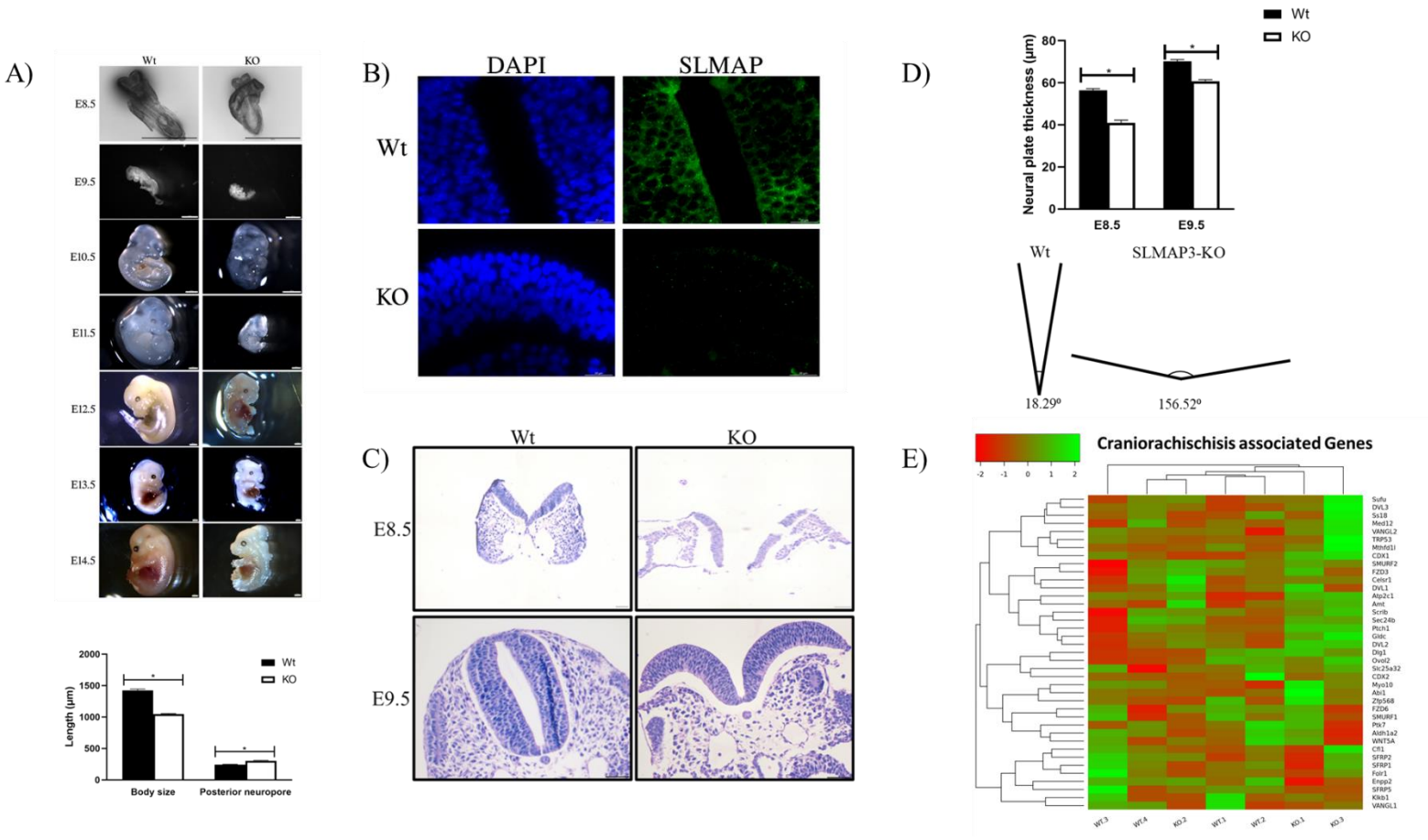

Figure 3. *Neurulation and convergent extension in Wt and SLMAP3-KO embryos*. A) Representative whole-mount images of Wt and KO embryos during prenatal development (E8.5-E13.5). Scale bar= 1mm. The bar graph represents body size and posterior neuropore in Wt and KO e8.5 embryos. B) Representative immunofluorescent imaging of E9.5 neural tube sections comparing expression of SLMAP in Wt and KO. Magnification=63x. Scale bar=0.02mm. n = 3 C) Representative transverse sectioning of Wt and KO E8.5 and E9.5 embryos at closure site 1. Sections were stained with hematoxylin and eosin to visualize cytoplasm and nucleus. Lens Magnification=20x. Scale bar=0.05mm. n = 3. D) Bar graphs comparing changes to neural plate thickness in E8.5 and E9.5 neural tubes and changes in E9.5 neural grove aperture in Wt and KO sections. E) Heatmap representing results of RNA-sequencing on e11.5 Wt and KO whole embryo identifying genes associated with craniorachischisis with Euclidean clustering to highlight similarities in gene expression and experimental animals. Red color signifies lower log2FC whereas green represents higher log2FC. N = 4. *: $\rho<0.05$. ρ value was calculated using non-paired two-way t-test.

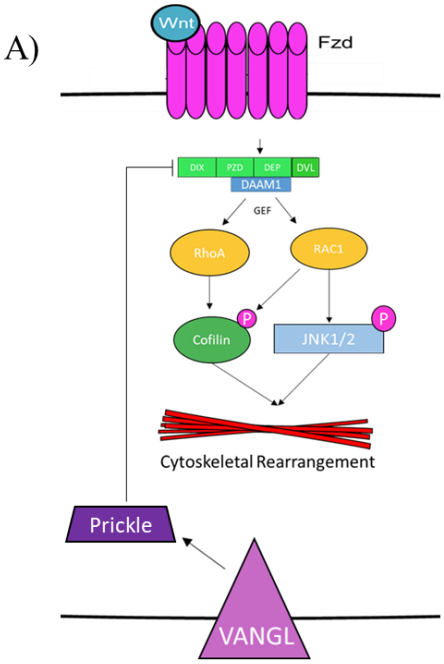
A)
Wnt
Fzd
DIX
PZD
DEP
DVL
DAAM1
GEF
RhoA
RAC1
Cofilin
JNK1/2
P
P
Cytoskeletal Rearrangement
Prickle
VANGL

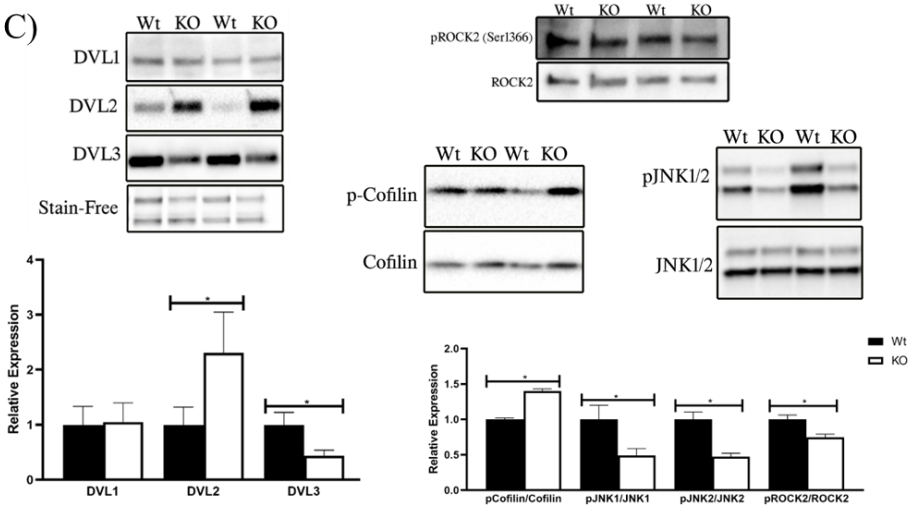
C)
Wt KO Wt KO
DVL1
DVL2
DVL3
Stain-Free
Relative Expression
DVL1
DVL2
DVL3
Wt KO Wt KO
pROCK2 (Ser1366)
ROCK2
Wt KO Wt KO
p-Cofilin
Cofilin
Wt KO Wt KO
pJNK1/2
JNK1/2
Relative Expression
pCofilin/Cofilin
pJNK1/JNK1
pJNK2/JNK2
pROCK2/ROCK2
Wt
KO

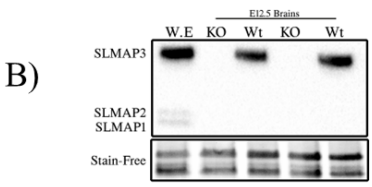
B)
E12.5 Brains
W.E KO Wt KO Wt
SLMAP3
SLMAP2
SLMAP1
Stain-Free

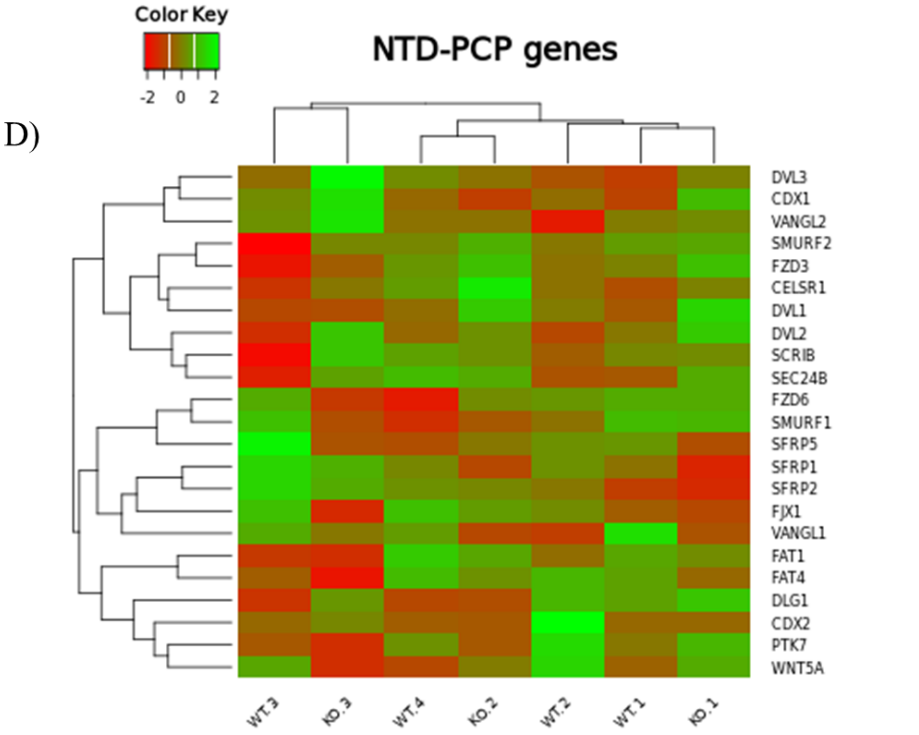
D)
Color Key
-2 0 2
NTD-PCP genes
DVL3
CDX1
VANGL2
SMURF2
FZD3
CELSR1
DVL1
DVL2
SCRIB
SEC24B
FZD6
SMURF1
SFRP5
SFRP1
SFRP2
FJX1
VANGL1
FAT1
FAT4
DLG1
CDX2
PTK7
WNT5A
WT.3
KO.3
WT.4
KO.2
WT.2
WT.1
KO.1

Figure 4. *Loss of SLMAP3 perturbs planar cell polarity signaling.* A) Schematic representing simplified PCP signaling regulating cytoskeletal dynamics through the asymmetrical distribution of components to proximal (Frizzled; Fzd and Dishevelled (DVL)) or distal (Van-gogh like protein; Vangl and Prickle) sides of the cell B) Representative western blot images with anti-SLMAP in Wt and KO E12.5 brain lysates with whole embryo (W.E) as a control. C) Representative western blot images with anti-PCP signaling transducers (DVL1 DVL2, DVL3) and PCP signaling targets (ROCK2, Cofilin, JNK1/2) in Wt and KO E12.5 brain lysates. Bar graphs represent relative expression of indicated proteins normalized to Stain-Free total protein or phosphorylated to total protein ratio. *N*=4. *: $\rho<0.05$. ρ value was calculated using non-paired two-way t-test. D) Heatmap representing RNA-seq of PCP genes with Euclidean clustering analysis representing gene expression between experimental animals. Red color signifies lower log2FC whereas green represents higher log2FC. N = 4.

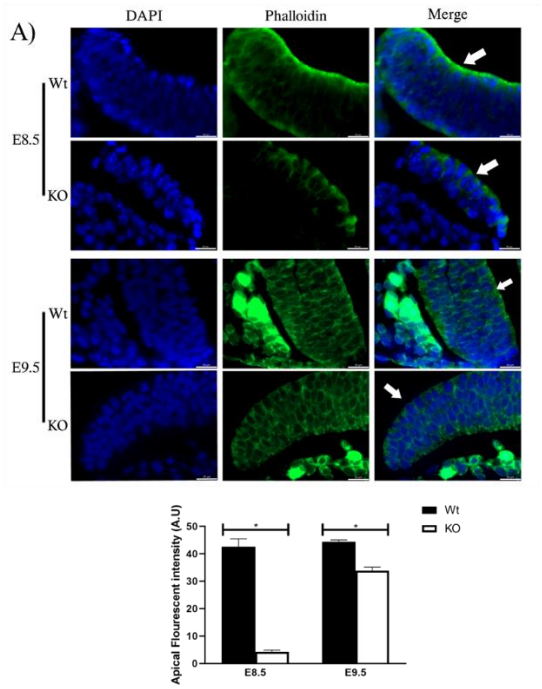
A)
DAPI
Phalloidin
Merge
Wt
KO
E8.5
E9.5
Apical Flourescent intensity (A.U)
Wt
KO
E8.5
E9.5

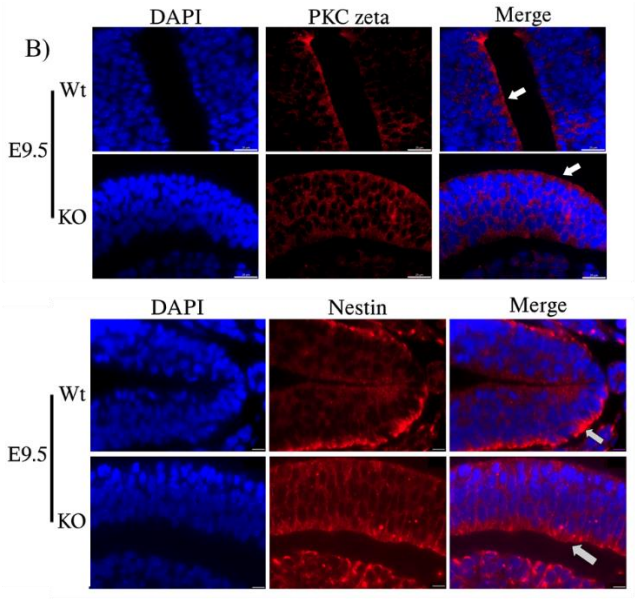
B)
DAPI
PKC zeta
Merge
Wt
KO
E9.5
PKC zeta Apical/Sub Apical (A.U.)
DAPI
Nestin
Merge
Nestin Basal/Sub Basal (A.U.)

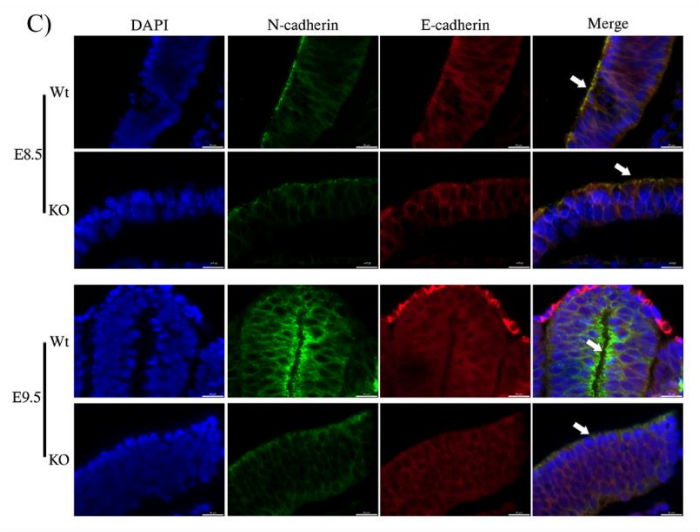
C)
DAPI
N-cadherin
E-cadherin
Merge
Wt
KO
E8.5
E9.5

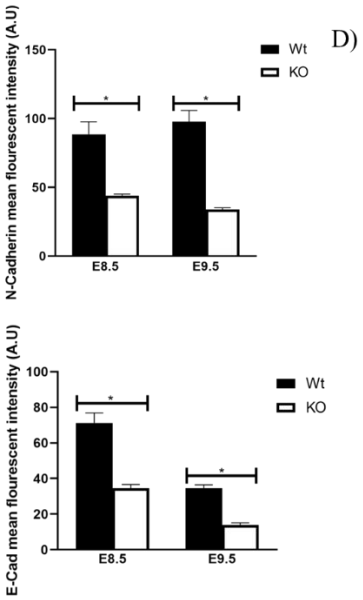
N-Cadherin mean flourescent intensity (A.U)
E-Cad mean flourescent intensity (A.U)
Wt
KO
E8.5
E9.5

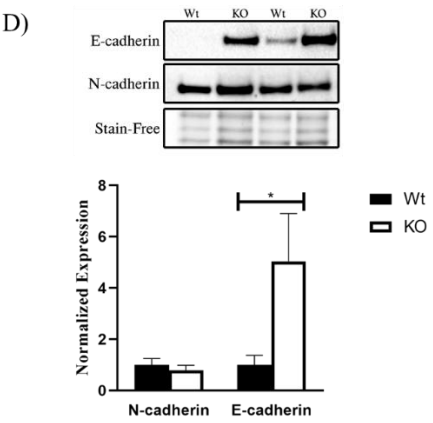
D)
Wt
KO
Wt
KO
E-cadherin
N-cadherin
Stain-Free
Normalized Expression
N-cadherin
E-cadherin

Figure 5. *Loss of SLMAP3 impacts actin and adherens junction.* A) Representative immunofluorescent images of sectioned Wt and KO neural tubes at E8.5 (top) and E9.5 (bottom) labelled with DAPI (nucleus, blue) and phalloidin (actin, green). Bar graph indicates apical (white arrow) localization of actin in neural tubes showing apical and basal distribution of actin. B) Representative immunofluorescent images of sectioned Wt and KO neural tubes at E9.5 labelled with DAPI (nucleus) and apical (white arrow) marker PKC zeta or basal (grey arrow) marker nestin (red) Bar graphs represent expression of indicate relative expression of markers at apical/basal regions relative to amounts at subapical/subbasal domains. C) Representative immunofluorescent images of sectioned Wt and KO neural tubes at E8.5 and E9.5 labelled with nucleus (DAPI, blue) and N-cad (green). Bar graphs represent apical (white arrow) fluorescent intensity of N-cad at E8.5 and E9.5 in Wt and KO neural tube. Lens Magnification=63x. Scale bar=0.02mm. D) Representative western blot images with anti-E-cad and N-cad in Wt and KO E12.5 brain lysates. Bar graphs represent relative expression of indicated proteins normalized to Stain-Free total protein. n=4. *: $\rho<0.05$. ρvalue was calculated using non-paired two-way t-test.

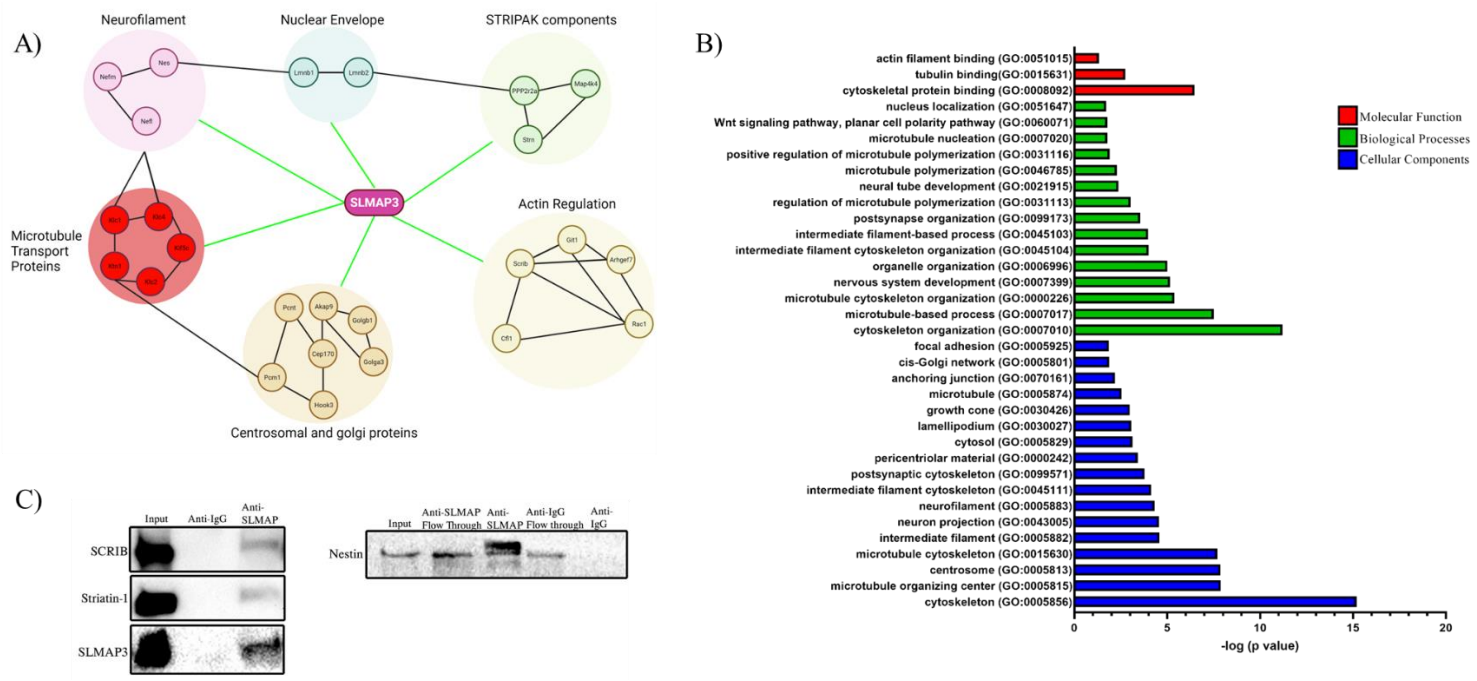

Figure 6. *SLMAP3 interacts with centrosomes, Golgi, and neurofilaments.* A) Protein-protein interaction network for SLMAP3 determined from mass spectroscopy peptide analysis of anti-SLMAP immunoprecipitated E12.5 brain lysates. B) GO analysis of molecular function, biological process, and cellular components associated to the network of proteins that interact with SLMAP3. Minimum p-value < 0.05. C) Representative Western blot displaying presence of SLMAP3, striatin-1, Scrib and Nestin after immunoprecipitation of e12.5 brain lysates with anti-SLMAP and anti-IgG and blotting with anti-Scrib, anti-striatin-1 and anti-nestin.

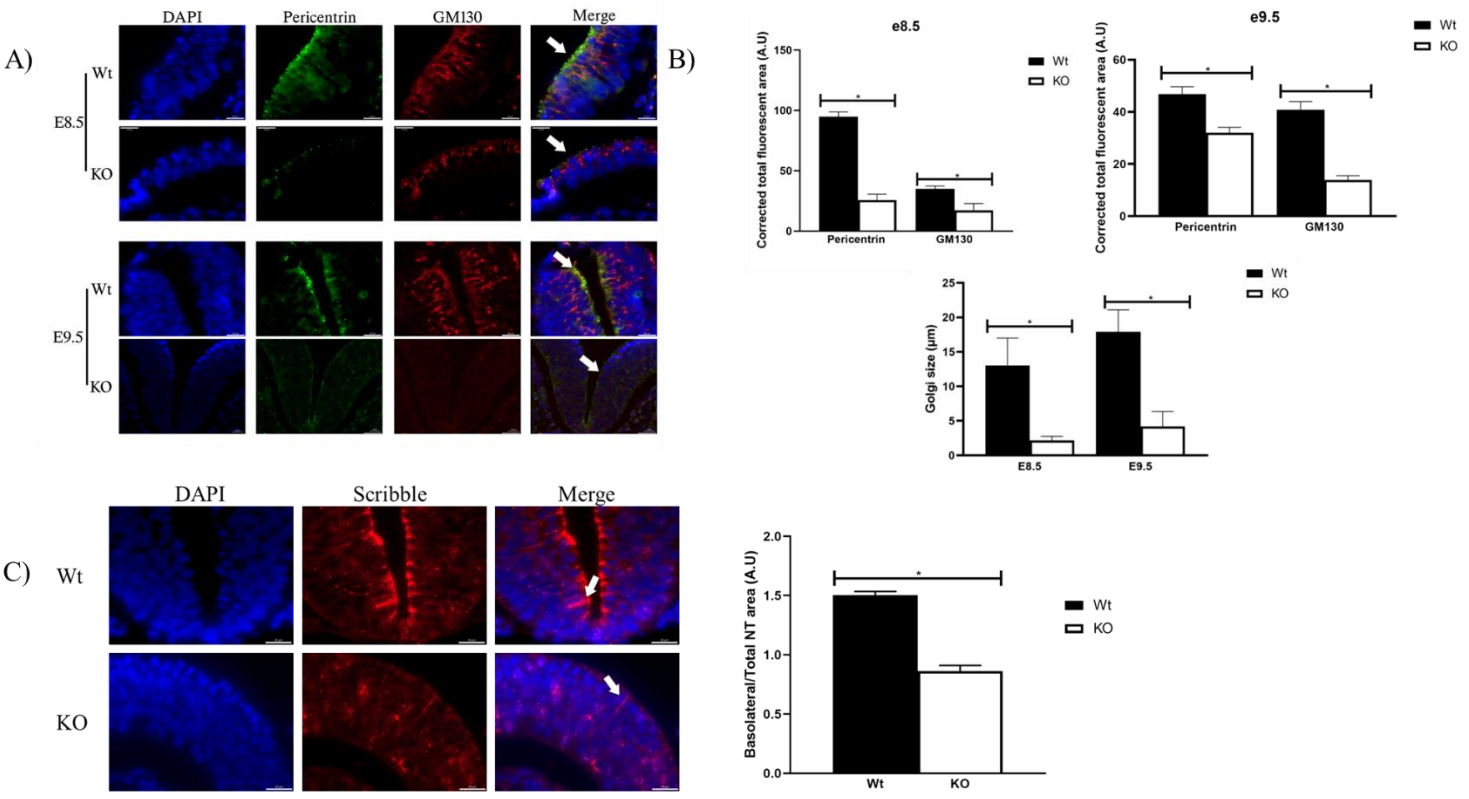

Figure 7. *SLMAP3 regulate apical-basal polarity proteins.* Representative immunofluorescent images of sectioned Wt and KO neural tubes at E8.5 (top) and E9.5 (bottom) labelled for nucleus (DAPI, blue), apically (white arrow) pericentrin (green) and GM130 (red). Lens Magnification=63x. Scale bar=0.02mm. n=4 B) Bar graphs analyzing the fluorescent intensity of centrosomes and Golgi in Wt and KO neural tubes at E8.5 and E9.5. Golgi size refers to comparison of Golgi lengths in Wt and KO neural tubes at E8.5 and E9.5. C) Representative immunofluorescent images of sectioned Wt and KO neural tubes at E9.5 (bottom) labelled for nucleus (DAPI, blue) and Scribble (red). Lens Magnification=63x. Scale bar=0.02mm. Bar graphs represent basolateral junctional intensity (white arrow) to total neural tube (NT) area of SCRIB in Wt and KO. n=4, *: $\rho<0.05$, ρ value was calculated using non-paired two-way t-test.

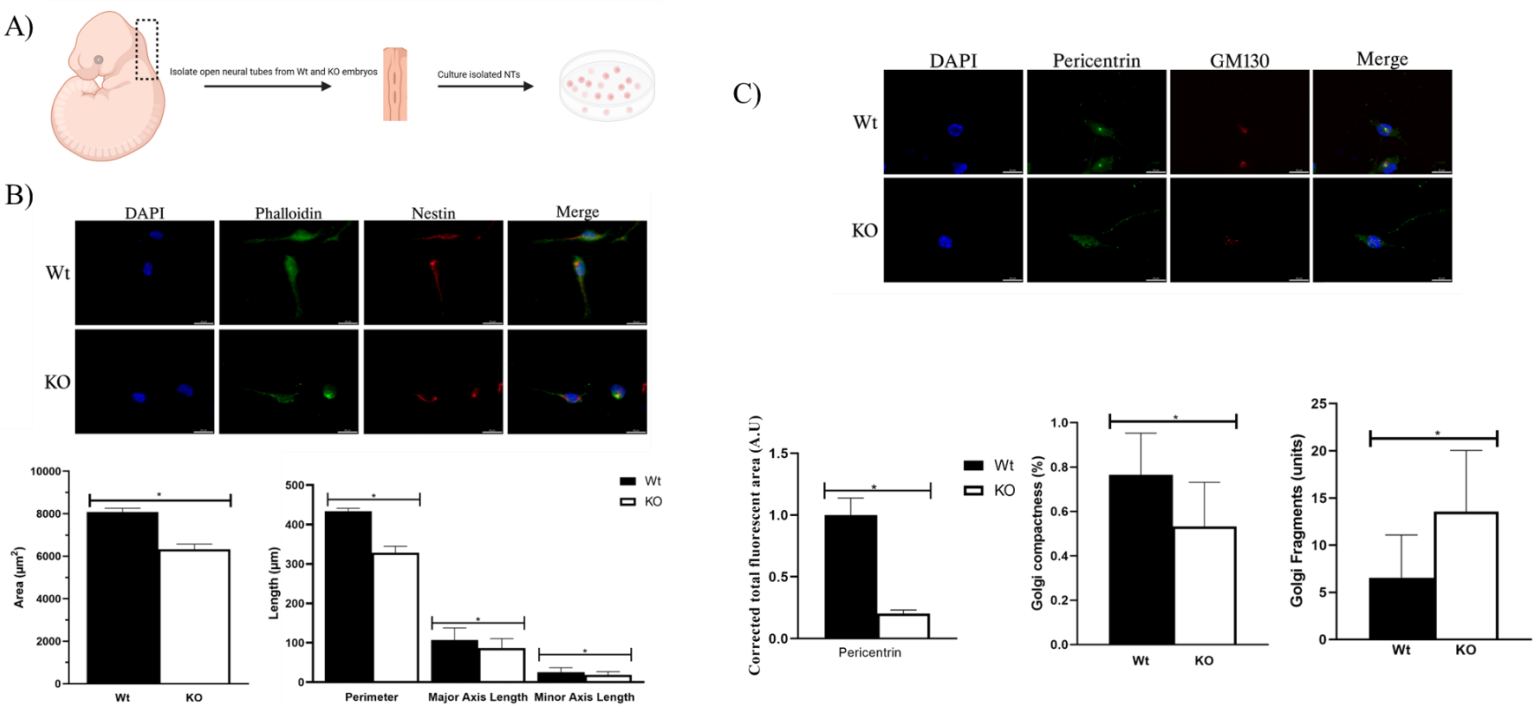

Figure 8. *SLMAP3 loss leads to decreased cell size, mislocalization of pericentrin and Golgi fragmentation in primary NEPCs*. A) Method of isolating and culturing neural tube tissue to gain a pool of primary neuroepithelial cells (NEPCs). B) Representative immunofluorescent images of Wt and KO NEPCs with DAPI (nucleus, blue), phalloidin (actin, green) and nestin (red). Lens Magnification=63x. Scale bar=0.02mm. The bar graphs represent quantification of cell characteristics such as area, perimeter, major and minor axis lengths. n=3. *: $\rho<0.05$. Lens Magnification=63x. Scale bar=0.02mm. C) Representative immunofluorescent images of Wt and KO NEPCs with DAPI (nucleus, blue), pericentrin (centrosome, green), and GM130 (Golgi, red). The left bar graph is quantified signal intensity of centrosome relative to the nucleus in KO and Wt. The right bar graph is quantification of Golgi compactness and fragmentation in Wt and KO NEPCs. *: $\rho<0.05$. Lens Magnification=63x. Scale bar=0.02mm.

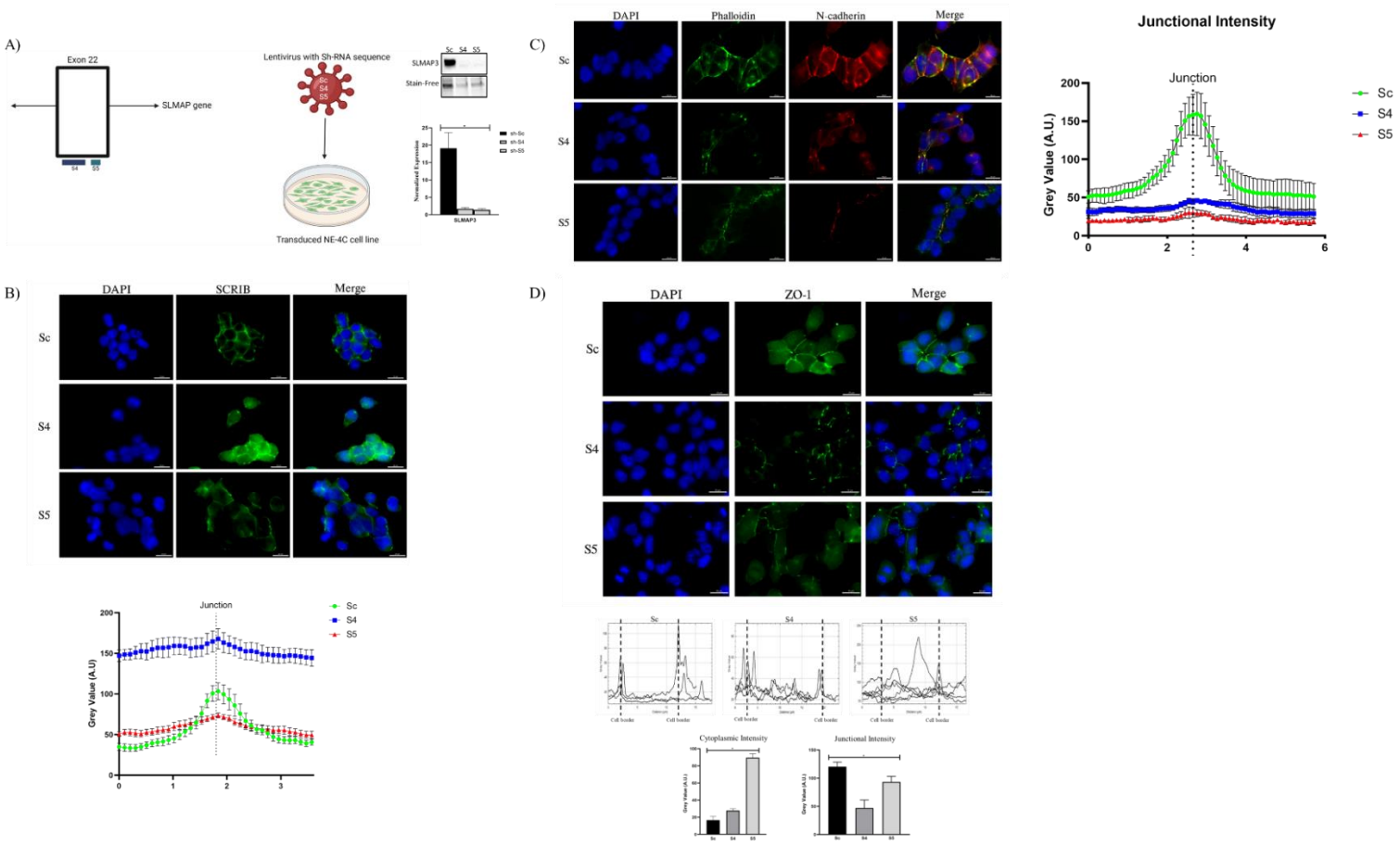

Figure 9. *SLMAP3 affects localization of Scribble, AJs and TJs* A) Construction of sh-RNA (S4&S5) at exon 22 of the SLMAP gene and scramble control (Sc) lentiviruses to transduce NE-4C. Western blot with anti-SLMAP in NE-4C cell lysates transduced with sh-S4, sh-S5, sh-Sc. The bar graph represents quantification of relative expression of SLMAP3 normalized to Stain-Free total protein. n=4. B) Immunofluorescent images depicting localization of actin (green), N-cad (red), and DAPI (blue). The line graph represents quantification of differences in junctional intensity of N-cadherin. N=3. C) Immunofluorescent images depicting DAPI (blue) and Scribble (green). The line graph represents differences in expression and junctional intensity of Scribble. n=3. D) Immunofluorescent images depicting localization of tight junction ZO-1 (green) and DAPI (blue). Line graph represents plot profile of ZO-1 expression across cell borders and cytoplasm of transduced NE-4C cells. The bar graph represents quantification of differences in cytoplasmic and junctional intensity of ZO-1. n=3. *: $\rho<0.05$. Lens Magnification=63x. Scale bar=0.02mm. ρ value was calculated one-way ANOVA statistical analysis.

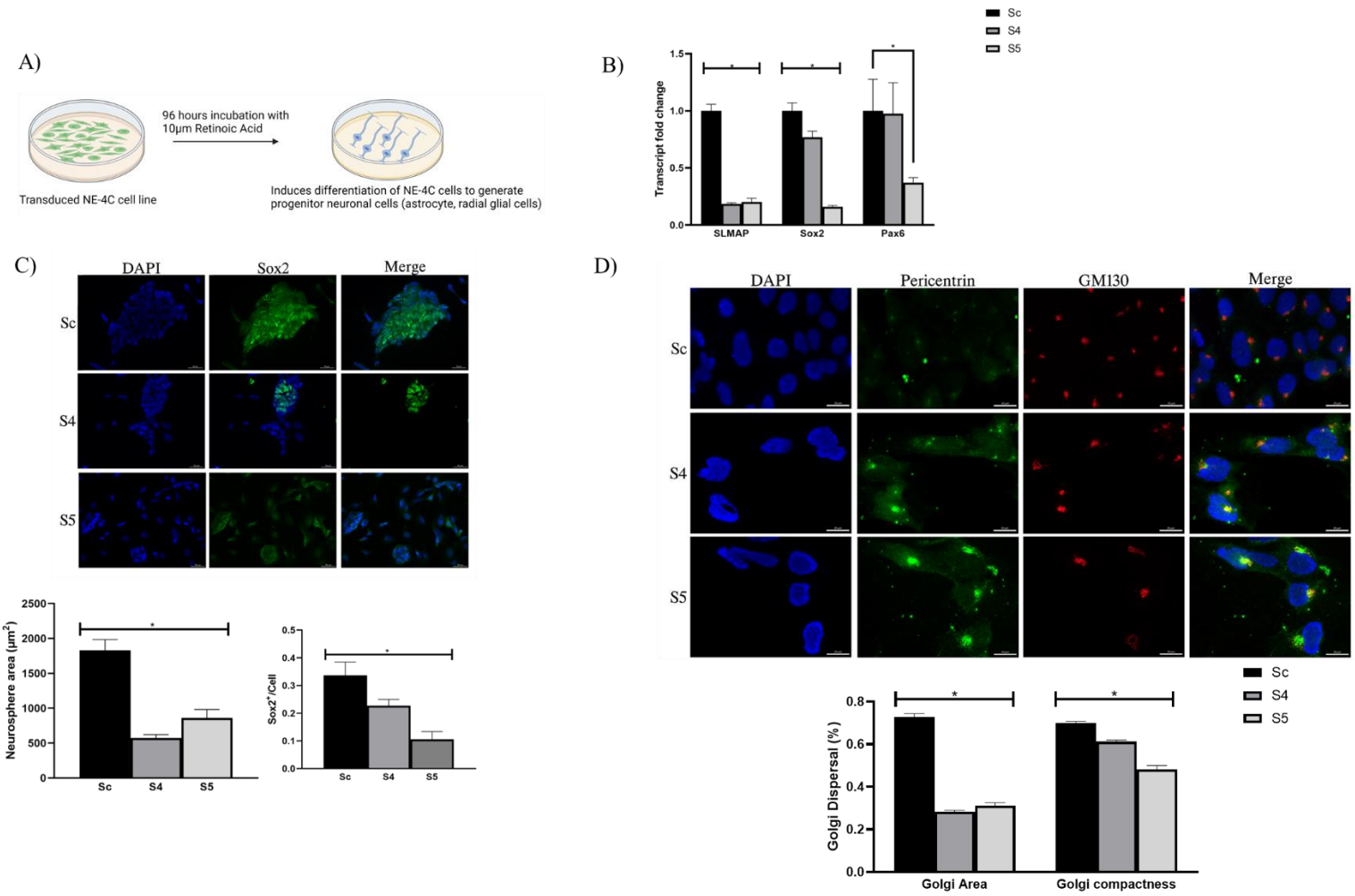

Figure 10. *SLMAP3 impacts differentiation of NE-4C cells.* A) Experimental procedure to differentiate NE-4C cells. B) Bar graphs represent transcript analysis for SLMAP, Sox2 and Pax6 in transduced NE-4C cells cultured for 96 hours with 10µm retinoic acid. C) Immunofluorescent images with anti-Sox2 and DAPI (blue) in transduced NE-4C cells differentiated for 96 hours in media containing 10µm retinoic acid. Bar graphs represent neurosphere size and $Sox2^{+}$/cell respectively. n=3. Lens Magnification=20x. Scale bar=0.05mm. ρ value was calculated using one-way ANOVA test. D) Immunofluorescent images with anti-pericentrin (green), anti-GM130 (red) and DAPI (blue). Bar graphs represent quantifications of Golgi area and Golgi compactness. n=3. *: $\rho<0.05$. Lens Magnification=63x. Scale bar=0.02mm. ρ value was calculated using paired students t-test.

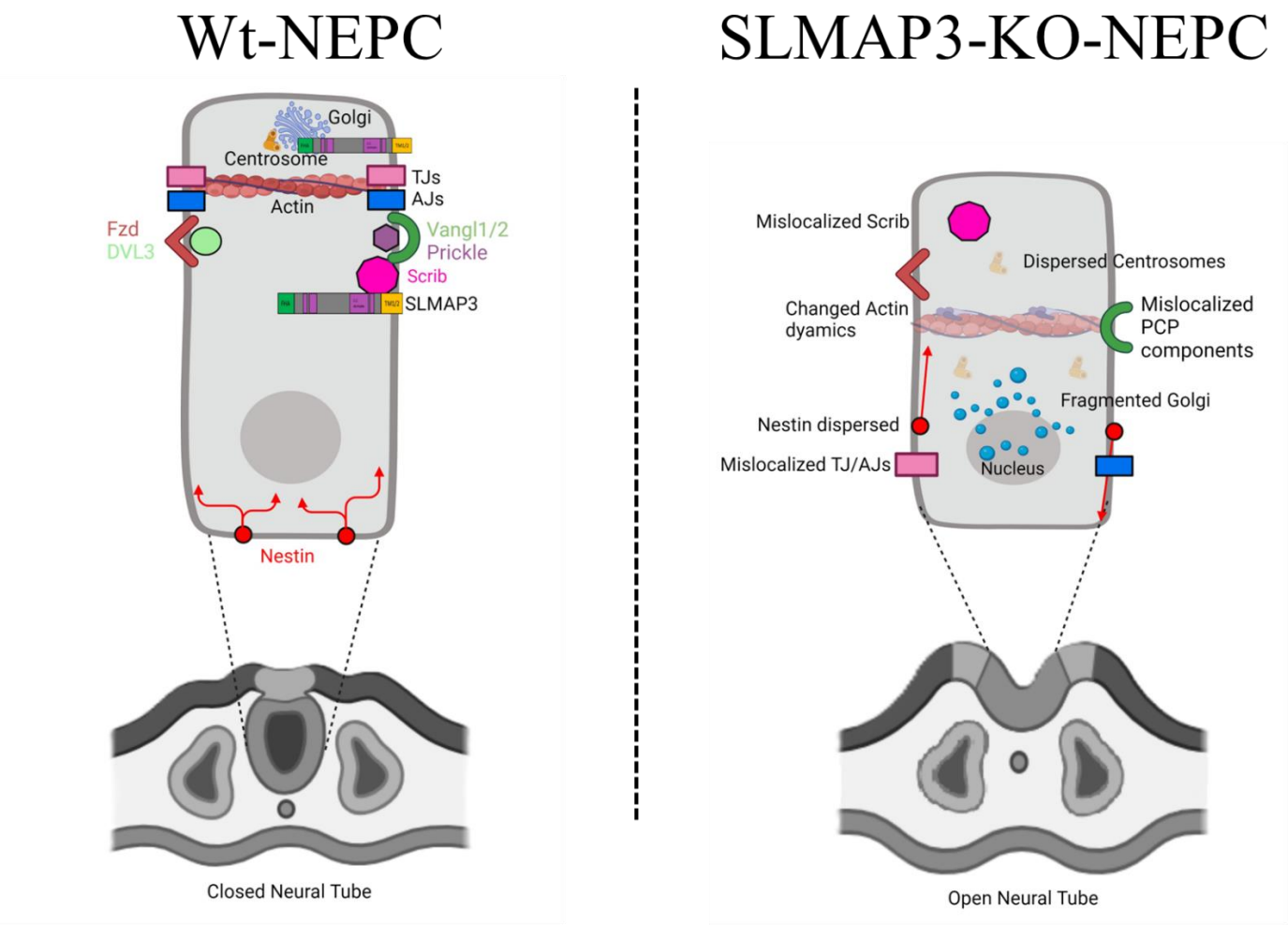

Figure 11. *Novel role of SLMAP3 within neuroepithelial cells during neurulation.* SLMAP3 organizes centrosomal/Golgi architecture, promoting appropriate distribution of PCP signaling and ABP components to localized to appropriate domains to generate orthogonal polarity axis working in tandem to bend and close the neural tube. However, loss of SLMAP3 leads to fragmented Golgi, dispersed centrosomes, altered PCP signaling due to changes in Scrib and actin dynamics with mislocalized TJ/AJs, resulting in structurally smaller unpolarized cells which are unable to undergo convergent extension to complete neurulation.

5.5 References

[1] C. C. Wesley, S. Mishra and D. L. Levy, "Organelle size scaling over embryonic development.," *WIREs Developmental Biology,* vol. 9, no. 5, 2020.

[2] A. Copp and N. Greene, "Neural tube defects—disorders of neurulation and related embryonic processes," *WIREs Dev Biol,* vol. 2, pp. 213-227, 2013.

[3] J. Wigle and D. Eisenstat, "Neural Induction and Regionalization.," *Neurodevelopmental Pediatrics. Springer, Cham,* 2023.

[4] A. Martin and B. Goldstein, "Apical constriction: themes and variations on a cellular mechanism driving morphogenesis.," *Development,* vol. 141, no. 10, pp. 1987-98, 2014.

[5] Y. Ravichandran, B. Goud and J. Manneville, "The Golgi apparatus and cell polarity: Roles of the cytoskeleton, the Golgi matrix, and Golgi membranes," *Curr Opin Cell Biol,* vol. 62, pp. 104-113, 2020.

[6] E. Nikolopoulou, G. Galea, A. Rolo, N. Greene and A. Copp, "Neural tube closure: cellular, molecular and biomechanical mechanisms," *Development,* vol. 144, no. 4, pp. 552-566, 2017.

[7] I. Zohn and A. Sarkar, "Modeling neural tube defects in the mouse.," *Curr Top Dev Biol,* vol. 84, pp. 1-35, 2008.

[8] J. Byers, R. Guzzo, M. Salih and B. Tuana, "Hydrophobic profiles of the tail anchors in SLMAP dictate subcellular targeting," *BMC Cell Biol,* vol. 10, no. 48, 2009.

[9] M. Nader, B. Westendorp, O. Hawari, M. Salih, A. F. Stewart, F. H. Leenen and B. S. Tuana, "Tail-anchored membrane protein SLMAP is a novel regulator of cardiac function at the sarcoplasmic reticulum," *Am J Physiol Heart Circ Physiol,* vol. 302, no. 5, pp. 1138-1145, 2012.

[10] J. Wigle, L. Demchyshyn, M. Pratt, W. Staines, M. Salih and B. Tuana, "Molecular cloning, expression, and chromosomal assignment of sarcolemmal-associated proteins. A family of acidic amphipathic alpha-helical proteins associated with the membrane," *J Biol Chem,* vol. 272, no. 51, pp. 32384-94, 1997.

[11] R. M. Guzzo, M. Salih, E. D. Moore and B. Tuana, "Molecular properties of cardiac tail-anchored membrane protein SLMAP are consistent with structural role in arrangement of excitation-contraction coupling apparatus.," *Am J Physiol Heart Circ Physiol,* vol. 288, no. 4, pp. H1810-9, 2005.

[12] R. Guzzo, S. Sevinc, M. Salih and B. Tuana, "A novel isoform of sarcolemmal membrane-associated protein (SLMAP) is a component of the microtubule organizing centre," *J Cell Sci. 2004 May 1;117(Pt 11):2271-81.,* vol. 117, no. 11, pp. 2271-81, 2004.

[13] P. Wielowieyski, S. Sevinc, R. Guzzo, M. Salih, J. Wigle and B. Tuana, "Alternative splicing, expression, and genomic structure of the 3' region of the gene encoding the sarcolemmal-associated

proteins (SLAPs) defines a novel class of coiled-coil tail-anchored membrane proteins.," *J Biol Chem,* vol. 275, no. 49, pp. 38474-81, 2000.

[14] I. Letunic and P. Bork, "20 years of the SMART protein domain annotation resource," *Nucleic Acids Res,* vol. 46, no. D1, pp. D493-496, 2018.

[15] D. Durocher and S. Jackson, "The FHA domain," *FEBS Lett,* vol. 513, no. 1, pp. 58-66, 2002.

[16] R. Guzzo, J. Wigle, M. Salih, E. Moore and B. Tuana, "Regulated expression and temporal induction of the tail-anchored sarcolemmal-membrane-associated protein is critical for myoblast fusion," *Biochem J,* vol. 381, no. 3, pp. 599-608, 2004.

[17] Y. Tang, M. Chen and L. Zhou, "Architecture, substructures, and dynamic assembly of STRIPAK complexes in Hippo signaling," *Cell Discov,* vol. 5, no. 3, 2019.

[18] M. Goudreault, L. D'Ambrosio, M. Kean, M. Mullin, B. Larsen, A. Sanchez, S. Chaudhry, G. Chen, F. Sicheri, A. Nesvizhskii, R. Aebersold, B. Raught and A. Gingras, "A PP2A Phosphatase High Density Interaction Network Identifies a Novel Striatin-interacting Phosphatase and Kinase Complex Linked to the Cerebral Cavernous Malformation 3 (CCM3) Protein," *Mol Cell Proteomics,* vol. 8, no. 1, pp. 157-71, 2009.

[19] B. Jeong, S. Bae, L. Ni, X. Zhang, X. Bai and X. Luo, "Cryo-EM structure of the Hippo signaling integrator human STRIPAK," *Nat Struct Mol Biol,* vol. 28, no. 3, pp. 290-299, 2021.

[20] R. Chen, R. Xie, Z. Meng, S. Ma and K.-L. Guan, "STRIPAK integrates upstream signals to initiate the Hippo kinase cascade.," *Nat Cell Biol,* vol. 21, pp. 1565-1577, 2019.

[21] T. Rehmani, J. Mlynarova, J. Byers, M. Salih and B. Tuana, "Specific Deletion of the FHA Domain Containing SLMAP3 Isoform in Postnatal Myocardium Has No Impact on Structure or Function.," *Cardiogenetics.,* vol. 11, no. 4, pp. 164-184, 2021.

[22] F. Schwenk, U. Baron and K. Rajewsky, "A cre-transgenic mouse strain for the ubiquitous deletion of loxp-flanked gene segments including deletion in germ cells.," *Nucleic Acids Research, 23(24), 5080-5081. https://doi.org/10.1093/nar/23.24.5080,* vol. 23, no. 24, pp. 5080-5081, 1995.

[23] A. Dias, T. Rehmani, M. Salih and B. Tuana, "The Tail Anchored Membrane Protein SLMAP3 Coordinates the Targeting of Centrosomal Proteins to the Nuclear Envelope for Skeletal Myogenesis," *iScience-Submitted,* 2023.

[24] "https://www.novusbio.com/support-by-application/Fluorescent-IHC-Staining-of-FFPE-Tissue," [Online].

[25] I. Mejia, Y. Chen and B. Díaz, "Analysis of Golgi Morphology Using Immunofluorescence and CellProfiler Software," *Methods Mol Biol.* , vol. 2557, pp. 765-784, 2023.

[26] H. Li, J. Zhang and L. Niswander, "Zinc deficiency causes neural tube defects through attenuation of p53 ubiquitylation," *Development,* vol. 145, no. 24, p. dev169797, 2018.

[27] "https://www.ncbi.nlm.nih.gov/geo/query/acc.cgi?acc=GSE230748," [Online].

[28] E. Afgan, D. Baker, M. van den Beek, D. Blankenberg, D. Bouvier, M. Čech, J. Chilton, D. Clements, N. Coraor, C. Eberhard, B. Grüning, A. Guerler, J. Hillman-Jackson, G. Von Kuster, E. Rasche, N. Soranzo, N. Turaga, J. Taylor, A. Nekrutenko and J. Goecks, "The Galaxy platform for accessible, reproducible and collaborative biomedical analyses: 2016 update.," *Nucleic Acids Res. 2016 Jul 8;44(W1):W3-W10.*, vol. 44, no. W1, pp. W3-10, 2016.

[29] "https://www.genscript.com/tools/create-scrambled-sequence-reference," [Online].

[30] "(https://en.vectorbuilder.com/design/pLV_shRNA_U6.html-reference," [Online].

[31] "https://www.addgene.org/12260/," [Online].

[32] "https://www.addgene.org/12259/," [Online].

[33] "https://www.addgene.org/protocols/lentivirus-production/," [Online].

[34] "https://www.addgene.org/protocols/generating-stable-cell-lines/-reference," [Online].

[35] ,. K. Schlett and E. Madarász, "Retinoic acid induced neural differentiation in a neuroectodermal cell line immortalized by p53 deficiency," *J Neurosci Res,* vol. 47, no. 4, pp. 405-15, 1997.

[36] A. Torroglosa, M. Murillo-Carretero, C. Romero-Grimaldi, E. R. Matarredona, A. Campos-Caro and C. Estrada, "Nitric oxide decreases subventricular zone stem cell proliferation by inhibition of epidermal growth factor receptor and phosphoinositide-3-kinase/akt pathway.," *Stem Cells,* vol. 25, no. 1, pp. 88-97, 2006.

[37] N. Naveen, Murlimanju, K. Vishal and A. Maligi, "Craniorachischisis totalis.," *J Neurosci Rural Pract.,* vol. 1, no. 1, pp. 54-5, 2010.

[38] N. Greene and A. Copp, "Neural tube defects.," *Annu Rev Neurosci,* vol. 37, pp. 221-42, 2014.

[39] S. McShane, M. Molè, D. Savery, N. Greene, P. Tam and A. Copp, " Cellular basis of neuroepithelial bending during mouse spinal neural tube closure.," *Dev Biol,* vol. 404, no. 2, pp. 113-24, 2015.

[40] S. Lee and J. Gleeson, "Closing in on Mechanisms of Open Neural Tube Defects," *Trends Neurosci,* vol. 43, no. 7, pp. 519-532, 2020.

[41] L. Kindt, A. Coughlin, T. Perosino, H. Ersfeld, M. Hampton and J. Liang, "Identification of transcripts potentially involved in neural tube closure using RNA sequencing," *Genesis,* vol. 56, no. 3, p. e23096, 2018.

[42] J. Wallingford, "Planar cell polarity and the developmental control of cell behavior in vertebrate embryos," *Annu Rev Cell Dev Biol,* vol. 28, pp. 627-53, 2012.

[43] D. Devenport, "The cell biology of planar cell polarity," *J Cell Biol,* vol. 207, no. 2, pp. 171-179, 2014.

[44] J. Zallen, "Planar polarity and tissue morphogenesis.," *Cell,* vol. 129, no. 6, pp. 1051-63, 2007.

[45] M. Harris and D. Juriloff, " An update to the list of mouse mutants with neural tube closure defects and advances toward a complete genetic perspective of neural tube closure," *Birth Defects Research Part A: Clinical and Molecular Teratology,* vol. 88, pp. 653-669, 2010.

[46] A. Ivanov, "Actin motors that drive formation and disassembly of epithelial apical junctions.," *Front Biosci.,* vol. 1, no. 13, pp. 6662-81, 2008.

[47] C. Zihni, C. Mills, K. Matter and M. Balda, "Tight junctions: from simple barriers to multifunctional molecular gates.," *Nat Rev Mol Cell Biol.,* vol. 17, no. 9, pp. 564-80, 2016.

[48] C. M. Niessen, D. Leckband and A. S. Yap, "Tissue Organization by Cadherin Adhesion Molecules: Dynamic Molecular and Cellular Mechanisms of Morphogenetic Regulation," *Physiological Reviews,* vol. 91, no. 2, pp. 691-731, 2011.

[49] K. Punovuori, M. Malaguti and S. Lowell, "Cadherins in early neural development.," *Cell Mol Life Sci.,* vol. 78, no. 9, pp. 4435-4450, 2021.

[50] G. Radice, H. Rayburn, H. Matsunami, K. Knudsen, M. Takeichi and R. Hynes, "Developmental defects in mouse embryos lacking N-cadherin.," *Dev Biol,* vol. 181, no. 1, pp. 64-78, 1997.

[51] C. D. Rogers, L. K. Sorrells and B. M. E. ., "A catenin-dependent balance between n-cadherin and e-cadherin controls neuroectodermal cell fate choices.," *Mechanisms of Development,* vol. 152, pp. 44-56, 2018.

[52] A. Davis, C. Grondin, R. Johnson, D. Sciaky, J. Wiegers, T. Wiegers and C. Mattingly, "The Comparative Toxicogenomics Database: update 2021.," *Nucleic Acids Res.* , vol. 8, no. 49(D1), pp. D1138-D1143, 2021.

[53] J. Carvajal-Gonzalez, S. Mulero-Navarro and M. Mlodzik, "Centriole positioning in epithelial cells and its intimate relationship with planar cell polarity," *Bioessays,* vol. 38, no. 12, pp. 1234-1245, 2016.

[54] F. Kharfallah, M. Guyot, A. El Hassan, R. Allache, E. Merello, P. De Marco, G. Di Cristo, V. Capra and Z. Kibar, "Scribble1 plays an important role in the pathogenesis of neural tube defects through its mediating effect of Par-3 and Vangl1/2 localization," *Hum Mol Genet,* vol. 26, no. 12, pp. 2307-2320, 2017.

[55] A. Hartsock and W. J. Nelson, " Adherens and tight junctions: structure, function and connections to the actin cytoskeleton.," *Biochimica Et Biophysica Acta (BBA) - Biomembranes,* vol. 1778, no. 3, pp. 660-669, 2008.

[56] S. Mercurio, L. Serra, M. Pagin and S. Nicolis, "Deconstructing Sox2 Function in Brain Development and Disease.," *Cells,* vol. 11, no. 10, p. 1604, 2002.

[57] K. Sakurai and N. Osumi, "The neurogenesis-controlling factor, Pax6, inhibits proliferation and promotes maturation in murine astrocytes.," *J Neurosci,* vol. 28, no. 18, pp. 4604-12, 2008.

[58] E. Taverna and W. Huttner, "The Golgi Apparatus in Polarized Neuroepithelial Stem Cells and Their Progeny: Canonical and Noncanonical Features.," *Results Probl Cell Differ.,* vol. 67, pp. 359-375, 2019.

[59] C. Liu, M. Mei, Q. Li, P. Roboti, Q. Pang, Z. Ying, F. Gao, M. Lowe and S. Bao, "Loss of the golgin GM130 causes Golgi disruption, Purkinje neuron loss, and ataxia in mice," *Proc Natl Acad Sci U S A,* vol. 114, no. 2, pp. 346-351, 2016.

[60] G. Aparicio, C. Arruti and F. R. Zolessi, "Marcks phosphorylation by pkc strongly impairs cell polarity in the chick neural plate," *Genesis,* vol. 56, no. 4, 2018.

[61] S. Paramore, "A quick guide to (transmembrane) planar cell polarity mouse strains," *Nat Rev Mol Cell Biol,* 2023.

[62] S. Bae, L. Ni, A. Osinski, D. Tomchick, C. Brautigam and X. Luo, "SAV1 promotes Hippo kinase activation through antagonizing the PP2A phosphatase STRIPAK.," *eLife,* vol. 6, no. 30278, 2017.

[63] Y. Zheng, B. Liu, L. Wang, H. Lei, K. Pulgar Prieto and D. Pan, "Homeostatic Control of Hpo/MST Kinase Activity through Autophosphorylation-Dependent Recruitment of the STRIPAK PP2A Phosphatase Complex," *Cell Reports,* vol. 21, no. 12, pp. 3612-3623, 2017.

[64] H. Blencowe, V. Kancherla, S. Moorthie, M. Darlison and B. Modell, "Estimates of global and regional prevalence of neural tube defects for 2015: A systematic analysis," *Ann. N. Y. Acad. Sci.,* vol. 1414, pp. 31-46, 2018.

[65] L. Mitchell, "Epidemiology of neural tube defects.," *Am J Med Genet C Semin Med Genet,* vol. 135C, no. 1, pp. 88-94, 2005.

[66] E. S. Robinson A, K. Doudney, M. Vekemans, R. Stevenson, N. Greene, A. Copp and P. Stanier, "Mutations in the planar cell polarity genes CELSR1 and SCRIB are associated with the severe neural tube defect craniorachischisis.," *Hum Mutat,* vol. 33, no. 2, pp. 440-7, 2012.

[67] A. Copp and N. Greene, "Genetics and development of neural tube defects.," *J Pathol,* vol. 220, no. 2, pp. 217-30, 2010.

[68] J. Murdoch, C. Damrau, A. Paudyal, D. Bogani, S. Wells, N. Greene, P. Stanier and A. Copp, "Genetic interactions between planar cell polarity genes cause diverse neural tube defects in mice.," *Dis Model Mech.,* vol. 7, no. 10, pp. 1153-63, 2014.

[69] I. Roszko, A. Sawada and L. Solnica-Krezel, "Regulation of convergence and extension movements during vertebrate gastrulation by the Wnt/PCP pathway.," *Semin. Cell. Dev. Biol.,* vol. 20, pp. 986-997, 2009.

[70] P. De Marco, E. Merello, A. Consales, G. Piatelli, A. Cama, Z. Kibar and V. Capra, "Genetic analysis of disheveled 2 and disheveled 3 in human neural tube defects.," *J Mol Neurosci.,* vol. 49, no. 3, pp. 582-8, 2013.

[71] Q. Shi and Y.-G. Chen, "Regulation of Dishevelled protein activity and stability by post-translational modifications and autophagy," *Trends in Biochemical Sciences,* vol. 46, no. 12, pp. 1003-1016, 2021.

[72] E. McGreevy, D. Vijayraghavan, L. Davidson and J. Hildebrand, "Shroom3 functions downstream of planar cell polarity to regulate myosin II distribution and cellular organization during neural tube closure.," *Biol Open.* , vol. 4, no. 2, pp. 186-96, 2015.

[73] M. van der Spuy, J. Wang, D. Kociszewska and M. White, "The cellular dynamics of neural tube formation.," *Biochem Soc Trans,* vol. 51, no. 1, pp. 343-352, 2023.

[74] J. Grego-Bessa, J. Hildebrand and K. Anderson, "Morphogenesis of the mouse neural plate depends on distinct roles of cofilin 1 in apical and basal epithelial domains.," *Development.,* vol. 142, no. 7, pp. 1305-14, 2015.

[75] S. Escuin, B. Vernay, D. Savery, C. Gurniak, W. Witke, N. Greene and A. Copp, "Rho -Kinase-Dependent Actin Turnover and Actomyosin Disassembly are Necessary for Mouse Spinal Neural Tube Closure.," *J. Cell Sci. 2015, 128, 2468–2481.,* vol. 128, pp. 2468-2481, 2015.

[76] M. Butler, N. Short, E. Maniou, P. Alexandre, N. Greene, A. Copp and G. Galea, "Rho kinase-dependent apical constriction counteracts M-phase apical expansion to enable mouse neural tube closure.," *J Cell Sci.,* vol. 132, no. 13, 2019.

[77] D.-L. Shi, "Wnt/planar cell polarity signaling controls morphogenetic movements of gastrulation and neural tube closure," *Cellular and Molecular Life Sciences,* vol. 79, no. 586, 2022.

[78] M. Williams, W. Yen, X. Lu and A. Sutherland, "Distinct apical and basolateral mechanisms drive planar cell polarity-dependent convergent extension of the mouse neural plate.," *Dev Cell.,* vol. 29, no. 1, pp. 34-46, 2014.

[79] P. Ybot-Gonzalez, D. Savery, D. Gerrelli, M. Signore, C. Mitchell, C. Faux, N. Greene and A. Copp, "Convergent extension, planar-cell-polarity signalling and initiation of mouse neural tube closure.," *Development,* vol. 134, no. 4, pp. 789-99, 2007.

[80] C. Buckley and D. St Johnston, "Apical–basal polarity and the control of epithelial form and function.," *Nat Rev Mol Cell Biol,* vol. 23, pp. 559-577, 2022.

[81] E. Hong, P. Jayachandran and R. Brewster, "The polarity protein Pard3 is required for centrosome positioning during neurulation.," *Dev Biol.,* vol. 341, no. 2, pp. 335-45, 2010.

[82] P. Chavali, M. Pütz and F. Gergely, "Small organelle, big responsibility: the role of centrosomes in development and disease.," *Philos Trans R Soc Lond B Biol Sci. ,* vol. 369, no. 1650, 2014.

[83] E. Taverna, F. Mora-Bermúdez, P. Strzyz, M. Florio, J. Icha, C. Haffner, C. Norden, M. Wilsch-Bräuninger and W. Huttner, "Non-canonical features of the Golgi apparatus in bipolar epithelial neural stem cells.," *Sci Rep. 2016 Feb 16;6:21206. doi: 10.1038/srep21206. PMI,* vol. 6, no. 21206, 2016.

[84] S. Kim, A. Hill, M. Warman and P. Smits, "Golgi disruption and early embryonic lethality in mice lacking USO1," *PLoS One,* vol. 7, no. 11, p. E50530, 2012.

[85] J. Brown and M. García-García, "Secretory pathway calcium ATPase 1 (SPCA1) controls mouse neural tube closure by regulating cytoskeletal dynamics.," *Development ,* vol. 145, no. 19, p. dev170019, 2018.

[86] J. Merte, D. Jensen, K. Wright, S. Sarsfield, Y. Wang, R. Schekman and D. Ginty, "Sec24b selectively sorts Vangl2 to regulate planar cell polarity during neural tube closure.," *Nat Cell Biol.,* vol. 12, no. 1, pp. 41-6, 2010.

[87] J. Mlynarova, M. Trentin-Sonoda, F. Gaisler da Silva, J. Major, M. Salih, M. Carneiro-Ramos and B. Tuana, "SLMAP3 isoform modulates cardiac gene expression and function.," *PLoS One,* vol. 14, no. 4, 2019.

[88] A. Dewan, M. Salih, C. Triggle, H. Ding and B. Tuana, "Sarcolemmal Membrane Associated Protein Isoform 1: a Unique Regulator of Glucose Uptake and Metabolism in the Myocardium [Abstract]," *http://circres.ahajournals.org/content/117/Suppl_1/A235.abstract,* 2015.

[89] M. Lohia, Y. Qin and I. Macara, "The Scribble polarity protein stabilizes E-cadherin/p120-catenin binding and blocks retrieval of E-cadherin to the Golgi," *PLoS One,* vol. 7, no. 11, p. e51130, 2012.

[90] J. Murdoch, D. Henderson, K. Doudney, C. Gaston-Massuet, H. Phillips, C. Paternotte, R. Arkell, P. Stanier and A. Copp, "Disruption of scribble (Scrb1) causes severe neural tube defects in the circletail mouse.," *Hum Mol Genet.,* vol. 12, no. 2, pp. 87-98, 2003.

[91] T. Nishimura, H. Honda and M. Takeichi, "Planar Cell Polarity Links Axes of Spatial Dynamics in Neural-Tube Closure," *Cell,* vol. 149, no. 5, pp. 1084-1097, 2012.

[92] D. Eom, S. Amarnath and S. Agarwala, "Apicobasal polarity and neural tube closure.," *Dev Growth Differ,* vol. 55, no. 1, pp. 164-72, 2012.

[93] A. Lesko, R. Keller, P. Chen and A. Sutherland, "Scribble mutation disrupts convergent extension and apical constriction during mammalian neural tube closure.," *Dev Biol.,* vol. 478, pp. 59-75, 2021.

[94] J. Métais, C. Navarro, M. Santoni, S. Audebert and J. Borg, "hScrib interacts with ZO-2 at the cell-cell junctions of epithelial cells.," *FEBS Lett.,* vol. 579, no. 17, pp. 3725-30, 2005.

SUPPLEMENTAL FIGURES:

Supplemental Table 1. *RNA-sequencing of Wt and SLMAP3-KO displaying the transcript reads of Hippo signaling, BMP signaling, SSh and Wnt signaling. N=4*

Hippo Signaling Target Genes	fpkm.KOAC10.2.WT	fpkm.KOAC8.1.WT	fpkm.KOAC10.7.WT	fpkm.KOAC9.1.WT	fpkm.KOAC8.6.KO	fpkm.KOAC10.5.KO	fpkm.KOAC10.8.KO		
mgi_symbol	WT1	WT2	WT3	WT4	KO-1	KO-2	KO-3	pvalue	log2FC
AMOTL2	37.46638281	42.27011598	39.31594084	47.6095203	44.29933533	39.43637448	44.75270769	0.948798203	0.01414899
ANKRD1	12.85905939	12.88817308	9.689267881	9.97859107	12.89851396	12.34509942	12.43134728	0.743777092	0.039541992
ARHGEF17	22.46255433	24.23565897	23.51428407	22.02722899	22.74448917	22.02049211	20.17230262	0.679900336	-0.053526799
ASAP1	25.15107164	25.22880531	24.28673246	26.9620398	25.06145584	24.27282612	28.42850432	0.955717542	0.013446554
AXL	23.36733438	29.00989981	29.18033045	27.98698866	21.48572993	26.35003579	21.31609058	0.3193209	-0.123359341
BIRC2	20.88791591	23.1706823	21.4998513	17.87628087	21.27555881	23.10733593	20.08880891	0.943214737	0.014761547
BIRC5	116.6208529	123.8567549	116.8290648	116.1957199	113.9634306	108.0327302	134.7451479	0.990885878	0.000455
CCDC80	9.451373421	8.156799683	9.740125306	13.22806895	12.9955429	7.137482074	7.070498129	0.879343036	-0.015222899
CCN1	13.55647834	18.32685194	16.51870911	14.3793285	14.944827	12.53799631	18.17718303	0.963926421	-0.008404008
CCN2	11.89983107	12.77918172	11.89601076	12.31933984	11.04369026	11.57120347	12.35509184	0.814200506	-0.035483023
CCNA2	78.58924577	86.50833465	77.18036004	79.47613795	88.69440138	81.70299895	92.3469074	0.518661163	0.075683118
CCNB1	110.7501695	112.5353907	114.324358	101.0805749	120.9481209	115.3215986	121.6866499	0.446968623	0.082193349
CDC20	95.50575008	89.73086753	88.3538796	91.54733575	93.54919107	92.85636394	106.1177706	0.672139057	0.057939466
COQ8A	1.245140342	2.813966452	1.285575274	1.622885015	1.222346197	1.266379606	2.089589475	0.91234744	-0.008966561
CRIM1	6.908360139	6.504272249	6.614846358	6.662708306	6.483446595	6.462259787	6.460649827	0.858890431	-0.028456085
DAPK1	20.3244836	19.47410408	18.88748891	18.97508879	20.09529474	19.14888999	17.88123956	0.942374834	-0.01493441
DOCK5	2.437274299	2.743536971	2.579900871	2.390599399	2.576739578	2.663005769	2.731886789	0.83783372	0.03310305
F3	3.091442382	3.203687987	2.730155174	2.89055767	2.478140784	2.479431715	3.169202816	0.817879612	-0.027379041
FJX1	16.2825021	13.80692392	14.88621168	16.29889487	13.18876565	15.34530028	12.49175681	0.559607095	-0.068629177
FOXF2	9.197802121	7.160956868	8.004636399	7.178840796	8.092600045	9.070716821	9.93000463	0.564325209	0.064501139
GADD45A	14.89954416	16.02907134	13.02710122	18.42457487	15.06964224	14.04009199	17.87791659	0.995770996	0.000892053
IGFBP3	39.90407782	43.54723561	48.75082297	49.91545206	39.87033413	43.00794932	30.00052936	0.382952133	-0.093103095
LATS2	8.787309741	9.851611951	9.020219566	9.732252215	10.21202403	8.155433895	10.28376673	0.963531726	0.011817915
MYCL	34.43535021	29.59863272	35.04587134	34.281528	32.30526602	36.76121436	34.27534116	0.917297038	0.020484525
MYOF	4.159447803	4.183642969	4.130125244	4.755958707	4.271356759	3.894778462	2.770121745	0.548421977	-0.057272271
NT5E	0.648994772	1.110687845	0.960142557	1.012097747	0.757287752	0.814552039	0.901846135	0.827776662	-0.020657943
NUAK2	**11.11013245**	**9.139083633**	**10.13887377**	**9.015577613**	**11.43902552**	**13.33656375**	**13.6664513**	**0.034195608**	0.308907744
PTPN14	6.870750512	7.240725802	7.179184395	6.620538461	7.056974396	6.899282957	5.724901872	0.793772065	-0.037080089
RBMS3	8.81828687	10.54551106	10.4196188	11.15959676	9.661837454	8.769908493	7.428672873	0.347470012	-0.112930423
SNAI2	11.43517168	13.60625929	12.91893025	16.44348582	11.95752419	10.91079248	13.08953349	0.66080614	-0.04805573
SOX2	**50.26463242**	**39.86907355**	**43.17301501**	**40.51551396**	**53.41269734**	**56.49016636**	**74.48875996**	**0.019150339**	0.415216824
TGFB2	**20.18268969**	**19.85286829**	**23.16152415**	**22.32254806**	**15.62307475**	**19.04972252**	**14.2903223**	**0.039613966**	-0.309940047

BMP Signaling Target Genes	fpkm.KOAC10.2.WT	fpkm.KOAC8.1.WT	fpkm.KOAC10.7.WT	fpkm.KOAC9.1.WT	fpkm.KOAC8.6.KO	fpkm.KOAC10.5.KO	fpkm.KOAC10.8.KO		
mgi_symbol	WT1	WT2	WT3	WT4	KO-1	KO-2	KO-3	pvalue	log2FC
Nog	4.005384987	4.08607891	4.086102122	4.365595505	5.048924561	4.512452824	4.139616724	0.913784	-0.018146
Gdf7	1.401326769	1.90235998	1.960925445	1.42810384	1.514279944	1.098614651	1.47925761	0.933938	-0.009198
Bmp1	45.38510408	54.76852032	55.10963917	65.54698632	62.83668145	48.93439244	58.65372769	0.083008	-0.217067
Bmp10	1.066342165	0.995773458	0.934882996	0.694186594	0.703657212	1.025013344	0.933571503	0.37782	0.081024
Bmp15	0.049993846	0.058621053	0.025657586	0.109950992	0.028445683	0.020594479	0.098526134	NA	-0.004729
Bmp2	2.176077086	2.719325569	2.892329762	3.098364021	3.365318443	1.926539757	2.333482085	0.34232	-0.083053
Bmp2k	5.674569138	4.496095359	6.581018389	4.910649717	5.578842149	5.381760094	4.962305921	0.889865	-0.020463
Bmp3	0.558101059	0.894359347	1.023560141	0.862091755	1.198670215	0.525020031	1.002543019	0.112145	-0.401316
Bmp4	25.49076484	32.48206963	26.65842241	26.26787965	27.98476519	26.21034548	35.00200045	0.959	-0.01063
Bmp5	4.114513284	3.720218558	4.690267274	4.730850537	5.405904499	3.588584859	3.817862053	0.304277	-0.124204
Bmp6	1.867396083	2.101774837	2.404690212	2.12160101	2.365990312	1.962278165	2.703704652	0.274896	-0.142277
Bmp7	11.22792682	11.69040038	11.24648154	11.79912664	12.59425355	13.66861605	12.08403809	0.959	0.0124074
Bmp8a	0.060064419	0.058557051	0.068521021	0.068305021	0.114831301	0.082277907	0.058679912	NA	-0.003013
Bmp8b	0.399765028	0.364316318	0.39650465	0.30795688	0.456529403	0.501940518	0.309604049	0.89663	0.0110252
Bmper	5.905258787	5.290388816	5.627276241	5.84770836	7.262051677	3.833945008	7.788850298	0.275257	-0.097355
Bmpr1a	32.17477483	32.18879239	33.84366711	35.86353318	35.56135373	32.74101524	33.22745048	0.462456	-0.07067
Bmpr1b	6.763167972	5.611455033	5.6268993	5.281131581	5.283059851	6.169610658	5.297446233	0.280768	0.1283236
Bmpr2	13.12407458	12.7028301	12.87825924	12.33601726	11.12778838	9.782775451	11.62168127	0.986507	-0.007511
Bms1	31.5005167	28.65020993	29.99604144	27.93166276	29.3135438	34.3083917	28.92826629	0.597256	0.0693087
Atoh1	1.919497414	1.580454933	1.478528426	1.094484476	1.217402428	2.47672281	1.894749354	0.389105	0.049347
Hoxb9	28.52462928	13.59462866	21.41250463	22.12015177	21.36131425	27.79482925	20.35251819	0.903021	0.0143406
Hoxb1	1.524919726	0.544910452	0.605523774	0.785064072	0.355505479	2.131979807	1.201425426	0.429314	0.021683
Hoxb2	13.41932138	10.98961092	12.01247833	11.68111708	11.76236919	15.56753297	12.79843824	0.737698	0.0416664
Hoxb3	29.40763456	26.872059	26.16047517	28.15825126	25.16311109	30.74780274	28.74903744	0.709392	0.0556827
Hoxb3os	6.592938174	4.271000018	4.001498409	6.107678582	4.070108052	8.137629205	3.609410589	0.354892	0.0537893
Hoxb4	8.499210693	6.488012252	7.439982733	6.35722148	6.938453065	9.450163881	6.630727551	0.465261	0.0792442
Hoxb5	12.1143608	10.23702889	12.43736385	11.81818516	13.88625326	13.32535626	12.63463021	0.839471	-0.029066
Hoxb5os	8.174849932	5.586433296	7.417248698	7.563774741	8.689466642	9.757779463	6.165296824	0.963454	0.0064103
Hoxb6	15.82344787	8.027656775	13.71076108	12.24064949	12.53454556	10.47740219	13.04916645	0.831707	-0.021261
Hoxb7	12.05609568	6.007279644	8.53532954	11.93903235	10.16849631	11.39178437	10.84483717	0.959	-0.007101
Hoxb8	27.34720163	16.57682801	23.99038399	25.09853399	29.73478228	23.41204761	23.75395245	0.731272	-0.037255
Hoxb9	28.52462928	13.59462866	21.41250463	22.12015177	21.36131425	27.79482925	20.35251819	0.903021	0.0143406
Hoxc10	4.230321617	0.041372182	2.741352324	3.17815905	1.342343784	0.064654521	9.211096772	0.785509	-0.003091

SSh Signaling Target Genes	fpkm.KOAC10.2.WT	fpkm.KOAC8.1.WT	fpkm.KOAC10.7.WT	fpkm.KOAC9.1.WT	fpkm.KOAC8.6.KO	fpkm.KOAC10.5.KO	fpkm.KOAC10.8.KO		
mgi_symbol	WT1	WT2	WT3	WT4	KO-1	KO-2	KO-3	pvalue	log2FC
Fkbp8	149.741843	153.1011676	156.9459327	148.7550819	153.4674185	159.9879025	164.3359409	0.971938	-0.008943
Gli1	25.46659655	23.15330204	19.71558466	24.67582262	21.48048929	33.80436867	22.80674197	0.304277	0.1253532
Gli2	12.52962115	12.4070924	12.32635647	12.17613319	11.02071206	13.12330343	12.45979198	0.722161	0.0474934
Gli3	19.80241863	17.35251872	17.49872772	18.25601421	16.19193368	19.93460328	17.24701927	0.487607	0.0825014
Luzp1	22.38455337	18.46803387	19.13718908	17.55902804	17.97042034	20.63403843	17.4622287	0.306611	0.1178748
Luzp2	1.163651407	1.371048812	1.378420856	1.237160931	1.502038071	0.833998953	1.17576928	0.716259	-0.031074
Prkaca	67.76866207	67.90300752	71.20129596	73.15642737	79.44005625	75.04032609	75.59164461	0.679397	-0.053743
Prkacb	32.12049188	32.91225607	32.72815818	31.62839645	32.54679933	28.35143957	31.71059213	0.889389	-0.027868
Ptch1	23.78829535	21.44139539	20.58361911	20.64217509	18.48620946	23.85529871	22.26501931	0.385467	0.1009815
Rab23	19.31314038	18.61212762	18.95084339	20.64151159	18.75030869	20.68327599	17.74462075	0.929704	0.0199505
Shh	8.046397223	6.650616393	5.266079691	5.470764735	3.92477135	10.02007429	7.212154368	0.117175	0.3804544
Sufu	20.67012091	21.16375806	19.54492346	20.57600024	19.69567193	22.95778514	20.99899085	0.614301	0.0602485
Tulp3	24.09700146	29.00442218	23.0442878	23.48963877	27.4723806	27.44588166	29.7292856	0.939829	0.0146883

Wnt Signaling Target Genes	fpkm.KOAC8.1.WT	fpkm.KOAC10.7.WT	fpkm.KOAC9.1.WT	fpkm.KOAC10.2.WT	fpkm.KOAC8.6.KO	fpkm.KOAC10.5.KO	fpkm.KOAC10.8.KO		
mgi_symbol	WT-1	WT-2	WT-3	WT-4	KO-1	KO-2	KO-3	padj	lg2FC
POSTN	58.93814733	52.24257392	68.82249039	60.63927148	39.18871324	46.18612203	29.32844328	**0.003735979**	**-0.5721866**
MYCN	22.27494878	21.86195412	21.91051587	26.55761041	28.21579046	27.27494664	39.14723367	0.067118946	0.336861024
JAG1	12.71521016	11.76527366	11.65317907	12.59606304	15.42513702	13.21959741	14.76410461	0.074103662	0.1966976
IRX3	17.23165622	18.43825049	15.99630084	20.16819265	20.38097312	22.42608086	25.05298085	0.080445454	0.251866567
GCG	2.260480553	2.387905864	2.965486884	2.220259521	1.517593556	0.17608988	1.122613068	0.167802139	-0.025441726
NKX2-2	3.607765217	2.728582957	3.466767967	5.10235717	5.569167411	5.081700456	5.613957485	0.175297727	0.211603354
PDK1	16.40901849	14.1614694	14.85538982	14.91520789	21.84073132	24.69790514	14.19826126	0.195770608	0.211791551
NeuroG1	6.656726009	6.396570345	7.679512765	9.878332686	8.968231451	8.870136054	12.89791026	0.318756438	0.082834512
AXIN2	26.86628767	27.12008228	26.23302853	27.90157445	28.79502752	28.62254051	32.898569	0.338768554	0.105517249
NeuroD1	6.581053729	7.000590744	7.581971894	7.134165399	8.076027247	7.490312718	8.898020404	0.364557415	0.109175273
SIX3	3.641158851	3.755394779	4.168500541	4.95322208	3.893902728	6.065207838	5.007391091	0.575652198	0.047932294
CCND1	100.1474718	99.41422593	95.69878968	107.7857915	101.5744444	105.2954562	122.3905942	0.623039099	0.06443256
FN1	214.6338341	223.1998811	205.030034	224.9253419	203.3243705	216.3435509	197.8762056	0.7129778	-0.048836983
PTGS2	0.107297788	0.104621744	0.068153688	0.101839938	0.071602711	0.064692154	0.062554965	0.730760445	-0.014005239
FGF4	0.160709502	0.078545781	0.113874834	0.085124278	0.126245464	0.03026027	0.064122077	0.803107132	-0.008211786
ZBTB2	9.406481651	8.140467312	8.593952848	7.884615211	8.916570106	8.129290176	10.37555706	0.808029975	0.034091277
SOX9	29.30592482	33.01763028	34.73552476	34.95425131	37.5707357	31.51802622	35.27027105	0.849478196	0.03047274
CDH1	4.683120096	5.200817353	5.323068368	4.761561843	4.8696467	5.170930772	5.739683833	0.854163515	0.029473581
SFRP2	53.00839682	60.31300882	71.77453882	63.9275646	50.94200844	62.61679706	67.05380767	0.953067146	-0.004890459
T	0.962047111	1.121258123	0.774332404	1.124182797	1.016062593	0.646378933	1.481409499	0.973867163	0.003727249
TBX3	13.73002391	14.34169399	12.88228973	11.32878101	15.04010681	12.49551531	12.16534797	0.982447847	0.005372638
EDA	1.889831738	2.113871604	1.732712692	1.866182158	2.13148364	1.929741872	1.679092822	0.989762119	0.002755234
GBX2	7.490245241	6.888661636	8.246849876	7.799962272	7.452826532	8.170382092	7.336874412	0.991762796	0.001263283
SP5	1.330658262	1.953240978	1.990328526	2.373575374	1.442152626	1.718846761	2.519749531	0.992972888	-0.001124374
KRT1	0.558387262	1.050199407	1.207651392	0.747175131	0.508980562	1.040282273	1.108216708	0.995027954	-0.000537407
MYC	15.17811419	14.90791975	19.1161557	12.64021999	13.03175116	13.82313312	19.40929589	0.995770996	-0.000620835
BGLAP	0.171812283	0.640628778	0.975296146	1.094392835	1.276012043	0.830701374	0.657135109	0.9999	0.002946251
CDX1	0.023060848	0.05231613	0.07608881	0.050791547	0.109534461	0.019798068	0.137457824	0.9999	0.005389659

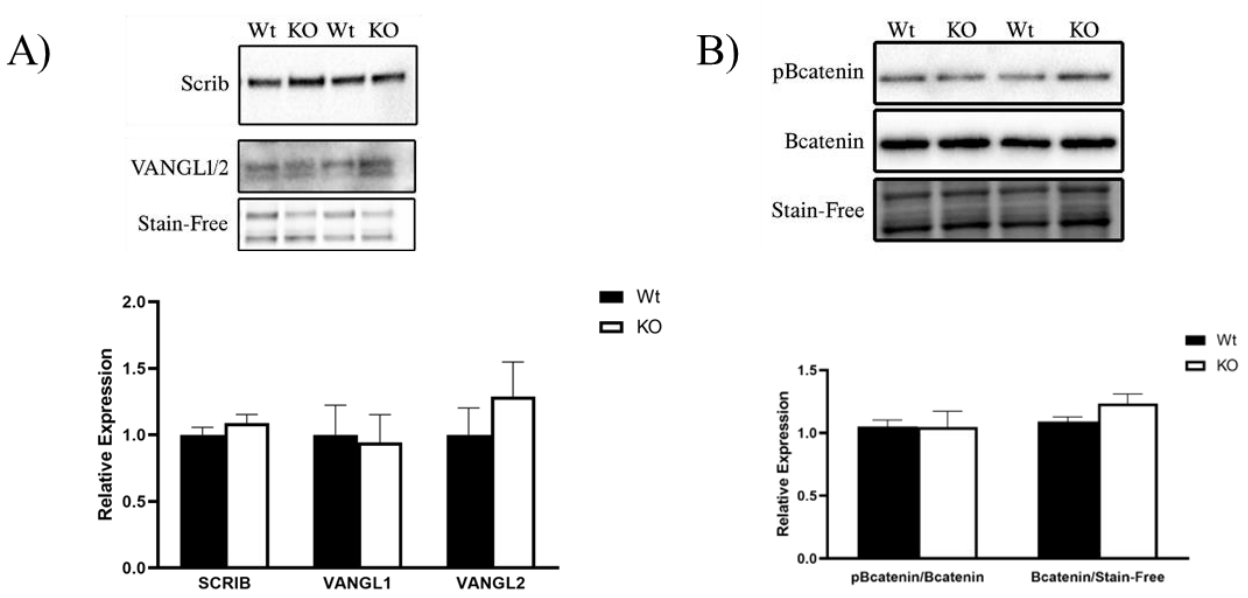

Supplemental Figure 1. *Loss of SLMAP3 does not impact other PCP signaling components or βcatenin.* Western blot with A) anti-Scrib, anti-VANGL1, and anti-VANGL2 or B) anti-phospho-βcatenin and βcatenin in Wt and KO E12.5 brain lysates. Bar graphs represent relative expression of indicated proteins normalized to Stain-Free total protein or phospho-to-total ratios. *n*=4. ρ value was calculated using non-paired two-way t-test.

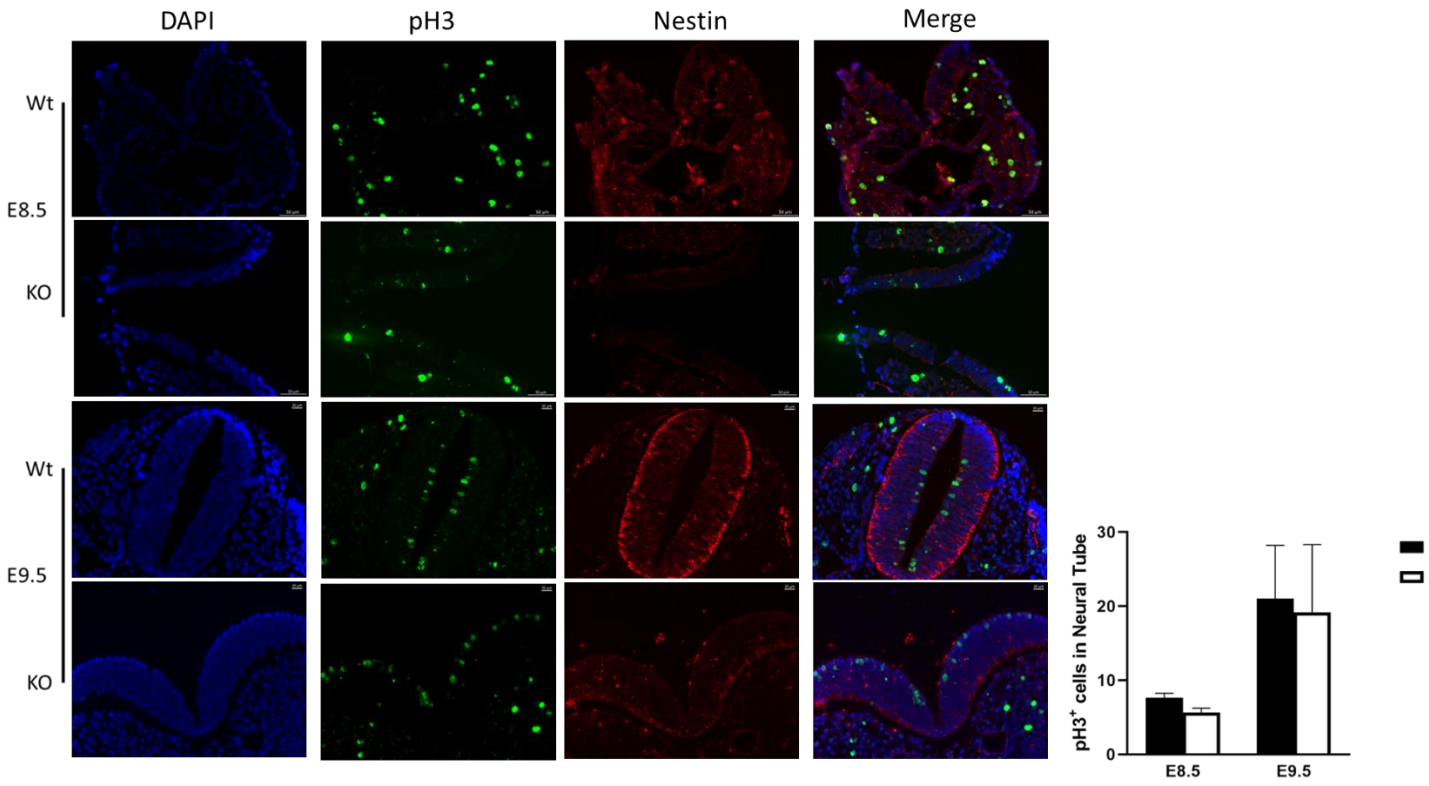

Supplemental Figure 2. *Cell proliferation in Wt and SLMAP3-KO neural tubes at E8.5 and E9.5.* Representative immunofluorescent images of sectioned Wt and KO neural tubes at E8.5 and E9.5 labelled with DAPI (nucleus), anti-phospho-histone3 (pH3, green), and anti-nestin (red). The bar graph represents the number of positive pH3 cells in nestin labelled neuroepithelial cells at E8.5 and E9.5. Lens Magnification=20x. Scale bar=0.05mm. n = 3.

Chapter Six: General Discussion and Conclusion

In this thesis my aim was to investigate the *in-vivo* role of SLMAP as studies from our lab and various research groups have identified that SLMAP isoforms may play important roles in the regulation of cell biology. My initial experimental approach was to generate a knockout mouse model to target all SLMAP isoforms as we believed that the excision of exon 3 of the SLMAP gene would disrupt transcription of all the SLMAPs. However, this genetic modification selectively impacted deletion of the largest isoform, SLMAP3, whilst expression of smaller isoforms, SLMAP2 and SLMAP1, were unaffected in prenatal and postnatal tissues. This observation suggests that the regulation of SLMAP isoforms is preserved, potentially due to the presence of alternative promoters (Ayoubi and Van De Ven 1996) located upstream of identified start sites at exons 10 and 16 for SLMAP2 and SLMAP1, respectively (**Chapter 1, Figure 1**). Therefore, utilizing the appropriate cre-driver mice I ablated SLMAP3 across numerous tissues to unravel its specific contributions to tissue development and homeostasis, thereby enhancing understanding of SLMAP3's physiological and potentially pathological roles.

6.1 Advantages and limitations using cre mouse models

Utilizing αMHC-MerCreMer, αMHC-cre, Nkx2.5-cre, and CMV-cre mouse lines, I investigated SLMAP3's role in postnatal, perinatal, prenatal hearts, and in a global context. The αMHC-Cre is widely utilized to target genes in the perinatal cardiac ventricle and atrium, although there is minute expression between E8-10.5, its robust expression is noted post birth, therefore can impact SLMAP3 in immature cardiomyocytes (Agah et al. 1997). The αMHC-MerCreMer model is a drug inducible gene targeting mouse line for greater temporal control for gene editing, activation of cre is achieved through addition of TAM (Verrou et al. 1999). Thus, this model is well-suited to evaluate SLMAP3 role in postnatal cardiac maintenance. The CMV-

cre mouse line can cause genetic modifications within the germ layers as the CMV-cre is expressed as early as zygote implantation, eviscerating SLMAP3 expression within the three germ layers allowing us to evaluate the SLMAP3 in a global context (Schwenk, Baron, and Rajewsky 1995). As loss of global SLMAP3 resulted in embryonic lethal phenotypes, it was hard to ascribe cardiac phenotypes to SLMAP3-loss or secondary effects. (Davis et al. 2012). Thus, we chose the cre-driver, Nkx2.5-cre mouse line as it is expressed within primitive cardiomyocytes during first stages of cardiogenesis; an ideal candidate to study impact of SLMAP3 during cardiogenesis (Biben et al. 2000; Stanley et al. 2002).

The cardiac-specific cre mouse models can cause cardiotoxicity as unregulated, or excessive cre recombinase activity can interfere with DNA replication and exacerbate DNA damage through genetic modifications of non-specific "lox-like" regions within the mammalian genome (Thyagarajan et al. 2000; Ito et al. 2011). In the αMHC-MerCreMer mouse model, TAM causes transient pathological cardiomyopathy that will dissipate following cessation of treatment, however an excessive dose of tamoxifen can prove lethal, due to DNA damage and myocyte death (Koitabashi et al. 2009; Bersell et al. 2013; Sohal et al. 2001). The αMHC-Cre mouse model has been extensively cited in over 150 publications (Agah et al. 1997). This model was reported to display evidence of a non-lethal HCM by 6 months of age, alluded due to DNA damage markers, p53 and Bax, being significantly upregulated in these hearts (Pugach et al. 2015). In contrast, analysis indicated that the αMHC-cre mice were exhibiting clinical features associated with lethal DCM by 7 months of age. Histological analysis on αMHC-Cre hearts indicated significantly thinner walls, dilated left ventricle and pronounced fibrosis network which was revealed by Masson's trichrome stain. ECHO analysis of αMHC-Cre hearts revealed that left ventricular walls were getting progressively thinner, revealing no evidence of HCM

before DCM took place. The molecular analysis indicated that DNA damage markers, p53 and Bax, were upregulated, thus we were unsure how to reconcile the two phenotypes. Notably, a previous study utilized a high-expressing αMHC-Cre strain (FVB) mice displayed DCM in young mice whilst lower expressers did not exhibit phenotypes although the impact of age was not examined (Buerger et al. 2006). Our αMHC-Cre caused phenotypes in hemizygous Cre^{+} mice, thus suggesting these cardiac phenotypes were due to increased activity of cre (Pugach et al. 2015). Our conclusion aligns with other studies (Davis et al. 2012; Pugach et al. 2015; Buerger et al. 2006) where we emphasize the need for caution and use of cre-only controls to avoid misattribution of cardiac phenotypes to genetic modification rather than cre-induced effects.

Finally, there is no published evidence that suggests the Nkx2.5-Cre mouse model exhibits cardiotoxicity, even though it can sustain expression until late adulthood in the postnatal myocardium (George, Colombo, and Targoff 2014). Consistent with this observation, my monitoring of heterozygous and homozygous Nkx2.5-Cre mice up to one year of age did not reveal any indication of poor health (Tuana, personal communication). Therefore, expression of Nkx2.5-cre did appear to cause any cardiac defects. For the CMV-Cre mouse model, I developed an experimental approach to "breed out" the CMV-Cre gene after generating SLMAP3-deficient mice to prevent any potential off target effects, thus ensuring the validity of our observations by ensuring phenotypic changes are linked to SLMAP3 only (**Chapter 5, Figure 1**).

6.2 The cardiac-specific knockout of SLMAP3 did not impact postnatal or perinatal mouse hearts.

Cardiovascular disease is a leading cause of death in North America, however despite recent medical advances many incidences of heart disease are idiopathic, therefore identifying cardiac regulator genes is critical (Hazebroek, Dennert, and Heymans 2012). These heart diseases display defects in sarcomere function, regulation of ion channels and ECG activity (Hazebroek, Dennert, and Heymans 2012). We and others have demonstrated that SLMAP3 is implicated in these cardiac processes, therefore we aimed to assess effects of its loss on cardiac maintenance. After successful crossing with αMHC-MerCreMer, tamoxifen was introduced to 8-week-old Wt and SLMAP3-KO mice then rested for one week to metabolize residual tamoxifen and reverse the transient cardiomyopathy. Echocardiography (ECHO) was performed every 4 weeks to identify any myocardium defects. However, ECHO analysis indicated no differences in cardiac structure or function due to postnatal loss of SLMAP3 in young or aged mice. Next, we administered isoproterenol to tamoxifen-treated mice to stress the myocardium and expose any underlying phenotypes (Major, Salih, and Tuana 2015). ECHO and histological analysis indicated an identical hypertrophic response in iso-treated Wt and SLMAP3-KO hearts implying that loss of SLMAP3 did not affect the cardiac stress response. SLMAP3 was implicated in Brugada syndrome, as SLMAP gene in patients had point mutations at exon 8 and 21 (Ishikawa et al. 2012). These mutations were shown to impair the trafficking of hNav1.5 and reduce electrophysiological signaling in transfected cells expressing mutant-SLMAP (Ishikawa et al. 2012). However, SLMAP3-KO ECG analysis indicated no significant differences in any cardiac-conduction parameters despite a minor decrease in Nav1.5 protein expression. Interestingly, in SLMAP3 overexpression model, we discovered a 50% reduction in the transcript and protein

level of Nav1.5 with minor aberrations in the ECG analysis (Mlynarova et al. 2019). Thus, SLMAP3 has a unique relationship with Nav1.5, however the intricacy of it remains elusive.

Further, as postnatal cardiac growth primarily occurs through the process of cardiomyocyte maturation, we sought to determine the impact of SLMAP3 on cardiomyocyte maturation we crossed with αMHC-Cre (Tuana, unpublished). ECHO analysis on 7-week-old to 12-week-old experimental mice displayed no significant differences in cardiac structure or function due to SLMAP3 deficiency. To invoke stress, we dosed these mice with ISO to provoke pathological hypertrophy in immature cardiomyocytes and potentially exacerbate a cardiac phenotype, (Yoshida T 2014; Cheng et al. 2023) however echocardiographic analysis revealed that SLMAP3-deficient mice exhibited cardiac responses identical to Wt. Therefore, our findings suggest that the perinatal loss of SLMAP3 does not significantly impact cardiomyocyte function.

Despite the complete ablation of SLMAP3 in the postnatal or perinatal mouse heart, they exhibited normal cardiac maintenance and maturation highlighting potential compensatory mechanism. SLMAP1 and SLMAP2 expression were unaffected however were approximately ninefold higher compared to SLMAP3 in the neonatal myocardium (Wielowieyski et al. 2000). SLMAP1 and SLMAP2 appear as truncated SLMAP3 variants, with conserved sequence identity at the c-terminus, housing identical protein interaction domains, and anchoring subcellular domains with TM1/TM2, therefore they may functionally compensate (Wielowieyski et al. 2000; Nader et al. 2012; Mlynarova et al. 2019). Thus, the interplay between these SLMAP isoforms could provide valuable insights into the molecular mechanisms underlying cardiac maintenance, particularly in the context of SLMAP3 deficiency.

6.3 Loss of SLMAP3 does not impact Hippo signaling

SLMAP3 is shown to negatively regulate the Hippo signaling pathway which will enhance cell proliferation, repress apoptosis, maintain tissue homeostasis and mediate organogenesis via transcriptional coactivators YAP and TAZ. (R. Chen, et al. 2019, Bae, et al. 2020, Zhou, et al. 2015). We aimed to investigate the impact to Hippo signaling in SLMAP3-null perinatal and postnatal heart as studies have shown that dysregulation of Hippo signaling in adult mice can lead to pathological outcomes such as pressure overload or heart failure (Del Re et al. 2013; Yamamoto et al. 2003; Wang et al. 2014; Xin et al. 2013). However no significant differences were noted in phosphorylation states of Hippo activating kinase, MST1/2 or YAP in SLMAP3-KO hearts compared to wildtype myocardium. The minimal impact in Hippo signalling due to perinatal/postnatal SLMAP3 ablation could be attributable to the extremely low proliferative rates of cardiomyocytes in postnatal heart development since Hippo signaling reaches its peak as early as 10 days of age in mice (Heallen et al. 2013; Bergmann et al. 2009).

Thus, our next aim was to assess the loss of SLMAP3 in prenatal tissues and hearts by crossing flox-SLMAP mouse line with CMV-Cre and Nkx2.5-cre. The prenatal global loss of SLMAP3 resulted in embryonic lethality with embryos presenting with dwarfed body, shorter limbs, and organs, whilst prenatal cardiac specific loss impacted cardiac size, all these phenotypes are linked to defective Hippo signaling (Misra and Irvine 2018; von et al. 2012). Phospho-protein expression analyzing activation of MST1/2 or YAP in SLMAP3-KO whole embryo, E12.5 brain or E16.5 cardiac lysates determined that Hippo signaling was not affected. Further, we performed RNA-Seq analysis on E11.5 whole embryos that in the absence of SLMAP3 did not significantly affect the target genes of many developmental signaling pathways, including Hippo signaling. (Durocher and Jackson 2002; Tang et al. 2019; Zhou et al.

2015). Thus, embryonic and cardiac size alterations in SLMAP3-KO embryos is not mediated through Hippo signaling.

Hippo signaling may not be affected due to a functional redundancy as several upstream kinases that can interact with striatin isoforms to create "alternative" STRIPAK complexes that can regulate Hippo signaling such as STK25, Striatin-3/4 and MAP4K4, as well as extracellular signaling molecular lysophosphatidic acid (Zheng et al. 2020) (Seo et al. 2020; Bae, Ni, and Luo 2020; Chen et al. 2019; Migliavacca et al. 2022). It is imperative to acknowledge that most studies investigating SLMAP-STRIPAK and Hippo signaling were conducted in highly proliferative cell lines such as HEK293 or in *Drosophila*. Thus, in an *in-vivo* mouse model, it does not appear that SLMAP3 alone can sufficiently disrupt Hippo signaling.

6.4 SLMAP3 delays embryonic cardiac development

SLMAP3 is robustly expressed within the developing myocardium, thus, we aimed to examine its impact during cardiac development by implementing the Nkx2.5-cre mouse line, which would ablate SLMAP3 during development of the atria, ventricles and outflow tract (Ma, Zhou, and Pu 2008; Stopp et al. 2017; Lopes et al. 2011). We discovered that the loss of SLMAP3 impacted myocardium size resulting in smaller hearts. However, there were no visible defects during septation of the ventricles, atria formation or outflow tract defects, evidenced by presence of 4-chambers at E12.5. This suggests that loss of SLMAP3 does not impact FHF/SHF differentiation or migration as these processes regulate cardiac chamber formation and septation (Chiapparo et al. 2016). The size differences were not linked with improper cardiomyocyte proliferation as cardiomyocytes displayed no significant changes to G2/M cell cycle marker, pH3 or G1 cell cycle marker Ki67. As cardiomyocyte proliferation was not affected, cardiogenesis

pathways such as Notch, Wnt/βCatenin, and FGF signaling were likely not affected either (Srivastava 2006).

We found that cardiomyocytes was significantly smaller in E12.5 SLMAP3-KO hearts, however this was not due to any impact to cardiomyocyte hypertrophy PI3K-AKT-MTOR pathway (Aoyagi and Matsui 2011) as analysis showed that AKT and MTOR were not significantly altered, suggesting that these cardiomyocytes are smaller due to other factors. We have previously shown that SLMAP3 interacts with Scribble, with global loss of SLMAP3 impacting Scribble localization, ABP protein localization, and defects in PCP signaling (Rehmani et al. Submitted). Cardiac-specific Scribble ablation caused cardiomyocyte disorganization in developing hearts, resulting in a transient non-lethal cardiac hypoplastic-like phenotype (Phillips et al. 2007; Boczonadi et al. 2014; Stephens et al. 2018). During early differentiation of the cardiac crescent, the heart will form a linear heart or heart tube which will exhibit epithelial properties. Research has shown regulation of ABP or PCP signaling is essential in the generation of the linear heart tube from cardiac crescent stage through the convergence of crescent to the midline and FHF/SHF migration to the arterial/venous poles (Cortes et al. 2018). Further, affecting "core" PCP signaling proteins (VANGL, FZD, DVL, Prickle) results in predominantly critical CHDs such as major septal defects and/or OFT alignment defects including double outlet right ventricle, overriding aorta, and tetralogy of Fallot (Li and Wang 2018). We did not observe any defects in septum or OFT, however disrupting PCP or ABP through Scrib or Rac1, can also result in minor CHDs that are similar to SLMAP3-KO model (Leung et al. 2021). Thus, we aim to investigate the early cardiac developmental stages to determine if the cardiac crescent or linear heart tube are affected in SLMAP3-KO model and if phenotypes are linked to Scrib, ABP, and PCP signalling.

Our recent publication highlights that SLMAP3 ablation causes a significant mislocalization of the centrosome and Golgi apparatus around the nucleus, impacting myofibril length in embryos and C2C12 myoblasts (Dias et al. 2023). This was linked to SLMAP3 predominantly interacting with centrosomal (pericentrin, AKAP9) and Golgi (Golga3, Golgb1) proteins in IP-MS. The myoblast cell and prenatal cardiomyocytes have similar cell architecture and studies have shown that centrosome and Golgi have been implicated in cardiomyocyte hypertrophy (Vergarajauregui et al. 2020; Nash et al. 2019).

By birth, the SLMAP3-KO hearts displayed relatively normal hearts. Echocardiographic evaluation of 10-week-old SLMAP3-null mice revealed no defects in cardiac structure or function. Despite the apparent normalcy in these animals, it is imperative to conduct further evaluations under stress conditions to exclude latent cardiac dysfunctions. For example, mice rendered incapable of oxidizing the ketone body 3-hydroxybutyrate through BDH1 inactivation displayed normal cardiac function under basal conditions, however through pathological overload and ischemic stress, these mice exhibited worsened heart failure (Horton et al. 2019). Thus, hearts may appear normal but may house undiscovered defects due to defective cardiac maturation.

As discussed earlier, SLMAP1 and SLMAP2 isoforms are identical to the c-terminus of SLMAP3 therefore they might functionally compensate as truncated variants of SLMAP3 (Guzzo et al. 2004). We discovered that the expression levels of SLMAP1 and SLMAP2 exponentially increased as the myocardium develops. The rat embryonic cardiomyocytes (H9C2 cells) were found to the express SLMAP1, SLMAP2 and SLMAP3 with identical molecular characteristics as mouse hearts and we discovered that total SLMAP depletion resulted in a significant decrease in growth and proliferation with enhanced senescence in these embryonic

myocytes. This data supports the contention that SLMAP isoforms are collectively critical for cardiomyocyte growth and that they can potentially compensate for each other. The depletion of SLMAP in H9C2 cardiomyocytes emphasizes the need to assess SLMAP1 and SLMAP2 *in-vivo* to evaluate heart and global tissue development/maintenance.

6.5 SLMAP3 is required for neural tube closure

Global loss of SLMAP3 resulted in lethality, as these mouse embryos displayed stunted growth, truncated tail, facial retrusion, and NTDs. SLMAP3-KO embryos mainly exhibited the fatal NTD, craniorachischisis, however we noted one instance of spina bifida and exencephaly. NTDs arise from defective neurulation implicating SLMAP3 as a key regulator during neurulation and suggests its specific involvement in the pathogenesis of NTDs, specifically craniorachischisis (Copp and Greene 2013). We attribute these neurulation defects through abnormal centrosomal positioning and Golgi formation which could perturb PCP or ABP in SLMAP3-KO mice.

The E8.5 and E9.5 SLMAP3-KO embryos were significantly shorter and wider whilst displaying significantly thinner and wider neural plate, thus implicating defective convergent extension. As convergent extension is mediated by the PCP signaling pathway (van der Spuy et al. 2023), analysis revealed substantial changes to the expression of PCP signaling transducers, DVL2 and DVL3 and downstream signaling targets ROCK2, Cofilin, and JNK. This is a significant finding as inhibiting PCP and ablating actin cytoskeletal regulators can causes incomplete neurulation at cranial and spinal regions causing NTDs (Escuin et al. 2015; Butler et al. 2019; Grego-Bessa, Hildebrand, and Anderson 2015; Roszko, Sawada, and Solnica-Krezel 2009). Our data suggests that DVL2 and DVL3 are dysregulated which could identify a plausible mechanism resulting in observed phenotypes as DVLs are tightly regulated by ubiquitination as their expression can enhance or inhibit the propagation of the Wnt signaling within tissues or embryo (De Marco et al. 2013; Shi and Chen 2021). Interestingly, SLMAP3 has been shown to interact with complexes that can regulate DVL expression, PLEKHA4-CUL3-KLHL12, USP9X and Prickle1/2, thus implicating that SLMAP3 may regulate posttranscriptional modification of

DVLs however it requires further investigation (Shami Shah et al. 2019; Pourhaghighi et al. 2020; Chan et al. 2006; Nielsen et al. 2019).

Our investigation revealed a marked reduction in the apical localization of actin filaments in SLMAP3-KO neural tubes, indicating that these cells may not be able to undergo apical constriction, a necessary phase in bending and fusing the neural tube. We assessed ABP domain localization of other proteins, PKCζ and Nestin, and found they were not within their specific apical or basal domain. Further, as it appeared that these neuroepithelial cells had impacted polarity, we assessed the localization of AJs and TJs as the proper localization of these junctions has conventionally been used to assess the cell polarity (Zihni et al. 2016). We discovered that AJs and TJs localization was impacted in SLMAP3-KO NTs and SLMAP3-deficient NE-4C cells. Thus, findings indicate that SLMAP3-KO may compromises ABP to impede proper cell formation, thereby obstructing processes like convergent extension, PCP signaling and/or NTC (Eom, Amarnath, and Agarwala 2012).

The PCP axis and the ABP polarity axis cooperate to generate polarized cell behavior and intercalation to narrow and elongate the NT for proper folding and fusion (Nishimura, Honda, and Takeichi 2012). Proteomic analysis displayed an interaction of SLMAP3 with the polarity protein, Scrib. Further, we showed that SLMAP3 guides Scrib as we saw aberrant junctional localization in SLMAP3-deficient NTs and NE-4C cells. Scrib may serves as a molecular bridge linking PCP and ABP, as aberrant expression is linked with mislocalization of PCP (VANGL2) and ABP components (AJs and TJs) impacting convergent extension and apical constriction, and causing craniorachischisis (Lesko et al. 2021; Murdoch et al. 2003). Thus, SLMAP3 may mediate Scrib localization and stability of AJs and TJs thus causing the craniorachichisis defect we mainly observed.

We observed a predominant interaction of SLMAP3 with centrosomal and Golgi proteins in proteomic analysis. Centrosomal and Golgi are localized apically and can regulate ABP as they can mediate microtubule nucleation and transport of vesicles to proper domains (Buckley and St Johnston 2022). SLMAP3-deficiency impacted the centrosomal intensity at apical regions whilst causing Golgi to become increasingly fragmented in neural tubes and primary neuroepithelial cells. In mice, knockout of centrosomal proteins (Chavali, Pütz, and Gergely 2014) can cause NTD, while Golgi is linked with neuronal defects such as ataxia, altered brain development, and embryonic lethality (Taverna and Huttner 2019; Kim et al. 2012; Liu et al. 2016). Interestingly, inhibiting the transport of proteins from ER-to-Golgi via Sec24b and improper Golgi calcium homeostasis via SPCA1, result in craniorachischisis, suggesting that proper Golgi function can regulate neurulation (Brown and García-García 2018; Merte et al. 2010).

NTDs represent some of the most common birth defects globally, approximately affecting 1% births (Blencowe et al. 2018). NTDs are linked to folate metabolism and genetic mutations in PCP components, however many cases are idiopathic, particularly craniorachischisis, and implicated to arise from genetic defects (Murdoch et al. 2014). Our results highlight that SLMAP3 could be considered a potential genetic biomarker for NTDs, thus, it is imperative to evaluate SLMAP expression in patients exhibiting NTDs.

Conclusion:

Overall, this data defines SLMAP3 as a novel and critical component of embryonic development without impacting Hippo signaling. We show that SLMAP3 is the only isoform expressed in neural tubes thus its loss impacted neurulation due to mislocalization of Scrib, AJs and TJs, through altered centrosomal and Golgi dynamics which could perturb PCP and ABP causing NTDs (**Figure 1A**). Cardiac-specific prenatal loss of SLMAP3 is shown to impact cardiogenesis, resulting in a smaller and thinner myocardium, which resolves by birth, characterizing this defect as a minor CHD (**Figure 1B**). However, as the knockdown of total SLMAP impacted growth and enhanced senescence in embryonic cardiomyocytes (**Figure 1B**), it suggests that SLMAP1 and SLMAP2 may functionally compensate potentially reversing the prenatal cardiac phenotype. Further, the perinatal and postnatal cardiac-specific knockout of SLMAP3 had no impact, which may also be due to accumulation of SLMAP1 and SLMAP2 in postnatal myocardium. Thus, this advances our understanding of SLMAP3's function and highlights its potential involvement in various diseases states, including, cardiogenesis, neurulation, and stunted growth, which should consider SLMAP as a potential as a biomarker for NTDs and CHDs.

A)

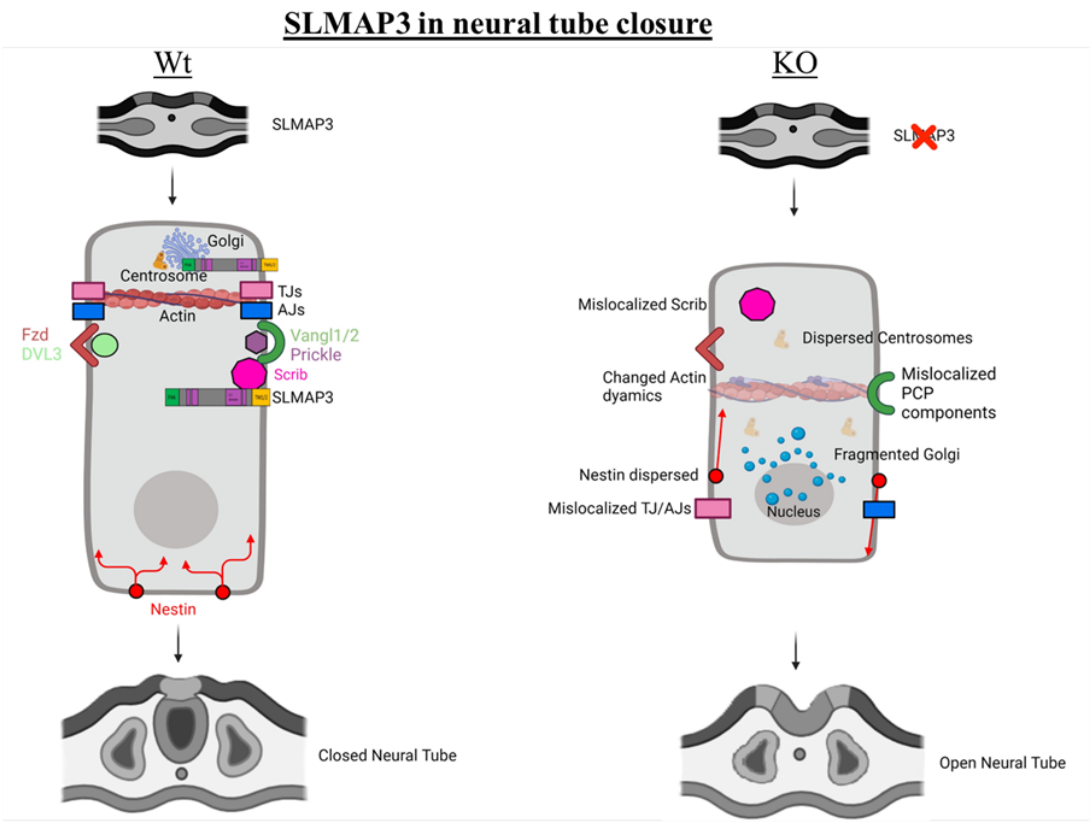
SLMAP3 in neural tube closure
Wt
KO
SLMAP3
Golgi
Centrosome
TJs
AJs
Actin
Fzd
DVL3
Vangl1/2
Prickle
Scrib
SLMAP3
Nestin
Closed Neural Tube
Mislocalized Scrib
Dispersed Centrosomes
Changed Actin dyamics
Mislocalized PCP components
Fragmented Golgi
Nestin dispersed
Mislocalized TJ/AJs
Nucleus
Open Neural Tube

B)

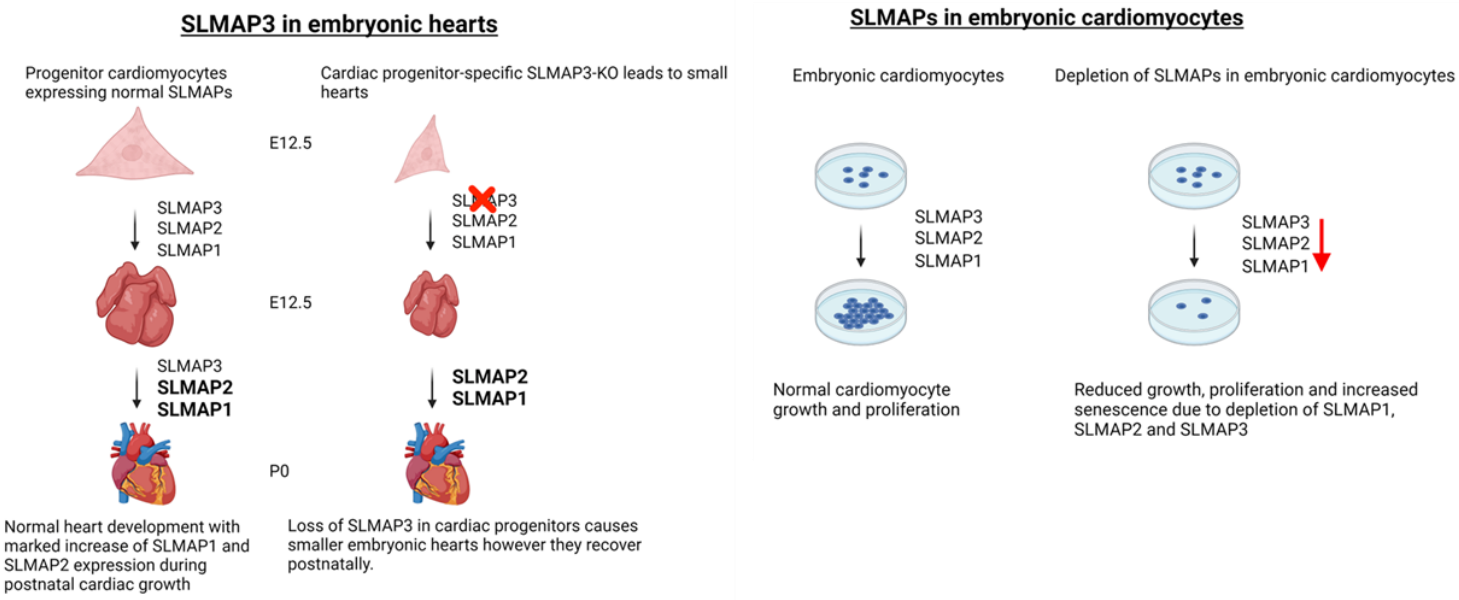
SLMAP3 in embryonic hearts
Progenitor cardiomyocytes expressing normal SLMAPs
Cardiac progenitor-specific SLMAP3-KO leads to small hearts
E12.5
SLMAP3
SLMAP2
SLMAP1
E12.5
SLMAP3
SLMAP2
SLMAP1
P0
Normal heart development with marked increase of SLMAP1 and SLMAP2 expression during postnatal cardiac growth
Loss of SLMAP3 in cardiac progenitors causes smaller embryonic hearts however they recover postnatally.
SLMAPs in embryonic cardiomyocytes
Embryonic cardiomyocytes
Depletion of SLMAPs in embryonic cardiomyocytes
SLMAP3
SLMAP2
SLMAP1
SLMAP3
SLMAP2
SLMAP1
Normal cardiomyocyte growth and proliferation
Reduced growth, proliferation and increased senescence due to depletion of SLMAP1, SLMAP2 and SLMAP3

Figure 1. *Loss of SLMAP impacts development*. A) SLMAP can impact neurulation. As neuroepithelial cells express only SLMAP3, its loss leads to fragmented Golgi, dispersed centrosomes, altered PCP signaling, mislocalized TJ/AJs, Scrib and actin resulting in smaller, unpolarized cells unable to complete neurulation. Figure modified with permission from Rehmani (Tuana) B) SLMAPs are essential for normal cardiac development. Loss of SLMAP3 resulted in smaller cardiomyocytes that formed a smaller embryonic heart. The SLMAP3-KO embryonic myocardium recovered with age, potentially due to accumulation of SLMAP isoforms during postnatal cardiac growth. The depletion of all SLMAP isoforms led to significantly reduced growth of embryonic cardiomyocytes, thus could prevent the proper formation and function of the heart.

Chapter Seven: References

Agah, R, PA Frenkel, BA French, LH Michael, PA Overbeek, and MD Schneider. 1997. "Gene recombination in postmitotic cells. Targeted expression of Cre recombinase provokes cardiac-restricted, site-specific rearrangement in adult ventricular muscle in vivo." *J Clin Invest* 100(1):169-79.

Aken, BL, S Ayling, D Barrell, and et al. 2016. "The Ensembl gene annotation system." *Database* baw093:Release 90.

Amin, S, A., Tan Hanno, and Arthur Wilde. 2010. "Cardiac ion channels in health and disease." *Heart Rhythm* 7(1):117-126.

An, L, Z Cao, P Nie, H Zhang, Z Tong, F Chen, Y Tang, Y Han, W Wang, Z Zhao, Q Zhao, Y Yang, Y Xu, G Fang, L Shi, H Xu, H Ma, S Jiao, and Z Zhou. 2022. "Combinatorial targeting of Hippo-STRIPAK and PARP elicits synthetic lethality in gastrointestinal cancers." *J Clin Invest* 132(9):e155468.

Aoyagi, T and T Matsui. 2011. "Phosphoinositide-3 kinase signaling in cardiac hypertrophy and heart failure.." *Curr Pharm Des.* 17(18):1818-24.

Ayoubi, TA and WJ Van De Ven. 1996. "Regulation of gene expression by alternative promoters." *FASEB J* 4(10):453-60.

Azimzadeh, O., T. Azizova, J. Merl-Pham, A. Blutke, M. Moseeva, O. Zubkova, N. Anastasov, A. Feuchtinger, S.M. Hauck, M.J. Atkinson, and S Tapio. 2020. "Chronic Occupational Exposure to Ionizing Radiation Induces Alterations in the Structure and Metabolism of the Heart: A Proteomic Analysis of Human Formalin-Fixed Paraffin-Embedded (FFPE) Cardiac Tissue.." *Int. J. Mol. Sci.* 21(18):6832.

Bae, SJ, L Ni, and X Luo. 2020. "STK25 suppresses Hippo signaling by regulating SAV1 -STRIPAK antagonism." *Elife* 9(e54863).

Bae, SJ, L Ni, A Osinski, DR Tomchick, CA Brautigam, and X Luo. 2017. "SAV1 promotes Hippo kinase activation through antagonizing the PP2A phosphatase STRIPAK.." *eLife* 6(30278).

Balse, E, D,F Steele, H Abriel, A Coulombe, D Fedida, and N Hatem S. 2012. "Dynamic of ion channel expression at the plasma membrane of cardiomyocytes." *Physiol Review* 92(3):1317-58.

Bergmann, O, RD Bhardwaj, S Bernard, S Zdunek, F Barnabé-Heider, S Walsh, J Zupicich, K Alkass, BA Buchholz, H Druid, S Jovinge, and J Frisén. 2009. "Evidence for cardiomyocyte renewal in humans." *Science* 324(5923):98-102.

Bersell, K, S Choudhury, M Mollova, B, D. Polizzotti, B Ganapathy, S Walsh, B Wadugu, S Arab, and B Kühn. 2013. "Moderate and high amounts of tamoxifen in αMHC-MerCreMer mice induce a DNA damage response, leading to heart failure and death." *Disease Models & Mechanisms* 6(6):1459-69.

Biben, C, R Weber, S Kesteven, E Stanley, L McDonald, DA Elliott, L Barnett, F Köentgen, L Robb, M Feneley, and RP Harvey. 2000. "Cardiac septal and valvular dysmorphogenesis in mice heterozygous for mutations in the homeobox gene Nkx2-5." *Circ Res* 87(10).

Björkblom, B, A Padzik, H Mohammad, N Westerlund, E Komulainen, P Hollos, L Parviainen, AC Papageorgiou, K Iljin, O Kallioniemi, M Kallajoki, MJ Courtney, M Mågård, P James, and ET Coffey. 2012. "c-Jun N-terminal kinase phosphorylation of MARCKSL1 determines actin stability and migration in neurons and in cancer cells.." *Mol Cell Biol.* 32(17):3513-26.

Blencowe, H., V. Kancherla, S. Moorthie, M.W. Darlison, and B Modell. 2018. “Estimates of global and regional prevalence of neural tube defects for 2015: A systematic analysis.” *Ann. N. Y. Acad. Sci.* 1414:31-46.

Boczonadi, V, R Gillespie, I Keenan, SA Ramsbottom, C Donald-Wilson, M Al Nazer, P Humbert, RJ Schwarz, B Chaudhry, and DJ Henderson. 2014. “Scrib:Rac1 interactions are required for the morphogenesis of the ventricular myocardium.” *Cardiovasc Res* 104(1):10.

Boutros, M, N Paricio, DI Strutt, and M Mlodzik. 1998. “Dishevelled activates JNK and discriminates between JNK pathways in planar polarity and wingless signaling.” *Cell* 94(1):109-18.

Brade, T, LS Pane, A Moretti, KR Chien, and KL Laugwitz. 2013. “Embryonic Heart Progenitors and Cardiogenesis.” *Cold Spring Harb Perspect Med.* 3(10):a013847.

Branda, CS and SM Dymecki. 2004. “Talking about a revolution: The impact of site-specific recombinases on genetic analyses in mice.” *Dev Cell* 6(1):7-28.

Brown, JM and MJ García-García. 2018. “Secretory pathway calcium ATPase 1 (SPCA1) controls mouse neural tube closure by regulating cytoskeletal dynamics.” *Development* 145(19):dev170019.

Brugada, R, O Campuzano, G Sarquella-Brugada, J Brugada, and P Brugada. 2014. “Brugada syndrome.” *Methodist Debakey Cardiovasc J* 10(1):25-8.

Bruneau, B. 2002. “Transcriptional Regulation of Vertebrate Cardiac Morphogenesis.” *Circ Res.* 90(5):509-19.

Buckley, C.E. and D St Johnston. 2022. “Apical–basal polarity and the control of epithelial form and function.” *Nat Rev Mol Cell Biol* 23:559-577.

Buerger, A, O Rozhitskaya, MC Sherwood, AL Dorfman, E Bisping, Abel, ED, WT Pu, S Izumo, and PY Jay. 2006. “Dilated cardiomyopathy resulting from high-level myocardial expression of Cre-recombinase.” *J Card Fail* 12(5):392-8.

Buijtendijk, MFJ, P Barnett, and MJB van den Hoff. 2020. “Development of the human heart.” *Am J Med Genet C Semin Med Genet* 184(1):7-22.

Burchfield, JS, Min Xie, and J Hill. 2013. “Pathological Ventricular Mechanisms.” *Circulation* 128(4):388-400.

Butler, MB, NE Short, E Maniou, P Alexandre, NDE Greene, AJ Copp, and GL Galea. 2019. “Rho kinase-dependent apical constriction counteracts M-phase apical expansion to enable mouse neural tube closure.” *J Cell Sci.* 132(13).

Butler, MT and JB Wallingford. 2017. “Planar cell polarity in development and disease.” *Nat Rev Mol Cell Biol* 18(6):375-388.

Byers, JT, RM Guzzo, M Salih, and BS Tuana. 2009. “Hydrophobic profiles of the tail anchors in SLMAP dictate subcellular targeting.” *BMC Cell Biol* 10(48).

Carvajal-Gonzalez, JM, S Mulero-Navarro, and M Mlodzik. 2016. “Centriole positioning in epithelial cells and its intimate relationship with planar cell polarity.” *Bioessays* 38(12):1234-1245.

Chan, DW, CY Chan, JW Yam, YP Ching, and IO Ng. 2006. “Prickle-1 negatively regulates Wnt/beta-catenin pathway by promoting Dishevelled ubiquitination/degradation in liver cancer..” *Gastroenterology* 131(4):1218-27.

Chavali, PL, M Pütz, and F Gergely. 2014. “Small organelle, big responsibility: the role of centrosomes in development and disease..” *Philos Trans R Soc Lond B Biol Sci.* 369(1650).

Chen, X and H Ding. 2011. “Increased expression of the tail-anchored membrane protein SLMAP in adipose tissue from type 2 Tally Ho diabetic mice.” *Exp Diabetes Res*.

Cheng, M, C Chen, K Yu, X Lv, Q Zeng, N Dong, and F Zhu. 2023. “Ablation of CXCR4 expression in cardiomyocytes exacerbates isoproterenol-induced cell death and heart failure.” *Int J Mol Med* 51(2):13.

Chen, R, R Xie, Z Meng, S Ma, and KL Guan. 2019. “STRIPAK integrates upstream signals to initiate the Hippo kinase cascade.” *Nat Cell Biol* 21(12):1565-1577.

Chen, R., R Xie, Z Meng, Shenghong Ma, and Kun-Liang Guan. 2019. “STRIPAK integrates upstream signals to initiate the Hippo kinase cascade..” *Nat Cell Biol* 21:1565-1577.

Chiapparo, G, X Lin, F Lescroart, S Chabab, C Paulissen, L Pitisci, A Bondue, and C Blanpain. 2016. “Mesp1 controls the speed, polarity, and directionality of cardiovascular progenitor migration.” *J Cell Biol.* 213(4):463-77.

Christoffels, V and B Jensen. 2020. “Cardiac Morphogenesis: Specification of the Four-Chambered Heart.” *Cold Spring Harb Perspect Biol* 10(a037143):12.

Christoffels, V and B. Jensen. 2020. “Cardiac Morphogenesis: Specification of the Four-Chambered Heart.” *Cold Spring Harb Perspect Biol.* 12(10):a037143.

Colombo, S, C de Sena-Tomás, V George, and et al. 2018. “Nkx genes establish second heart field cardiomyocyte progenitors at the arterial pole and pattern the venous pole through Isl1 repression.” *Development* 145(3).

Copp, AJ and ND Greene. 2010. “Genetics and development of neural tube defects..” *J Pathol* 220(2):217-30.

Copp, AJ and ND Greene. 2013. “Neural tube defects--disorders of neurulation and related embryonic processes.” *Wiley Interdiscip Rev Dev Biol* 2(2):213-227.

Cortes, C, A Francou, C De Bono, and RG Kelly. 2018. “Epithelial Properties of the Second Heart Field..” *Circ Res.* 122(1):142-154.

Couzens, AL, JD Knight, MJ Kean, G Teo, A Weiss, WH Dunham, ZY Lin, RD Bagshaw, F Sicheri, T Pawson, JL Wrana, H Choi, and AC Gingras. 2013. “Protein interaction network of the mammalian Hippo pathway reveals mechanisms of kinase-phosphatase interactions.” *Sci Signal* 6(302).

Davis, J, M Maillet, J Miano, and J Molkentin. 2012. “Lost in transgenesis: A user’s guide for genetically manipulating the mouse in cardiac research.” *Circ. Res* 111:761-777.

de Goederen, V, R Vetter, K McDole, and D. Iber. 2022. “Hinge point emergence in mammalian spinal neurulation..” *Proc Natl Acad Sci U S A* 119(20):e2117075119.

De Marco, P, E Merello, A Consales, G Piatelli, A Cama, Z Kibar, and V Capra. 2013. “Genetic analysis of disheveled 2 and disheveled 3 in human neural tube defects..” *J Mol Neurosci.* 49(3):582-8.

Del Re, DP, Y Yang, N Nakano, J Cho, P Zhai, T Yamamoto, N Zhang, N Yabuta, H Nojima, D Pan, and J Sadoshima. 2013. "Yes-associated protein isoform 1 (Yap1) promotes cardiomyocyte survival and growth to protect against myocardial ischemic injury." *J Biol Chem* 288(6):3977-3988.
Devenport, D. 2014. "The cell biology of planar cell polarity." *J Cell Biol* 207(2):171-179.
Dewan, Aaraf. 2016. "A Unique Role for Sarcolemmal Membrane Associated Protein Isoform 1 (SLMAP1) as a Regulator of Cardiac Metabolism and Endosomal Recycling." Retrieved August 19, 2016 (http://dx.doi.org/10.20381/ruor-843).
Dias, A, T Rehmani, M Salih, and BS Tuana. 2023. "The Tail Anchored Membrane Protein SLMAP3 Coordinates the Targeting of Centrosomal Proteins to the Nuclear Envelope for Skeletal Myogenesis." *iScience-Submitted*.
Durocher, D and SP Jackson. 2002. "The FHA domain." *FEBS Lett* 513(1):58-66.
Elramli, N, B Karahoda, Ö Sarikaya-Bayram, D Frawley, M Ulas, CE Oakley, BR Oakley, S Seiler, and Ö. Bayram. 2019. "AssemblyAssembly of a heptameric STRIPAK complex is required for coordination of light-dependent multicellular fungal development with secondary metabolism in Aspergillus nidulans." *PLoS Genet.* 15(3):e10008053.
Eom, DS, S Amarnath, and S Agarwala. 2012. "Apicobasal polarity and neural tube closure.." *Dev Growth Differ* 55(1):164-72.
Escuin, S, B Vernay, D Savery, C Gurnaik, W Witke, N Greene, and A Copp. 2015. "Rho-kinase-dependent actin turnover and actomyosin disassembly are necessary for mouse spinal neural tube closure." *J Cell Sci* 128(14):2468-2481.
Escuin, S., B. Vernay, D. Savery, C.B. Gurniak, W. Witke, N.D. Greene, and A.J. Copp. 2015. "Rho-Kinase-Dependent Actin Turnover and Actomyosin Disassembly are Necessary for Mouse Spinal Neural Tube Closure.." *J. Cell Sci. 2015, 128, 2468–2481.* 128:2468-2481.
George, V, S Colombo, and KL Targoff. 2014. "An early requirement for nkx2.5 ensures the first and second heart field ventricular identity and cardiac function into adulthood." *Dev Biol* 400(1):10-22.
Goudreault, M, LM D'Ambrosio, MJ Kean, MJ Mullin, BG Larsen, A Sanchez, S Chaudhry, GI Chen, F Sicheri, AI Nesvizhskii, R Aebersold, B Raught, and AC Gingras. 2009. "A PP2A Phosphatase High Density Interaction Network Identifies a Novel Striatin-interacting Phosphatase and Kinase Complex Linked to the Cerebral Cavernous Malformation 3 (CCM3) Protein." *Mol Cell Proteomics* 8(1):157-71.
Greene, ND and AJ Copp. 2014. "Neural tube defects." *Annu Rev Neurosci* 37:221-42.
Grego-Bessa, J, J Hildebrand, and KV. Anderson. 2015. "Morphogenesis of the mouse neural plate depends on distinct roles of cofilin 1 in apical and basal epithelial domains." *Development.* 142(7):1305-14.
Guo, N, C Hawkins, and J Nathans. 2004. "Frizzled6 controls hair patterning in mice.." *Proc Natl Acad Sci U S A* 101(25):9277-9281.
Guo, Y and WT Pu. 2020. "Cardiomyocyte Maturation: New Phase in Development." *Circ Res.* 126(8).
Gurniak, CB, E Perlas, and W Witke. 2005. "The actin depolymerizing factor n-cofilin is essential for neural tube morphogenesis and neural crest cell migration." *Dev Biol* 278(1):231-41.

Guzzo, R, M., M Salih, E, D. Moore, and B, S. Tuana. 2005. “Molecular properties of cardiac tail-anchored membrane protein SLMAP are consistent with structural role in arrangement of excitation-contraction coupling apparatus.” *Am J Physiol Heart Circ Physiol* 288(4):H1810-9.

Guzzo, RM, S Sevinc, Salih M, and BS Tuana. 2004. “A novel isoform of sarcolemmal membrane-associated protein (SLMAP) is a component of the microtubule organizing centre.” *J Cell Sci* 117(11):2271-81.

Guzzo, RM, J Wigle, M Salih, ED Moore, and BS Tuana. 2004. “Regulated expression and temporal induction of the tail-anchored sarcolemmal-membrane-associated protein is critical for myoblast fusion.” *Biochem J* 381(3):599-608.

Hall, John. 2011. *Guyton and Hall textbook of medical physiology*. Philedelphia: Saunders/Elsevie.

Hall, ME, Smith G, JE Hall, and DE Stec. 2011. “Systolic dysfunction in cardiac-specific ligand-inducible MerCreMer transgenic mice.” *Am J Physiol Heart Circ Physiol* 301(1):253-60.

Hartsock, A and W. J. Nelson. 2008. “ Adherens and tight junctions: structure, function and connections to the actin cytoskeleton.” *Biochimica Et Biophysica Acta (BBA) - Biomembranes* 1778(3):660-669.

Hauri, S, A Wepf, A van Drogen, M Varjosalo, N Tapon, R Aebersold, and M Gstaiger. 2013. “Interaction proteome of human Hippo signaling: modular control of the co-activator YAP1.” *Mol Syst Biol* 9(713).

Hazebroek, M, R Dennert, and S Heymans. 2012. “Idiopathic dilated cardiomyopathy: possible triggers and treatment strategies.” *Neth Heart J* 20(7-8):332-5.

Heallen, T, Y Morikawa, J Leach, G Tao, J. T. Willerson, R. L. Johnson, and J. F. Martin. 2013. “Hippo signaling impedes adult heart regeneration.” *Development* 140(23):4683-4690.

Heallen, T, M Zhang, J Wang, M Bonilla-Claudio, E Klysik, RL Johnson, and JF Martin. 2011. “Hippo pathway inhibits Wnt signaling to restrain cardiomyocyte proliferation and heart size.” *Science* 332(6028):458-61.

Hensley, N, J Dietrich, D Nyhan, N Mitter, MS Yee, and M Brady. 2015. “Hypertrophic cardiomyopathy: a review.” *Anesth Analg* 120(3):554-69.

Hochman, L, N Segev, N Sternberg, and G Cohen. 1983. “Site-specific recombinational circularization of bacteriophage P1 DNA.” *Virology* 131(1):11-17.

Horton, JL, MT Davidson, C Kurishima, RB Vega, JC Powers, TR Matsuura, C Petucci, ED Lewandowski, PA Crawford, DM Muoio, FA Recchia, and DP Kelly. 2019. “The failing heart utilizes 3-hydroxybutyrate as a metabolic stress defense.” *JCI Insight* 4(4):e124079.

Hu, D, H Barajas-Martinez, E Burashnikov, and et al. 2009. “A Mutation in the β3 Subunit of the Cardiac Sodium Channel Associated with Brugada ECG Phenotype.” *Circulation Cardiovascular genetics* 2(3):270-278.

Hwang, J and DC Pallas. 2013. “STRIPAK complexes: Structure, biological function, and involvement.” *The International Journal of Biochemistry* 47:118-48.

Ibrahim, M, J Gorelik, MH Yacoub, and CM Terracciano. 2011. “The structure and function of cardiac t-tubules in health and disease.” *Proceedings of the Royal Society B: Biological Sciences* 278(1719):2714-2723.

Ishikawa, T, A Sato, CA Marcou, DJ Tester, MJ Ackerman, L Crotti, PJ Schwartz, YK On, JE Park, K Nakamura, M Hiraoka, K Nakazawa, H Sakurada, T Arimura, N Makita, and A Kimura. 2012. "A novel disease gene for Brugada syndrome: sarcolemmal membrane-associated protein gene mutations impair intracellular trafficking of hNav1.5." *Circ Arrhythm Electrophysiol* 5(6):1098-107.

Ito, M, K Yamanouchi, K Naito, MP Calos, and H Tojo. 2011. "Site-specific integration of transgene targeting an endogenous lox-like site in early mouse embryos." *J Appl Genet* 52(1):89-94.

Ivanov, AI. 2008. "Actin motors that drive formation and disassembly of epithelial apical junctions." *Front Biosci.* 1(13):6662-81.

Janbandhu, VC, D Moik, and R Fässler. 2013. "Cre recombinase induces DNA damage and tetraploidy in the absence of loxP sites." *Cell Cycle* 13(3):462-70.

Jeong, BC, SJ Bae, L Ni, X Zhang, XC Bai, and X Luo. 2021. "Cryo-EM structure of the Hippo signaling integrator human STRIPAK." *Nat Struct Mol Biol* 28(3):290-299.

Karbassi, E, A Fenix, S Marchiano, N Muraoka, K Nakamura, X Yang, and CE Murry. 2020. "Cardiomyocyte maturation: advances in knowledge and implications for regenerative medicine." *Nat Rev Cardiol* 17(6):341-359.

Kaya-Çopur, A, F Marchiano, MY Hein, D Alpern, J Russeil, NM Luis, M Mann, B Deplancke, BH Habermann, and F Schnorrer. 2021. "The Hippo pathway controls myofibril assembly and muscle fiber growth by regulating sarcomeric gene expression." *Elife* 10:e63726.

Kelly, RG, ME Buckingham, and AF Moorman. 2014. "Heart fields and cardiac morphogenesis." *Cold Spring Harb Perspect Med.* 4(10):a015750.

Kelly, MC and P Chen. 2009. "Development of form and function in the mammalian cochlea." *Curr Opin Neurobiol* 19(4):395-401.

Kim, S, A Hill, ML Warman, and P Smits. 2012. "Golgi disruption and early embryonic lethality in mice lacking USO1." *PLoS One* 7(11):E50530.

Kindt, LM, AR Coughlin, TR Perosino, HN Ersfeld, M Hampton, and JO Liang. 2018. "Identification of transcripts potentially involved in neural tube closure using RNA sequencing." *Genesis* 56(3):e23096.

Koitabashi, N, D Bedja, AL Zaiman, YM Pinto, M Zhang, KL Gabrielson, E Takimoto, and DA Kass. 2009. "Avoidance of transient cardiomyopathy in cardiomyocyte-targeted tamoxifen-induced MerCreMer gene deletion models." *Circ Res* 105(1):12-5.

Kück, U, D Radchenko, and I Teichert. 2019. "STRIPAK, a highly conserved signaling complex, controls multiple eukaryotic cellular and developmental processes and is linked with human diseases." *Biol Chem.* 400(8):1005-1022.

Kuhn, Ralf and Raul, M. Torres. 2002. "Cre/LoxP Recombination System and Gene Targeting." *Transgenesis Techniques* 180(V):175-204.

Lee, S and JG Gleeson. 2020. "Closing in on Mechanisms of Open Neural Tube Defects." *Trends Neurosci* 43(7):519-532.

Lesko, AC, R Keller, P Chen, and A Sutherland. 2021. "Scribble mutation disrupts convergent extension and apical constriction during mammalian neural tube closure." *Dev Biol.* 478:59-75.

Leung, C, A Engineer, MY Kim, X Lu, and Q Feng. 2021. “Myocardium-Specific Deletion of Rac1 Causes Ventricular Noncompaction and Outflow Tract Defects.” *J Cardiovasc Dev Dis.* 8(3):29.
Liu, C, M Mei, Q Li, P Roboti, Q Pang, Z Ying, F Gao, M Lowe, and S Bao. 2016. “Loss of the golgin GM130 causes Golgi disruption, Purkinje neuron loss, and ataxia in mice.” *Proc Natl Acad Sci U S A* 114(2):346-351.
Li, D and J Wang. 2018. “Planar Cell Polarity Signaling in Mammalian Cardiac Morphogenesis..” *Pediatr Cardiol.* 39(5):1052-1062.
Lopes, Floro K., ST Artap, JI Preis, D Fatkin, G Chapman, MB Furtado, RP Harvey, H Hamada, DB Sparrow, and SL Dunwoodie. 2011. “Loss of Cited2 causes congenital heart disease by perturbing left-right patterning of the body axis.” *Hum Mol Genet* 20(6):1097-110.
Luk, A, E Ahn, GS Soor, and J Butany. 2009. “Dilated cardiomyopathy: a review.” *J Clin Pathol* 62(3):219-25.
Mahaffey, JP, J Grego-Bessa, Liem K. Jr, and KV Anderson. 2013. “Cofilin and Vangl2 cooperate in the initiation of planar cell polarity in the mouse embryo.” *Development* 140(6):1262-1271.
Mahmoud, AI, D Canseco, F Xiao, and HA Sadek. 2014. “Cardiomyocyte cell cycle: Meis-ing something?” *Cell Cycle* 13(7):1057-1058. Retrieved 2.
Major, JL, M Salih, and BS Tuana. 2015. “Interplay between the E2F pathway and β-adrenergic signaling in the pathological hypertrophic response of myocardium.” *J Mol Cell Cardiol* (84):179-90.
Marian, AJ and R Roberts. 2001. “The Molecular Genetic Basis for Hypertrophic Cardiomyopathy.” *Journal of molecular and cellular cardiology* 33(4):655-670.
Martin, AC and B Goldstein. 2014. “Apical constriction: themes and variations on a cellular mechanism driving morphogenesis.” *Development* 141(10):1987-98.
Ma, Q, B Zhou, and WT Pu. 2008. “Reassessment of Isl1 and Nkx2-5 cardiac fate maps using a Gata4-based reporter of Cre activity.” *Dev Biol* 323(1):98-104.
McNally, EM, JR Golbus, and MJ Puckelwartz. 2013. “Genetic mutations and mechanisms in dilated cardiomyopathy.” *The Journal of Clinical Investigation* 123(1):19-26.
McShane, SG, MA Molè, D Savery, ND Greene, PP Tam, and AJ Copp. 2015. “ Cellular basis of neuroepithelial bending during mouse spinal neural tube closure..” *Dev Biol* 404(2):113-24.
Meilhac, SM, F Lescroart, C Blanpain, and ME Buckingham. 2014. “Cardiac cell lineages that form the heart.” *Cold Spring Harb Perspect Med* 4(9):a013888.
Merte, J, D Jensen, K Wright, S Sarsfield, Y Wang, R Schekman, and DD Ginty. 2010. “Sec24b selectively sorts Vangl2 to regulate planar cell polarity during neural tube closure..” *Nat Cell Biol.* 12(1):41-6.
Migliavacca, J, B Züllig, C Capdeville, MA Grotzer, and M Baumgartner. 2022. “Cooperation of Striatin 3 and MAP4K4 promotes growth and tissue invasion.” *Commun Biol.* 5(1):795.
Misra, JR and KD Irvine. 2018. “The Hippo Signaling Network and Its Biological Functions.” *Annu Rev Genet* 52:65-87.

Missirlis, PI, DE Smailus, and RA Holt. 2006. “A high-throughput screen identifying sequence and promiscuity characteristics of the loxP spacer region in Cre-mediated recombination.” *BMC Genomics* 7(73).

Mitchell, LE. 2005. “Epidemiology of neural tube defects.” *Am J Med Genet C Semin Med Genet* 135C(1):88-94.

Mlynarova, J, M Trentin-Sonoda, F Gaisler da Silva, JL Major, M Salih, MS Carneiro-Ramos, and BS Tuana. 2019. “SLMAP3 isoform modulates cardiac gene expression and function.” *PLoS One* 14(4):e0214669.

Mohamed Farhan, H, M Nassar, M Hassan Ahmed, K Abougabal, and N. Abd Elazim Taha. 2022. “An association between the sarcolemmal membrane-associated protein gene and microvascular endothelial diabetic retinopathy in patients with type 2 diabetes mellitus: A preliminary case control study.” *Diabetes Metab Syndr.* 16(11):102653.

Murdoch, JN, C Damrau, A Paudyal, D Bogani, S Wells, ND Greene, P Stanier, and AJ Copp. 2014. “Genetic interactions between planar cell polarity genes cause diverse neural tube defects in mice..” *Dis Model Mech.* 7(10):1153-63.

Murdoch, JN, DJ Henderson, K Doudney, C Gaston-Massuet, HM Phillips, C Paternotte, R Arkell, P Stanier, and AJ. Copp. 2003. “Disruption of scribble (Scrb1) causes severe neural tube defects in the circletail mouse..” *Hum Mol Genet.* 12(2):87-98.

Nader, M, E Alsolme, S Alotaibi, R Alsomali, D Bakheet, and N. S. Dzimiri. 2019. “SLMAP-3 is downregulated in human dilated ventricles and its overexpression promotes cardiomyocyte response to adrenergic stimuli by increasing intracellular calcium.” *Can J Physiol Pharmacol.* 97(7):623-630.

Nader, M, B Westendorp, O Hawari, M Salih, A, F. Stewart, F, H. Leenen, and B, S. Tuana. 2012. “Tail-anchored membrane protein SLMAP is a novel regulator of cardiac function at the sarcoplasmic reticulum.” *Am J Physiol Heart Circ Physiol* 302(5):1138-1145.

Nash, CA, W Wei, R Irannejad, and AV Smrcka. 2019. “Golgi localized β1-adrenergic receptors stimulate Golgi PI4P hydrolysis by PLCε to regulate cardiac hypertrophy..” *Elife* 8(e48167).

Neal, SJ, Q Zhou, and F Pignoni. 2020. “STRIPAK-PP2A regulatesHippo-Yorkie signaling to suppress retinal fate in the Drosophila eye disc peripodial epithelium..” *J Cell Sci* 133(10):jcs237834.

Nerbonne, JM and RS Kass. 2005. “Molecular physiology of cardiac repolarization.” *Physiol Rev* 85(4):1205-53.

Nielsen, CP, KK Jernigan, NL Diggins, DJ Webb, and JA MacGurn. 2019. “USP9X Deubiquitylates DVL2 to Regulate WNT Pathway Specification..” *Cell Rep.* 28(4):1074-1089.

Niessen, Carien M., Deborah Leckband, and Alpha S. Yap. 2011. “Tissue Organization by Cadherin Adhesion Molecules: Dynamic Molecular and Cellular Mechanisms of Morphogenetic Regulation.” *Physiological Reviews* 91(2):691-731.

Nikolopoulou, E, GL Galea, A Rolo, ND Greene, and AJ Copp. 2017. “Neural tube closure: cellular, molecular and biomechanical mechanisms.” *Development* 144(4):552-566.

Nishimura, T, H Honda, and M Takeichi. 2012. “Planar Cell Polarity Links Axes of Spatial Dynamics in Neural-Tube Closure.” *Cell* 149(5):1084-1097.
Nordzieke, S, T Zobel, B Fränzel, DA Wolters, U Kück, and I Teichert. 2015. “A fungal sarcolemmal membrane-associated protein (SLMAP) homolog plays a fundamental role in development and localizes to the nuclear envelope, endoplasmic reticulum, and mitochondria.” *Eukaryot Cell* 14(1):345-58.
Orban, PC, Chui D, and JD Marth. 1992. “Tissue- and site-specific DNA recombination in transgenic mice.” *Proceedings of the National Academy of Sciences of the United States of America.* 89(15):6861-6865.
Park, TJ, SL Haigo, and JB Wallingford. 2006. “Ciliogenesis defects in embryos lacking inturned or fuzzy function are associated with failure of planar cell polarity and Hedgehog signaling.” *Nat Genet* 38(3):303-311.
Phillips, HM, HJ Rhee, JN Murdoch, V Hildreth, JD Peat, RH Anderson, AJ Copp, B Chaudhry, and DJ Henderson. 2007. “Disruption of planar cell polarity signaling results in congenital heart defects and cardiomyopathy attributable to early cardiomyocyte disorganization.” *Circ Res* 101(2):137-45.
Pinto, AR, A Ilinykh, MJ Ivey, JT Kuwabara, ML D'Antoni, R Debuque, A Chandran, L Wang, K Arora, NA Rosenthal, and MD Tallquist. 2016. “Revisiting Cardiac Cellular Composition..” *Circ Res.* 118(3):400-9.
Pourhaghighi, R, PEA Ash, S Phanse, F Goebels, LZM Hu, S Chen, Y Zhang, SD Wierbowski, S Boudeau, MT Moutaoufik, RH Malty, E Malolepsza, K Tsafou, A Nathan, G Cromar, H Guo, AA Abdullatif, DJ Apicco, LA Becker, AD Gitler, SM Pulst, A Youssef, R Hekman, PC Havugimana, CA White, BC Blum, A Ratti, CD Bryant, J Parkinson, K Lage, M Babu, H Yu, GD Bader, B Wolozin, and A Emili. 2020. “BraInMap Elucidates the Macromolecular Connectivity Landscape of Mammalian Brain..” *Cell Syst* 10(4):333-350.
Prévilon, M, M Le Gall, P Chafey, C Federeci, M Pezet, G Clary, C Broussard, G François, JJ Mercadier, and P Rouet-Benzineb. 2013. “Comparative differential proteomic profiles of nonfailing and failing hearts after in vivo thoracic aortic constriction in mice overexpressing FKBP12.6.” *Physiol Rep.* 1(3):e00039.
Pugach, EK, PA Richmond, JG Azofeifa, RD Dowell, and LA Leinwand. 2015. “Prolonged Cre expression driven by the α-myosin heavy chain promoter can be cardiotoxic.” *J Mol Cell Cardiol* 86:54-61.
Punovuori, K, M Malaguti, and S Lowell. 2021. “Cadherins in early neural development..” *Cell Mol Life Sci.* 78(9):4435-4450.
Qi, ZHENG, HU Rong-cui, ZHU Cui-yun, JING Jing, LOU Meng-yu, ZHANG Si-huan, LI Shuang, CAO Hong-guo, ZHANG Xiao-rong, and LING Ying-hui. 2023. “Identification of transition factors in myotube formation from proteome and transcriptome analyses.” *Journal of Integrative Agriculture* 10(2023):22.
Ravichandran, Y, B Goud, and JB Manneville. 2020. “The Golgi apparatus and cell polarity: Roles of the cytoskeleton, the Golgi matrix, and Golgi membranes.” *Curr Opin Cell Biol* 62:104-113.
Rehmani, T, A Dewan, M Salih, C Triggle, H Ding, and BS Tuana. 2016. “The cardiac specific isoform of tail anchored membrane protein SLMAP1 enhances GLUT4 levels by directing endosomal size and recycling.”.

Rehmani, T, A. P. Dias, M Salih, and B. S. Tuana. Submitted. “SLMAP3 is essential for neurulation through mechanisms that impact centrosomal and Golgi dynamics.” *EMBO Reports*.

Rehmani, T, J Mlynarova, J Byers, M Salih, and BS Tuana. 2021. “Specific Deletion of the FHA Domain Containing SLMAP3 Isoform in Postnatal Myocardium Has No Impact on Structure or Function.” *Cardiogenetics* 11(4):164-184.

Robinson A, Escuin, S., K Doudney, M Vekemans, RE Stevenson, ND Greene, AJ Copp, and P Stanier. 2012. “Mutations in the planar cell polarity genes CELSR1 and SCRIB are associated with the severe neural tube defect craniorachischisis.” *Hum Mutat* 33(2):440-7.

Rogers, C. D., L. K. Sorrells, and Bronner, M. E.. 2018. “A catenin-dependent balance between n-cadherin and e-cadherin controls neuroectodermal cell fate choices..” *Mechanisms of Development* 152:44-56.

Roszko, I., A. Sawada, and L Solnica-Krezel. 2009. “Regulation of convergence and extension movements during vertebrate gastrulation by the Wnt/PCP pathway.” *Semin. Cell. Dev. Biol.* 20:986-997.

Sabapathy, K, W Jochum, K Hochedlinger, LF Chang, M Karin, and , E. Wagner. 1999. “Defective neural tube morphogenesis and altered apoptosis in the absence of both JNK1 and JNK2..” *Mech Dev* 89:115-124.

Sallam, M, M Mysara, MA Benotmane, APG Crijns, D Spoor, F Van Nieuwerburgh, D Deforce, S Baatout, PJ Guns, A Aerts, and R. Ramadan. 2022. “DNA Methylation Alterations in Fractionally Irradiated Rats and Breast Cancer Patients Receiving Radiotherapy..” *Int J Mol Sci* 23(24):16214.

Santana, LF, EP Cheng, and WJ Lederer. 2010. “How does the shape of the cardiac action potential control calcium signaling and contraction in the heart?” *J Mol Cell Cardiol* 49(6):901-903.

Savolainen, SM, JF Foley, and SA Elmore. 2009. “Histology atlas of the developing mouse heart with emphasis on E11.5 to E18.5.” *Toxicol Pathol* 37(4):395-414.

Schleich, JM, T Abdulla, R Summers, and L Houyel. 2013. “An overview of cardiac morphogenesis.” *Arch Cardiovasc Dis* 106(11):612-623.

Schmidt, EE, DS Taylor, JR Prigge, S Barnett, and MR Capecchi. 2000. “Illegitimate Cre-dependent chromosome rearrangements in transgenic mouse spermatids.” *Proc Natl Acad Sci U S A* 97(25):13702-7.

Schwenk, F., U. Baron, and K. Rajewsky. 1995. “A cre-transgenic mouse strain for the ubiquitous deletion of loxp-flanked gene segments including deletion in germ cells.” *Nucleic Acids Research, 23(24), 5080-5081. https://doi.org/10.1093/nar/23.24.5080* 23(24):5080-5081.

Seidman, CE and JG Seidman. 1998. “Molecular genetic studies of familial hypertrophic cardiomyopathy.” *Basic Res.Cardiol* 93:13-6.

Seo, G, H Han, RE Vargas, B Yang, X Li, and W Wang. 2020. “MAP4K Interactome Reveals STRN4 as a Key STRIPAK Complex Component in Hippo Pathway Regulation.” *Cell Rep* 32(1):107860.

Severs, N. J. 2000. “The cardiac muscle cell.” *Bioessays* 2(22):188–199.

Shami Shah, A, AG Batrouni, D Kim, A Punyala, W Cao, C Han, ML Goldberg, Smolka, MB, and JM Baskin. 2019. “PLEKHA4/kramer Attenuates Dishevelled Ubiquitination to Modulate Wnt and Planar Cell Polarity Signaling.” *Cell Rep.* 27(7):2157-2170.

Shi, De-Li. 2022. “Wnt/planar cell polarity signaling controls morphogenetic movements of gastrulation and neural tube closure.” *Cellular and Molecular Life Sciences* 79(586).

Shi, Q and Y-G Chen. 2021. “Regulation of Dishevelled protein activity and stability by post-translational modifications and autophagy.” *Trends in Biochemical Sciences* 46(12):1003-1016.
Shi, Z, S Jiao, and Z Zhou. 2016. “STRIPAK complexes in cell signaling and cancer.” *Oncogene* 35(35):4549-57.
Sohal, D, S., M Nghiem, M, A. Crackower, S, A. Witt, T, R. Kimball, K, M. Tymitz, J, M. Penninger, and J, D. Molkentin. 2001. “Temporally regulated and tissue-specific gene manipulations in the adult and embryonic heart using a tamoxifen-inducible Cre protein.” *Circ Res.* 89(1):20-5.
Srivastava, D. 2006. “Making or breaking the heart: from lineage determination to morphogenesis.” *Cell* 126(6):1037-48.
Srivastava, D. 2006. “Making or breaking the heart: from lineage determination to morphogenesis.” *Cell* 126(6):1037-48.
Stanley, EG, C Biben, A Elefanty, L Barnett, F Koentgen, L Robb, and RP Harvey. 2002. “Efficient Cre-mediated deletion in cardiac progenitor cells conferred by a 3'UTR-ires-Cre allele of the homeobox gene Nkx2-5.” *Int J Dev Biol* 46(4):431-9.
Statistics Canada. 2014. “Leading causes of death, total population, by age group and sex, Canada, annual.” Canada. Retrieved May 27, 2016 (http://www5.statcan.gc.ca/cansim/a26?lang=eng&id=1020561).
Stephens, R, K Lim, M Portela, M Kvansakul, PO Humbert, and HE Richardson. 2018. “The Scribble Cell Polarity Module in the Regulation of Cell Signaling in Tissue Development and Tumorigenesis.” *J Mol Biol* 430(19):3585-3612.
Stopp, S, M Gründl, M Fackler, and et al. 2017. “Deletion of Gas2l3 in mice leads to specific defects in cardiomyocyte cytokinesis during development.” *Proc Natl Acad Sci U S A* 114(30):8029-8034.
Sueishi, M, M Takagi, and Y Yoneda. 2000. “The forkhead-associated domain of Ki-67 antigen interacts with the novel kinesin-like protein Hklp2.” *J Biol Chem* 275(37):28888-92.
Swärd, K, KK Krawczyk, B Morén, B Zhu, L Matic, J Holmberg, U Hedin, B Uvelius, K Stenkula, and C Rippe. 2019. “Identification of the intermediate filament protein synemin/SYNM as a target of myocardin family coactivators..” *Am J Physiol Cell Physiol.* 317(6):C1128-1142.
Tadevosyan, K, O Iglesias-García, MM Mazo, F Prósper, and A Raya. 2021. “Engineering and Assessing Cardiac Tissue Complexity.” *Int J Mol Sci* 22(3):1479.
Tang, Y, M Chen, L Zhou, J Ma, Y Li, H Zhang, Z Shi, Q Xu, X Zhang, Z Gao, Y Zhao, Y Cheng, S Jiao, and Z Zhou. 2019. “Architecture, substructures, and dynamic assembly of STRIPAK complexes in Hippo signaling.” *Cell Discov* 5(3).
Taverna, E and WB Huttner. 2019. “The Golgi Apparatus in Polarized Neuroepithelial Stem Cells and Their Progeny: Canonical and Noncanonical Features.” *Results Probl Cell Differ.* 67:359-375.
Thyagarajan, B, MJ Guimarães, AC Groth, and MP Calos. 2000. “Mammalian genomes contain active recombinase recognition sites.” *Gene* 244(2):47-54.
van den Berg, G, R Abu-Issa, B. A. de Boer, M. R. Hutson, P. A. de Boer, A. T. Soufan, J. M. Ruijter, M. L. Kirby, M. J. van den Hoff, and A. F. Moorman. 2009. “A caudal proliferating growth center contributes to both poles of the forming heart tube.” *Circ Res* 104(2):179-188.

van den Hoff, MJ, BP Kruithof, AF Moorman, RR Markwald, and A Wessels. 2001. "Formation of myocardium after the initial development of the linear heart tube." *Dev Biol* 240(1):61-76.
van der Spuy, M, JX Wang, D Kociszewska, and MD White. 2023. "The cellular dynamics of neural tube formation." *Biochem Soc Trans* 51(1):343-352.
Vergarajauregui, S, R Becker, U Steffen, M Sharkova, T Esser, J Petzold, F Billing, MS Kapiloff, G Schett, I Thievessen, and FB Engel. 2020. "AKAP6 orchestrates the nuclear envelope microtubule-organizing center by linking golgi and nucleus via AKAP9. Elife. 2020 Dec." *eLife* 9(e61669.).
Verrou, C, Y Zhang, C Zürn, WW Schamel, and M Reth. 1999. "Comparison of the tamoxifen regulated chimeric Cre recombinases MerCreMer and CreMer." *Biol Chem* 380(12):1435-8.
Vincent, SD and ME. Buckingham. 2010. "How to make a heart: the origin and regulation of cardiac progenitor cells.." *Curr Top Dev Biol* 90:1-41.
von, Gise A., Z Lin, K Schlegelmilch, LB Honor, GM Pan, JN Buck, Q Ma, T Ishiwata, B Zhou, FD Camargo, and WT Pu. 2012. "YAP1, the nuclear target of Hippo signaling, stimulates heart growth through cardiomyocyte proliferation but not hypertrophy." *Proc Natl Acad Sci U S A* 109(7):2394-9.
Wallingford, JB. 2012. "Planar cell polarity and the developmental control of cell behavior in vertebrate embryos." *Annu Rev Cell Dev Biol* 28:627-53.
Wallingford, JB and R Habas. 2005. "The developmental biology of Dishevelled: an enigmatic protein governing cell fate and cell polarity." *Development* 132(20):4421-36.
Wang, T, L Chen, T Yang, P Huang, L Wang, L Zhao, S Zhang, Z Ye, L Chen, Z Zheng, and J Qin. 2019. "Congenital Heart Disease and Risk of Cardiovascular Disease: A Meta-Analysis of Cohort Studies." *J Am Heart Assoc* 8(10):e012030.
Wang, L, K Choi, T Su, B Li, X Wu, R Zhang, JH Driskill, H Li, H Lei, P Guo, EH Chen, Y Zheng, and D Pan. 2022. "Multiphase coalescence mediates Hippo pathway activation." *Cell* 185(23):4376-4393.
Wang, J, NS Hamblet, S Mark, and et al. 2006. "Dishevelled genes mediate a conserved mammalian PCP pathway to regulate convergent extension during neurulation." *Development* 133(9):1767-1778.
Wang, P, B Mao, W Luo, B Wei, W Jiang, D Liu, L Song, G Ji, Z Yang, YQ Lai, and Z Yuan. 2014. "The alteration of Hippo/YAP signaling in the development of hypertrophic cardiomyopathy." *Basic Res Cardiol* 109(5):435-8.
Wang, M, P Marco, V Capra, and Z Kibar. 2019. "Update on the Role of the Non-Canonical Wnt/Planar Cell Polarity Pathway in Neural Tube Defects." *Cells* 8(10):1198.
Westendorp, B, JL Major, M Nader, M Salih, FHH Leenen, and BS Tuana. 2012. "The E2F6 repressor activates gene expression in myocardium resulting in dilated cardiomyopathy." *FASEB Journal* 26(6):2569-2579.
Wexler, R, T Elton, A Pleister, and D Feldman. 2009. "Cardiomyopathy: An Overview." *American family physician* 79(9):778-784.
Wielowieyski, PA, S Sevinc, R Guzzo, M Salih, JT Wigle, and BS Tuana. 2000. "Alternative splicing, expression, and genomic structure of the 3' region of the gene encoding the sarcolemmal-associated proteins

(SLAPs) defines a novel class of coiled-coil tail-anchored membrane proteins." *J Biol Chem* 275(49):38474-81.

Wigle, JT, L Demchyshyn, MA Pratt, WA Staines, M Salih, and BS Tuana. 1997. "Molecular cloning, expression, and chromosomal assignment of sarcolemmal-associated proteins. A family of acidic amphipathic alpha-helical proteins associated with the membrane." *J Biol Chem* 272(51):32384-94.

Williams, M, W Yen, X Lu, and A Sutherland. 2014. "Distinct apical and basolateral mechanisms drive planar cell polarity-dependent convergent extension of the mouse neural plate." *Dev Cell.* 29(1):34-46.

Woodcock, E and Scot Matkovich. 2005. "Cardiomyocytes structure, function and associated pathologies." *The International Journal of Biochemistry & Cell Biology* 37(9):1746-51.

Wu, G, J Ge, X Huang, Y Hua, and D Mu. 2011. "Planar cell polarity signaling pathway in congenital heart diseases." *J Biomed Biotechnol* 589414.

Xiao, S and RM Shaw. 2015. "Cardiomyocyte protein trafficking: Relevance to heart disease and opportunities for therapeutic intervention." *Trends Cardiovasc Med* 25(5):379-89.

Xin, M, Y Kim, LB Sutherland, M Murakami, X Qi, J McAnally, ER Porrello, AI Mahmoud, W Tan, JM Shelton, JA Richardson, HA Sadek, R Bassel-Duby, and EN Olson. 2013. "Hippo pathway effector Yap promotes cardiac regeneration." *Proc Natl Acad Sci U S A. 2013 Aug 20;110(34* 110(34):13839-44.

Yacoub, MH. 2014. "Decade in review--cardiomyopathies: Cardiomyopathy on the move." *Nat Rev Cardiol* 11(11):628-9.

Yamamoto, S, G Yang, D Zablocki, J Liu, C Hong, SJ Kim, S Soler, M Odashima, J Thaisz, G Yehia, CA Molina, A Yatani, DE Vatner, SF Vatner, and J Sadoshima. 2003. "Activation of Mst1 causes dilated cardiomyopathy by stimulating apoptosis without compensatory ventricular myocyte hypertrophy." *J Clin Invest* 111(10):1463-1474.

Ybot-Gonzalez, P, D Savery, D Gerrelli, M Signore, CE Mitchell, CH Faux, ND Greene, and AJ Copp. 2007. "Convergent extension, planar-cell-polarity signalling and initiation of mouse neural tube closure." *Development* 134(4):789-799.

Yin, Z, J Ren, and W Guo. 2015. "Sarcomeric Protein Isoform Transitions in Cardiac Muscle: A Journey to Heart Failure." *Biochimica et biophysica acta* 1852(1):47-52.

Yoshida T, Yamashita M. H. C. H. M. 2014. "Kruppel-like factor 4 protein regulates isoproterenol-induced cardiac hypertrophy by modulating myocardin expression and activity." *J Biol Chem* 289(38):26107-26118.

Yotti, R, CE Seidman, and JG Seidman. 2019. "Advances in the genetic basis and pathogenesis of sarcomere cardiomyopathies." *Annu Rev Genomics Hum Genet* 20:129-153.

Yu, FX, B Zhao, and KL Guan. 2015. "Hippo Pathway in Organ Size Control, Tissue Homeostasis, and Cancer." *Cell* 163(4):811-28.

Zallen, JA. 2007. "Planar polarity and tissue morphogenesis." *Cell* 129(6):1051-63.

Zheng, M, J Jacob, SH Hung, and J Wang. 2020. "The Hippo Pathway in Cardiac Regeneration and Homeostasis: New Perspectives for Cell-Free Therapy in the Injured Heart." *Biomolecules* 10(7).

Zheng, Y, B Liu, L Wang, H Lei, KD Pulgar Prieto, and D Pan. 2017. “Homeostatic Control of Hpo/MST Kinase Activity through Autophosphorylation-Dependent Recruitment of the STRIPAK PP2A Phosphatase Complex.” *Cell Reports* 21(12):3612-3623.
Zheng, Y and D Pan. 2019. “The Hippo Signaling Pathway in Development and Disease.” *Dev Cell* 50(3):264-282.
Zhou, Q, L Li, B Zhao, and K.L Guan. 2015. “The Hippo pathway in heart development, regeneration, and diseases.” *Circulation research* 116(8):1431-1447.
Zihni, C, C Mills, K Matter, and MS Balda. 2016. “Tight junctions: from simple barriers to multifunctional molecular gates.” *Nat Rev Mol Cell Biol.* 17(9):564-80.
Zohn, IE. 2020. “ Mouse Models of Neural Tube Defects..” *Adv Exp Med Biol. 2020;1236:39-64. doi: 10.1007/978-981-15-2389-2_2. PMID: 32304068.* 1236:39-64.
Zohn, IE and AA Sarkar. 2008. “Modeling neural tube defects in the mouse.” *Curr Top Dev Biol* 84:1-35.